Information Engineering Department

University of Pisa

Ph.D. Thesis

"MEM Resonators for RF Applications and Chemical Sensing"

Curriculum "Micro and nanoelectronic technologies, devices and systems"

XIX CICLO

Tutors: | **Ph. D. Student:**

Prof. A. Nannini | ***Ing. Dario Paci***

Ing. F. Pieri

Acknowledgements

I would like to thank everybody who helped me during these three years of Ph.D., first of all my parents who gave me the necessary support to achieve my goals. I would like especially thank my advisors Andrea Nannini and Francesco Pieri for their helpful suggestion and for the topic they proposed to me to investigate. A great thank you also to people from IMEC, especially Harrie Tilmans and Steve Stoffels, who collaborated with me during my staying at IMEC, as well as to people from PEL-ETHZ, where I spent three very fruitful months.

Then I thank all the people of the Microsystems Laboratory, professors researchers and other Ph.D students, as Antonio, Lucanos and Pietro which shared with me this important experience of my life. Thank also to the master degree students, as Massimo and Andrea, which achieved their thesis with an activity developed at Microsystems Laboratory and which gave in this way also a big contribution to this Ph.D. thesis.

And a final thank you to my beloved girlfriend Giovanna, who stayed always close to me, through all this time, even if sometimes I was too much concentrated on my work or I was even in another country to pursue my Ph.D.

Indeed she was the most important person for me during these last three years and without her no result would be possible or important.

To my parents

“There are more things in heaven and earth, Horatio,
Than are dreamt of in your philosophy.”

W. Shakespeare

Introduction

MEMS (*MicroElectroMechanical Systems*) offer nowadays several stimulating possibilities to the research of new devices and new architectures for electronics systems. Such devices are composed of mechanical components and transducers, which convert electrical signals (voltages or currents) in mechanical quantities (such as forces, displacements) and vice versa. Their main feature is that they can be fabricated with technologies similar to the ones used to produce integrated circuits, so that MEMS can be fabricated on a chip and in some cases on the same chip together with an electronics system if their fabrication process is fully IC-compatible.

The way MEMS can be produced allows the integration in a *system on a package* or even *in a system on a chip* of devices once macroscopic, like many sensor or like mechanical resonators, commonly quartzes, often used in electronics systems as frequency references.

Among MEMS, MEM resonators are particularly attractive: indeed the expression “MEM resonator” includes a lot of different devices, whose operating principle is based on the mechanical resonance of one or more moveable part composing the device.

Several are the proposed potential applications of MEM resonators: they can be used as frequency references in electronic systems or as fundamental components in electronic filters, local oscillators or mixers in RF communication systems. They can be even designed so as to maximize the sensitivity of their resonance frequency to temperature, humidity or the adsorption of a particular kind of molecule, in order to obtain sensors of these respective physical quantities.

MEM resonators for RF applications are especially important because they potentially allow the integration on a single-chip RF transceiver of some of the components, as filters and oscillators, which are currently out-of-chip components. Furthermore, the possibility of integrating a large number of resonators on a single chip leads to the possibility of new architectures for RF transmission systems [1]. In a different field, resonators for chemical sensing can allow new solutions for chemical analysis: a huge number of sensors on a single chip will make the detection of a very large number of different molecules possible, enabling very complex, simultaneous analyses and making the idea of a “lab on a chip” viable.

Fundamental parameters for a MEM resonator are the resonance frequency and the quality factor. This last parameter measures the frequency selectivity of the filter: a high quality factor means high selectivity in filter architectures and a low phase noise in oscillator architecture.

The goal of this Ph.D. thesis is to give a small, but hopefully important contribution to the research in the field of MEM resonators, and in particular to the design of RF MEM resonators and resonator-based chemical sensors.

The research activity discussed in this thesis starts from the design of MEM resonators for RF applications with resonance frequency in the range 5-50 MHz and high quality factor, intended to be used as filters or as frequency selective element in oscillator. These devices are based on bending polysilicon beams. Among them two innovative devices are presented: the first, namely *free-free third-mode resonator with flexural supports*, allow theoretically to reach higher resonance frequencies and lower insertion losses than other resonators based on bending beams; the second is a resonator with tuneable resonance frequency.

The design, and the characterization of these devices, will be largely discussed in the following, as well as the results from FEM simulations, which were especially useful to understand the behaviour of these devices when it was different from the expected one. The fabrication of the devices was carried out using *THELMA* process, provided by *STMicroelectronics*.

Since the importance of the long-term stability of the resonance frequency of the device if it is used as a frequency reference, the effect of temperature on the resonance frequency of flexural-beam resonators was studied both analytically and by FEM simulations. On the other hand the effect of residual stresses was taken into account, because it can make the device to have a resonance frequency different to the nominal one.

Last but not least, an equivalent circuit for the designed resonators was extracted. Equivalent circuits for MEMS are very important both to allow the simulation of MEMS together with electronics systems with a typical tool for the simulation of electronics circuits (for example Pspice), and to provide a handy and quick synthesis and analysis tool to the system-level designer. Practically equivalent circuits are necessary to facilitate the integration of MEMS with electronic circuits almost as much as the fabrication processes.

The topology of the flexural-beam resonators presented in this thesis was optimized to reach a high resonance frequency. Nonetheless, this kind of resonator can reach only resonance frequency not higher than 100 MHz. To reach higher resonance frequencies, which are needed for several RF applications, it is necessary to choose another kind of MEM resonators, the so-called *bulk-mode resonator*, which are based on mechanical structures, such as squares or disks, which are locally compressed or expanded at the resonance. The deformed shape at the resonance of different devices can be dissimilar, but in any case bulk-mode resonators generally allow to obtain a resonance frequency as high as 1 GHz, retaining quality factor higher than in flexural-beam resonators (from 1000 to 100.000 in dependence of the resonance frequency).

Thus, in the framework of a collaboration with the international research centre IMEC (Interuniversity MicroElectronics Centre) of Leuven (Belgium), bulk-mode disk resonators were studied in order to find a way of optimizing their layout. The fundamental task of this optimization was the maximization of the quality factor of the device at the particular resonance frequency given by the specification.

An analysis of the main physical mechanisms determining the quality factor was consequently done. This analysis led to the theoretical models and simulation methods, which will be shown in this thesis and which were essential to optimize the devices design.

While this activity was carried out with respect to MEM resonators for RF application, another research was pursued in the field of MEM resonators for chemical sensing.

In this thesis, the design, fabrication and characterization of an innovative MEM microbalance will be presented. A microbalance is a resonator, which changes its resonance frequency proportionally to the mass of a particular molecule adsorbed by a sensitive layer deposited on the device. Such layer has to be chosen to adsorb maximally one kind of molecule and minimally all the other kind of molecules. A microbalance can be thus used to sense the presence of a particular gas, as well as complex organic molecules, such as proteins or DNA. But it can be even used for other purpose, as for example the measurement of the thickness of a layer deposited on a chip during typical steps of IC fabrication process, such as sputtering or evaporation.

The microbalance which will be presented in this thesis is innovative both because of its mechanical structure and for the actuation.

The resonator is magnetically driven, exploiting the “bias” provided by an external and constant magnetic field, which interacts with an input current flowing in a loop, generating a Lorentz force, which actuates the device. Besides the magnetic field is also used to sense the device movements, which leads to variation of the flow of the magnetic field through another metallic loop, generating an electromotive force as an output signal. Magnetic actuation and sensing are not often used in MEMS, despite their potentiality and only in few cases they are used together.

Finally, a very important feature of the presented device is that it is fabricated with a low-cost CMOS-compatible process. The first steps of the process were carried out using the standard mixed technology *BCD6* (including BJT, CMOS and DMOS), provided by *STMicroelectronics*, while the last steps, including the release of the mechanical structure were accomplished in the Microsystems Laboratory of the Information Engineering Department of the University of Pisa.

1. State of the art of MEM resonators for RF applications and chemical sensing

1.1 MEM resonators: from the working principle to the applications

Before any discussion about the topic dealt with in this thesis, it is necessary to define the class of devices addressed: a “MEM resonator” is a micro-electro-mechanical system (MEMS), that is, a machine composed by micrometric transducers, changing electrical signals into mechanical ones and vice versa, and mechanical moveable parts, which can be integrated together on a chip by technologies similar to the ones used to fabricate integrated electronics circuits and sometimes they can be even fabricated on the same chip with an electronic system, if the fabrication processes for MEMS and electronics are compatible. A MEM resonator is usually composed of a mechanical structure (rotor) and one or more transducers, which are used to actuate a force by an electrical signal (input signal), driving consequently the structure into motion, and to transduce its movements in another electrical signal (output signal) proportional to their amplitude (Figure 1). The relation between input electrical signal and force actuated on the rotor depends on the kind of actuation, but can be generally considered as linear at least for small signals, unless the resonator is used as a component in mixers [1] or is characterized employing some particular system of measurements, which requires a non-linear actuation [2]. The same usually holds also for the relation between rotor movements and output signal. If the driving signal is a sinusoid with frequency equal to one of the resonance frequencies of the mechanical structure, the rotor movements are much higher than if the input signal was at a frequency far from any resonance frequencies. As a consequence, being the electrical output signal proportional to the amplitude of rotor movements, also the output signal will be a sinusoid at the same frequency of the input signal and with amplitude higher than at any other frequency.

Generally in a MEM resonator, the mechanical structure and the input transducers are properly designed in order to obtain the highest movements amplitude, when the input signal frequency is equal to one particular frequency chosen among all the resonance frequencies, while the movements amplitude is minimized for all the other resonance frequencies: in this case, if the resonator is considered as a "black box", the whole device can be considered as an electrical bandpass filter with central frequency equal to the selected resonance frequency. The same can be obtained also by properly designing the output transducers in order to reduce the output electrical signal amplitude when the device resonates at resonance frequency different from the chosen one. If it is not possible to lessen enough the output signal for all the resonance frequency different from the central frequency of the filter, it can be useful to have a large separation between the selected resonance frequency and all the others, in order to have ideal bandpass behaviour, at least in a certain range of frequencies.

Besides the resonance frequency, the other fundamental parameter, which characterizes a MEM resonator is the frequency selectivity, that is, the ability of cut the input signal at frequencies close but different to the central frequency of the filter.

The selectivity of a resonator is measured by the *"quality factor"* Q. One of the possible definitions for the quality factor is:

$$Q = \frac{f_0}{B_{-3dB}} \tag{1}$$

where f_0 is the resonance frequency and B_{-3dB} is the 3dB bandwidth, the distance from the resonance frequency at which the output signal is 3dB lower than at the resonance. It is clear that this definition is strictly related to the frequency selectivity concept and that the higher the Q, the higher the selectivity.

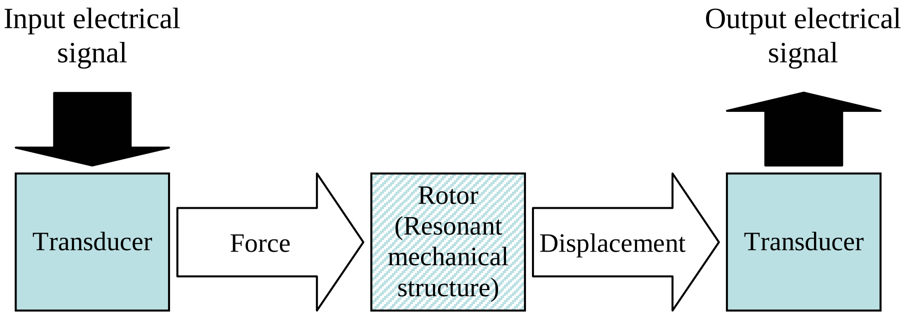

Figure 1: Standard structure of a MEM resonator.

1.1.1 Actuation and sensing mechanisms

The main actuation mechanism used in MEM resonators is based on the electrostatic force: with respect to two conductors (i.e. a capacitor), if they are at a different electric potential they exert a force on each other and if one of the two can move in a direction it can be driven into motion and consequently work as rotor, or be connected to the rotor to actuate it. As an example, it is possible to consider the parallel plate capacitor in Figure 2a: one of the conductors can move in a rigid way in a direction parallel to the other one. In this condition, according to the virtual work principle, the actuated force F_e is:

$$F_e = \frac{\partial U_e}{\partial u_x} = \frac{1}{2}\frac{\partial C}{\partial u_x}V^2 = \frac{1}{2}\frac{\varepsilon_0 H}{d}V^2 \tag{2}$$

where U_e is the energy stored in the electric field, u_x a infinitesimal displacement in x direction, C the capacitance and V the applied voltage; ε_0 is the dielectric constant of the air between the two conductors, H their thickness (in z direction) and d the distance. This kind of electrostatic actuation, constant with the actuation was used often in the oldest resonators [3], but it is not too much efficient.

If the moveable plate is forced to move in direction perpendicular to the other conductor as in Figure 2b, the actuated force is:

$$F_e = \frac{\partial U_e}{\partial u_y} = \frac{1}{2}\frac{\partial C}{\partial u_y}V^2 = \frac{1}{2}\frac{\varepsilon_0 HL}{\left(d - u_y\right)^2}V^2 \tag{3}$$

where L is the length along which the electrodes face each other. This time the force is $L\backslash d$ times higher than in the previous case, so that designing long and close electrodes, it is easy to reach values of the force even 100 times higher than in the previous case, applying the same actuation voltage. The drawbacks of the configuration in Figure 2b is that the force depends on the moveable plate displacement u_y, introducing a limit to the linearity of equations, which rules the device behaviour. However the displacement amplitude is generally much smaller than the gap between electrodes, so that this electrostatic actuation is generally preferred to the other one, not only for the resonators but also for other MEMS.

In both cases the relation between the input voltage and the actuated force is quadratic, and thus non-linear, so that the signal is generally superposed to a DC voltage V_{DC} higher enough than the signal Vs, in order to make Eqs. (2) and (3) linear with respect to V_S for small value of the signal[1].

The actuators in Figure 2 can be used also as sensing elements, i.e. to convert the movements of the rotor in an output electrical signal. If a DC bias voltage V_{DC} is applied between the two electrodes and if the moveable plate displacement u_y in direction perpendicular to the electrodes is a function of the time (Figure 2b, with $V_{DC} = V_S$), a current I flows in the capacitor:

$$I = \frac{\partial\left(CV_{DC}\right)}{\partial t} = V_{DC}\frac{\partial C}{\partial t} = V_{DC}\frac{\partial C}{\partial u_y}\frac{\partial u_y}{\partial t} = V_{DC}\frac{1}{2}\frac{\varepsilon_0 HL}{\left(d-u_y\right)^2}\frac{\partial u_y}{\partial t} \tag{4}$$

Considering rotor displacements u_x in the other direction (Figure 2a, with $V_{DC} = V_S$) an expression similar for the current can be extracted:

$$I = \frac{\partial\left(CV_{DC}\right)}{\partial t} = V_{DC}\frac{\partial C}{\partial t} = V_{DC}\frac{\partial C}{\partial u_x}\frac{\partial u_x}{\partial t} = V_{DC}\frac{1}{2}\frac{\varepsilon_0 H}{d}\frac{\partial u_x}{\partial t} \tag{5}$$

Like the actuation, the sensing mechanism exploiting rotor movements in direction perpendicular to the plates is non-linear but more efficient than the one which converts movements parallel to the electrodes in current, so that it is anyway preferred to this. In general the rotor can also deform, as in the bi-dimensional example in Figure 3. In this case, the forces per unit length, f_x along x and f_y along y can be defined as:

$$\begin{pmatrix} f_x\left(x,t\right) \\ f_y\left(x,t\right) \end{pmatrix} = \frac{1}{2}V^2 \begin{pmatrix} \dfrac{\partial c\left(x,t\right)}{\partial u_x\left(x,t\right)} \\ \dfrac{\partial c\left(x,t\right)}{\partial u_y\left(x,t\right)} \end{pmatrix} \tag{6}$$

where c is a capacitance per unit length. While the linear current density j flowing through the capacitor will be, if a DC bias voltage V_{DC} is applied:

$$j\left(x,t\right) = V_{DC}\frac{\partial c\left(x,t\right)}{\partial t} = V_{DC}\left[\frac{\partial c\left(x,t\right)}{\partial u_x\left(x,t\right)}\frac{\partial u_x\left(x,t\right)}{\partial t} + \frac{\partial c\left(x,t\right)}{\partial u_y\left(x,t\right)}\frac{\partial u_y\left(x,t\right)}{\partial t}\right] \tag{7}$$

---

[1] $V^2 = \left(V_{DC} + V_S\right)^2 \approx V_{DC}^2 + 2V_{DC}V_S$

Eqs. (6) and (7) can be easily generalized to the 3D case, defining current density, forces and capacitance per unit area.

Other mechanisms used to actuate MEM resonators or sense their movements exploit magnetic interactions, piezoelectricity, thermal expansion (thermomechanical actuation) and piezoresistivity. These actuation/sensing mechanism are the same used in also all the other MEMS, but in the following they will be discussed with respect to their usage in MEM resonators.

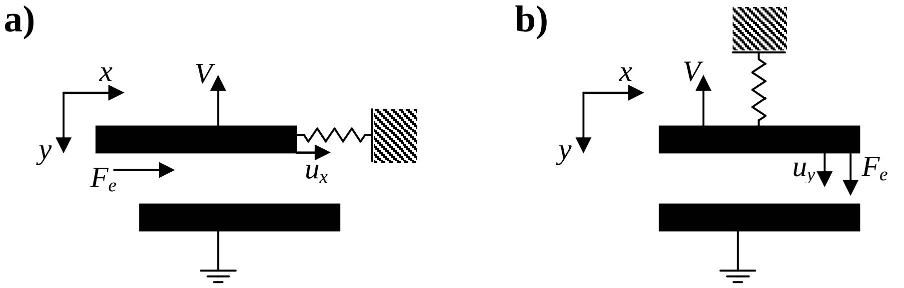

Figure 2: Electrostatic actuation/sensing: a) the moveable plate is forced to move in direction parallel to the plates (x direction); b) the rotor can move only in direction perpendicular to the plates (y direction). The moveable plates are connected to the anchor through a spring.

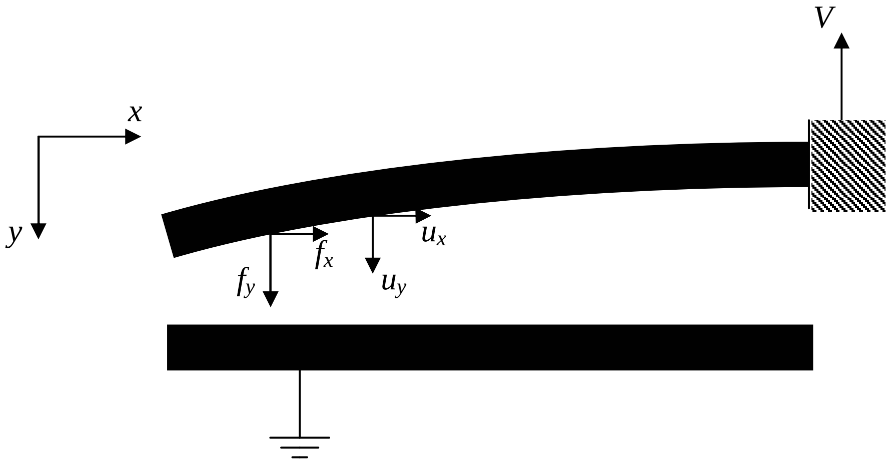

Figure 3: Electrostatic actuation/sensing of a deformable rotor, leading to a distributed load/current: the moveable electrode is a cantilever, a slender beam clamped at one end.

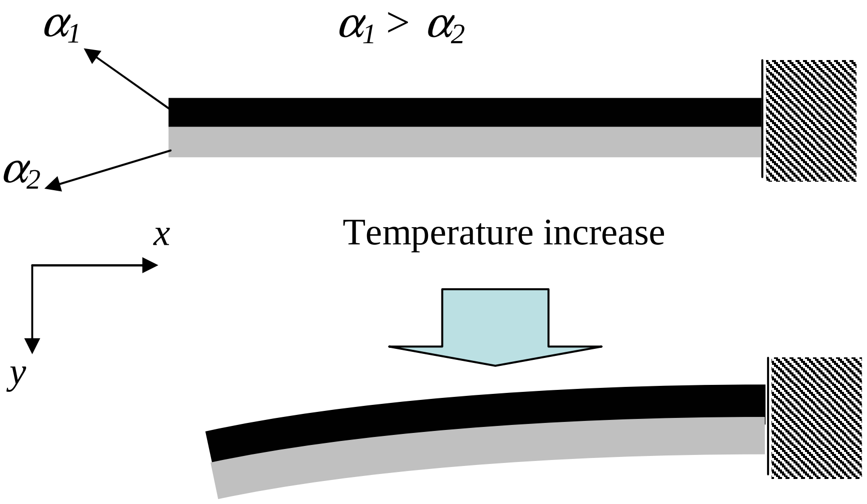

Figure 4: Thermomechanical actuation exploiting the bimorphic effect: a cantilever is made of two layers with different coefficient of thermal expansion α_1 *and* α_2*, so that heating the cantilever it is possible to bend it.*

The magnetic driving [4] generally exploits the Lorentz force acting on a current-carrying wire in a magnetic field, and will be discussed in detail in chapter 4. In this case the input signal is the current flowing in the wire and the relation between driving signal and actuated force is linear. Also a magnetic sensing [6] is possible and in this case the change in magnetic flux through an integrated moving inductance can be exploited. The implementation of magnetic actuation or sensing is complicated by the need of generating a magnetic field and is less efficient than electrostatic when device dimensions scale down. Being necessary to reduce the dimension of devices to reach high resonance frequencies, the magnetic actuation and sensing can be used only for low-frequencies applications.

Piezoelectric actuation and sensing [7] are based on the fact that some particular materials deform if an electric field is applied on them and is directed in a proper direction. They are more efficient than electrostatic, but require the deposition of materials such as AlN (aluminium nitride) or PZT (lead zirconate titanate), which cannot be easily included in fabrication flows compatible with standard electronic processes like the CMOS. This technological complexity generally prevents from implementing piezoelectric actuation and sensing, because the possibility of integration of

MEMS together with electronics is one of the main advantages of these devices.

The thermal expansion of materials can be exploited to actuate a resonator if it is composed of materials with different coefficients of thermal expansion (CTE) α [8] as the bilayer cantilever in Figure 4: heating the cantilever a compressive stress is exerted on the layers with the highest CTE, while a tensile stress loads the material with the lowest CTE. Thus a stress gradient in transverse direction (y direction in Figure 4) is obtained and it makes the cantilever to bend. This effect is known also as bimorphic effect. The heating of the cantilever can be achieved by driving a current I in heating resistors integrated along the cantilever. The relation between input current and actuated force is non-linear, being non linear the heat q generated by the current ($q = RI^2$ due to the Joule heating). Another important drawback of this actuation is that the highest frequency of the actuated force is limited by the thermal time constant. The time needed for the heat transfer by conduction cuts the higher-frequency excitations. Thus this actuation mechanism was used only for low-frequency resonators (less than 1 MHz) [8].

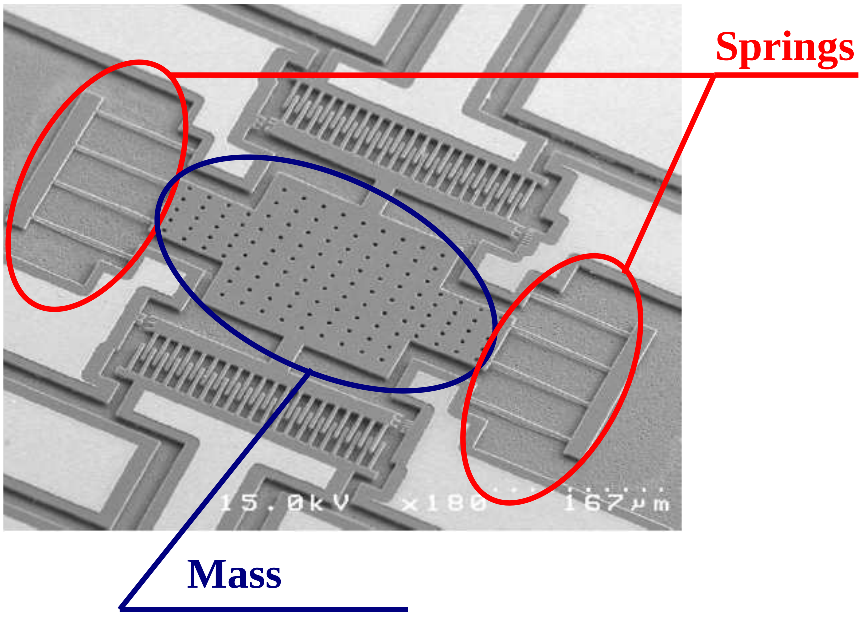

Figure 5: SEM picture of a lumped-parameter resonator taken from [11]. Regions considered as concentrated springs and mass are indicated.

Finally, the piezoresistivity can be used as a sensing mechanism [4]: resistors made of crystalline materials as silicon, change the value of their resistivity if they are stressed. In this case the resonator output voltage can be extracted by a Wheatstone bridge where one of the resistances is under stress and the others not. Also transistors show piezoresistivity [5]: in this case it is possible to exploit the stress-induced change of electron mobility in the channel.

This sensing mechanism can be easily implemented in CMOS compatible processes, and it is certainly efficient if the resonator or a portion of it is made of crystalline materials where it is possible to fabricate diffused resistors. However piezoresistive sensing is plagued by thermal drifts.

1.1.2 A possible classification of MEM resonators

In the past years many different kinds of resonators have been proposed, so that there are a lot of possible classifications of these devices. One of these involves the way they are actuated and their movements are sensed, so that it is possible for example to talk about electrostatically, magnetically or piezoelectrically actuated resonator. Another classification is connected to the way of model the mechanical structure: it is generally a deformable solid, which can be described as a *distributed-parameter system* [9], but sometimes it can be considered as a mass-spring-damper system [10], at least for the lowest resonance frequencies. This is possible if the mechanical structure can be separated in two region: one big and rigid whose inertial properties are mainly important and which can be considered as the *mass*; the other smaller but composed by one ore more flexible structures, which can be considered as pure *springs*, because their mass can be neglected with respect to the mass of the other region. In this case the resonator can be modelled as *lumped-parameter system* [10].

The first resonators proposed in literature [3] were lumped-parameter resonators. A more recent example is shown in the SEM picture in Figure 5 [11], where the “mass” and the “springs” are indicated too.

As an example of distributed-parameter resonator, a flexural-beam resonator is shown in Figure 6 [12]. This last device is composed of a beam, that is, a solid with one dimension (length) much higher than the other two (width and thickness), whose deformed shape or *mode shape* at the resonance is given by a pure bending of the beam.

With lumped-parameter resonator is impossible to reach resonance frequency higher than some hundreds of kHz and it is a limit for a lot of applications, so that generally distributed-parameter resonators were more successful.

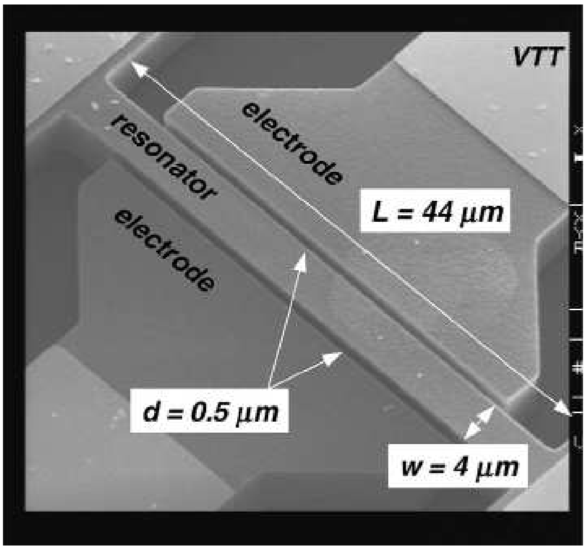

Figure 6: SEM picture of a flexural-beam resonator from [12]. Electrodes are indicated as well as the distributed-parameter structure, called "resonator".

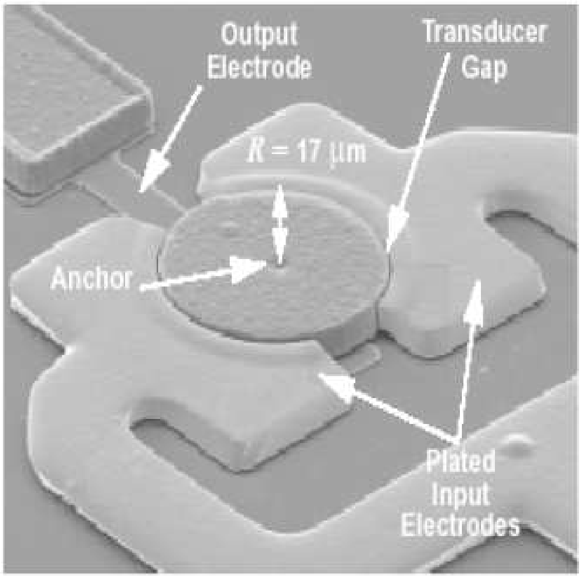

Figure 7: SEM picture of a bulk-mode disk resonator from [13]: if a sinusoidal signal is applied to input electrodes the disk is alternatively compressed and expanded in radial direction.

Among distributed-parameter resonators an important division can be done between *flexural resonators* and *bulk-mode resonators*: flexural resonators can be plate or beam as the one in Figure 6, or even systems of more beams connected together, which bend when they resonate, while bulk-mode resonators show resonance mode shapes defined by a deformation of the volume, or better by an acoustic wave confined inside the volume. Examples of bulk-mode resonators are bars, which are alternatively compressed and expanded in longitudinal direction, as well as disks or square blocks, alternatively compressed and expanded (Figure 7, [13]).

1.1.3 MEM resonators applications

Being MEM resonators basically filters, they can be used in all the applications which include filters or components based on filter. Furthermore, if packaged under vacuum[2], they often show a very high quality factor, so that they can be used as frequency-selective elements in oscillator.

Besides, they can be integrated on the same chip with electronics, with advantages in terms of occupied space, with respect to non-integrable solutions. Consequently they are very attractive for all the applications in portable devices, and especially in portable RF communication systems [1] (i.e. GPS, mobile). They can be used as filters or fundamental components in local oscillator, but also to obtain mixers [1], exploiting the intrinsic non-linearity of electrostatic actuation.

They could be useful also for communication systems on satellite, where the miniaturization is very important in order to save weight and the under vacuum package is not needed anymore, because the spatial environment is already at a high level of vacuum.

To be useful for RF applications, MEM resonators have to reach resonance frequency at least higher than 1 MHz, and for some applications even higher than 1 GHz. Given this limits, actuation and sensing in RF MEM resonators are electrostatic, because it do not limit the higher reachable resonance frequency, as magnetic and thermomechanical sensing/actuation do. Electrostatic actuation and sensing are preferred also to piezoelectric, because of its easier technological implementation. RF MEM resonators are generally distributed-parameters resonators because of the impossibility of reaching high resonance frequencies with lumped-

---

[2] As shown in the following one of the main mechanism which limits the quality factor of these devices is the energy dissipation due to the interaction between air and resonator surface (air damping).

parameters resonators. The use in RF communication systems is the more attractive application for MEM resonators and the research around this topic is the main subject of this thesis. Thus it will be separately dealt with in the next section. But there are a lot of other possible applications of MEM resonators: they can be used to create frequency reference not only for RF applications but also for all the low-frequency portable applications where a clock is needed.

Besides a MEM resonator can be used as a sensor: a temperature change leads to a change of the resonance frequency of the mechanical structure, as well as the deposition of some material on the surface. Thus using the resonator as a frequency-selective element in an oscillator it is possible to obtain a temperature sensor [14], or by covering the resonator with a proper sensitive layer adsorbing only a particular analyte (the water and thus the humidity, a particular inorganic molecule or a complex organic module as DNA or a protein) [5].

Of course if a temperature sensor is the target, all the molecules adsorbed by the surface introduce an error and, vice versa, if sensing a particular analyte is desired, temperature changes and adsorption of other analytes decrease the sensors selectivity. On the other hand the sensitivity of the resonance frequency to temperature adsorbed mass is only a problem for MEM resonator used as components of filters and oscillators in communication systems: temperature and mass adsorption lead to long-term instability of the central frequency in the first case and of the oscillation frequency in the second case. Limiting the interference introduced by the mass adsorption is thus another reason to package MEM resonator for RF applications under vacuum, while proper materials and topologies [15] have to be chosen in order to reduce the effect of temperature.

The state of the art of chemical sensors based on MEM resonators will be discussed in the 3rd section of this chapter as the second fundamental topic of this thesis. Now the only thing which is interesting to anticipate is that electrostatic actuation and sensing is not obliged as for RF resonators, because it is not necessary that they resonate at high frequency, so that all the actuation and sensing mechanism discussed in this section have been proposed in literature about MEM resonators for chemical sensing.

MEM resonators were proposed also as magnetic sensors: in [16] an external magnetic filed is detected by sensing the movements’ amplitude of a resonator actuated by the Lorentz force exerted on a current-carrying wire. The movements’ amplitude is proportional to both the external magnetic field and the current flowing in the wire. MEM resonators can even work as pressure because of the dependence of their quality factor on the pressure [2].

Finally, MEM resonators were proposed even as components in scanning probe microscope systems [6] and in electrometers [17].

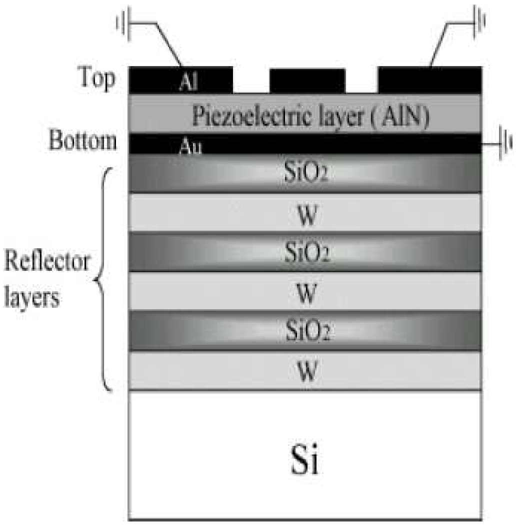

Figure 8: Typical cross-section of an FBAR [21].

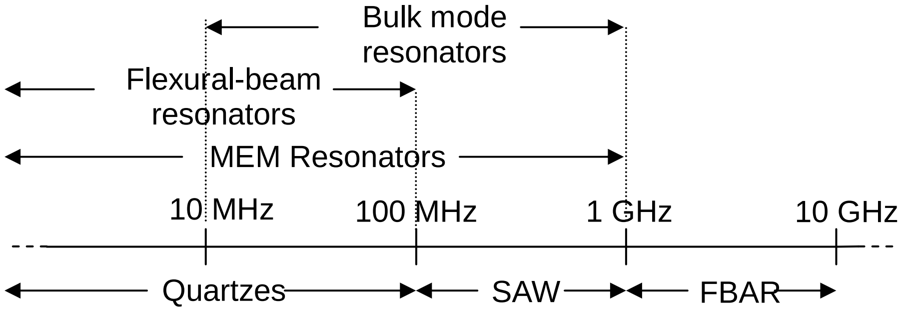

Figure 9: Range of use of MEM resonators, quartzes, SAW and FBAR for RF applications.

1.2 MEM resonators in RF communication systems

MEM resonators are very attractive for RF communications, basically because they can be integrated on chip. This advantage is very important especially if their use in filters and oscillators is considered: nowadays bulky and non-integrable devices as quartz and SAW filters are commonly used to obtain filters and oscillators at frequencies below 1 GHz.

A quartz filter is simply a portion of piezoelectric material such as PZT, with two electrodes attached to two sides of the device. The piezoelectric effect is used to drive into vibration the quartz crystal, by applying an external voltage signal between the two electrodes. But quartz vibrations amplitude influences the current flowing in the device, so that the impedance of the quartz is minimum when the input voltage frequency is equal to the resonance frequency of the quartz and is very high when the input signal frequency is far from the resonance frequency. Practically quartz can be modelled as a series RLC circuit. These devices are very huge and cannot be integrated, but they have very good performance from some hundreds of kHz to 100 MHz: in this range they show very high quality factors and small insertion losses, which are defined as the ratio in dB between the voltages at the output and at the input terminals/ports of a filer at the central frequency, when the output terminal/port is loaded with a standard impedance (generally a 50 Ω resistance). Besides they show also a small sensitivity to the temperature, long-term stability of the resonance frequency and slow aging [18]. If having low insertion losses is very important for a filter, because they quantify the attenuation introduced by the device, an high quality factor is very important for a filter used as frequency-selective element in an oscillator, because an high quality factor reduces the phase noise [19], that is, the short-term variations of the frequency of the output signal from the oscillator, so that an high quality factor of the frequency-selective filter increases the oscillator short-term stability.

SAW (Surface acoustic wave) filters are made of piezoelectric materials as quartz filters, but instead of exploiting a bulk resonance in these filters the wave is confined to the surface. Except for this difference the working principle is the same. They are smaller than quartz filters but cannot be integrated on the same chip with the other electronic components of a communication system, because of the substrate needed to fabricate it (generally $LiTaO_3$ o $LiNbO_3$), which is not compatible with fabrication process for electronics. They are generally used for applications between 100 MHz and 1 GHz and consequently they are especially suitable to be employed as intermediate frequency (IF) filters. Their performance is very good with respect to the quality factor and the long-term stability but worse than quartz performance with respect to the insertion losses [18].

Another class of devices have been recently proposed as fundamental components for RF filter and oscillators: they are called FBAR (Field Bulk Acoustic Resonators). They can work at frequencies from 600 MHz to 10 GHz, but their performance with respect to the quality factor and the insertion losses are excellent especially in the range between 1 GHz and 10 GHz, so that Agilent include them in its commercial duplexers [20]. FBAR can be considered as a sort of integrated quartz filters [21]: they are generally made of a piezoelectric layer (typically AlN) deposited on a bottom electrode, which lies on some layers of different materials (Figure 8), working as a “distributed reflector”: choosing properly the acoustic impedance and the thickness of each layer in the reflector it is possible to confine the acoustic wave inside the piezoelectric layer; on the other side the same target is automatically obtain because the piezoelectric layer is interfaced with the air, apart from the small region where the second electrode is applied. The resonance frequency increases if the thickness of the piezoelectric layer decreases, and cannot be lower than 600 MHz because too thick piezoelectric layer are required to reach this frequency, leading to a too complex process. Unlike quartz and SAW filters, FBAR are IC (integrated circuits) compatible and it is a very important advantage.

RF MEM resonators have to be compared to SAW and Quartz filters because the highest resonance frequency MEM resonators can reach nowadays is 1.5 GHz [22], even if one of the research issues for RF MEM resonators is increasing the highest resonance frequency, in order to enlarge the range of applications for these devices. Figure 9 summarizes the range of frequencies where each device can be used.

The quality factor of MEM resonators is generally very high and sometimes comparable with quartzes quality factor [23], but their main advantage is the possibility of being integrated on the same chip with the electronics of the communication system. This leads to more compact RF receivers and transmitters for portable applications and to a reduction of parasitic elements introduced by the off chip connection, resulting in smaller power dissipation [1]. But the small dimensions of MEM resonators and the possibility of integrating filters and local oscillators with the other electronic components can lead also to revolutionary architectures for communication systems, as suggested by C.T.-C. Nguyen in [1]. For example the possibility of having a large quantity of filter integrated in a small space allows to design a bank of filters with different central frequencies and high quality factor, which can be used to select the channel just after the antenna and before the LNA (Low Noise Amplifier), obtaining the architecture represented in Figure 10 for an RF receiver with SSB (Single Side Band) demodulator. This bank of selectable filters is a very efficient implementation of an accordable filter with high quality factor, which would be very useful for the first selection of the channel, because it would reduce the complexity of the LNA: in such a way, indeed, the other channels are much more attenuated than if a classical electronic accordable filter is used, so that the specification of linearity for the LNA can be less strictly (this specification being generally due to the need of decreasing the effect of cross-channel interference). Furthermore also noise specification can be released because the input noise is largely cut owing to the high selectivity of MEM filters.

In the receiver in Figure 10 the selection among one of filters in the bank is done with MEM integrated switches. Besides, also the mixer is replaced with a MEM resonator-based device. It is interesting to consider that a single resonator can have at the same time the function of multiplier and intermediate frequency filter: if the actuation is electrostatic and if a sinusoidal voltage at different frequency is added to the input signal, according to Eqs. (2) to (3) and (6) the quadratic non-linearity of the resonator produces a component of the force equal to the product of the local oscillation and the signal, while the mechanical structure selects the force frequency components around the resonance frequency.

A MEM resonator-based mixer has the great advantage to be a passive element: its power consumption is much lower than the one of the mixers based on active components, which is generally used in RF transmission systems.

MEM resonators can be used to obtain not only high selectivity filers but also relatively large bandwidth filers with high stopband rejections: this can be obtained by coupling two or more resonators with a mechanical element such as a soft beam [24] (Figure 11), or by an electrical coupling element, such as a capacitor [25]. In such a way, if designed properly, the overall resonator has two or more very close resonance frequencies, so that the bandwidth is increased with respect to the case of a single-resonator filter, even if a ripple in the passband is introduced (Figure 11). The high quality factor of each resonator assures a great stopband rejection in multi-resonator filters.

Thus MEM resonators use for RF applications is very attractive owing to the high quality factor, the possibility of large scale integration and the large amount of different devices which can be replaced by a MEM resonator-based counterpart.

But, apart from the quality factor, the performance indicators of RF MEM resonator are generally worse than quartz and SAW filters: the insertion losses are higher and the long-term stability is less than quartz, because of the dependence of resonance frequency on temperature, humidity and mass adsorption and desorption of the resonator surfaces. The problems related to humidity and mass adsorption/desorption can be solved by packaging under vacuum the resonator [26], while with respect to temperature the problem is more complicated as shown in chapter 2.

The biggest problem is connected to the insertion losses. In resonators with electrostatic driving and sensing the insertion losses can be reduced increasing the electromechanical coupling, that is, the actuated force when a unitary input voltage is applied and the output current per unitary displacement. According to Eqs. from (2) to (7), the easiest way to achieve a higher electromechanical coupling is to increase the bias DC voltage applied between the rotor and both input and output electrodes. But to obtain acceptable insertion losses, many authors ([23],[24]) proposed bias voltage from 10 V to 100 V, which are too high for portable communications systems, usually working with bias voltages below 5 V. Charge pumps circuits, even MEMS-based [27], were proposed to solve the problem, but even considering this possibility the bias voltage cannot off course reach value as high as 100 V. Another way to increase the electromechanical coupling is to optimize the electrodes and the mechanical structure or select the better resonance modes. This strategy can lead to a reduction of both bias voltage and insertion losses and is the strategy developed also in this thesis and in the author’s master thesis [18] as discussed in the chapter 2.

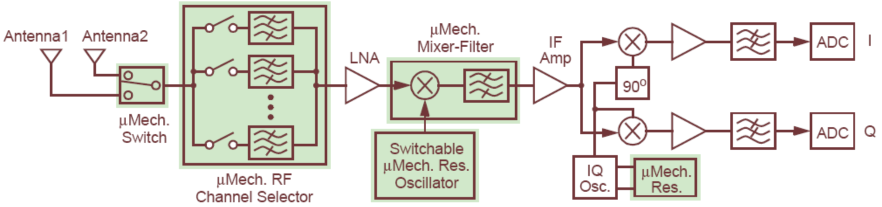

Figure 10: Innovative architecture for an RF receiver for SSB modulated signal, presented in [1]. The components replaced with MEMS are in grey.

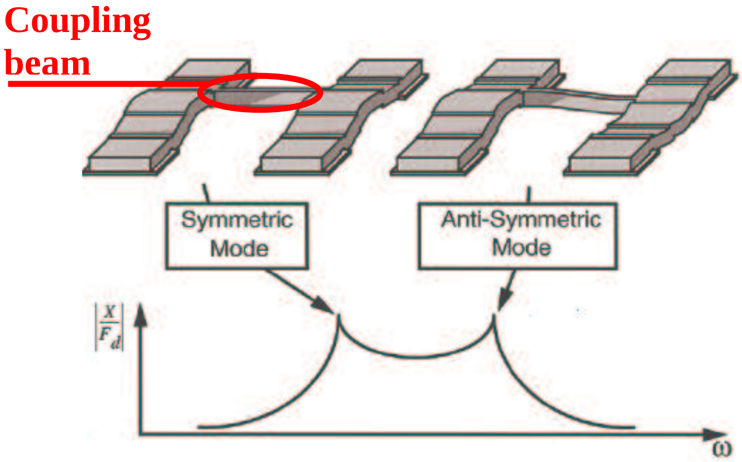

Figure 11: Schematic representation of the two resonance modes for a two-resonator filter and of the expected frequency response (from [24]). The resonator is composed of two flexural-beam resonators connected by a coupling beam: on the first resonance mode the two beams move symmetrically, on the second one anti-symmetrically.

Finally, the insertion losses can be reduced also increasing the quality factor *Q*: the output current at the resonance is proportional to *Q* if the resonator can be represented as a second order system, as it is generally reasonable ([9],[10]). This is a further reason to maximize the quality factor, besides its importance to have high-selective resonator-based filters, multi-resonator filters with high stopband rejection and resonator-based oscillator with low phase noise (high short-term stability). For all this reasons the maximization of quality factor was the main issue of the work about modelling and design of disk resonators, which is discussed in chapter 3.

A parameter strictly connected to the insertion losses is the motional resistance, which is the electrical resistance the resonator can be consider equivalent to at the resonance.

Summarizing, in the research about electrostatically driven RF MEM resonators, the main open issues are, in order of importance:

I. Reducing the insertion/losses (motional resistance), without increasing the bias voltage
II. Increasing the quality factor
III. Increasing the maximum resonance frequency which can be obtained
IV. Increasing the long-term stability of the resonance frequency (temperature effect)

Issues I, II and III were considered in the design of beam flexural resonators presented chapter 2 of this thesis as well as in the optimization of the design of bulk-mode disk resonators discussed in chapter 3. With respect to long-term stability (point IV) an estimation of the sensitivity to temperature of resonance frequency was done only for the flexural-beam resonators.

In the following some solutions presented in literature to solve especially problem I, II and IV are presented. The mechanical structures are generally made of single-crystal Silicon, Polysilicon or Poly Silicon-Germanium (SiGe), a promising structural material for CMOS-compatible process to fabricate MEMS [28]. Recently diamond and Silicon Carbide (SiC) resonators were as well proposed in order to reach high resonance frequencies through the high Young’s modulus of these materials ([11],[22],[29]).

1.2.1 Flexural resonators

Because of the reasons already discussed (resonance frequencies needed and technological complexity) the large majority of RF MEM resonators have an electrostatic actuation and sensing, apart few cases with piezoelectric actuation and/or sensing [30]. Also the RF resonators cited from literature in the following, as well as the RF devices developed in this thesis, have electrostatic sensing and actuation, thus starting from this point all the RF MEM resonator considered in this thesis, will have electrostatic actuation and the sensing.

Besides, being the resonance frequencies achievable with lumped-parameter resonators well below 1 MHZ, the RF MEM resonators are always distributed parameters systems and they are divided in flexural resonators and in bulk-mode resonators, as already said.

Flexural-beam resonators were the earliest distributed-parameter resonators proposed and among them *clamped-clamped* beam resonators were the first: the resonant mechanical structure is a beam anchored at both the ends, where beam cross section cannot move or rotate, which means that the ends are both clamped (Figure 6). It is a very easy structure composed by only one beam, and among all the resonators composed of only one beam it is the one which has the higher resonance frequency, if the comparison is done among beams with the same length and cross-section. For example if compared with a *cantilever* resonator, which is a beam clamped at one end and free at the other (as the structure in Figure 3), the resonance frequency of the fundamental mode of clamped-clamped beam is about six times higher than the first resonance frequency of a cantilever with the same lengths and cross-section. This relation is strictly dependent on the different boundary conditions and can be verified using the formulas in [31].

Like every flexural resonator, clamped-clamped beams can be *laterally* actuated, as the one in Figure 6 [12], when resonator and electrodes lies on the same plane parallel on the substrate, or they can be *vertically* actuated by an electrode lying on the substrate beneath the beam [1], as the resonator in Figure 12. In the first case the beam bends in direction parallel to the substrate, while in the second case in direction perpendicular to the substrate.

Clamped-clamped beam resonators have a significant quality factor (some thousands), when they work in vacuum and their resonance frequency is less than 15 MHz ([12],[32]). But their quality factor dramatically decreases increasing the resonance frequency [32], so that for higher frequencies clamped-clamped resonators are practically useless. Thus a more complex device, the so-called free-free beam resonator, was proposed: this architecture enhances the quality factor (and thus it also reduces insertion losses) and allows to reach resonance frequencies as high as 90 MHz, retaining a quality factor more than 20 times higher than a clamped-clamped beam working at the same frequency [33]. A SEM picture of a free-free resonator is presented as Figure 13a.

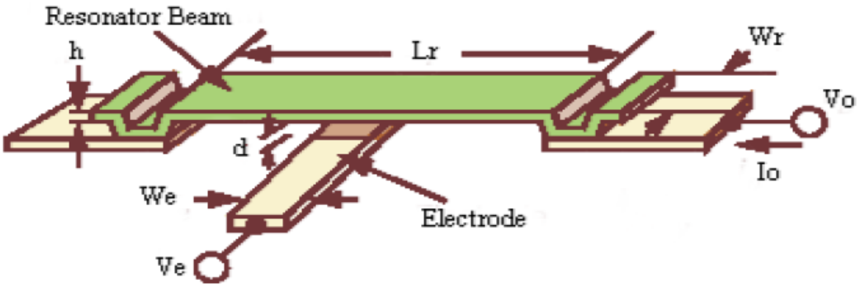

Figure 12: Schematic representation of a one-port clamped-clamped beam resonator actuated by an electrode lying on the substrate. The figure is taken by [1].

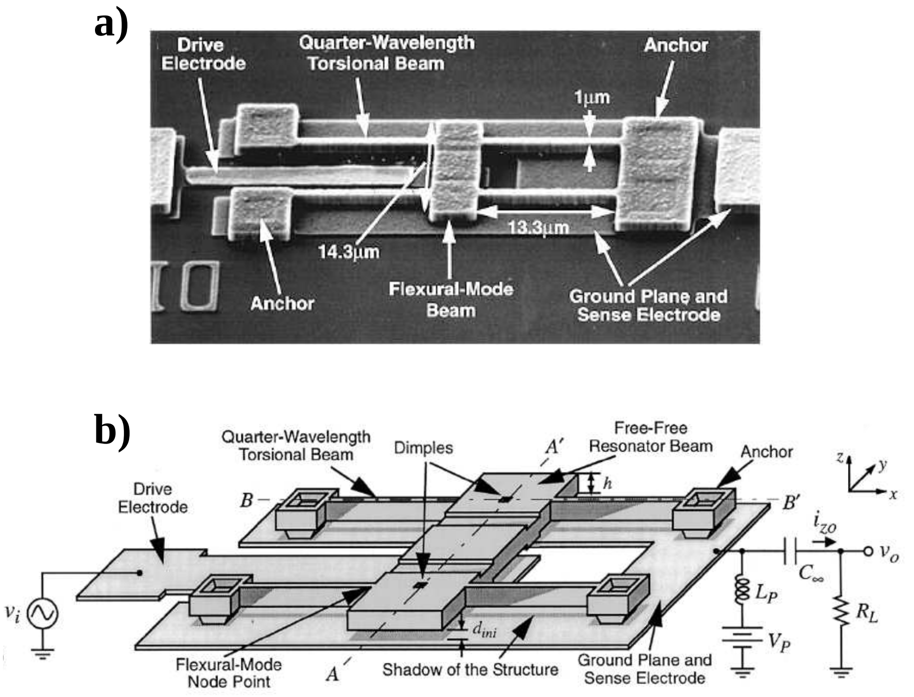

Figure 13: Free-free resonator with torsional supports from [33]: a) SEM picture; b) schematic structure.

In order to understand how the free-free design can improve the quality factor with respect to clamped-clamped beam resonators, it is necessary to discuss shortly the physical mechanisms which limit a resonator quality factor. An expression alternative to (1) for the quality factor Q is:

$$Q = 2\pi \frac{W_{imm}}{\Delta W_L} \tag{8}$$

where W_{imm} is the energy stored in the resonator at the resonance and ΔW_L, the energy lost per cycle. Thus the quality factor can be extracted by measurement of the frequency response, using Eq. (1), but it can be also estimated from (8), the only thing needed is to find the energy losses or damping mechanisms. In Figure 14 the three main energy losses are represented for a clamped-clamped beam resonator:

a. The surface losses, due (at atmospheric pressure) mainly to the air damping, that is, to the collisions of the air molecules at the resonator surfaces.
b. The intrinsic losses, due to internal friction and vibration-induced heat generation (*thermoelasticity*). They are localized inside the material and are strictly connected to material properties.
c. The anchor losses, due to interaction between the resonator and the substrate: because of resonators movements a propagating acoustic wave is driven in the substrate at the resonance and the amount of energy stored in the wave is lost, unless it is reflected back by some material discontinuity in the substrate.

The discussion, held in the last years by academics, about the estimation the quality factor in MEM resonators will be detailed later in this chapter, because it was very important for this Ph.D. thesis, whose aim is also to give a small contribution to this subject (see chapter 3). At this point the only important aspect of the problem is that by the dependence of quality factor on the pressure ([2],[32]), it can be demonstrated that the air damping is the higher loss, and thus limits the quality factor at atmospheric pressure. But both to increase the quality factor and to improve the long-term stability of the resonance frequency, resonators has to work in vacuum and in this case the internal losses are always too small to explain the measured quality factor ([18],[36]). Besides in many cases a smaller quality factor was measured increasing the anchor size [37], so that it was concluded by many authors that anchor losses cause the main energy dissipation in vacuum. In chapter 3 it will be shown that this dependence between anchor size and quality factor is not always true. It holds, however, in the aforementioned cases [37], so that the observation can support the thesis of the centrality of the anchor losses.

To reduce anchor losses and thus increase quality factor, in [33] was proposed an architecture where the beam driven by the input electrode (or main beam) is minimally coupled with the anchor, so that the energy fed by the input signal is maximally confined inside the beam and does not flow into the substrate through the anchors. This condition is obtained (Figure 13b) by connecting the main beam to the anchors through two other beams namely *supports*. The main beam has ‘free’ ends, so that its resonance frequencies can be found solving the problem for a *free-free* beam (from this come the device name). Supports minimally affect the principal beam mode shape at the resonance, if they are connected at the nodes of the deformed shape of the main at the resonance. The nodes are points which do not move, but around which the beam cross-section is free to rotate. Thus the supports must also not exert any bending moment on the main beam. This can be obtained by considering the beams as mechanical lines of transmission and choosing the supports length in order to obtain a $\lambda/4$ adaptation, with a perfect analogy with the $\lambda/4$ adaptation usually done in electric transmission lines: the supports when the main beam bends (in z direction according to Figure 13b), are twisted, so that they behave as *torsional* support and in this case the dynamic equations relating the torsional moment and the derivative of the twisting angle with respect to the time have exactly the same form of the equations relating voltage and current in electric transmission lines, if the moment is replaced by the voltage, the derivative of the angle with respect to the time by the current and the velocity of the torsional acoustic wave by the light velocity.

This $\lambda/4$ adaptation leads to the possibility to obtain MEM resonator with Q about 8000 till about 90 MHz, achieving a great improvement with respect to clamped-clamped resonators.

With respect to the maximum achievable resonance frequency, the free-free beam resonance frequencies are equal to the one of a clamped-clamped beam, so that concerning this point the two solutions are practically equivalent. The only small disadvantage of free-free beam is that it occupies a slightly larger surface of the chip, because of the supports.

Another possible architecture is anyway presented by Nguyen for a free-free resonator (Figure 15). This time the resonator is laterally driven and consequently also the supports bend because the free-free beam bends in a direction parallel to the substrate.

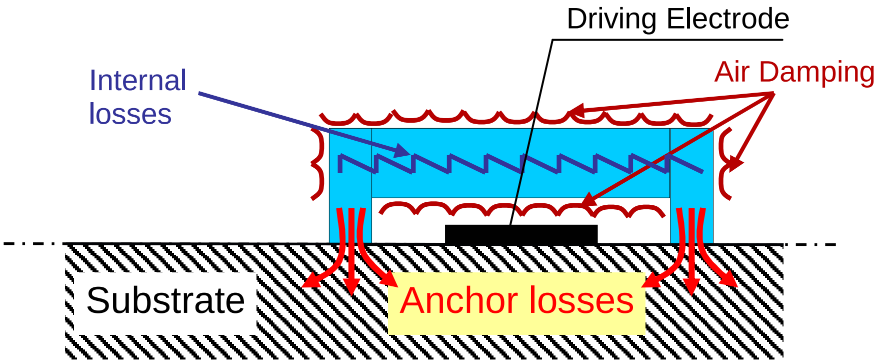

Figure 14: Damping source limiting the quality factor in a MEM resonator, shown in the schematic longitudinal cross-section of a vertically actuated clamped-clamped beam resonator.

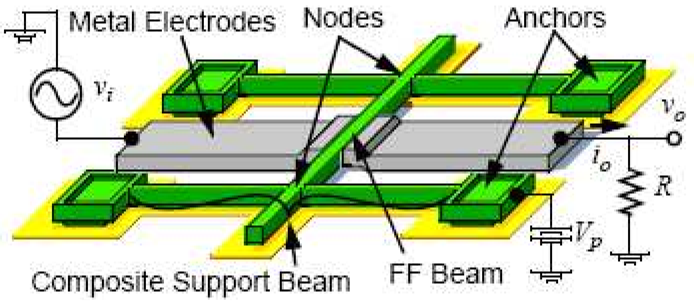

Figure 15: 3D sketch of the free-free resonator with flexural supports presented in [38].

Also in this case the supports are connected with the main beam at its nodal points and a sort of λ/4 adaptation is done, even if dynamic equations for a bending beam are not equivalent to equations for an electrical transmission line, and thus the analogy is less rigorous than in the case of free-free resonator with torsional supports. The adaptation anyway works, leading to quality factor around 10000 at 10 MHz [38].

The problem of supports adaptation in a free-free resonator with flexural supports will be detailed in chapter 2, where structures similar to the one in Figure 15 will be presented.

In [33] and [38] are presented resonators where the free-free beam resonates on its first resonance mode; designing resonators with free-free beam resonating on higher resonance modes is a way to reach higher resonance frequencies and lower motional resistances with flexural-beam resonators. Nguyen did it for free-free resonators with torsional supports [39], while in the author's master thesis, from which these Ph.D. research activities start, a free-free resonator resonating on the third resonance mode with flexural support is presented [18] almost at the same time as the device in [39].

To complete the state of the art of flexural-beam resonator it is mandatory also to introduce another possibility of MEM resonators: their resonance frequency can be varied changing the bias DC voltage applied between rotor and electrodes and thus a MEM resonator can be an accordable filter. This effect is well known in literature ([38],[40]) and will be quickly discussed in chapter 2. But it was also observed that in free-free resonators an increasing of bias DC voltage reduces the quality factor [38]. This quality factor decrease is probably due to the fact that $\lambda/4$ adaptation works exactly only at the resonance frequency the free-free beam is supposed to resonate. If it resonates at a different frequency owing to the effect of bias voltage, the adaptation does not work anymore. In chapter 2 a possible solution to this problem is presented, in order to show a way to exploit the intrinsic accordability of a high-Q filter such as the free-free resonator.

1.2.2 Bulk-mode resonators

Even exploiting higher order modes, it is impossible to reach resonance frequency higher than 500 MHz [18] because of the small dimensions needed. As a matter of fact, it is not practical to design flexural resonators at frequency higher than 100 MHz ([18],[33],[38],[39]), in order to obtain reasonable value for the motional resistance, retaining low bias voltage.

Thus, to obtain higher resonance frequencies the bulk-mode resonators were introduced: the most simple bulk-mode resonator is a beam inside which a longitudinal compressive wave propagates [23] (Figure 16). The beam resonates at about 12 MHz and has a Q about 180000, but the rigidity of the structure and the inefficient electromechanical coupling (the only parts of the beam facing the electrodes are the two short ends), lead to a high motional resistance despite the high-Q.

Bulk-mode resonators better performing than the compressed beam in [23], are the square ([29], [41]) and the disk ([13],[22],[37],[42]) resonators. In both cases if the resonator alternatively is expanded and compressed increasing and decreasing its volume without changing its shape, the device is a *contour mode resonator*, because it resonates on a contour resonance mode ([13],[22],[37],[41]) (Figure 17a). But, if the actuation electrodes are properly shaped, it is possible to exploit resonance mode shapes according to which the mechanical structure is expanded in a direction and compressed in the orthogonal direction, preserving its volume ([29],[42]). These resonance modes are called *Lamé modes* (Figure 17b). All these devices show very high quality factors at every frequency from the value of 130000 at 13.1 MHz presented in [41] to the quality factor about 2600 at 1.156 GHz in [37]. The last value is obtained by exciting the third contour mode of a silicon disk, with a disk radius equal to 10 μm. Using other materials more rigid than silicon, such as diamond, it is possible to reach frequency even higher preserving very high quality factor. In [22] a nanocrystalline diamond disk resonator is presented: its radius is again 10 μm, resulting in a resonance frequency about 1.5 GHz with a quality factor higher than 10000. The disk resonates on the second contour mode.

Furthermore, square and disk resonators reduce a lot the motional resistance with respect to the beam under compression in [23], because they show a better electromechanical coupling, having a larger lateral surface which can be faced by electrodes.

A further reduction of the motional resistance can be achieved with the radial bulk annular resonator (RBAR) presented in [44], where theoretically the resonance frequency is proportional to the difference between the internal and external radius of the ring (W_r in Figure 18), while the motional resistance increase if the average radius increase (r_{av} in Figure 18). The authors of [44] propose a design to obtain a Poly-Silicon-Germanium resonator at 1 GHz with 50 Ω of motional resistance guaranteed if the quality factor is at least 10000. It could be a very advanced result, if confirmed by experimental results.

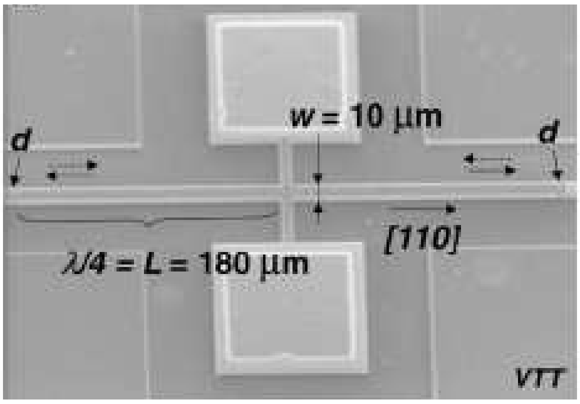

Figure 16: SEM picture of the bulk-mode beam resonator presented in [23]: the arrows represent the directions of propagation of the progressive and regressive longitudinal compressive waves.

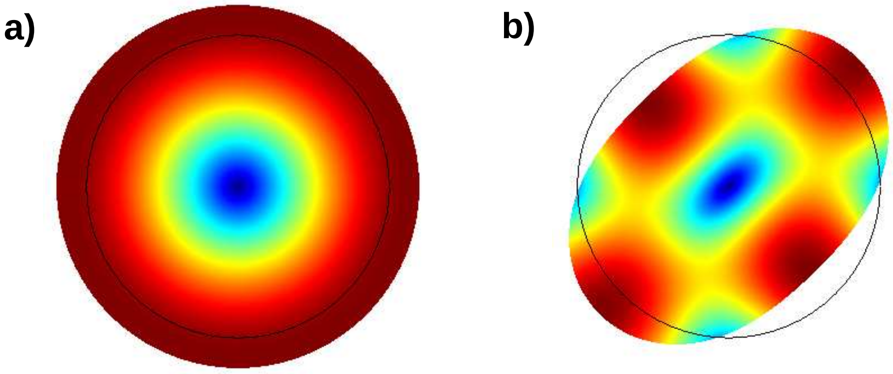

Figure 17: Deformed shapes of bulk-mode disk resonators: a) a disk vibrating on its first contour mode; b) a disk vibrating on its first Lamé mode. The relaxed geometry edges are represent by a black line in both case, while the map of colours show the displacements amplitude (from blue which is zero to red which is the maximum displacement). Both the deformed shapes were taken from FEM eigenfrequency simulations performed with FEMLAB [43].

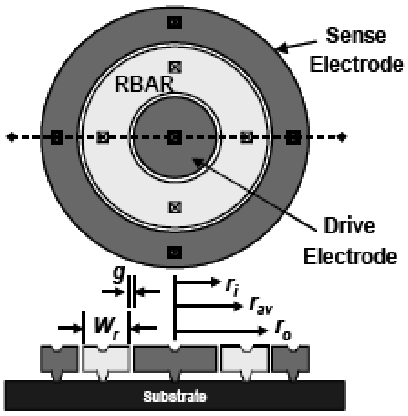

Figure 18: Schematic top view and radial cross-section of the radial bulk annular resonator (RBAR) presented in [44].

At frequencies higher than 100 MHz it is possible to obtain results which cannot be achieved with flexural-beam resonators, but in the frequency range between 1-100 MHz the flexural-beam resonators show acceptable performance, even if worse with respect the quality factor (less than 10000 vs. more than 100000) and they have at least the advantage to be much more compact than bulk-mode resonator: the square resonator in [41] occupies an area larger than 300x300 μm, while a free-free resonator at the same frequencies needs an area smaller than a square 100x100 μm. Thus if the resonance frequency required belong to the interval 1-100 MHz and the quality factor required is not too high, it could be useful to choose a flexural-beam resonator in order to save area and put more devices on the same chip. Thus in the first part of the research activity presented in this thesis the devices proposed in the author's master thesis were characterized, identifying possible improvements. Their performance with respect to temperature variations was modelled as well as the effect of residual stresses on the resonance frequency and equivalent electrical circuits were extracted to better understand their behaviour and to make easier their use by system-level designers in complex electronics systems. But owing to the great importance of the range of frequencies from 100 MHz to 1 GHz for RF communications systems [1], in a second part, the optimization of the design of a MEM disk resonator was considered[3]. The main target of the design was the maximization of the quality factor and for this purpose a strategy based on FEM simulations to evaluate the Q was found. Thus this chapter about the state of the art of RF MEM resonator will be concluded by a short description of the different theoretical models, analytical approximations and simulative approaches presented in literature as methods to estimate the quality factor.

1.2.3 The problem of estimation of the quality factor of RF MEM resonator

Due to the great importance of the quality factor for RF MEM resonators, a lot of research has been done to find methods to estimate it. Air damping, intrinsic dissipation mechanisms and above all anchor losses has been investigated.

Air damping can be simply due to the drag force generated by to the friction between air and resonator surface ([45],[46]). But if the resonator moveable structure is surrounded by thin layers of air, the damping is strictly connected to the thin film properties. This situation usually occurs when the resonator is electrically actuated, because according to Eqs. from (2) to (7) the gap between the rotor and the electrodes has to be reduced as much as possible, in order to increase the electromechanical coupling and consequently the insertion losses. If the resonator movements are parallel to

---

[3] This activity was carried out in collaboration with IMEC (Interuniversity MicroElectronics Centre).

the air film (as in Figure 2a) the structure is affected by a *slide film damping* [47], if the rotor moves in direction perpendicular to the film (as in Figure 2b), so that it compresses it, the resonator loses energy through a *squeeze film damping* [46].

Squeeze film damping has been studied by many authors for many different MEM structures ([48],[49],[50]) and it generally reduces to very small value the resonator quality factor when the electrodes/rotor gap scale down (if d is the electrodes/rotor gap, the damping is proportional to $1/d^3$ as it is possible to find from [48], [49] or [50]). Thus electrostatic actuation and sensing are generally unfitted to be used in resonator working in air, because of the squeeze film damping, even if with some bulk resonators with electrostatic actuation and sensing it is possible to reach high quality factor also at atmospheric pressure ([22],[37]).

However, as it was already discussed, in RF MEM resonators air damping is totally removed by packaging the device under vacuum. Of course this leads to a higher technological complexity and increase devices costs, but the advantages are considerable not only because of the increase of the quality factor but also with respect to the long-term stability of the device resonance frequency [26], which is fundamental when the resonator is used as oscillator component. A lot of research activities in the world are about RF MEM resonators packaging, involving also zero-level packaging [51], in order to reduce package leakages and the package cost. If the air damping is removed by a proper packaging, only intrinsic and anchor losses limit the quality factor.

Internal damping is strictly connected with the properties of the materials the resonator is made of, so that the choice of proper materials is primary to reduce the effect of this energy loss. Intrinsic dissipation include a great number of mechanisms which can be modelled by considering the material as viscoelastic ([18],[34]), but also assuming the damping source as caused by a thermoelastic dissipation or by the *phonon-phonon effect* [52]. Both losses are due to the interaction between an acoustic wave propagation and heat transfer.

Phonon-phonon dissipation happens because an acoustic wave propagating in a material disturbs the condition of equilibrium of thermal phonons corresponding to the thermal lattice vibration. The recovering of the equilibrium condition produces the loss of a part of the energy stored in the acoustic wave [53]. This effect usually leads to a very small energy dissipation and can be generally neglected in MEM resonator [52].

More important is the thermoelastic damping: if the resonator vibrates, the mechanical structure is alternatively locally compressed and expanded. According to the model for thermoelastic damping presented in [35], a time-variant state of compression leads to a heat generation. Thus, owing to heat transfer by conduction, a time-variant temperature gradient is generated and this gradient drives a dilatation or compression of the material which opposes the vibrations which cause it, resulting in energy dissipation.

Thermoelastic dissipation is very important in flexural-beam resonators, as shown in [35] and [36]. To our knowledge nobody has ever evaluated the effect of thermoelastic damping in bulk-mode resonator, but according to the analysis presented in chapter 3 of this thesis, it is much smaller than thermoelastic damping effect in flexural-beam resonator, at least in the bandwidth from 1 MHz to 1 GHz. Nonetheless thermoelastic dissipation is very small if compared with the anchor losses, which are certainly the main damping mechanism in vacuum, because the small value of intrinsic losses cannot explain alone the experimental values and because the quality factor generally increases if the dimensions of the interface resonator/substrate increases [37].

Despite their importance, methods to estimate anchor losses were presented only recently in literature (all the papers about this topic have been published during the last three years). This is due to the complexity of the problem which prevents from finding easily the solution. Owing to such complexity an approach based to simulations seems to be an efficient solution to estimate the anchor losses in a MEM resonator. Nonetheless any simulation strategy has to face the problem of the substrate: being the anchor losses related to the propagation of an acoustic wave in the substrate, the substrate has to be included in the simulations, but it is much larger than the resonator so that including all the substrate in the simulations would lead to a too large number of element in the simulation and consequently to a too large amount of RAM needed and a too long time of simulation. Furthermore, the effective attenuation coefficient for an acoustic wave propagating in the substrate is expected to be small as it will be discussed in chapter 3, so that it is not possible to simulate only a small portion of substrate, assuming that in that portion all the propagating wave it is absorbed.

The substrate problem can be solved replacing the substrate with a smaller domain, with an extension comparable to the one of the resonator, if this element absorbs all the energy propagating from the resonator to the substrate, even if it is different from the substrate, with respect to material properties and behaviour. In order to estimate the anchor losses, it is important that the element which substitutes the substrate in the simulation has the same effect on the resonator and not that it behaves exactly as the substrate. Of course doing this substitution it is fundamental to avoid spurious reflection at the interface resonator/substrate-equivalent element which can be caused changing the substrate with the alternative element.

One element proposed to replace the substrate in anchor loss simulations is the PML (*Perfectly Matched Layer*), an element for FEM simulation which has a function similar to the homonymous element used in electromagnetic simulations [54]. PML for acoustic simulations is obtained by applying a complex-value change of coordinate in the substrate, which changes its properties with respect to the attenuation of an acoustic propagating wave. PML was used for simulation of anchor losses in bulk-mode disk resonator in [55]. The quality factor only due to anchor losses was extracted from the simulations and compared with the quality factor given by the experimental results: the agreement between simulations and measurements is good, confirming both the validity of the method and the hypothesis according to which anchor losses are the damping mechanism which limits the quality factor of the resonator in vacuum [55].

In chapter 3, an element alternative to PML will be discussed. This strategy has some limits: it is very critical to choose properly the size of the substrate-equivalent element as well as some parameters which change the attenuation of the incoming acoustic waves, as for example the parameters defining the complex-value change of coordinates used to obtain the PML. Besides this proper choice could be efficient only for a particular substrate, resonator or frequency range and the limits of validity of the choice does not seems to be immediately detectable. Finally, these parameters are not connected with the physical properties of the substrate material. Thus in chapter 3 an alternative simulation strategy is presented and it is used to evaluate the anchor losses in a bulk-mode disk resonator: the substrate-equivalent element is removed and proper boundary conditions are forced at the interface resonator/substrate. Such boundary conditions can be extracted through a rigorous analytical approach for the calculation of the profile of the wave propagating in the substrate, so that any “non-physical” parameter is removed from the model and the limits of the approach descend directly from the limits of validity of the hypotheses used to find that boundary conditions.

Another alternative approach was proposed in [56] and [57] to find the anchor losses in a clamped-clamped resonator: an approach similar to the one discussed in chapter 3 was used to solve the problem of the propagation of an acoustic wave in a substrate, even if the problem is more complicated with respect to the case of the disk dealt with in chapter 3, because the geometry does not allows some important simplifications discussed in chapter 3. In this paper the problem is not solved by extracting boundary conditions at the substrate/resonator interface, but dividing the substrate in thin layers and then solving in each layer the problem of propagation of acoustic wave. Finally, forcing the condition of the continuity of displacements at each layer interface, a linear system was found and can be solved assuming that the load at the interface resonator/substrate is forced by the resonator, whose deformed shape is assumed to be unaffected by the substrate, as well as the internal stress condition. This assumption does not always hold, because sometimes the substrate radically changes the deformed shape of a resonator as it will be discussed in chapter 3. The approach is very flexible because can also deal with multilayer structure as the dielectric layers which generally lies between resonator and substrate, but when the influence of these layers is not too important, the approach is not so useful. To obtain accurate results as well as efficient simulations, such method should be used only for the dielectric layers, setting a boundary condition at the interface between the last dielectric layer and the silicon substrate.

Finally, some analytical formulas to evaluate anchor losses were proposed by Ayazi for cantilever and clamped-clamped beam resonators in [36] and for contour mode disk resonators in [58]: again the problem of wave propagation in the substrate is solved in a way similar to [56], [57] and to the one discussed in the chapter 3 of this thesis, while very strong assumptions were done with respect to the load forced by the resonator at the interface with the substrate, whose effect on the resonator mode shape is assumed to be negligible. The analytical expression provided for cantilever and clamped-clamped beam resonators in [36] seems to fit properly with experimental data, if also thermoelastic damping is considered, while the formula proposed for contour mode disk resonators is compared with few experimental data and the agreement is not so good, even if the authors justify it with the high sensitivity of quality factor value to some parameters strongly dependent on the process [58]. The most important limit of Ayazi's model for disk resonators is the assumption on the shape of stress driven by the resonator on the substrate: in chapter 3 simulation results which cannot be explained by Ayazi's model will be discussed and an explanation of the disagreement will be given.

1.3 MEM resonators for chemical sensing applications

MEM resonators are not only useful devices for RF communication, but they can also used as sensors to detect the presence of particular analytes from chemical molecules to complex organic compounds: any molecule which is attached to (adsorbed by) or is absorbed by a micromechanical structure changes the mass of this structure and thus its resonance frequency. Consequently, if the resonator is used as frequency-selective element in an oscillator, the oscillator output is a sinusoidal signal at a frequency variable with the adsorbed mass and the device works as a *microbalance*.

A micromechanical resonator is generally made of material such as silicon, polysilicon, SiGe, silicon oxide or other typical materials used in technological process for MEMS and traditional electronics. Thus it can adsorb many kinds of molecules, and among them not necessarily the target molecules, so that it is necessary to cover the resonator surface with a *sensitive layer* able to adsorb only (or at least "principally") the target analyte in order to obtain a sensor for such molecule. If the sensitive layer is enough selective, a change of the oscillator output frequency can be connected to a change of the adsorbed mass of target molecules and then to the concentration of them in the environment surrounding the resonator [59] (Figure 19). Because of their small mass, MEM resonators are very sensitive to the adsorbed mass, so that they are very attractive as chemical sensors. Anyway their main advantage is that a lot of them can be integrated in a small space on a chip. This leads to the possibility of integrating an array of microbalances (Figure 20), so that, if each microbalance is covered with a different sensitive layer, a system of sensors sensitive to a lot of different analytes is obtained on a single chip [60].

Furthermore, MEM resonators can be integrated with the control electronics, needed at least to build the oscillator. If other devices useful for chemical or a biological analysis are included, such as microchannel for microfluidic operations on the solution under analysis, it is possible to obtain a "Lab On a Chip", a fully integrated system which can perform on a small chip, many of the operations usually done by a laboratory for chemical analyses.

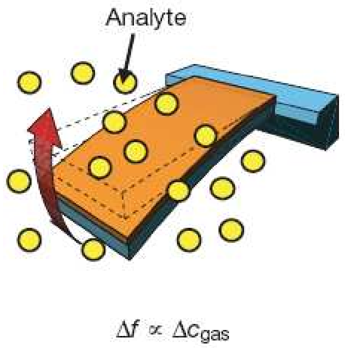

Figure 19: Working principle of a MEM microbalance, used as gas sensor from [59]: a cantilever covered with a proper sensitive layer, has a resonance frequency which changes of an amount Δf, proportional to gas concentration ΔC_{gas}.

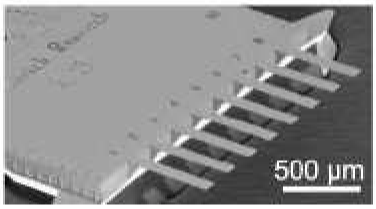

Figure 20: Picture of an array of MEM resonant cantilevers for chemical sensing from [60] .

Such fully integrated system can be a very cheap diagnostic device, because it can be produced with the same logic of integrated circuits. Due to its low-cost, a Lab On a Chip can be even used only once. Besides it can be included in portable instrumentation and due to the small size of the system, the analysis time is generally shortened. As it is integrable, the single MEMS-based chemical sensor is also cheaper than any other alternative macroscopic devices.

1.3.1 Devices alternative to MEM microbalances

Their integrability is the main advantage of MEM microbalances with respect to their macroscopic counterpart, the QCM (*Quartz Crystal Microbalance*) ([60],[62]): despite their name this devices are quite bulky if compared with MEM microbalance, because they are oscillator using a quartz crystal as frequency-selective element. Quartz crystal anyway can have quality factor as high as 100000, so that using a quartz it is possible to obtain oscillator with very low phase noise and very high short-term stability. Therefore the resolution of a QCM is generally very high, because even very small variations of the resonance frequency due to a mass loading of the quartz surface are much higher than the fluctuation due to the noise. Besides also the temperature dependence and long-term stability of quartz crystal resonance frequency is generally pretty good. Quartz Crystal Microbalances are often used in laboratory for many different kinds of chemical analyses, but they are currently used also to check the thickness of deposited or growth layers in IC fabrication processes. It is difficult to replicate QCM’s good performance, but the small mass of MEM resonator can help, even if quality factor of MEM resonator at atmospheric pressure is generally much smaller than quartz crystal, so that it is possible to obtain performance comparable with QCM's, or even better, with respect to the sensitivity to the adsorbed mass, by using MEM resonators ([61],[62],[63],[64]).

MEM microbalances are not the only chemical sensor which can be integrated on chip with the electronics: among them there are of course a lot of sensors based on solid state devices such as EIS (electrode-insulator-semiconductor) or EMIS (electrode-metal-insulator-semiconductor) structures, as well as sensors based on solid state devices employing porous silicon to increase the surface which the analyte can be adsorbed by [65]. Other integrated chemical sensors are based on changes induced on the dielectric properties of a polymer, when it absorbs a particular analyte: they are capacitors whose capacitance changes proportionally to the amount of analyte absorbed by the polymer, and consequently to its concentration [59] (Figure 21a). In Figure 21b a further example of an integrable chemical sensor [59] is represented. The concentration of an analyte is determined through a calorimetric measure carried out by a thermopile: any adsorption or desorption generates heat which increases the temperature of the hot junctions of some thermopiles, so that from the output voltage of the thermopiles it is possible to find the time derivative of the analyte concentration. This sensor detects only transitory changes in concentration and not its absolute value [59]. Even if it is not a MEMS, this sensor is fabricated with a MEMS process because it requires a membrane of thermally insulated material (i.e. Silicon Oxide) where thermopiles hot junction are placed, while cold junctions are placed where the silicon substrate under the oxide was not removed.

An interesting integrable chemical sensor is proposed in [66]: it is practically an FBAR (Figure 22) covered with a sensitive layer able to adsorb molecules, which change resonance frequency of the device with their mass. As the FBAR is a kind of integrated quartz filter, this device is a sort of integrated QCM. The device show quality factor smaller than in the case of QCM and it results in a reduction of the minimum shift of frequency which can be considered as due to a change in analyte concentration, but the high frequencies which can be reached with such device (some GHz versus some MHz of quartz crystals) leads to an acceptable resolution [66]. Even if integrable, this solution requires processing steps, including piezoelectric layers deposition, more complex and expensive than those needed for MEM microbalances fabrication.

Finally, there are some devices which are alternative to MEM microbalances also among MEMS: these devices exploit the fact that some molecules ([60],[67]) drive compressive or tensile stress on a surface where they stick to it. These devices are generally cantilevers, whose top surface is covered by a sensitive layer where a particular kind of molecule can stick to, among the ones which can drive a stress on the surface.

When analytes are attached to the cantilever top surface, a stress gradient is generated inside the cantilever as a consequence of the surface stress driven by stuck molecules, so that the cantilever bends ([60],[67]). In such device the deposition of the sensitive layer (generally a polymer or organic material) has to be carried out carefully in order to avoid that also the bottom surface is covered: in this case the molecules would attach also at the bottom of the cantilever, driving the same surface stress which is driven at the top and thus preventing the cantilever from bending (a tensile stress at the top bends the cantilever in the opposite direction with respect to the bending induced by a tensile stress at the bottom surface).

Chemical sensors based on statically bending cantilever are especially attractive for analysis in liquid environment ([60],[66]), where MEM microbalances are not efficient, because their quality factor in liquids is much smaller than in air. These cantilever-based devices can be also driven into resonance [60], working as a microbalance so that the same MEMS gives two different measurements one based on the static bending and the other on the shift of resonance frequency, due to the adsorbed mass. The double measure can be an advantage when the selectivity of the sensitive layer is not good enough, so that more different kinds of molecules are adsorbed: for example a kind of molecule could shift with its mass the cantilever resonance frequency, but not drive a surface stress, so that can be distinguished from another that causes both a static deflection and a resonance frequency change. Thus a static and a dynamic measure could improve the sensor selectivity if combined together.

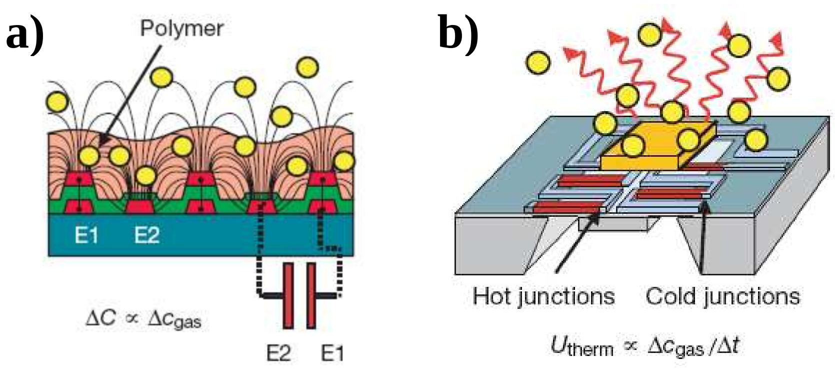

Figure 21: a) Working principle of a capacitive gas sensor from [59]: capacitance changes are proportional to gas concentration. b) Working principle of a calorimetric gas sensor from [59]: analyte adsorption/desorption generates or absorbs heat and thus changes the temperature of a thermally insulted membrane and thermopiles measure the temperature gradient with respect to the chip area outside the membrane. Thermopiles output voltage is proportional to changes in analyte concentration.

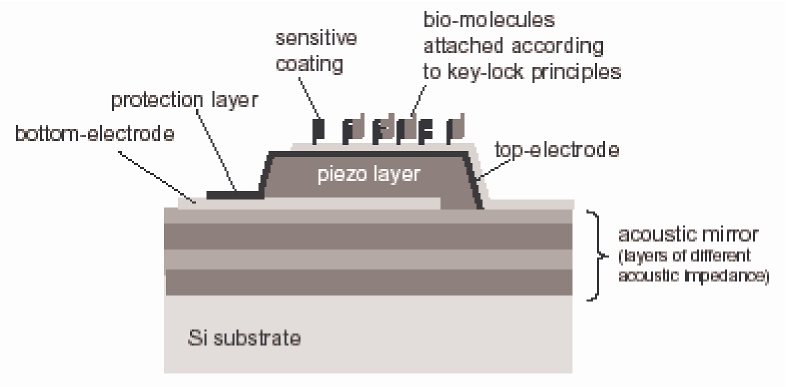

Figure 22: Cross-section of a chemical sensor based on a piezoelectric resonator from [65].

1.3.2 MEM microbalances proposed in literature: designs and applications

Because of the advantages related to their integrability a lot of MEM microbalances have been presented in literature in the last years. Apart from some rare example as in [64], the mechanical structure in MEM microbalance is generally a cantilever: resonant cantilevers coated with a proper polymer (polyurethane, polyetherurethane polyvinylchloride, etc.) have been proposed as sensors for alcohols or other volatile organic compounds as ethanol, methanol [60] and octane [8]. These sensors can have selectivity problems connected with the selectivity of the coating polymer: even if it is more sensitive to one analyte it can absorb also other chemical molecules. Nonetheless the possibility of large number of cantilever integrable on a chip can be exploited to increase the selectivity, combining measurements from cantilever with different coating layers. Furthermore, also a measure of the static deflection induced by analytes attached on the cantilevers can be utilized to improve the selectivity as explained in the previous section.

MEM microbalances based on resonant cantilevers were used also to detect more complex molecules as in the DNA sensor in [69] and they show a selectivity higher than resonant cantilever used as gas sensors: in [69] the sensitive layer is made of DNA filaments, which link steadily only with their complementary filament, which is the target DNA sequence (Figure 23). The resonator surface can anyway adsorbs other smaller molecules whose mass can be anyway neglected with respect to the mass of the target DNA filament. A similar sensitive layer made of “complementary molecules” can be done also for other complex organic molecules such as proteins, leading to the same advantages with respect to the selectivity. Thus the complexity of the analyte guarantees sensor selectivity whatever the mechanical structure, the actuation and the sensing are. Besides their intrinsic high sensitivity to heavy molecules, this is a further reason to use MEM microbalance to detect the presence of complex organic molecules.

Even if the cantilever is undoubtedly the preferred mechanical structure for MEM resonators used as microbalances, with respect to the mechanisms used to actuate and to sense resonator movements there are many different proposed solutions: electrostatic actuation is not the best actuation/sensing mechanisms for MEM microbalances, because, unlike RF MEM resonators, they should not necessarily resonate at high frequencies between 1 MHz and 1 GHz. The resonance frequency shift per nanogram increases, decreasing the resonator mass and increasing the resonance frequency, but the quality factor of MEM resonators generally decreases very much at high frequencies, if not owing to air damping, at least for anchor losses as it is possible to see from references about RF MEM resonators in section 1.2.3. Thus an increase of resonator resonance frequency does not always lead to an improvement of the sensor resolution.

Moreover a MEM microbalance cannot work in vacuum, because has to be exposed to the surroundings in order to sense analyte concentration and the environment could be a gas, generally at atmospheric pressure or a solution. In this conditions electrostatic actuation and sensing does not work as well as in vacuum, because they generally need very small gaps between electrodes and moveable structure to be effective, as it is clear in Eqs. from (2) to (7). But at atmospheric pressure small gaps usually means high squeeze film damping [46], which leads to a small quality factor and subsequently to a small sensor resolution. If the microbalance has to detect the presence of a protein or a DNA sequence in a solution the situation is even worse: the sensor is usually first dipped in the solution under analysis and then dried [69], because in liquid phase the quality factor is in any case too low, but this dipping and drying operation can lead to stiction problems in the structure with small electrode/resonator gaps [70], resulting in the collapse of the rotor on the electrodes, with the consequent destruction of the device. In spite of all these observations electrostatically-driven MEM microbalances has been anyway proposed for example in [71], where the resonant mechanical structure is a cantilever, and in [72], where the resonator is a clamped-clamped beam.

Using a bulk-mode resonant structure could partly reduce these problems with the use of electrostatic actuation: their higher rigidity with respect to cantilever and other flexural-beam resonators usually results in smaller movements and thus in a smaller effect of squeeze film damping, as it is possible to observe for example by comparing quality factors in vacuum and in air from [22] or [37]. Besides the high rigidity makes more difficult the stiction, when the resonator is dried after it was rinsed in a solution.

Being the electrostatic actuation not so efficient for MEM microbalances, all the actuation and sensing mechanisms which are not used for RF MEM resonators have been experimented in resonators for chemical sensing: there are cantilevers which are actuated through bimorphic effect as in [8] and cantilevers piezoelectrically actuated as in [63], where two electrodes drive a PZT layer into vibration which is mechanically transmitted to the cantilever, driving it into resonance (Figure 24). Also magnetic actuation was used [5]: a static magnetic field B_{ext} generated by a micro magnet, interacts with the current I flowing in a current loop integrated on the top of the cantilever, producing a Lorentz force which bends the cantilever according to what in shown in Figure 25.

To detect resonators movements, optical methods and Wheatstone bridges with piezoresistive elements have been proposed. Optical methods have been proposed in several papers ([60],[72]), but they require a bulky detection set-up, at least composed of a laser and a photo detector, which cannot be integrated on sensor chip. Piezoresistive detection can employ piezoresistances or piezo-transistors ([5],[8]), does not need any external equipment and has good performance when piezoresistive elements are fabricated in monocrystalline silicon, but performance are not easily predictable when resistors are made of polycrystalline materials and probably depends on the fabrication process very much. Besides, this sensing mechanism is plagued by thermal drifts.

To conclude the overview about the state of the art of MEM microbalance, it is necessary also to mention that in few cases a shift of resonance frequency greater than expected was observed [63]: it is probably due to the surface stress which is induced by analyte adsorption. When this stress is high enough it can change greatly the stiffness of the resonator and thus its resonance frequency [63].

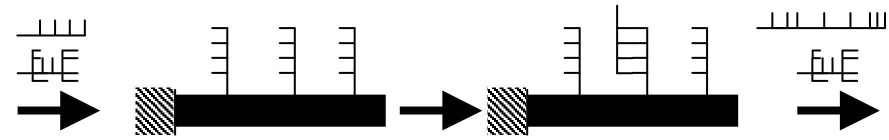

Figure 23: Resonant cantilever for the detection of complex organic molecules as DNA sequences or proteins: the sensitive layer is composed by organic molecules which can link steadily only with their complementary molecule.

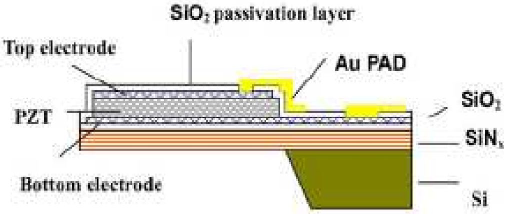

Figure 24: Schematic longitudinal cross-section of a piezoelectrically actuated resonant cantilever for proteins detection, from [63].

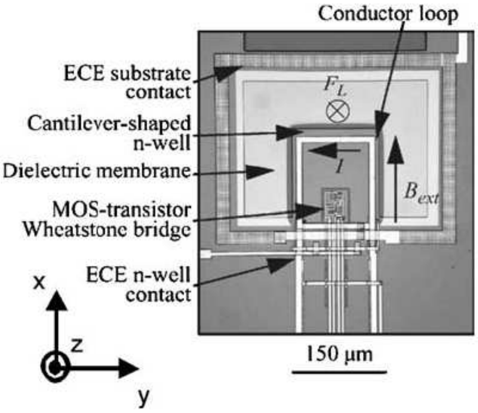

Figure 25: Top-view picture of a magnetically actuated resonant cantilever for chemical sensing, from [4]. The external magnetic field B_{ext} and driving current I, as well as the actuated force F_L are indicated.

In chapter 4 of this Ph.D. thesis the design, fabrication and characterization of a MEM microbalance fabricated with a low-cost CMOS-compatible process is presented. The resonator is not the usual cantilever, but a *torsional resonator*, as it will be detailed in chapter 4. Besides it is magnetically actuated and its movements are sensed magnetically. As shown in chapter 4 the choice of actuation and sensing mechanisms was done basically in order to obtain the compatibility with a CMOS process in the less expensive way and also to guarantee good performance with no need of any external equipment for movements sensing.

Magnetic sensing was seldom used to detect MEMS movements ([6],[73]) and it was never used in MEM microbalances. The resonator proposed in chapter 4 is to our knowledge the only MEM microbalance with magnetically actuation and sensing, while the only other example of MEMS with magnetically actuation and sensing is the resonant cantilever for scanning probe microscope in [6], which is anyway totally different from the torsional resonator presented in chapter 4.

2. Design and modelling of RF free-free flexural resonators

In this chapter the experimental characterization of the free-free resonators presented in the author's Master Degree thesis [18] will be discussed as well as the modelling of their sensitivity to temperature and residual stress. The fundamental result was the measure of the basic operation of a novel free-free third-mode resonator, with flexural support. Potential improvements of the design are also suggested.

A possible equivalent electrical circuit is also proposed in order to refine the model used to design some the proposed devices and to provide a quick a handy analysis tool to system-level designers which could use RF MEM resonators in more complex electronics system. Besides, equivalent circuits allow to include models for MEMS in simulations of the entire on-chip system.

The main results of these research activities described in this chapter, have been presented also at conferences and published on scientific journal ([74],[75],[76],[77]). The discussion will start with a short review of the design issue and of the devices designed in [18].

2.1 Design issues

As anticipated in the first chapter, the main issues of the design of the flexural-beam resonators presented in [18] were the reduction of motional resistance and/or the bias voltage needed to keep low the motional resistance, as well as obtaining resonators with high quality factors. Another important issue was to find topologies, allowing to reach resonance frequency higher than the one presented in literature, even if the target for resonance frequencies of the designed devices was from 5 to 50 MHz, a specification which can be obtained also using other flexural-beam resonator already proposed in literature (for example in [12] and [33]).

The last issue was to find a way to obtain high-Q resonators whose resonance frequency is accordable with a bias voltage, avoiding any decrease of the quality factor when the resonance frequency is changed as is [38].

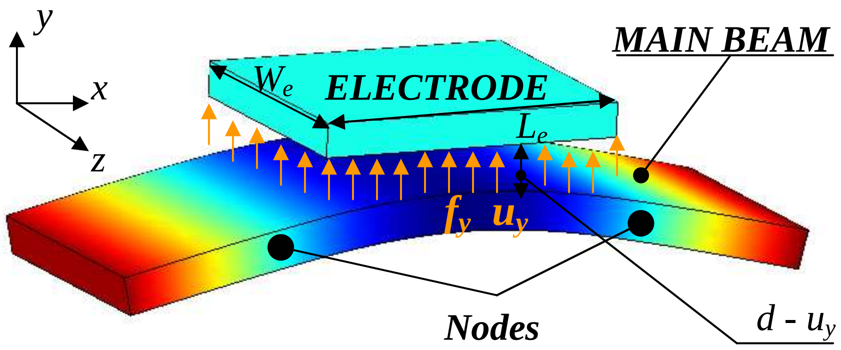

Figure 26: 3D sketch of the deformed shape of the main beam of a free-free resonator, resonating on the first resonance mode. W_e *is the width of the electrode surface which faces the beam and* L_e *its length. Supports are not included in order to show a general situation, valid for free-free resonators both with torsional supports and with bending supports.*

2.1.1 Choice of the laterally-driven free-free resonator as basic structure

In order to obtain a high quality factor the free-free architectures presented in [33] and [38] were considered: these structures guarantee a higher quality factor than that of a clamped-clamped resonator, and consequently lower motional resistance and insertion losses.

Between the vertically-driven [33] and the laterally-driven [38] topology the second one was chosen because of the technological process selected to fabricate the device: this process will be detailed in the third section of this chapter, but its main features is that its structural layer is a thick polysilicon layer, i.e. all the suspended structure and thus all the mechanical moveable parts are made of a thick layer of polysilicon. Conversely the beam width has to be smaller than the thickness, in order to assure the complete release of the beam. Thus lateral actuation and sensing were chosen because the force per unit length actuated by an electrode on a beam is proportional to the width of the resonator surface faced by the electrode as well as the density of current due to resonator movements.

Indeed, considering the system of reference in Figure 26 and neglecting the displacement in direction parallel to the beam length (*x* direction in Figure 26), which is usually much smaller than displacement in the direction along which the beam bends (y direction in Figure 26), the force per unit length f_y in y direction and the current density j are, from (6) and (7):

$$\begin{aligned} f_y(x,t) &= \frac{1}{2}(V_S+V_{DC})^2\,\frac{\partial c(x,t)}{\partial u_y(x,t)} = \frac{1}{2}(V_S+V_{DC})^2\,\frac{\varepsilon_0 W_e}{\left[d-u_y(x,t)\right]^2} \\ j(x,t) &= \frac{\partial\left[c(x,t)\cdot V\right]}{\partial t} = (V_S+V_{DC})\frac{\partial c(x,t)}{\partial u_x(x,t)}\frac{\partial u_x(x,t)}{\partial t} + \frac{\partial V_s}{\partial t}c(x,t) = \\ &= (V_s+V_{DC})\frac{\varepsilon_0 W_e}{\left[d-u_y(x,t)\right]^2} + \frac{\partial V_s}{\partial t}\frac{\varepsilon_0 W_e}{\left[d-u_y(x,t)\right]} \end{aligned} \tag{9}$$

where W_e is the width of the electrode surface, d the gap between the resonator and the electrode, u_y the displacement along y direction and ε_0 the dielectric constant of the air. The voltage V applied to between electrode and resonator is considered as a superposition of a signal V_S and a DC bias voltage V_{DC}. In (9) there is also a parasitic component dependent of the density of current $c(x,t)\cdot(\partial V_s/\partial t)$, which is not due to rotor movements and does not appear in (7) according to which only a DC voltage is applied between electrode and rotor.

Usually $V_S << V_{DC}$ and $u_y << d$, so that (9) can be approximated as:

$$\begin{aligned} f_y(x,t) &\approx \left(V_S V_{DC} + \frac{V_{DC}^2}{2}\right)\frac{\varepsilon_0 W_e}{d^2} \\ j(x,t) &\approx V_{DC}\frac{\varepsilon_0 W_e}{d^2}\frac{\partial u_y}{\partial t} + \frac{\partial V_s}{\partial t}\frac{\varepsilon_0 W_e}{d} \end{aligned} \tag{10}$$

From (10) is clear that W_e has to be high in order to increase electromechanical coupling, but this is not the only reason why a laterally driven resonator was preferred: from (10) it is also clear that the gap between resonator and electrode is even more important than W_e, in order to obtain a high electromechanical coupling. In the following it will be shown that electrostatic actuator can be used to reduce d, while analogous device cannot be designed for vertically driven resonators.

Finally, laterally-driven resonators can be designed also as two-port devices, while vertically-driven resonators have to be one-port devices. Indeed all the free-free resonators presented in this thesis are two-port devices.

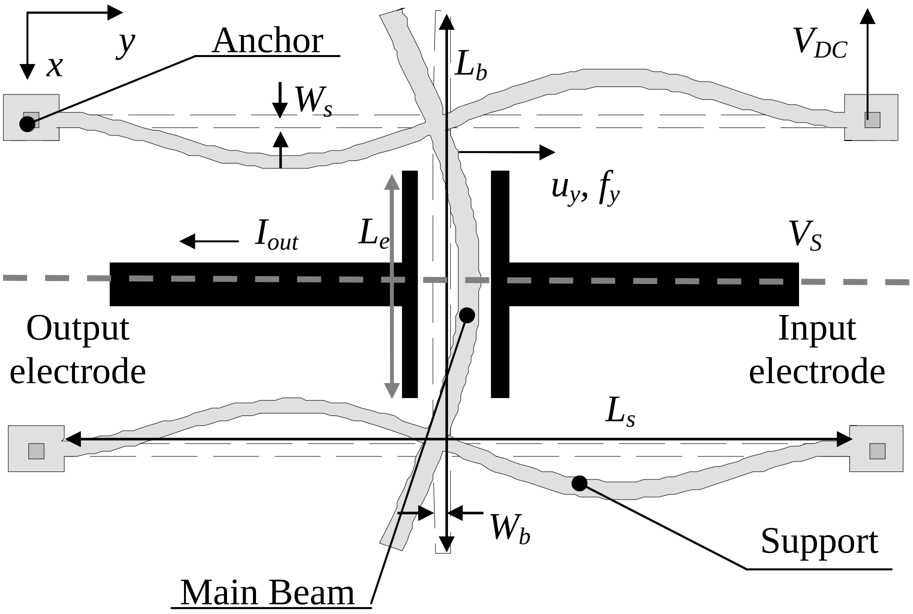

Figure 27: Schematic top view of a two-port free-free resonator with flexural support, with the main beam resonating on its first free-free mode. The symmetry axis of the structure, parallel to y direction, is indicated by grey dashed line.

Thus the devices presented in [18] are basically free-free laterally-driven resonators, which were designed in order to improve the performance of the two-port free-free resonator, resonating on the first resonance mode, presented by Nguyen in [38]. A sketch of this device is represented in Figure 27.

2.1.2 Motional resistance and resonance frequency

The main goal of the design work in [18] was to reduce the motional resistance of the free-free architecture proposed in [38]. This result is important not only in order to reduce the insertion losses of the resonator when it is used as a filter, but also to reduce the amplification of the active element needed when the resonator is used as a frequency-selective element in an oscillator. Furthermore, if the motional resistance is too high, it is impossible to build an oscillator, at least in three-point architecture [78], because in this case the Barkhausen conditions cannot be satisfied, even if the amplification of the active element is infinite, as discussed in [18]. In the specific motional resistance has to be lower than a function which decreases if the parasitic capacitances between electrodes and between each electrode and ground increase [18].

Of course it is fundamental also to set the resonance frequency by design, because it determines the central frequency if the resonator is used as a filter or the oscillation frequency if the device is employed in oscillator architecture. Besides, the need of filters and oscillators for RF applications at frequency even higher than 1 GHz compels to research architectures which allows to obtain resonance frequencies as high as possible.

Due to the importance of motional resistance and resonance frequency, it can be useful to remind how they can be found and the expression used to evaluate it in [18] for a free-free structure like the one in Figure 27.

Assuming that supports do not load the main beam, they were neglected and a free-free beam in the space like in Figure 26 was considered. Considering the beam deflection u_y, the dynamic equation for a single vibrating beam is, according to the Euler-Bernoulli equation with a damping term added [9]:

$$EI\frac{\partial^4 u_y}{\partial x^4}+\mu\frac{\partial^2 u_y}{\partial t^2}+c(x)\frac{\partial u_y}{\partial t}=f_y\approx\begin{cases}\dfrac{\varepsilon_0 W_e}{d^2}V_{DC}V_S & x\in[L_e]\\ 0 & x\notin[L_e]\end{cases}\qquad(11)$$

where E is the beam Young's modulus, μ its linear mass density and $c(x)$ is a damping parameter; $[L_e]$ is interval of length along which the resonator is faced by the driving electrode, while W_e and d are respectively the input electrode width and the gap between it and the beam. I is the inertia moment of the beam cross-section, given by the expression $I=W_b^3H/12$, where W_b is the width of the beam in the direction in which the beam bends (y direction in Figures 26 and 27), while H is the thickness of the beam in the third direction, orthogonal to both the length and the width (z direction in Figures 26 and 27). The static component of the distributed force in (10) is neglected in (11) because practically does not affect the resonator behaviour close to the resonance[4]. Besides if the bias voltage is applied on the rotor as in Figure 27 another static force actuated by the output electrode has to be considered and this force has a sign opposite to the static component in (11), reducing the effect of the static component.

---

[4] The only considerable effect of the static component of the force can be a static deflection of the beam, leading to a gap $d(x)$ dependent on x direction. Anyway this effect is usually neglectable.

The beam is considered as homogeneous with respect to mass density and Young's modulus, because the resonators in [18] were designed to be fabricated in homogeneous polysilicon, while with respect to the damping a possible dependence is retained with respect to the x direction, parallel to the beam length, because $c(x)$ is not always homogeneously distributed: for example if consider anchor losses is more reasonable to consider damping as concentrated at the anchor or at the points of connection between main beam and supports in the model used for free-free beam in [18], so that $c(x)$ is proportional to a Dirac delta function. The dependence of damping on the beam transversal dimensions (z and y directions), can be anyway neglected if the beam is slender.

In order to use the Euler-Bernoulli equation the beam has to be slender, i.e. its length is enough larger than its width in the direction in which the beam bends (y direction in Figures 26 and 27 for the main beam). If the hypothesis does not hold the beam has to be model with the more complex Timoshenko approach [31]. All the resonators designed in [18] are composed of beams where the ratio length/width is larger than 10, so that the hypothesis of slender beam should hold in that case.

Following the approach in [9] it is possible to find the resonance frequencies of the resonator, as well as an equivalent electrical circuit for a single-beam resonator, working close to the resonance. From this equivalent circuit an expression for the motional resistance can be found.

The fundamental hypothesis in considering the solution u_y of (11) as approximately equal to the solution of the following simplified equation obtained by neglecting damping and external force:

$$EI\frac{\partial^4 u_y}{\partial x^4}+\mu\frac{\partial^2 u_y}{\partial t^2}=0 \tag{12}$$

which is the equation usually solved to find the resonance modes of a slender beam [31].

The hypothesis is reasonable close to the resonance if the resonator quality factor is very high: this means that the damping coefficient, related to energy loss, has to be very small according to the quality factor definition given by (8), so that is generally negligible with respect to the other terms in the equation. Besides a high quality factor means that beam deflection is very high at the resonance even if actuated by a small distributed force, which is consequently negligible with respect to the deflection dependent terms at the resonance (the ratio between the maximum displacement and the actuated force is Q times higher than with a static actuation, if the device is approximately considered as a second order system). Thus Eq. (12) can be used to approximate the deflection at the resonance of the beam.

According to the so-called modal analysis technique [9], solutions of Eqs. (11) and (12)can be found by assuming u_y as a superposition of function written as a product of a part only dependent on the time $\xi(t)$ and a part only dependent on x, $\Phi(x)$:

$$u_y = \sum_{m=1}^{\infty} \Phi_m(x)\xi_m(t) \tag{13}$$

Each term of the sum in (13) represents a resonance mode of the device. The parts only dependent on x, $\Phi_m(x)$ are also known as mode shapes, because describe the deformed shape of the structure. They can be found exploiting the linearity of equation (12), which allows to find each $\xi_m(t)\Phi_m(x)$ by substituting it in (12). Considering in particular $m = n$, such equation becomes after some straightforward manipulations:

$$\frac{EI}{\Phi_n}\frac{\partial^4 \Phi_n}{\partial x^4} = \frac{\mu}{\xi_n}\frac{\partial^2 \xi_n}{\partial t^2} \tag{14}$$

A function only dependent on the spatial variable x can be equal to a variable only dependent on the time t, only if they are both constant with respect to x and t, leading to:

$$\frac{\partial^4 \Phi_n}{\partial x^4} = \left(\frac{\lambda_n}{L_b}\right)^4 \Phi_n \tag{15}$$

where the constant is normalized with respect to the beam length L_b; λ_n is defined as the n^th^ eigenvalue of the structure, related to the nth resonance mode. Applying the proper boundary conditions it is possible to find both $\Phi_n(x)$ and λ_n. These boundary conditions are bending moment M and shear force S zero at the ends (assumed to be at $x = 0$ and $x = L$ of a free-free beam (free ends condition) [31]:

$$\begin{aligned} M &= EI\frac{\partial^2 u_y}{\partial x^2} &&\Rightarrow \left.\frac{\partial^2 u_y}{\partial x^2}\right|_{x=0} = \left.\frac{\partial^2 u_y}{\partial x^2}\right|_{x=L} = 0 \\ S &= EI\frac{\partial^3 u_y}{\partial x^3} &&\Rightarrow \left.\frac{\partial^3 u_y}{\partial x^3}\right|_{x=0} = \left.\frac{\partial^3 u_y}{\partial x^3}\right|_{x=L} = 0 \end{aligned} \tag{16}$$

Applying the boundary conditions in (16), the solution of (15) is[5]:

$$\begin{aligned}\Phi_n = A\Bigg\{&\left[\cosh\left(\lambda_n \frac{x}{L_b}\right) + \cos\left(\lambda_n \frac{x}{L_b}\right)\right] + \\ &+ \frac{\cosh(\lambda_n)\text{-}\cos(\lambda_n)}{\sinh(\lambda_n) - \sin(\lambda_n)}\left[\sinh\left(\lambda_n \frac{x}{L_b}\right) + \sin\left(\lambda_n \frac{x}{L_b}\right)\right]\Bigg\}\end{aligned} \tag{17}$$

with the eigenvalue λ_n given by the n$^{\text{th}}$ solution of the equation:

$$1 - \cos(\lambda_n)\cosh(\lambda_n) = 0 \tag{18}$$

A is a constant which can be chosen arbitrarily [31]. In [18] it was chosen in order to obtain the following normalization condition:

$$\int_0^{L_b} \Phi_n^2 dx = L_b \tag{19}$$

From (14) it is possible also to find the resonance frequency of each resonance mode. If the function $\xi_n(t)$ is assumed to be a sinusoid with frequency f_n, Eq. (14), combined with (15), gives:

$$\frac{1}{\Phi_n}\frac{\partial^4 \Phi_n}{\partial x^4} = -\frac{\mu}{EI}(2\pi f_n)^2 = \left(\frac{\lambda_n}{L_b}\right)^4 \tag{20}$$

which leads to the following expression for the resonance frequency f_n of the n$^{\text{th}}$, if the expressions for the inertia moment I and for the linear mass density μ are expanded ($\mu = \rho H W_b$, where ρ is the volumetric mass density or simply mass density):

$$f_n = \frac{1}{2\pi}\left(\frac{\lambda_n}{L_b}\right)^2 \sqrt{\frac{E}{12\rho}} W_b \tag{21}$$

---

[5] Details can be found in both [18] and [31].

To find an equivalent electrical circuit, solutions as expressed in (13) have to be replaced in (11), leading to:

$$EI\sum_{n=1}^{\infty}\frac{\partial^4\Phi_m}{\partial x^4}\xi_m+\mu\sum_{n=1}^{\infty}\Phi_m\frac{\partial^2\xi_m}{\partial t^2}+c\sum_{n=1}^{\infty}\Phi_m\frac{\partial\xi_m}{\partial t}=\begin{cases}\frac{\varepsilon_0 W_e}{d^2}V_{DC}V_S & x\in\left[L_e\right]\\ 0 & x\notin\left[L_e\right]\end{cases}\tag{22}$$

At this point in [9] the orthogonaility property of the mode shapes is used to simplify the problem in Eq. (22). The equation is multiplied for the n^{th} mode shape and integrated along the cantilever length, but being the mode shape orthogonal:

$$\int_0^{L_b}\Phi_n\left(x\right)\Phi_m\left(x\right)=0 \qquad \text{if}\quad m\neq n\tag{23}$$

the following equation can be found after straightforward calculations:

$$K_n\xi_n+r_n\dot{\xi}_n+M_n\ddot{\xi}_n=P_n\tag{24}$$

where a generalized stiffness K_m is defined, as well as a generalized mechanical resistance r_m, a generalized mass M_m and a generalized load P_m. The expressions for these parameters are:

$$\begin{aligned}&K_n=EI\int_0^{L_b}\Phi_n\frac{\partial^4\Phi_m}{\partial x^4}dx=EI\left(\frac{\lambda_n}{L_b}\right)^4\int_0^{L_b}\Phi_n^2dx=EI\frac{\lambda_n^4}{L_b^3} \qquad && R_n=\int_0^{L_b}c\left(x\right)\Phi_n^2dx\\ &M_n=\mu\int_0^{L_b}\Phi_n^2dx=\mu L_b=M && P_n=\frac{\varepsilon_0 W_e}{d^2}V_{DC}V_S\int_{\left[L_e\right]}\Phi_n dx=\Gamma_{INn}V_S\end{aligned}\tag{25}$$

In (25) Γ_{INn} is the input electromechanical coupling factor for the n^{th} resonance mode. The subscript $[L_e]$ means that the integral defining P_m and Γ_{INn} is calculated along the length of the beam faced by the driving electrode. The normalization condition expressed in (19) makes the generalized mass equal to the actual mass of the beam.

The same approach can be used to find equation analogous to (24) for each ξ_m, finding a system of infinite equations, one for each mode shape.

Considering the output electrode in Figure 27, the displacement due to each mode shape produces a current density according to Eq. (10), leading to a current I_{out} flowing out from the output electrode:

$$I_{out} = \sum_{m=1}^{\infty} \xi_m V_{DC} \frac{\varepsilon_0 W_e}{d^2} \int_{[L_e]} \Phi_m dx = \sum_{m=1}^{\infty} \Gamma_{OUTm} \xi_m = \sum_{m=1}^{\infty} \Gamma_{INm} \xi_m = \sum_{m=1}^{\infty} \Gamma_m \xi_m \quad (26)$$

where the output electrode is assumed to be exactly equal to the input electrode and placed in symmetric position with respect to it, as in Figure 27, in order to obtain $\Gamma_{INm} = \Gamma_{OUTm} = \Gamma_m$. This condition is respected by all the resonators in [18], because the geometry and the position of the input electrode, which maximize the input electromechanical coupling, maximize also the output electromechanical coupling if applied at the output electrode, so that there is no reason to design the two electrodes in a different way. This electrode symmetry produces also the total cancel of the static component of the actuated force, if the bias voltage is applied on the rotor as in Figure 27, because in this case the static force actuated by output electrode totally counterbalance the static force actuated by the input electrode. The polarization in Figure 27, consequently avoid a static deflection of the resonator if electrodes are equal and symmetric.

Considering $\dot{\xi}_n$ as a current and P_n as a voltage, Eq. (24) is equivalent to the equation which rules the behaviour of a series RLC circuit with a M_m instead of the inductance, $1/K_n$ in place of the capacitance and r_n replacing the electrical resistance. The same holds of course for any resonance mode.

Finally, the electromechanical couplings factors Γ_n have the function of ideal transformers, changing for each mode shape a voltage in a generalized force and a generalized displacement ξ_n in a current, which is summed with all the currents generated by the other mode shapes, giving the global output current. The device can be thus described by the equivalent circuit in Figure 28. If the resonance frequencies of the beam are not close (as usually it is) and if the quality factor of the resonance mode is high, close to the nth resonance mode, considering only the nth RLC circuit in Figure 28 is an acceptable approximation. Thus to find the motional resistance of a free-free resonator, with the main beam resonating on the nth resonance mode, it is possible to refer to the simplified circuit in Figure 29.

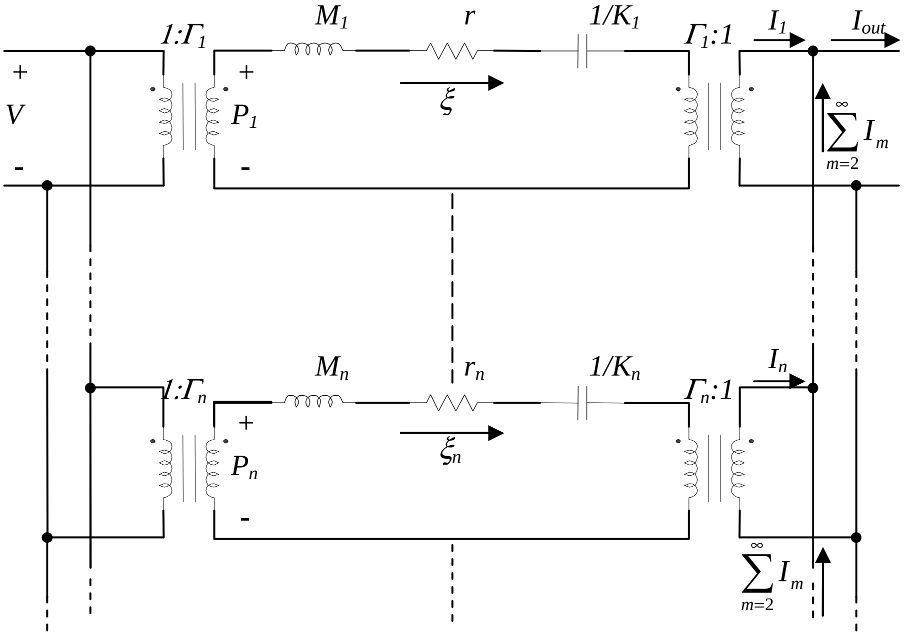

Figure 28: General equivalent circuit for a single-beam resonator: it can be applied to a free-free resonator if it is possible to neglect the effect of the supports (the free-free beam was considered totally free in the space).

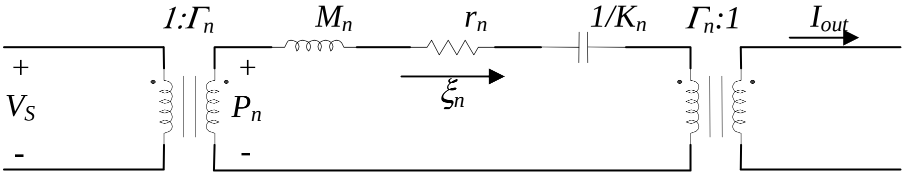

Figure 29: Equivalent circuit for a single beam resonator, considering only the nth resonance mode: it holds if the actuation frequency is close to the nth resonance frequency, the quality factor of the nth resonance mode is high and the nth resonance frequency is far enough from the other resonance frequencies.

As shown in [18] if the input and output electromechanical coupling factors are equal, at the nth resonance frequency of the beam, the circuit in Figure 29 is equivalent to an electrical resistance, which can be defined as motional resistance R_n for the n$^{\text{th}}$ resonance mode, whose value can be calculated by:

$$R_n = \frac{r_n}{\Gamma_n^2} = \frac{K_n}{2\pi f_n Q_n \Gamma_n^2} = \frac{2\pi f_n M_n}{Q_n \Gamma_n^2} \tag{27}$$

where Q_n is the quality factor of the n$^{\text{th}}$ resonance mode, which can be calculated by the expression $Q_n = 2\pi f_n M_n / r_n$. Combining Eq. (27) with the expressions for M_m and Γ_n from (25) and (26), the motional resistance can be expressed as:

$$R_n = \frac{2\pi f_n \rho W_b L_b d^4}{Q_n \varepsilon_0^2 H V_{DC}^2 \left(\int_{[L_e]} \Phi_n dx \right)^2} \tag{28}$$

where the width of the electrode area facing the resonator W_e is considered equal to resonator thickness H because electrodes and resonator are supposed to be fabricated with the same structural layer, as it was for the resonators presented in [18].

Eq. (28), as well as Eqs. (18) and (21) for the resonance frequencies, is fundamental for the design choice discussed in section 2.2.

2.1.3 Accordability of a MEM resonator

Resonance frequency tunability of MEM resonators can be very useful for RF applications: in some application having tuneable oscillator or filter with accordable central frequency is very important, but even more significant is the possibility of using this tunability to correct errors in the resonance frequency value of the fabricated devices with respect to the designed value, due to process parameter dispersion.

A variation of the resonance frequency can be achieved by changing the bias voltage V_{DC}. To evaluate the effect of V_{DC} on the resonance frequency of the device, it is necessary to consider an approximation for the distributed force f_y in (9) which is more accurate than the one used to find Eqs. (10) and (11). In this case, instead of neglecting u_y, a linearization of the expression for the distributed force f_y in (9) with respect to u_y has to be done, obtaining:

$$f_y \approx \frac{1}{2}\left(V_S + V_{DC}\right)^2 \left(\frac{\varepsilon_0 W_e}{d^2} + 2\frac{\varepsilon_0 W_e}{d^3} u_y \right) \approx \frac{\varepsilon_0 W_e}{d^2} V_{DC} V_S + \frac{\varepsilon_0 W_e}{d^3} V_{DC}^2 \, u_y \tag{29}$$

where as in (10), the assumption $V_S << V_{DC}$ is exploited and as in (11) the static component of the force is neglected. Besides if the device is biased as in Figure 27, in the expression for the force has to be included also the force actuated by the output electrode which has no more only a static component, but also a component dependent on the deflection u_y. If output and input electrode are equal and placed in the same position with respect to the beam, it is possible to demonstrate that the term proportional to u_y doubles [18]:

$$f_y \approx \frac{\varepsilon_0 W_e}{d^2} V_{DC} V_S + 2\frac{\varepsilon_0 W_e}{d^3} V_{DC}^2 u_y \tag{30}$$

If the expression in (30) is replaced to the distributed force in (11), and the same approach described in 2.1.2 is repeated a new equation ruling the equivalent circuits in Figures 28 and 29 is found instead of Eq. (24):

$$\left(K_n - 2\Delta K_n\right)\xi_n + r_n\dot{\xi}_n + M_n\ddot{\xi}_n = P_n \tag{31}$$

where K_n, r_n, M_n, P_n have the same expressions shown in (25), while for ΔK_n it is possible to find ([9],[18]):

$$\Delta K_n = \frac{\varepsilon_0 W_e}{d^3} V_{DC}^2 \int_{[L_e]} \Phi_n^2 dx \tag{32}$$

ΔK_m is always positive, thus an increase of the bias voltage produces a decrease of the equivalent stiffness of the device according to (31). This leads to a reduction of the resonance frequency according to the following relation:

$$f_n^* = \sqrt{\frac{\left(K_n - 2\Delta K_n\right)}{M_n}} = f_n\sqrt{1 - \frac{2\Delta K_n}{K_n}} = f_n\sqrt{1 - \frac{\varepsilon_0 W_e}{d^3} V_{DC}^2 \frac{L_b^3}{EI\lambda_n^4} \int_{[L_e]} \Phi_n^2 dx} \tag{33}$$

where f^*_n is the resonance frequency calculated considering the effect of the bias voltage, while f_n is the resonance frequency calculated neglecting it.

On the other hand, in a free-free architecture the tuning of the resonance frequency through the bias voltage leads to a decrease of the quality factor, probably because the support $\lambda/4$ adaptation works exactly only at the resonance frequency the free-free beam is supposed to resonate [38]. A solution of this problem was proposed in [18] and will be discussed in the next section.

2.2 Designed devices

In [18] were proposed two innovative devices: a free-free resonator, resonating on the third resonance mode, with flexural supports and a free-free resonator, resonating on the first resonance mode, with flexural supports and with additional electrodes for the frequency tuning. The first device has theoretically a motional resistance lower than the one of a free-free resonator resonating on the first resonance mode, if the resonance frequency and the quality factor are the same. The second solution in theory allows to tune the resonator resonance frequency, without any quality factor decrease.

In the fabricated chip were included also a clamped-clamped beam and a free-free resonator, resonating on the first resonance mode similar to the one presented in [38], in order to compare the performance of the innovative devices which were presented in [18] with devices already presented in literature. The design of the clamped-clamped beam resonator was very easy: the width was fixed to be equal to the minimum value allowed by layout rules, in order to limit the section of the anchors and consequently the anchor losses (the choice is in agreement with the model presented in [36]); the length was fixed to select the resonance frequency (10 MHz) exploiting Eq. (18) and (21) for $n = 1$ (first resonance mode), because as shown in [31], the equation for the resonance frequency is the same for clamped-clamped and free-free beams.

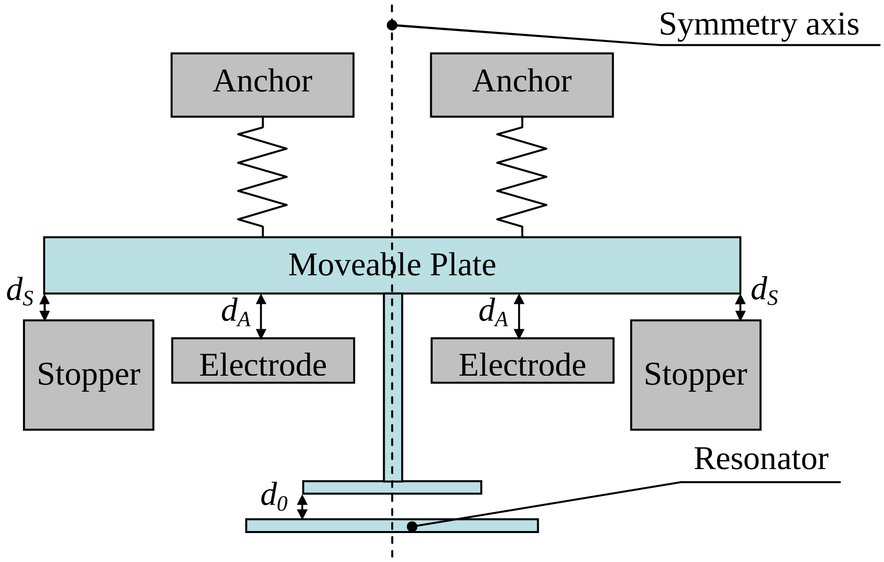

Figure 30: Schematic top view of the electrostatic actuator used to reduce the resonator gap. In grey are represented the anchored parts, in cyan the moveable parts.

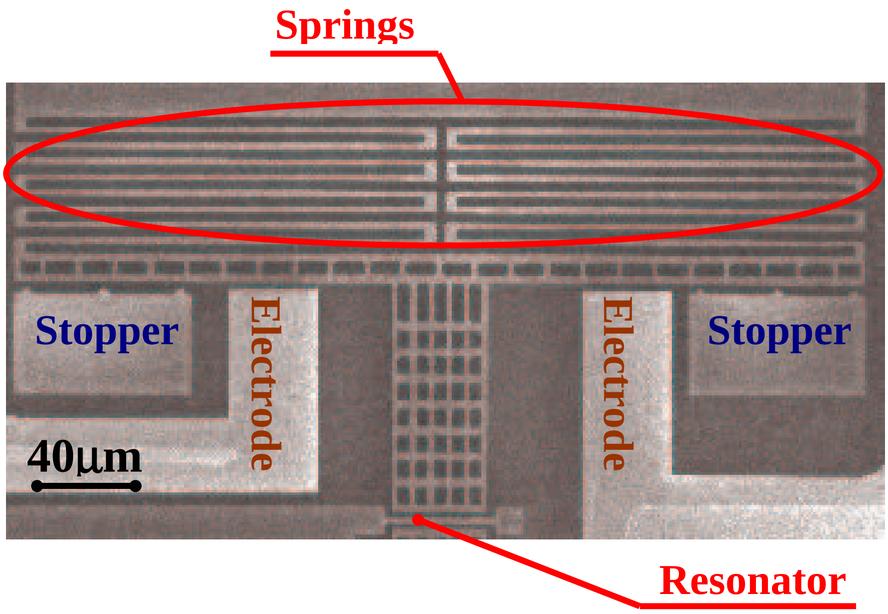

Figure 31: SEM picture of one of the electrostatic actuators fabricated.

The design of the other devices will be discussed in detail in the next subsections. It is however necessary to introduce now an auxiliary device, used to reduce the gap d between electrodes: indeed the motional resistance critically depends on this value (R_n is proportional to d^4 according to (28)). Being the minimum gap allowed by layout rules of the process chosen to fabricate the device too high (higher than 2 µm) to have reasonable motional resistances, the introduction of an actuator able to reduce d is of fundamental importance.

2.2.1 Auxiliary electrostatic actuators to reduce electrode/resonator gap

To reduce the gap between electrodes and beam, a solution already presented in [32] was used. The electrode was connected to a moveable plate which is anchored to the substrate via two system of springs and actuated by two fixed electrodes (Figure 30) through a static voltage V_{ON} applied between fixed electrodes and moveable plate (or resonator input or output electrode). If V_{ON} is higher than the pull-in voltage V_{pi} of the system springs/electrostatic actuators, the moveable plate falls onto some stoppers which avoid the collapse of the moveable part on the fixed electrodes. This collapse has to be stopped to prevent structure damage, which can occur because the high static voltage V_{ON}.

This electrostatic actuator fixes the final gap between resonating beam and actuation electrode to a value d_0-d_S, where d_0 is the initial gap and d_S the gap between stoppers and moveable plate of the actuator (Figure 30). The value of the final gap is very accurate because depend on a difference between two distance and consequently if there is a process parameter dispersion, it can be modified only by matching errors and not by errors which affect in the same way the two distance.

The positioning system was dimensioned in order to obtain a reduction of the resonator/electrodes gap from a value higher than 2 μm to 0.2 μm.

As already mentioned, the actuators exploit the pull-in mechanisms: it consists in an instability of the electrostatic actuator/spring system, due to the fact that if the voltage is too high (i.e. higher than pull-in voltage) the elastic force exerted by the springs cannot equilibrate anymore the electrostatic force. The value of the pull-in voltage was calculated in details in [18]:

$$V_{pi} = \sqrt{\frac{8}{27}\frac{Kd_A^{\ 3}}{\varepsilon_0 A}} \tag{34}$$

where K is the overall stiffness of the system of springs d_A the gap between moveable part and fixed electrodes of the actuator, A the surface of the fixed electrodes and ε_0 is the dielectric constant of the air.

Eq. (34) was used to design actuators with V_{ON} = V_{pi} about 40 V in the final layout: even if it is possible to obtain lower actuation voltage, it would be achieved only increasing the area occupied by the device. Thus a trade-off was chosen between actuator efficiency and occupied area. In Figure 31 a SEM picture of one of the fabricated electrostatic actuator is included in order to show the large area occupied by the electrostatic actuator if compared with a resonator.

Finally, springs electrodes and stoppers where symmetrically placed with respect to a symmetry axis (Figure 30) in order to obtain a pure translation of the structure in direction perpendicular to the main beam of the resonator, without any spurious rotation or displacement in direction parallel to the main beam.

2.2.2 Free-free resonator resonating on the first resonance mode

The typical structure for a free-free resonator, resonating on the first mode (type FF1) is represented in Figure 27. The structure dimensions were chosen to maximize the quality factor, minimize the motional resistance a target resonance frequency. First the supports width W_s was chosen as the minimum allowed by layout rules fixed by the chosen process. This was done both to reduce the contact area between anchors and supports and to minimize the area of connection between the main beam and supports. Thus this choice should minimize supports anchor losses and the interaction between supports and main beam, better approximating the condition of free-free beam for the main beam. Indeed one fundamental condition to obtain a free-free beam is to join the supports to the main beam in two points which correspond to the nodes of the first free-free resonance mode of the main beam. In this way supports do not hinder the deflection of main beam, because the point of connection is fixed, but this is strictly true only if the two beam have zero width: for example if the width of the support is larger than zero the support is connected to the beam also in a region where its deflection is not zero. If the support width is small this deflection is small, while if the width is large, the region of connection can reach even sections of the main beam where the deflection of the main beam should be high.

Also the beam width was set to the minimum value allowed by layout rules in order to minimize the region of interaction between main beam and supports. Besides even if the quality factor is constant with W_b, if the resonance frequency is fixed, by properly manipulating Eq. (28) it is possible to show that the motional resistance is proportional to $\sqrt{W_b}$ [6], at least if the main beam is long enough [18]. Thus even if the beam width does not affect the quality factor, the motional resistance is minimized if W_b is as small as possible.

It is necessary to say that damping mechanisms different from anchor losses were neglected during this design: some authors ([35],[36]) showed the importance of thermoelastic losses in beam resonators and with respect to this mechanism, choosing the minimum value allowed by layout for the beams width could be not the optimum.

Once the beam width is fixed and the resonance mode order is chosen, according to (18) and (21) the resonance frequency can be fixed by properly

---

[6] This dependence is not linear as in (28), because if the resonance frequency is fixed if W_b changes also L_b as to change accordingly as well as the electrodes length L_e, which the integral $EC = \int_{[L_e]} \Phi_m dx$ depends on.

choosing the beam length L_b (the material properties E and ρ are fixed by the process). For example for one of these devices, designed to resonate at 10 MHz, the value chosen for L_b was about 42 µm.

To find the nodes of the first free-free mode of the main beam, the zeros of Eqs. (17) for $n = 1$ and consequently for $\lambda_n = \lambda_1$, whose value is 4.73 according to Eq. (18). The mode shape has two nodes one for $0.224L_b$, the other for $0.776L_b$.

In order to obtain the free-free condition on the main beam, supports have not only to be connected to the main beam at the nodal point, but they have also to exert no bending moment on the main beam. In this there is not a strict analogy with transmission lines as in the case of free-free with torsional supports [33], but the condition can be achieved if each support half resonates on its first *clamped-pinned* mode at the resonance frequency of the first free-free mode of the main beam. In this fashion the pinned condition, which means zero displacement and bending moment, is automatically satisfied at the centre of the support, i.e. at the connection with the main beam, obtaining the desired behaviour. The clamped condition at the other end is forced by anchoring the support beams at each end. The resonance of each support half on its first clamped-pinned mode, when the main beam resonates on its first free-free mode, can be obtained by choosing properly the supports length L_s, once the supports width W_s is chosen, according the already mentioned criterion.

In [18] it was shown that the overall support resonates on its second clamped-clamped mode when each support half resonates on its first clamped-pinned mode. Thus an easy way to fix L_s is to exploit Eqs. (18) and (21), which hold also for clamped-clamped beams as shown in [31]. In this way the value for L_s can be found from the following expression:

$$L_s = \lambda_2 \sqrt{\frac{W_s}{2\pi f_0}\sqrt{\frac{E}{12\rho}}} \tag{35}$$

where $\lambda_2 = 7.85$ and f_0 is the resonance frequency of the free-free resonator. Therefore supports are longer than the main beam: L_s is almost 70 µm for the first-mode free-free resonator designed to resonate at 10 MHz.

Finally, the electrodes are placed as in Figure 27 in order to maximize the electromechanical coupling factors Γ_m and consequently to minimize the motional resistance: according to Eqs. (25),(26) and (28), this can be achieved by maximizing the integral $EC = \int_{[L_e]} \Phi_m dx$. Thus electrodes are placed in regions where the mode shape is maximum and has constant sign. On the other hand the choice represented in Figure 27 minimizes the integral for many other resonance modes of the structure. Among them there are all the resonance modes according to which the main beam vibrates antisymmetrically with respect to the symmetry axis of the structure parallel to y direction: for these modes the integral EC and consequently the electromechanical coupling Γ_m are zero. This reduce the number of spurious peak in the device frequency response, which alters the ideal behaviour of the resonator as a filter and can make interfering channel and disturbs to pass through the filter when it is used in RF communication systems.

The other resonance modes of the structure are however attenuated also because it is expected that they have a quality factor lower than the first free-free mode, because the adaptation of the support does not work for them.

2.2.3 Free-free resonator resonating on the third resonance mode

According to Eq. (28) the motional resistance strongly decreases if the integral EC increases. This integral is proportional to the length of electrodes L_e [18], so that the motional resistance for the nth mode is proportional to $1/L_e^2$, which is in turn proportional to $1/L_b^2$, because the longer is the beam, the longer could be the electrodes. On the other hand if the target resonance frequency is fixed $L_b \propto \lambda_n$ according to (21), so that from (28) it can be found that:

$$R_n \propto \frac{1}{\lambda_n F\left(\Phi_n\right) Q_n} \tag{36}$$

where F is function of the mode shape and of the way of placing the electrodes. Changing the resonance mode of the free-free beam, at least among the lower ones, the function F does not change so much, if for each mode the electrode position is optimized to minimize the motional resistance. The eigenvalues λ_n monotonically increase with m, thus, considering a group of resonance modes, if the quality factor of each mode is the same, the highest mode has a lowest motional resistance. It happens basically because in order to obtain the target resonance frequency, it is necessary to design a beam longer[7] than if the selected mode is a lower one, allowing consequently longer electrodes and a better electromechanical coupling.

---

[7] Of course the comparison has to be done between beam with the same width , according to (21)

The idea of designing a third-mode free-free resonator comes directly from the observation which has been just discussed: if the main beam resonates on the third mode instead of on the first one, to obtain the same resonance frequency the length has to be higher and the ratio between the motional resistances of the first-mode resonator and the one of the third-mode resonator is approximately:

$$\frac{R_1}{R_3} \approx \frac{\lambda_3}{\lambda_1} \approx 2.3 \tag{37}$$

where it was assumed $F(\Phi_3) \approx F(\Phi_1)$ and the quality factor is considered the same for the two modes. Thus, implementing a third-mode resonator the motional resistance could be reduced to more than a half of the one of a first-mode free-free resonator.

The designed third-mode free-free resonator (type FF3) is schematically represented in Figure 32, where the deflected shape of the resonator is represented as well the undeformed structure. The beams widths W_b and W_s were set equal to the minimum value allowed by layout for the same reasons discussed in 2.2.2 about the design of the first-mode resonator. Then L_b was set in order to obtain the target resonance frequency (with respect to the designed structures, about 98 μm to obtain 10 MHz), using Eqs. (18) and (21), with $n = 3$.

The free-free condition is obtained by connecting the supports to the main beam at two nodal points of its third free-free resonance mode. According to (17) this mode has four nodes: at $0.094L_b$, $0.356L_b$, $0.644L_b$ and $0.906L_b$. The nodes position are different from the ones of the first mode and thus if the support are connected to one of these nodes, they hinder the movements of the first mode of the free-free beam, which correspond to a lower resonance frequency of the structure, resulting in a positive effect with respect to the spectral purity of the device.

The external nodes at $0.094L_b$ and $0.906L_b$ were chosen as connection points for the supports, but there are no specific reasons to prefer these nodes to the others.

As for the first-mode free-free resonator the length of the supports L_S was chosen in order to make them to resonate on their second mode clamped-clamped at the resonance frequency of the device, in order to make them to exert no bending moment at the connection with the main beam. Thus their length is the same as for a first-mode resonator resonating at the same frequency (with respect to the designed structures, about 70 μm at 10 MHz).

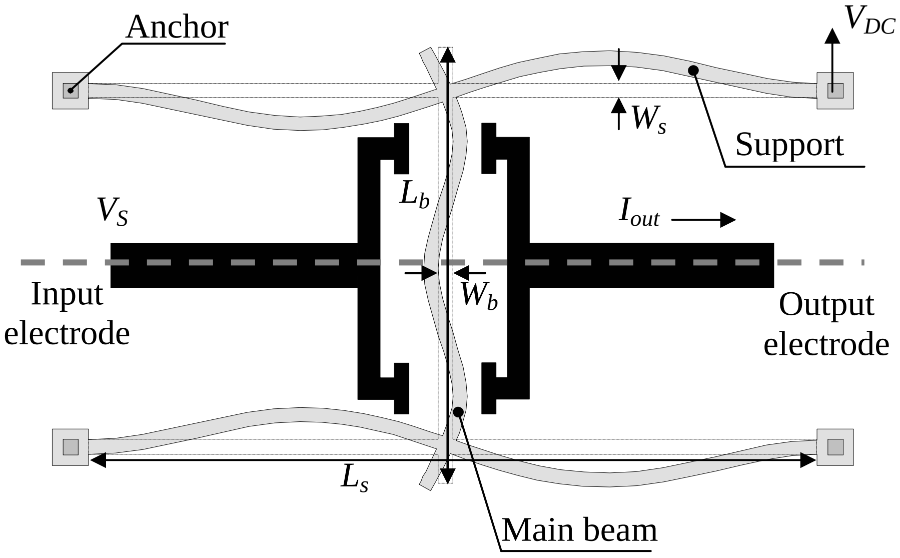

Figure 32: Schematic top view of a two-port free-free resonator with flexural support, with the main beam resonating on its third free-free mode. The symmetry axis of the structure, parallel to y direction, is indicated by grey dashed line.

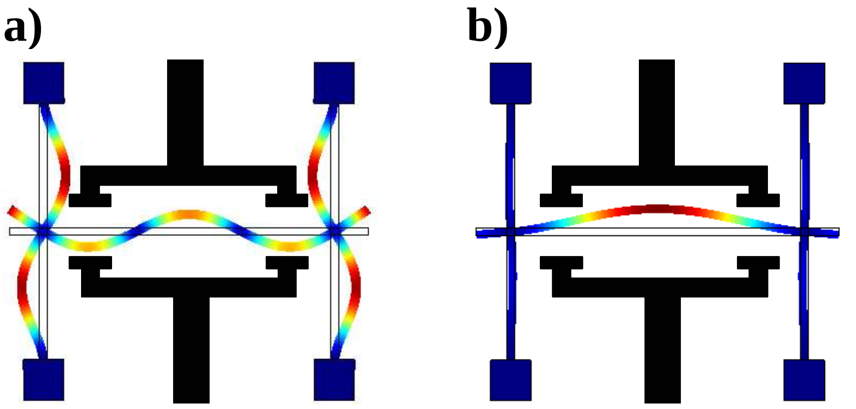

Figure 33: Deflected shapes of two resonance mode of a third-mode free-free resonator from a 2D FEM modal simulation performed with Femlab [43]: a) the fundamental mode, according to which the main beam resonates on its third resonance mode; b) a parasitic mode associated to the first free-free mode of the main beam: in this the supports do not resonate on their second resonance mode and they hinder the main beam movements. The electrodes, represented in black, are clearly placed in order to maximize the electromechanical coupling with the fundamental mode and to minimize it with the parasitic mode.

The electrodes were placed as in Figure 32 in order to maximize the integral *EC*, by placing them so that they face the resonator where the third mode shape is maximum and with a constant sign (Figure 33a). Through this electrodes positioning, a high value of $F(\Phi_m)$ is obtained, so that considering it in (36), the ratio between R_1 and R_3 is even slightly higher than the one given by (37).

This choice also reduce the electromechanical coupling with the mode of the overall structure, connected to the first free-free mode of the main beam (Figure 33b): electrodes do not cover the region where the deflection due this mode is maximum. Besides the symmetric configuration of the electrodes leads to zero electromechanical coupling for all the mode shape antisymmetric with respect to the symmetry axis represented in Figure 32.

Finally, the third-mode free-free resonator has a further important advantage with respect to the first-mode resonator: according to (18) and (21), the maximum resonance frequency achievable is higher because if the width and the length are the same the third-mode resonator reach frequency much higher than the first-mode device. With respect to the technological process chosen to fabricate the device in [18], it was estimated that the maximum resonance frequency which can be reached with the third-mode resonator represented in Figure 32, is almost 300 MHz, while it is slightly higher than 40 MHz[8] for a first-mode resonator as the one in Figure 27. However, at such frequencies the motional resistance is too high, even with high bias voltage [18], so that practically the maximum resonance frequency is lower for both the architectures.

2.2.4 Free-free resonator resonating on the first resonance mode, with frequency tuning

A new device was designed in order to obtain the tunability of a free-free resonator by changing the bias voltage, without decreasing the quality factor.

The idea is quite simple and comes from the following observation: according to what shown in the previous sections, supports exert no bending moment on the main beam only at a certain frequency, i.e. the frequency which they resonate at on their second clamped-clamped mode. Thus the

---

[8] According to (18), the ratio between the two maximum frequencies should be equal to $(\lambda_3/\lambda_1)^2$. The ratio calculated in [18] is higher because it was considered also the necessity of inserting the electrodes between the two supports as required by Figures 28 an 33, respecting layout rules of the process, such as the minimum width of the suspended structures of the minimum distance between them.

adaptation condition works only if the main beam resonates on one of its free-free modes at the same frequency (this discussion is general and holds for both first-mode and third-mode free-free resonators).

If the structure was designed without considering the *“electrostatic softening”*, described by (33), the adaptation would never work when a bias voltage is applied. On the other hand if this effect is considered, the adaptation can work only at one specific bias voltage.

The problem can be solved if the same electrostatic softening acting on the main beam is reproduced on the supports. This can be obtained if a couple of auxiliary electrodes are placed in front of the support as in Figure 34. If a DC voltage V_{tune} is applied to such electrodes a DC voltage V_{tune} - V_{DC} induce a variation of the supports resonance frequency, according to Eq. (33).

If this variation is the same driven on the main beam by the bias voltage V_{DC} supports adaptation work as if no bias voltage is applied.

Tuning electrodes in Figure 34 allow to tune the resonance frequency of the device, obtaining exactly the desired resonance frequency in spite of any in process parameter dispersion, or allow to use the device in tuneable filters and oscillators, even if, according to the calculations [18], the tuning range is small.

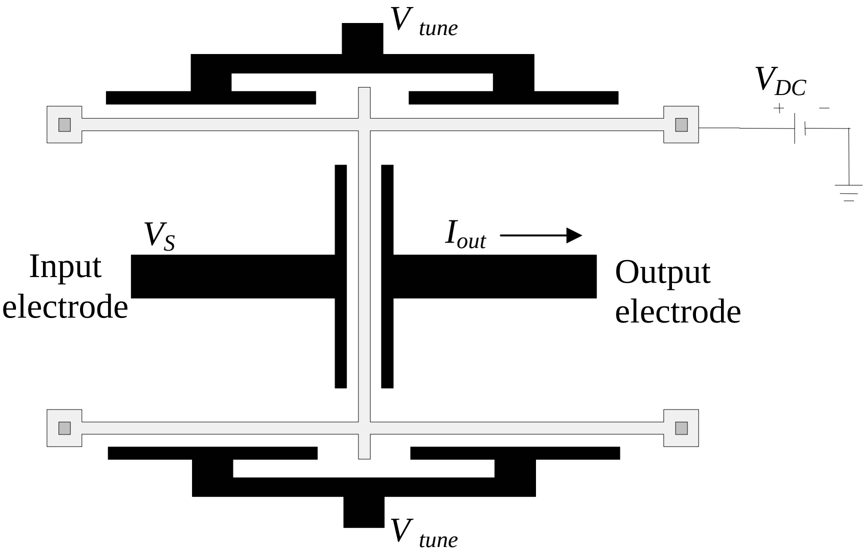

Figure 34: Schematic top view of a two-port free-free resonator with flexural support, with two auxiliary electrodes which are used to retain a high quality factor when the device resonance frequency is tuned by changing the bias voltage V_{DC} .

Besides if supports width and/or length of the fabricated device are different from the designed dimensions as a consequence of process parameter dispersion, it is possible to correct a decrease of the quality factor which can be due to this parameter dispersion, by setting properly the voltage V_{tune} applied to the tuning electrodes.

A first-mode free-free resonator with tuneable electrodes was included in the chip where also the other kinds of resonator presented in this section were fabricated. Tuning electrodes could be anyway added also to a third-mode free-free resonator.

2.3 Fabrication

The resonators were fabricated by using the *THELMA* MEMS technology, developed by STMicroelectronics.

THELMA is a surface micromachining process developed to fabricate capacitive inertial sensors. In the process flow a first polysilicon thin layer, used for electrical connectivity, is followed by a silicon dioxide sacrificial layer, and by a second, thick, epitaxially grown polysilicon layer, which constitutes the structure of the presented resonators and of their driving electrodes. The structures are defined in this layer by a *deep reactive ion etching* (DRIE). Selective etching of the silicon dioxide releases the thick polysilicon structures, which become free to move under electrostatic forces. The high thickness of the epitaxial polysilicon implies a large capacitance between electrodes, and thus a large electromechanical coupling ([25],[32]). A cross-section of a generic device fabricated with *THELMA* is represented in Figure 35. In spite of the high thickness of the polysilicon structural layer the electromechanical coupling factor which can be obtained fabricating resonators with this process, is too low, because the minimum distance allowed between two suspended structure (i.e. between resonator and actuation or sensing electrode) is higher then 2 μm, even if the DRIE allows a good aspect ratio of the trench. As already mentioned, owing to the strong dependence of the motional resistance on the gap between electrodes and resonator, this process limit compels to introduce the actuators described in 2.2.1 to reduce the gap.

Among the fabricated device there is a clamped-clamped beam designed to resonate at 10 MHz (a SEM picture of its is represented in Figure 31), as well as some FF1 resonators with resonance frequencies from 5 MHz to 15 MHz some FF3 resonators with resonance frequency from 10 MHz to 50 MHz; a FF1 resonator designed to resonate at 10 MHz is represented in the picture in Figure 36, while a FF3 resonator with the same resonance frequency is shown in the picture in Figure 37.

The electrostatic actuators occupy a lot of space on the chip, especially if compared with resonator as shown in Figures 31 and 36, and thus limit the number of device which can be integrated on the same chip. Due to the great area occupied by the electrostatic actuator the device which require more area on the chip is the resonator with tuneable electrodes presented in 2.2.4: also the gap between tuneable electrodes and supports have to be decreased by actuators as the input and output electrodes of the device because also the electromechanical softening is critical dependent on the gap ($\Delta K_m \propto 1/d^3$ according to (32)). If the tuneable electrodes/supports gap is not decreased to value comparable to the gap between signal electrodes and resonator, it is practically impossible to obtain the same shift of the resonance frequency for the supports and the main beam, needed to retaining a high quality factor when the resonance frequency is tuned.

Thus a resonator with tuneable electrodes occupies an area approximately twice as large as the area needed by a resonator without them. For this reason only one tuneable device was included in the fabricated chip: such device is a first-mode free-free resonator nominally resonating at 10 MHz.

The most important aspects of the design and the fabrication of all these devices were also presented in [74].

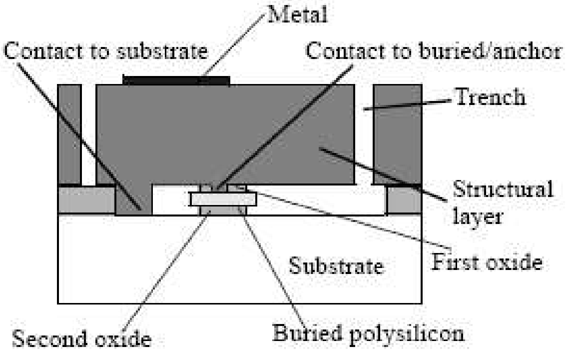

Figure 35: Cross-section of a generic device fabricated with THELMA, taken from [32].

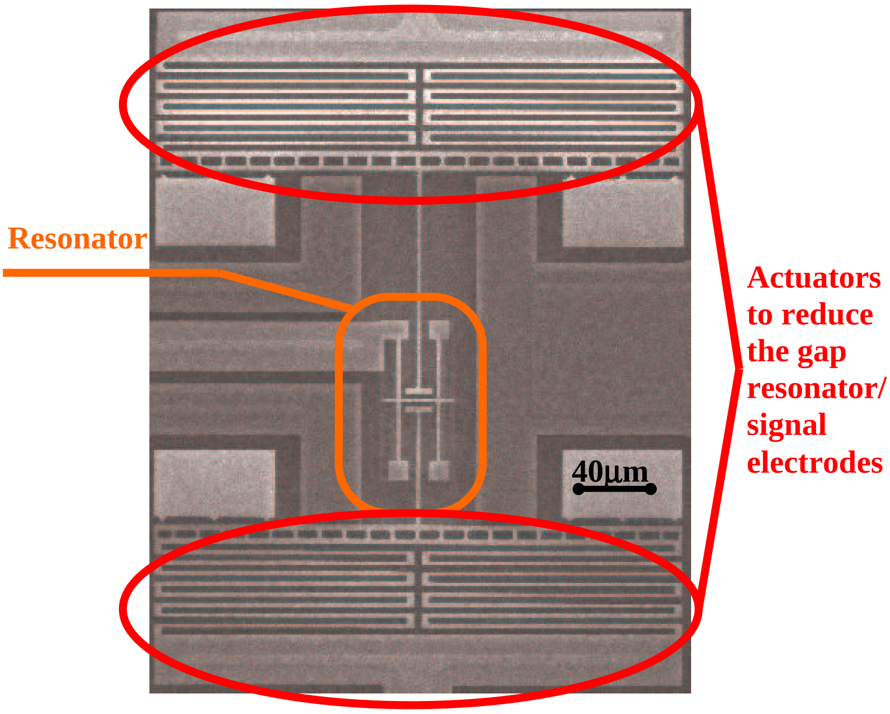

Figure 36: SEM picture of a fabricated FF1 resonator with nominal resonance frequency 10 MHz. The area occupied by the resonator is indicated as well as the region with the two actuators needed to reduce the gap between the resonator and both the sensing and the actuation electrode.

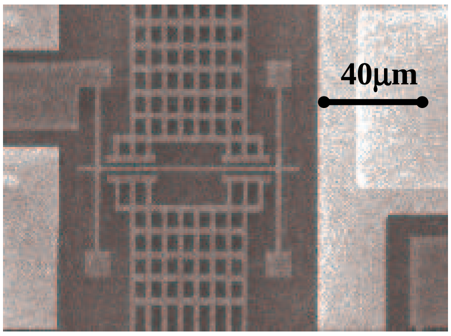

Figure 37: SEM picture of a fabricated FF3 resonator with nominal resonance frequency 10 MHz.

2.4 Failure mechanisms and preliminary tests

Before the presentation of the measurements setup utilized to characterize the device and the results of the characterization, it could be useful to discuss some mechanisms failures which made impossible the characterization of considerable number of devices in each of the tested chips, reducing the number of available experimental data.

Since the first preliminary tests, it was found that the fabricated devices can fail for two different reasons: failure of the system for the positioning of driving and sensing electrodes and presence of unexpected parasitic paths connecting terminals nominally insulated, leading to a current flow even in DC, even if capacitive parasitic paths do not work. These parasitic paths were equivalent to small resistances, leading practically to a short-circuit between for example input and output or signal electrodes and resonator, leading to the impossibility of using the device. Sometimes the resistive path was between bias voltage and ground, leading to extremely large currents, with the consequent risk of device damage. These resistive currents were unexpected because all the terminals of the designed devices are connected theoretically only through capacitive path as it is clear from their schematic views in Figures 27, 32 and 34.

An accurate analysis of this “parasitic resistance” carried out with a parameter analyzer shows that they are only in first approximation linear: for high voltage the current flowing through them increases much than linearly, showing a strongly non-linear behaviour. In some case keeping the voltage low enough allowed to limit the current flowing through the parasitic path and to make some measurement on the device. On the other hand sometimes the amplitude of these parasitic currents was observed to increase with the use of the device, making the device useless after a short usage.

Even if it is not completely clear the cause of such resistive path a possible explanation can be supposed: when the chip pads are soldered to carry out the wire bonding[9], the oxide which insulates the devices with respect to the substrate could be cracked. The oxide damage allows a path for the current through the substrate: if the oxide under two pads is damaged the substrate act as a shortcut connecting the two pads. This should explain the non-linear behaviour and the decrease of the parasitic resistance with the usage, which was observed especially with respect to the terminals where high voltage was applied: time after time the high voltage could increase the oxide damage. Anyway the soldering was clearly identified as the cause of these currents: setting properly the soldering parameters, a decrease of the number of devices per chip affected by these parasitic currents was observed.

---

[9] The wire bonding was done in our laboratory by a wedge bonding technique.

While the problem of the resistive parasitic currents was unforeseen and of difficult understanding, troubles connected to the electrostatic actuators described in 2.2.1 were expected and can be easily explained: for example the complex structure of springs could be not perfectly released, so that the structure is blocked and cannot move, or if it can, it could not only translate but also rotate because even if the structure is designed to be symmetric, this symmetry can be broken for the reason that some of the beams, the springs are composed of, are blocked. Furthermore, the systems of springs are very sensitive to mechanical shocks because of the low stiffness of the springs, which is needed to keep low the actuation voltage. Mechanical shocks as well as an imperfect release can lead to structure blocked in such way that the positioning system cannot work anymore, as in the case of the device represented in Figure 38. Another reason of the failure of the system for the positioning of the electrodes was the presence of a parasitic path between the actuation electrodes and ground leading to an increase of the actuation voltage to too high values, because of the voltage partition introduced by the parasitic resistance.

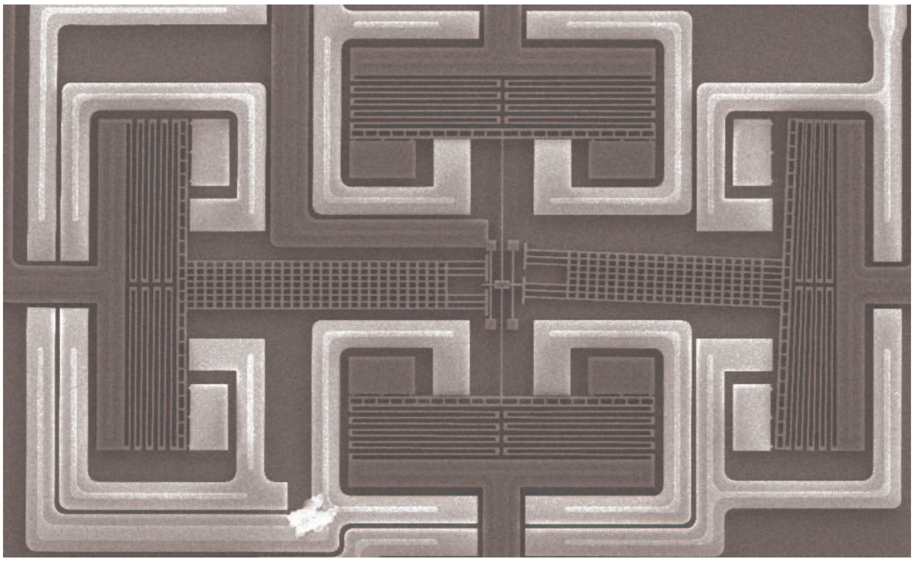

Figure 38: SEM picture of a fabricated FF1 resonator with auxiliary electrodes for the tuning. The tuning electrode on the right is rotated as a consequence of an imperfect release of the electrostatic actuators or some mechanical shocks. The nominal resonance frequency of the device is 10 MHz.

Finally, a last cause of failure was observed: sometimes a sudden short-circuit was observed between terminals on which a high difference of voltage was applied. This was due to a ring of polysilicon surrounding the pads, which is included generally in all the chips fabricated with *THELMA*: wires carrying high voltage can pass very close to this ring and if two of them are to close to the ring, a short-circuit could happen, as was observed by chance at the optical microscope, while it was observed if the electrode positioning system was working.

The probability of short-circuit was reduced by increasing the height of the arc described by each wire from package leads to chip pads.

All these failure mechanisms are especially important for the free-free resonator with tuning electrodes: its high complexity, the higher number of pads and systems for the positioning of the electrodes (Figure 38), make the failure of this device very common. The incidence of a failure for this device was so high that was impossible to characterize any free-free resonator with tuning electrode.

2.5 Characterization of the devices

In this section it is shown how it is possible to measure the basic features of the fabricated resonators, such as the resonance frequency and the quality factor, by the acquisition of the mechanical frequency response of the device under vacuum.

The technique to acquire such frequency response will be shown in the following and compared with some of the other possible techniques. The time needed for each acquisition is long because the resonator output is evaluated for a long span of frequency of the force actuated on the resonator and because the frequency step has to be small, because the expected quality factor is high.

Thus before any acquisition the devices were preliminary tested to find if they were affected by the failure mechanisms introduced in section 2.4.

First the insulation of the terminals of any device was verified by using a parameter analyzer. Then devices, which had not problems of parasitic resistive currents, were tested with respect to the system for the electrodes positioning: a voltage V_{ON} higher than the pull-in voltage was applied to drive each electrostatic actuator and observing the device with an optical microscope it was possible observe if the electrodes moved. All the devices which did not pass these two tests were preliminary excluded from the measurement of mechanical frequency response of the device.

In the following after the description of the set-up chosen to acquire such frequency response, results from some devices will be given. It will be observed that the measured resonance frequency is significantly lower than the expected one and a possible reason of this disagreement will be proposed, by considering the results from some FEM simulations.

2.5.1 Measurement set-up

The main problem in the characterization of MEM resonator are the parasitic capacitances [79]: even if no parasitic resistive path connects input and output, there is at least a capacitive path connecting input and output, so that a parasitic current is superposed to the current due to rotor movements, which is expressed in (26). Besides there are the capacitance between signals electrodes and ground: they can be important as an additional input or output load. Adding the parasitic capacitances to the equivalent circuit for small signal and close to the resonance represented in Figure 29, for a free-free resonator resonating on the nth, it is possible to find the circuit in Figure 39.

Due to the parasitic capacitance C_{IO} between the input and the output electrode of the resonator, the output current I_{out} is given by the sum of the current I_n due to the main beam movements and of a parasitic current I_p flowing through the capacitive feed-through between input and output. This superposition leads to a transfer function different from the second order system which is expected for a filter. If the series impedance Z_S to the input voltage is neglected and considering that input admittance Y_{IN} as the parallel of a capacitance C_{IN} and a resistance R_{IN}, it is possible to find the following function for the transfer function as a function of the angular frequency $\omega = 2\pi f$ (f is the frequency):

$$\frac{V_{out}}{V_S} = \frac{j2\pi f \cdot R_{in}\dfrac{\Gamma_n^2}{K_n}\left[1+\dfrac{K_m C_{IO}}{\Gamma_m^2}\left(1-\dfrac{M_n}{K_n}\omega^2 + j\omega\dfrac{r_n}{K_n}\right)\right]}{-\dfrac{j\omega^3 M_n C_P}{K_n} - \omega^2\left(r_n R_{IN} C_P + M_n\right) + j\omega\left[R_{IN}\left(C_P + \dfrac{\Gamma_n^2}{K_n}\right) + \dfrac{r_n}{K_n}\right] + 1} \qquad (38)$$

where $C_P = C_O + C_{IO} + C_{IN}$. Capacitance C_{IO} does not affect the result because the output impedance Z_S of the voltage generator V_S is neglected. The assumption of neglecting Z_S corresponds to the optimal condition, according to which the voltage V_S is totally used to actuate the force (if Z_S is big enough the voltage which is used to actuate the force is a partition of V_S). On the other hand the hypothesis on the shape of the load Y_{IN} is reasonable working at high frequencies (even using a pure resistance as a load the capacitance has to be considered. The transfer function in (38) is totally different from the second order system, which would be obtained without parasitic capacitance. The problem is even more evident if $C_P >> \Gamma_n^2 / K_n$ is assumed:

$$\begin{aligned}\frac{V_{out}}{V_S} &\approx \frac{j\omega \cdot R_{in} \dfrac{\Gamma_n^2}{K_n}\left[1+\dfrac{K_n C_{IO}}{\Gamma_n^2}\left(1-\dfrac{M_n}{K_n}\omega^2 + j\omega\dfrac{r_n}{K_n}\right)\right]}{-j\omega^3 \dfrac{M_n}{K_n} C_P - \dfrac{\omega^2}{K_n}\left(r_n R_{IN} C_P + M_n\right) + j\omega\left(R_{IN} C_P + \dfrac{r_n}{K_n}\right) + 1} = \\ &= \frac{j\omega \cdot R_{in} \dfrac{\Gamma_n^2}{K_n}\left[1+\dfrac{K_n C_{IO}}{\Gamma_n^2}\left(1-\dfrac{M_n}{K_n}\omega^2 + j\omega\dfrac{r_n}{K_n}\right)\right]}{\left(1-\dfrac{M_n}{K_n}\omega^2 + j\omega\dfrac{r_n}{K_n}\right)\left(1+j\omega \cdot R_{in} C_P\right)} = \qquad (39) \\ &= \frac{j2\pi f \cdot R_{in} \dfrac{\Gamma_n^2}{K_n}\left[1+\dfrac{K_n C_{IO}}{\Gamma_n^2}\left(1-\dfrac{f^2}{f_n^2} + j\dfrac{f}{Q_n f_n}\right)\right]}{\left(1-\dfrac{f^2}{f_n^2} + j\dfrac{f}{Q_n f_n}\right)\left(1+j2\pi f \cdot R_{in} C_P\right)}\end{aligned}$$

where K_n / M_n is substituted with $2\pi f_n$ and r_n / K_n with $1/(2\pi f_n Q_n)$; f_n represents the resonance frequency and Q_n the quality factor. In this case the transfer function has two poles exactly at the resonator resonance frequency, but it has also two zeros whose frequency f_z is pretty close to the resonance frequency:

$$f_z = f_n \sqrt{1+\frac{\Gamma_n^2}{K_n C_{IO}}} \qquad (40)$$

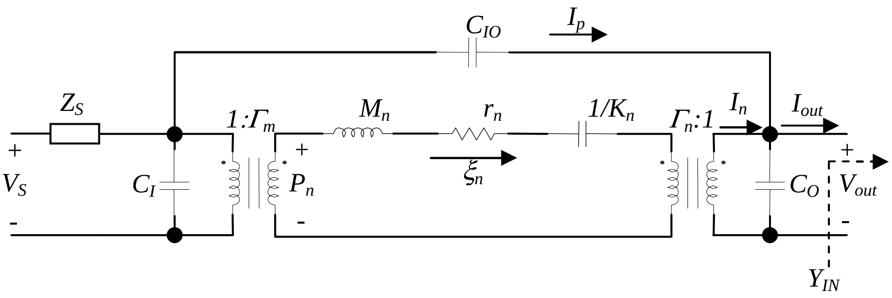

Figure 39: Equivalent circuit for a single beam resonator resonating on its n^th^ mode, complete of parasitic capacitances. It holds if the actuation frequency is close to the n^th^ resonance frequency, the quality factor of the n^th^ resonance mode is high and the n^th^ resonance frequency is far enough from the other resonance frequencies.

Zeros frequency is closer to the poles corresponding to the resonator resonance frequency as much as C_{IO} is higher. If $C_{IO} >> \Gamma_n^2/K_n$ the two frequencies are almost equal so that zeros almost cancel poles and the device cannot work anymore as a filter.

Hypotheses $C_P >> \Gamma_n^2/K_n$ and $C_{IO} >> \Gamma_n^2/K_n$ can be easily satisfied: the value for Γ_n^2/K_n is generally about some fF while if the device is inserted in a PCB board for the measurement, parasitic capacitance between terminals and ground can be even higher than 1 pF. The feed-through capacitance C_{IO} could be lower, but is anyway much higher than Γ_n^2/K_n. Thus the configuration in Figures 27 and 32 cannot be used to characterize the devices, even if it is the typical configuration used to obtain a linear behaviour of the filter.

A possible idea to reduce the effect of the parasitic capacitance is the use of the device as one-port resonator with differential driving, as represented in Figure 40. The output current is collected from the rotor. If $V_{DC} >> V_S$ and $V_{DC} >> V_{out}$, the force actuated by the electrode IN2 is negligible with respect to the force actuated by IN1 and no current due to the resonator movements flows through the capacitance composed by the electrode IN1 and the resonator. Thus only the current due to the parasitic capacitance C_O flows through IN2 and the equivalent circuit can be represented in Figure 41 (Z_S is neglected).

The transfer function in this configuration can be expressed by solving the equivalent circuit [80]:

$$\frac{V_{out}}{V_S}=\frac{j\omega\cdot R_{in}\frac{\Gamma_n^2}{K_n}\left[1+\frac{K_n\left(C_I-C_O\right)}{\Gamma_n^2}\left(1-\frac{M_n}{K_n}\omega^2+j\omega\frac{r_n}{K_n}\right)\right]}{-\frac{j\omega^3 M_n C_{P2}}{K_n}-\frac{\omega^2}{K_n}\left(r_n R_{IN} C_{P2}+M_n\right)+j\omega\left[R_{IN}\left(C_{P2}+\frac{\Gamma_n^2}{K_n}\right)+\frac{r_n}{K_n}\right]+1}\approx$$

$$\approx\frac{j2\pi f\cdot R_{in}\frac{\Gamma_n^2}{K_n}\left[1+\frac{K_m\left(C_I-C_O\right)}{\Gamma_n^2}\left(1-\frac{f^2}{f_n^2}+\frac{jf}{Q_n f_n}\right)\right]}{\left(1-\frac{f^2}{f_n^2}+j\frac{f}{Q_n f_n}\right)\left(1+j2\pi f\cdot R_{in}C_{P2}\right)} \tag{41}$$

where $C_{P2} = C_I + C_0 + C_{IN}$. The transfer function is approximated, assuming $C_{P2} >> \Gamma_n^2/K_n$, which is reasonable for the same motivations just discussed about the traditional linear driving. The capacitance C_{IO} between the two electrodes plays no role in this configuration.

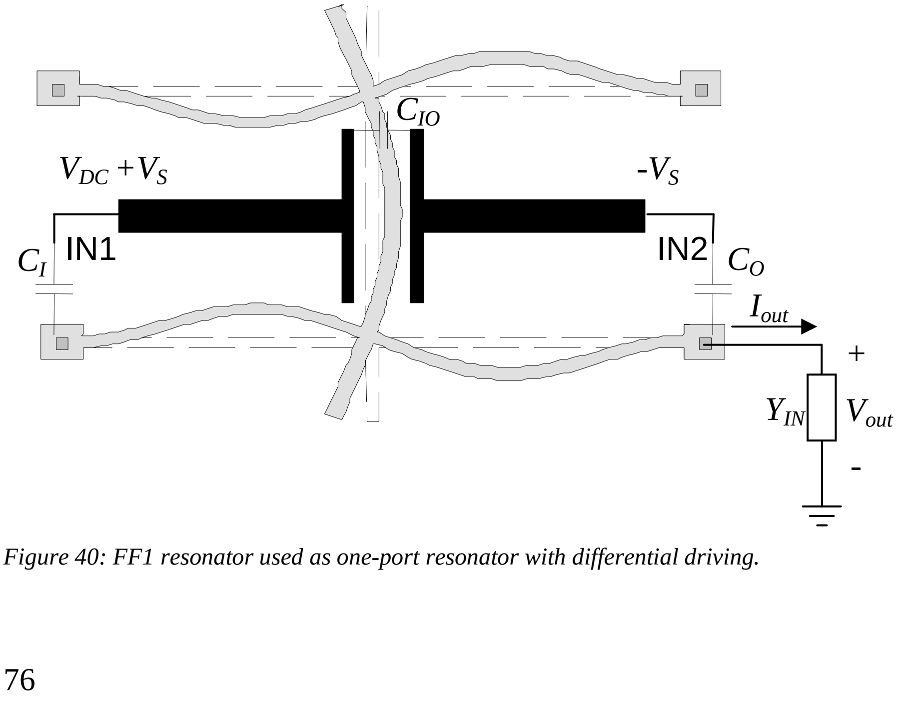

Figure 40: FF1 resonator used as one-port resonator with differential driving.

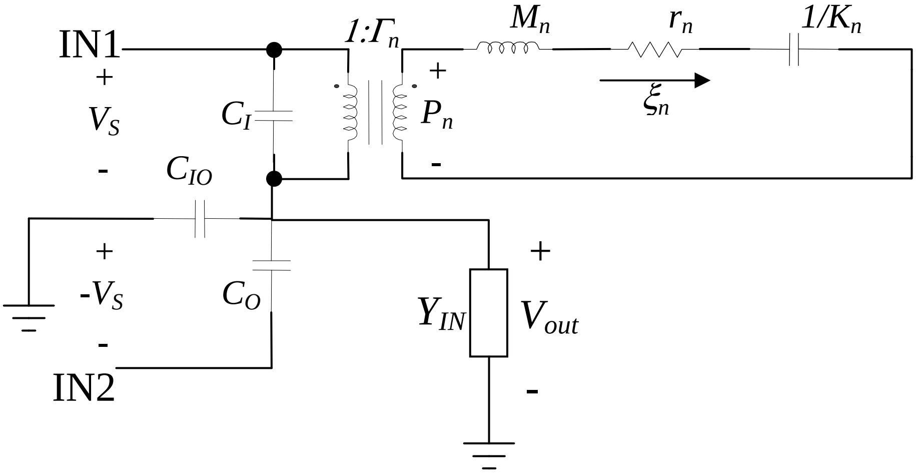

Figure 41: Equivalent circuit for a free-free resonator, with the main beam resonating on its n^{th} *mode, complete of parasitic capacitances, for the differential driving.*

As in (39), the frequencies of the poles connected to the device resonance frequency are not affected by parasitic components, but the frequency of the zeros is given by:

$$f_z = f_n\sqrt{1+\frac{\Gamma_n^2}{K_n\left(C_I - C_O\right)}} \tag{42}$$

which can be much higher than f_m if the two capacitances C_I and C_O match.

Unfortunately is very difficult to reduce the mismatch to some fF, because C_I and C_O are high and given mainly by the PCB board used to characterize the device. The method is an improvement of the classic linear method but it could be significant only if the output signal from the resonator is pre-amplified by some active element fabricated on the same chip of the device: in this way the in-chip parasitic capacitances become more important than parasitic elements introduced by the board, so that the mismatch between C_I and C_O can be reduced a lot because they are smaller and their value can be very similar if electrodes are designed symmetrically, as well as their connection to the pads.

Thus for the characterization of the devices presented in [18], the so-called *"2nd harmonic method"* [2] was used: according to this measurement strategy the input electrode is driven by a signal with any *DC* voltage superposed, the rotor is grounded and the output electrode is biased with the voltage V_{DC} in order to convert rotor movements in current (Figure 42).

The method exploit the intrinsic non-linearity of electrostatic actuation, so that if the input signal is a sinusoid $V_S = A\sin(2\pi ft)$, the actuated force per unit length is:

$$f_y(x,t) \approx \frac{\varepsilon_0 W_e}{d^2}\frac{V_S^2}{2} = \frac{A^2}{4}\left[1-\cos(2\pi ft)\right]\frac{\varepsilon_0 W_e}{d^2} \tag{43}$$

The actuated force is composed of a static part and another at a frequency twice the input signal frequency. Neglecting the static components the other generates a displacement and consequently an output current I_m at frequency twice the input signal frequency. Thus the frequency of I_m is also twice the frequency of the parasitic current due to the feed-through capacitance C_{IO}. The output current I_{out} is thus a superposition of a current at the same frequency of the input voltage V_S, the parasitic I_P, and another I_m at twice the frequency of V_S. The two components of the output current can be converted in voltage, amplified and then fed to a lock-in amplifier, which receive also V_S as a reference signal. The lock-in can extract the component at frequency twice the frequency of the reference channel. Alternatively the total amplified signal can be given as input of a "digitizer", i.e. a PCI acquisition card connected to a PC: both the two components can be extracted from the *FFT* (Fast Fourier Transform of the global signal). The method allows to make the characterization of the devices but the parasitic current has to be kept low anyway, because, if too high, it can saturate the amplifier stage used to amplify the resonator output or even the lock-in or the acquisition card. If the resonator is driven with an input signal with frequency f, varying around the frequency $f_n/2$, where f_n is the nth resonance frequency of the device, the parasitic current can be extracted by the circuit in Figure 43a suitable for the component of the output voltage at frequency f, if around frequency $f_n/2$ there is no other resonance frequency. According to this assumption it is possible to neglect the impedance seen by the output port of the resonator and due to resonator movements (i.e. the LRC circuit of each resonance mode, in Figure 29. Thus the component of the output voltage $V_{p,}$ due to the parasitic current, is given by:

$$I_p = \frac{j2\pi f \cdot C_{IO} R_{IN}}{j2\pi f\left(C_{IO}+C_{IN}\right)R_{IN}+1} V_S \tag{44}$$

considering again Y_{IN} as the parallel of a resistance R_{IN} and a capacitance C_{IN}.

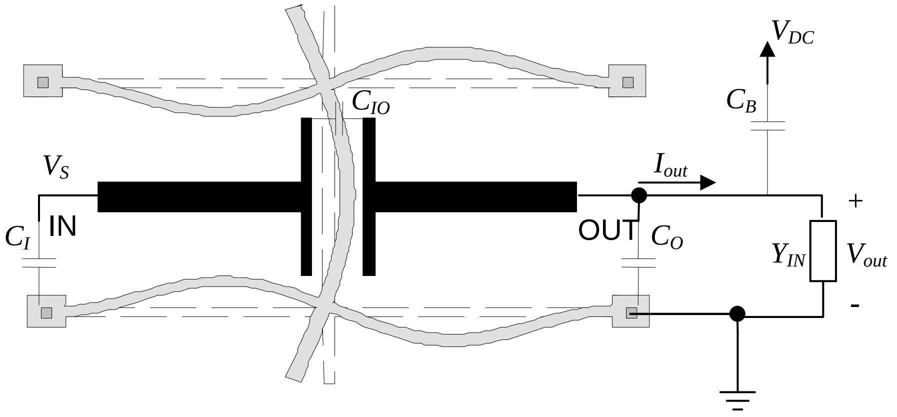

Figure 42: Schematic configuration for the characterization of a free-free resonator with the 2nd harmonic method.

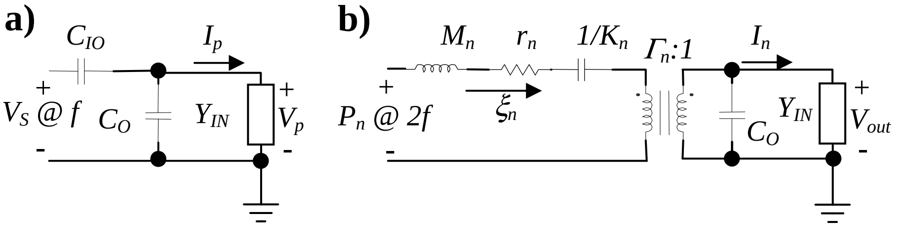

Figure 43: Equivalent circuits for a free-free resonator driven with the 2nd harmonic method: a) parasitic component at frequency f, extracted assuming that no beam resonance modes are close to frequency ω; b) component due to beam movements at frequency 2f.

The component of the output voltage V_n current I_n at frequency $2f$ close to f_n can be found by the equivalent circuit in Figure 43b: the circuit is extracted considering the capacitance C_{IO} as open (indeed no current flows through C_{IO} at frequency $2f$) and P_n is the generalized load corresponding to the actuation load at frequency $2f$ defined similarly to the linear case as:

$$P_n = \frac{\varepsilon_0 W_e}{d^2}\frac{A^2}{4}\cos\left(2\pi f t\right)\int_{[L_e]}\Phi_n dx \qquad (45)$$

Solving the circuit in Figure 43b and assuming $C_{P3} = C_O + C_{IN} >> \Gamma_n^2 / K_n$, which is reasonable as already said many times, it is possible to find V_n as:

$$V_n = \frac{j\omega \cdot R_{in} \frac{\Gamma_n}{K_n} \cdot \frac{\varepsilon_0 W_e}{d^2} \frac{A^2}{4} \cos(\omega t) \int_{[L_e]} \Phi_n dx}{-j\omega^3 \frac{M_n}{K_n} C_{P3} - \frac{\omega^2}{K_n}\left(r_n R_{IN} C_{P3} + M_n\right) + j\omega \left[R_{IN}\left(C_{P3} + \frac{\Gamma_n^2}{K_n}\right) + \frac{r_n}{K_n} \right] + 1} \approx$$

$$\approx \frac{j2\pi f \cdot R_{in} \frac{\Gamma_n}{K_n} \Gamma_n^* \frac{A^2}{2} \cos(2\pi f t)}{\left(1 - \frac{f^2}{f_n^2} + j\frac{f}{Q_n f_n}\right)\left(1 + j2\pi f \cdot R_{in} C_{P3}\right)} \tag{46}$$

where $\Gamma_n^* = \varepsilon_0 W_e / \left(2d^2\right) \int_{[L_e]} \Phi_n dx$ is a coupling coefficient between the component frequency *2f* of V_S^2 and the generalized force P_m. The actuation is less efficient than in the linear and differential architecture, because it is not multiplied by V_{DC}, which is generally much higher than V_S, and thus the signal has to be amplified much more than in other cases.

The 2nd harmonic method is similar to the *EAM* [79], where the non-linearity of the electrostatic actuation is used to multiply the signal, at frequency f_s, by a carrier at higher frequency f_c in order to obtain a component of the actuated force at frequency f_c - f_s, close to the resonance frequency. The result is the same of 2nd harmonic method: the two components are separated in frequency.

This method can be used to characterize any MEMS composed of a moveable mass and at least 2 electrodes: during the initial months of the author's Ph.D. course, 2nd harmonic method was employed to estimate some important feature of a two-axis accelerometer, such as the mechanical frequency response, the cross-sensitivity and maximum voltage which can be applied between electrodes and moveable mass[10]. The acceleration was mimicked with an electrical signal applied to one of the electrodes usually employed for the sensing, avoiding the use of apparatus for the generation of the mechanical load, such as shakers or turntables. Despite the importance of

---

[10] This voltage is the pull-in voltage and was extracted without driving the structure till the collapse.

the results obtained during this activity, the accelerometer characterization was excluded by this thesis because it did not deal with a resonator. Detail of the results can be anyway found in [81] and [82].

With respect to the board for the generation of the input signal and amplification of the output signal from the resonator, the design is more complex than in the case of accelerometer, because if in that case the board had to work till some tens of kilohertz, it has to reach frequency higher than 1 MHz to characterize the devices designed in [18].

Thus the routing and the placement of the discrete components on the board have to be more careful, especially to reduce the effect of the feed-though capacitance, whose admittance is proportional to the frequency. At high frequency if the capacitance is too high, according to(44), the parasitic component V_p of the resonator output voltage can be so high to saturate the following amplifier stage. Besides any other coupling or RF interference can disturb the measure: thus it is necessary to use coaxial cables and BNC connectors for the connections of the board with other needed instrumentation such as the lock-in or the PC acquisition card. The board includes a voltage buffer which is fed by an external voltage generated by a waveform generator (an Agilent 33120A). The buffer provide the input voltage to the resonator, in order to obtain an output impedance Z_S as close as possible to zero, for the stage driving the resonator. This buffer was obtained employing an op-amp AD8001, suitable for applications in the HF band (over than 1 MHz and till some hundreds of MHz).

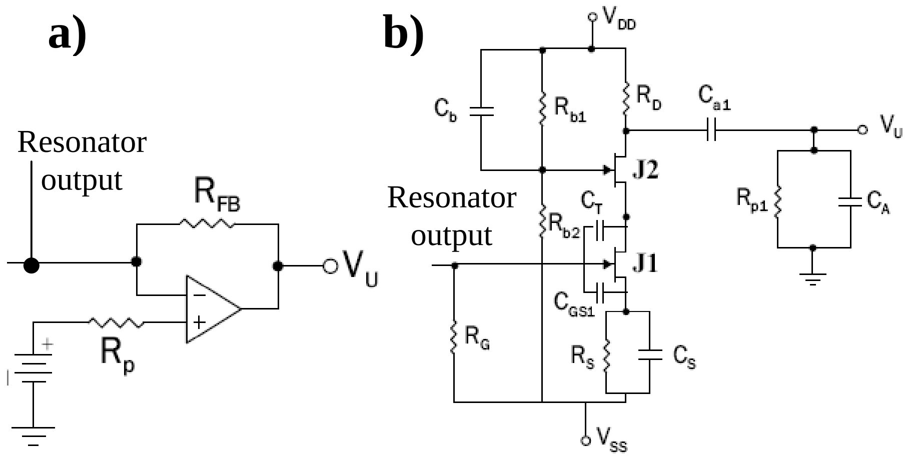

Figure 44: Two alternatives considered during the design of the first amplifier stage of the board used for the characterization of the fabricated RF MEM resonators: a) transresistive amplifier based on an op-amp; b) a cascode jfet-amplifier.

The crucial part of the board is the stage which receives the output from the resonator as an input. It has to convert the output current in a voltage and amplify it, as well as to provide the bias DC voltage V_{DC}. Being the processed signals at frequency higher than 1 MHz also its bandwidth has to be relatively large.

The need of a high V_{DC} (at least 15 V) prevents to use a transresistive stage based on an op-amp as in ([81],[82]) and as represented in Figure 44a, because op-amp working in HF band cannot support high bias voltages: generally bias voltage has to be lower than 5 V and consequently also the voltage V_{DC} as applied in Figure 44a has to be much lower than 5 V to allow the correct working of the stage. Thus the jfet-amplifier in Figure 44b was chosen: the DC voltage on the input terminal of the circuit can be as high as 20 V and can be changed by changing the bias voltages V_{DD} and V_{SS} of the jfet-amplifier. Naturally the range of variation of V_{DD} and V_{SS} cannot be too large, because it is necessary to guarantee the correct biasing of the stage and an adequate amplification.

The amplifier stage in Figure 44b is a *"cascode"* in order to obtain the maximum bandwidth possible with the lowest circuital complexity (in this case only two jfet are needed).

With respect to the noise the estimated performance are good and the jfet noise is negligible with respect to thermal noise generated R_G [80], whose value has thus to be not too high. Flicker noise is filtered by the CR filters which follow this and the following amplifier stage. This filters reduce also low frequency disturbs and DC offsets which can saturate the amplifiers.

The cascode amplifier is followed by two non-inverting voltage amplifier based on op-amps AD8001. The gain of each of this stage is about 20 leading to an overall gain about 400.

Bias voltage for the AD8001 are provided by two voltage regulators (7805 for the positive voltage, 7905 for the negative one), in order to reduce disturbs coming from the power supply, as well as the possibility of op-amp damages. The voltages V_{DD} and V_{SS} for the biasing of jfet-amplifier and resonator are directly fed by the power supply, because they could be changed, as well as the voltage V_{mot} used to actuate the system for the positioning of the input and output electrodes. Finally, a second power supply provides trough a buffer the voltage V_{lat}, in case of test of a resonator with tuning electrodes. The overall circuit is represented in Figure 45. The device package is a PLCC68.

The board output voltage, *Voutput* in Figure 45 is acquired by a PC through the 14-bit digitizer *NI PCI-5122*. The large bandwidth (100 MHz) and the high maximum sampling rate (100 MSa/s) allow to deal with signal frequencies around the resonance frequencies of the fabricated devices.

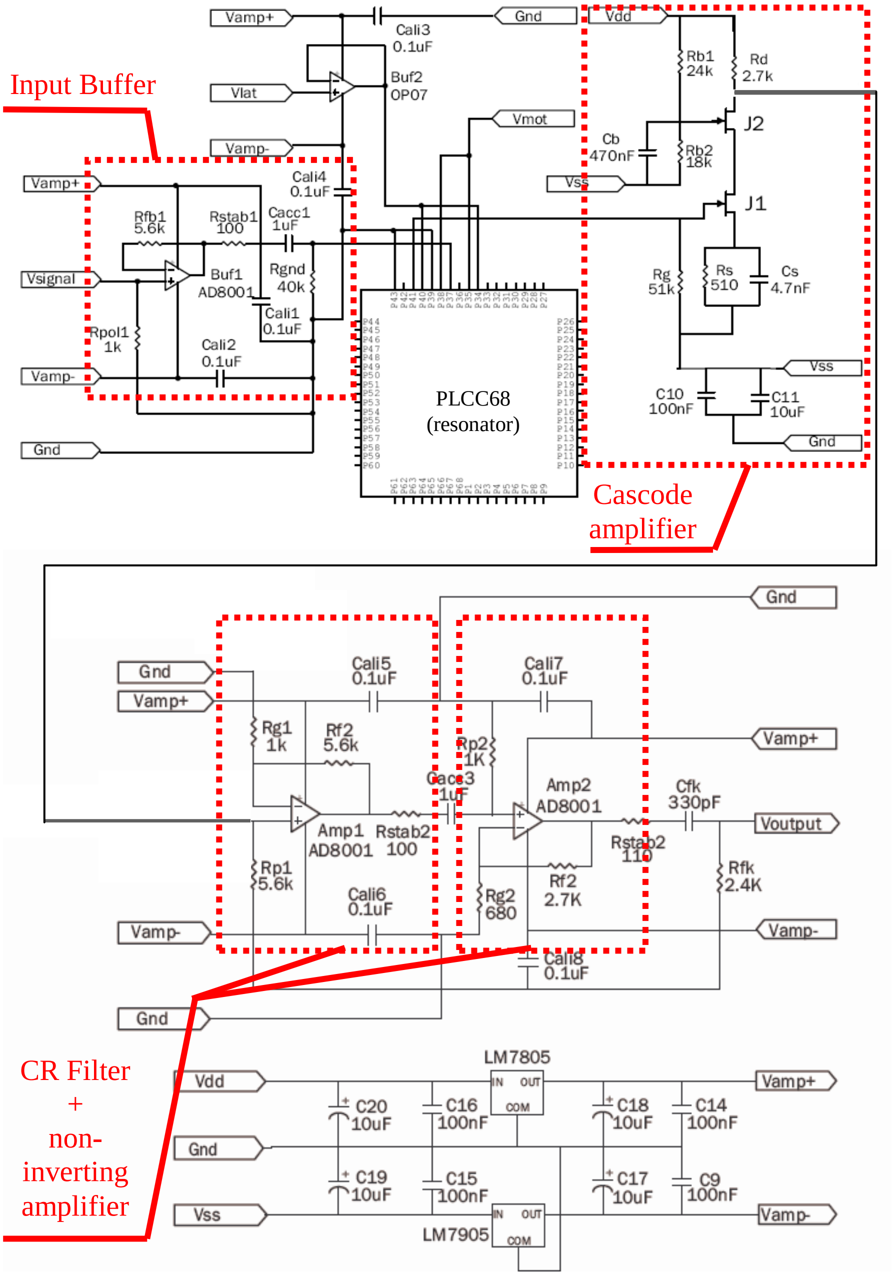

Figure 45: Schematic of the overall circuit for the driving of the resonator and amplification of the device output current: the circuit was fabricated on a PCB board, using discrete components.

If the waveform generator feeds the input buffer with a sinusoid at frequency *f*, *Voutput* spectrum contains two peak, the first at frequency *f* corresponding to the parasitic signal, the second at frequency *2f*, corresponding to the signal components proportional to resonator movements, in the specific proportional to derivative of the deflection with respect to the time, according to (10). Thus if the PC process *Voutput* in order to extract its FFT, it is possible to extract the second harmonic component of *Voutput*, which is proportional to the resonator displacement when the frequency of the actuation force is *2f*. Repeating this procedure changing the frequency of the signal provided by the waveform generator from f_1 to f_2, it is possible to extract the mechanical frequency response of the device, i.e. the ratio between the deflection derivative with respect to the time and the actuated force, for a frequency from $2f_1$ to $2f_2$.

An IEEE-488 card, connected to a PC, was used to drive the waveform generator, so that the acquisition of the frequency response was done automatically, driving both the waveform generator and the digitizer with Labview [83].

Being the devices not packaged under vacuum, the board was inserted in a vacuum chamber in order to minimize the air losses and obtain high quality factors. The vacuum was obtained by a system based on a combined membrane pump/turbomolecular pump, while the pressure was measured with a standard thermocouple gauge. The investigated pressures were between 2 and 4 Pa.

2.5.2 Measurement results

Measurement results are not so much and their quality is not so high, because of both the described failure mechanisms and the difficulty of the measure at high frequencies. Nonetheless a significant number of measurements were extracted for a FF1 resonator, with nominal resonance frequency 5 MHz and for a FF3 resonator, whose nominal resonance frequency is 10 MHz. This last result is fundamental because of the novelty of the device.

The second harmonic component V_O of *Voutput* is represented as a function of the frequency *2f* of actuated force is represented in Figure 46a for the FF1 resonator and in Figure 46b for the FF3 resonator. In both the case a high level of the signal floor is observed: it decreases the quality of the measure and it is probably due to noise and to amplifier distortions, which can generate a second harmonic component of the high parasitic signal. The effect of two complex zeros before the resonance is clearly observable in both the frequency responses and this seems to confirm the contribution of a distortion of the parasitic current due to a capacitive feed-through between resonator input and output.

The FF1 device resonates at 3.955 MHz while the FF3 resonator at 8.537 MHz. The measured resonance frequency is much lower than the nominal one in both cases. Such large discrepancy cannot be explained by the variation of some process parameters, for example as in the case of an overetch higher or lower than usual, which results in a difference between the dimensions of the fabricated devices and the nominal ones. This discrepancy can be explained by the non-ideal behaviour of anchors as will be discussed in 2.5.3.

From different chips the value of the resonance frequency is enough repeatable, varying for example from 3.891 to 3.955 MHz for FF1 resonators with nominal frequency 5 MHz coming from different chips.

On the other hand the resonance frequency is affected by a long term instability, as shown in Figure 47, where two measurement of the same FF3 resonator were done keeping the same biasing condition and approximately the same pressure, but in two different days. The shift of the resonance frequency between the two measurements is about 600 ppm and could be due probably to adsorption of some particle from the surrounding, because as it will be shown in section 2.6, the effect of the temperature fluctuation is too low to explain such a shift.

The dependence of the resonance frequency and quality factor was tested as well: in Figure 48 the frequency response of the FF3 resonator with $V_{DC} = 15\ V$ is compared with the frequency response acquired with $V_{DC} = 17\ V$. A decrease of the resonance frequency can be observed, as predicted by (33). But this measurement of the shift of the resonance frequency with respect to the applied bias voltage is not reliable because the value of frequency change is comparable by the one due to the long term instability as shown by Figure 47. Indeed sometimes this last shift was higher than the variation due to the change in bias voltage, resulting that for an increase of the voltage the resonance frequency was observed to increase. On the other hand with respect to the quality factor the expected decrease was always observed when V_{DC} was raised as it is evident from 49, where the peak in the curve obtained with $V_{DC} = 17\ V$ is significantly larger than the peak obtained with $V_{DC} = 15\ V$. This shift can be due only on the change in the bias voltage because at the pressure the measurements were done, pressure variations do not affect results (i.e. air damping is negligible). Finally, the quality factors of the FF1 and FF3 resonators were extracted. The presence of the large signal floor and of the two zeros before the resonance makes complicated the fitting. To get an estimation of the quality factor, the second harmonic component V_O of *Voutput* was assumed to be given by the sum of the typical output of a second order system, which is due to resonator movements according to (46), and a signal, resulting from the distortion of the parasitic signal, assumed to be equal to $j2\pi fD$:

$$
\begin{aligned}
V_O &= \frac{j\dfrac{f}{Qf_m}V_{MAX}}{\left(1-\dfrac{f^2}{f_m^2}+j\dfrac{f}{Q_m f_m}\right)}+j2\pi f\cdot D= \\
&= \frac{j2\pi f\cdot D\left(1+\dfrac{V_{MAX}}{2\pi f_m D Q_m}-\dfrac{f^2}{\omega_m^2}+j\dfrac{f}{Q_m f_m}\right)}{\left(1-\dfrac{f^2}{f_m^2}+j\dfrac{f}{Q_m f_m}\right)}
\end{aligned}
\tag{47}
$$

where V_{MAX} is the value of V_O at the resonance, f_m the resonance frequency and Q_m the quality factor. The effect of the real pole $p=1/(2\pi R_{in}C_{P3})$ in (46) can be neglected in (47) if only a small portion of the frequency response around the resonance is considered.

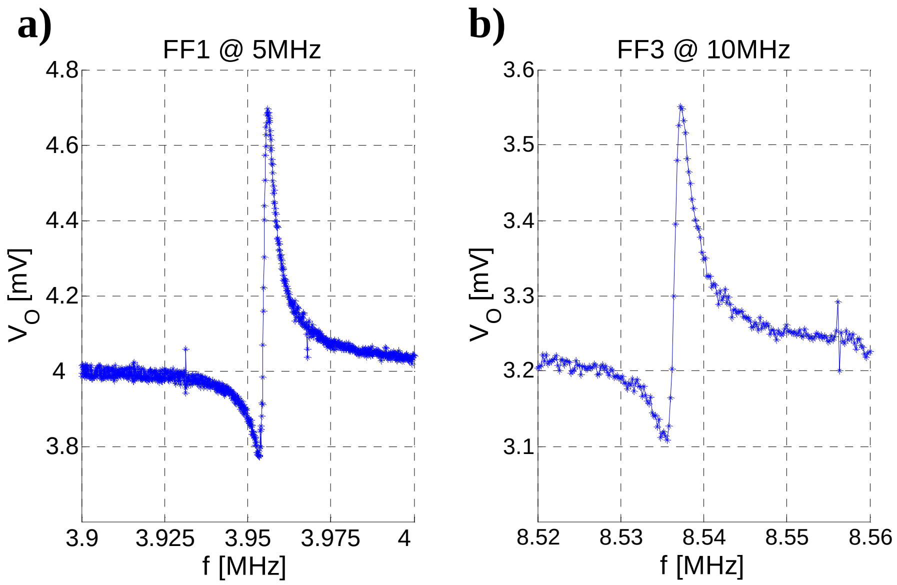

Figure 46: Frequency responses for two fabricated devices: a) a FF1 resonator with nominal resonance frequency 5 MHz (Pressure 2.5 Pa, amplitude of the input signal V_S 1 V, bias voltage V_{DC} = 12 V); b) a FF3 resonator with nominal resonance frequency 10 MHz (Pressure 4 Pa, amplitude of the input signal V_S 1 V, bias voltage V_{DC} = 15 V).

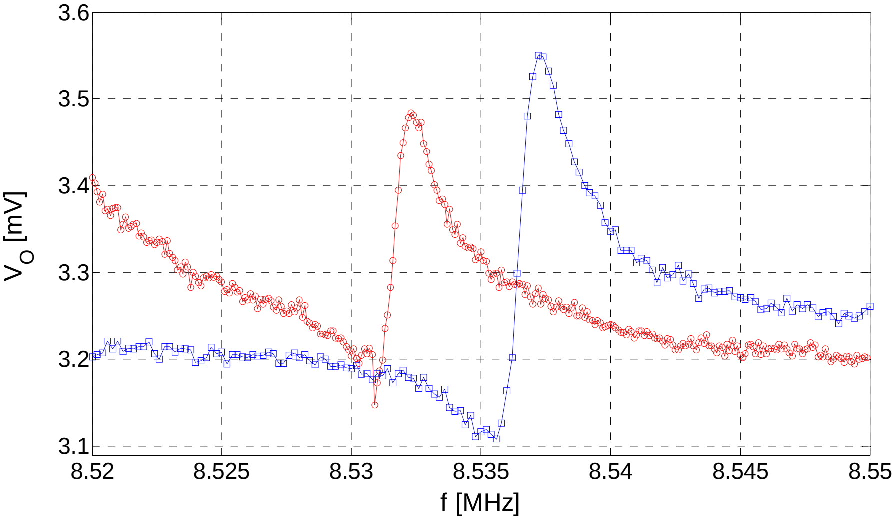

Figure 47: Long term instability of the resonance frequency: both the two curves represent the frequency response for the same FF3 resonator biased with $V_{DC} = 15$ *V and driven with an input signal* V_S*, whose amplitude is 1 V. Also the pressure is quite the same: in both cases is around 4 Pa.*

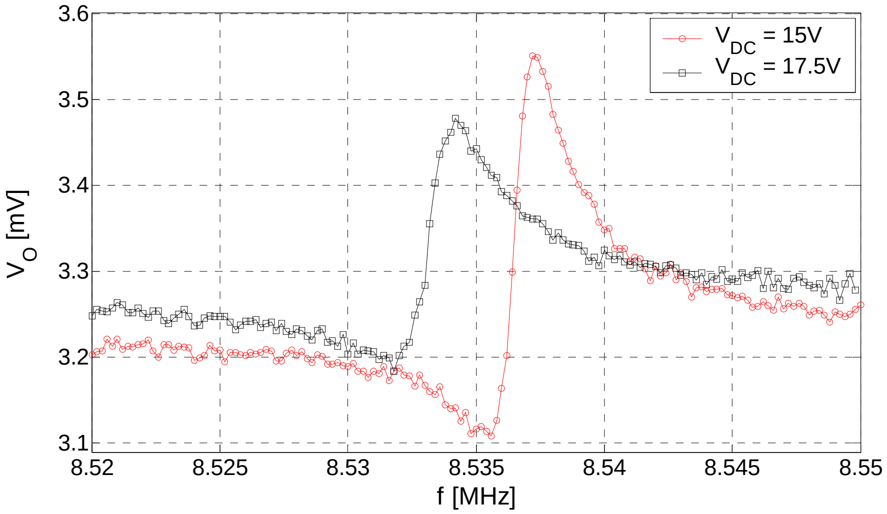

Figure 48: Frequency responses of FF3 resonators biased with two different DC voltages. In both cases the input signal amplitude is 1 V and the pressure is about 4 Pa.

The supposed parasitic signal explains the presence of two zeros close to the resonance. With respect to all the curves shown in this section, D has to be negative, because zeros are at lower frequency than the poles.

Eq. (47) was used as fitting function for the measured curves, using as fitting parameters D, f_m, Q_m and V_{max}. The fitting is not too much robust owing to the high number of fitting parameters, even if f_m can be fixed because its value is evident from the curves even without doing a fitting.

The described fitting can give an estimate of the quality factor of the measured devices: from curves in Figure 46 it is possible to find a quality factor about 1600 for the FF1 device and about 5000 for the FF3 resonator. Thus quality factor of the new device is higher than the one obtained with a classic FF1. The high measured quality factor demonstrates how much the proposed FF3 is promising. Nonetheless this does not mean that the quality factor of FF3 devices is higher than the one of FF1 resonators in general: further measurements on more devices are needed to draw any conclusion about the quality factor of the two kind of device.

The main results from measurements of FF1 and FF3 devices can be found also in [76].

2.5.3 A possible reason of the difference between the nominal and measured resonance frequency of the devices

The discrepancy between the measured and the nominal resonance frequencies of both FF1 and FF3 devices can be explained considering the anchors where the supports are clamped: during the design of the resonator the square at the end of the supports beam were assumed to be immobile at the resonance, allowing to consider clamped their interface with the supports (i.e. this cross section does not deflect nor rotate), as shown in Figure 49. In this condition, unless width and length of the fabricated beams differ very much from their nominal values, the obtained resonance frequencies should be very close to the nominal ones, as confirmed by both 2D and 3D FEM modal simulations performed with FEMLAB, forcing the section indicated in Figure 49 to be clamped. But a better approximation of the working conditions of the resonators can be obtained if the area of contact between resonator and substrate is considered as clamped instead of the ends of the beam. Thus a 3D FEM modal simulation was done with the structure clamped at the anchors, i.e. the dark grey areas in Figure 49, and with the beam ends, i.e. cross-sections in red in Figure 49, considered as free.

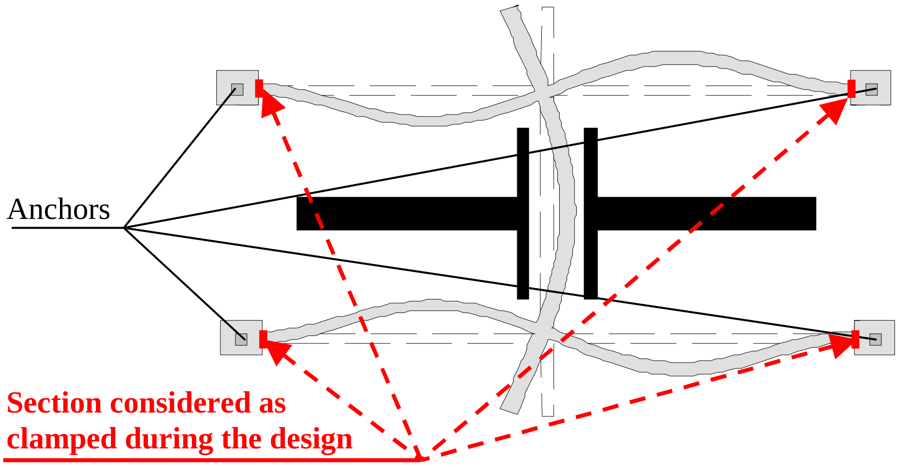

Figure 49: Schematic top view of FF1: anchors are in dark grey, the cross section considered as clamped during the design in red.

Results presented in Figure 50 for a FF1 resonator demonstrate that the squares at the supports ends moves significantly: they “bends” as shown in the particular in Figure 50b, leading to a torsion movements of the supports and to a radical change of the mode shape and resonance frequency.

The fundamental mode for a FF1 device with nominal resonance frequency at 5 MHz, changes in the one represented in Figure 50, whose resonance frequency is 4.24 MHz according to the simulations.

This value is still higher than the measured 3.955 MHz but the size of the anchors (i.e. the side of the dark grey square in Figure 49) critically affects simulation results. The value used in simulations for anchor sizes is the nominal one, i.e. 4 μm, if the real one is for example 0.5 μm smaller simulated and measured resonance frequency match perfectly. Of course also other smaller errors in the fabrication can be a cause of the difference between the simulated frequency with nominal anchor size and the measured one. Besides a further reduction of the resonance frequency is probably due to the fact that even the anchor/substrate interfaces are not perfectly clamped: the substrate can allow small movements which reduce the rigidity of the overall system.

The unexpected behaviour of the anchors explains at least the large part (almost 0.8 MHz) of the difference between measured and nominal resonance frequency.

The unforeseen behaviour of anchors probably do not affect only the resonance frequency but also the quality factor: supports do not resonate on their second clamped-clamped mode but on a hybrid mode characterized by the superposition of torsional and bending mode, so that the described supports adaptation do not strictly hold anymore.

The anchor sizes were fixed to be as small as possible in order to reduce the area of interaction between substrate and resonator and thus to minimize the anchor losses, but the effect of small anchors size on resonator mode shapes seems to suggest the need to increase it, in order to avoid spurious torsional movements of the supports, which can affect their adaptation.

Finally, torsion of the main beam can also be observed from a careful exam of the mode shape in Figure 50 and such torsion can alter the electromechanical coupling coefficient Γ_1.

A further complication is due to the fact that one of the square at the supports ends is connected to a line of thick polysilicon used to bring the bias voltage (or ground in 2nd harmonic configuration) to the resonator: the line partially prevents resonator movements, making more ideal the behaviour of one of the anchor. Overestimating the contribution of the bias line, modal simulations FEM modal simulations were carried out with only one end of one support clamped as well as the anchor/substrate interfaces.

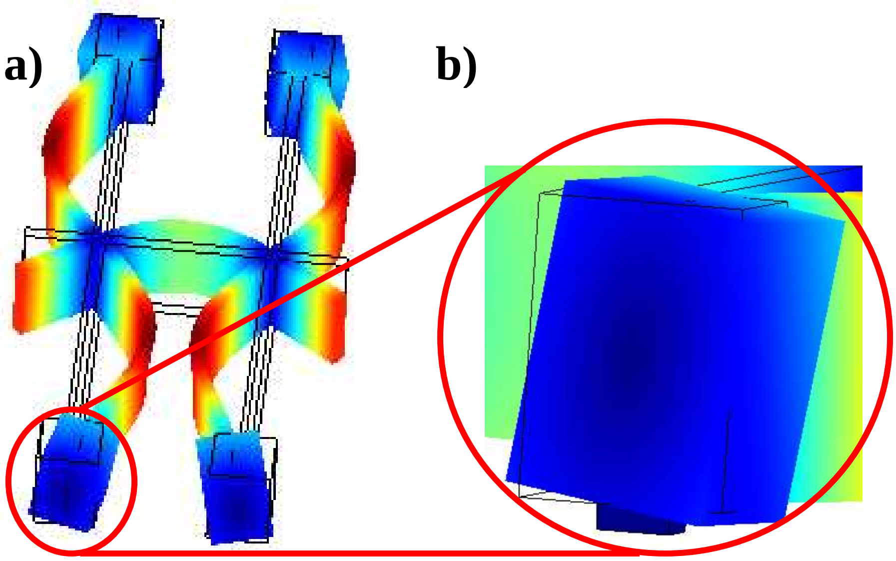

Figure 50: Mode shape of the fundamental mode of a FF1 resonator with nominal resonance frequency 5 MHz, from FEM simulations including anchors movements: a) overall mode shape; b) detail of one anchor.

Blocking one of the squares at the supports ends slightly raises the resonance frequency (from 4.24 MHz to 4.39 MHz) and the torsion of one of the supports is reduced, but the greater difference with respect to the previous simulations is that the symmetry of the mode shape is compromised. The real mode shape of the fabricated mode shape is probably something between the behaviour represented in Figure 50 and the one in Figure 51. However the conclusions about the quality factor and the induced discrepancy between the measured and nominal resonance frequency do not change, even considering one of the supports ends as blocked.

FEM simulations of the third-mode resonator, with nominal frequency 10 MHz, confirm what observed in simulations of the FF1 device: considering all the support ends as free a resonance frequency about 8.90 MHz was found, while if the ends corresponding to the anchor connected to the bias line is blocked the extracted resonance frequency was 8.98 MHz. The shape of the fundamental mode according to the two simulations is represented in Figure 52. As for the FF1 resonator, the real mode shape will be something between the two mode shapes in Figure 52.

In both cases the resonance frequency is higher than the measured one but much closer to than the nominal one (difference between nominal and simulated resonance frequency is in this case about 1 MHz). The torsion of supports and main beam is more evident than for FF1 resonator, so that the supports adaptation is even more reduced in this case: thus it is possible to presume that if the anchor size was large enough to obtain a more ideal anchor behaviour, the quality factor of FF3 resonator would be much larger than the one of the FF1 device, considering the good result from measurements of these devices.

Finally, the torsion of FF3 main beam in Figure 52 is much higher than in the case of FF1 device, leading to a higher change in the electromechanical coupling factor with respect to the nominal value.

In conclusion, a redesign of the devices with higher anchors size is recommended in order to obtain a reduced discrepancy between nominal and real value of the resonance frequency, as well as a higher control on the electromechanical coupling. An increase of anchor size should also raises the quality factor obtaining a condition of supports adaptation closer to the ideal one. With respect to the supports adaptation and electromechanical coupling, the anchor size increase especially needed for the FF3 device.

According to the simulation, the minimum value of anchor size to neglect the effect of anchor movements on device resonance modes is 9 μm for both the FF1 and the FF3 device.

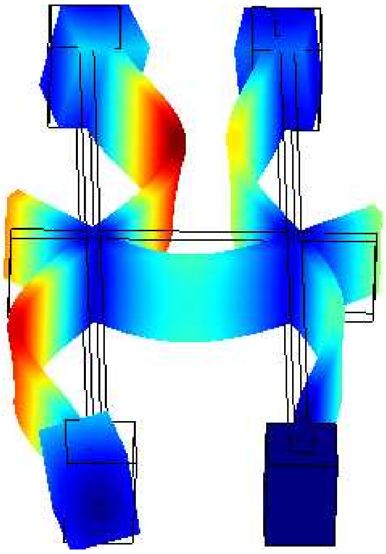

Figure 51: Mode shape of the fundamental mode of a FF1 resonator with nominal resonance frequency 5 MHz, from FEM simulations including anchors movements, with one of the supports ends blocked in order to consider the effect of the polysilicon line carrying the bias voltage (or ground in 2nd harmonic configuration).

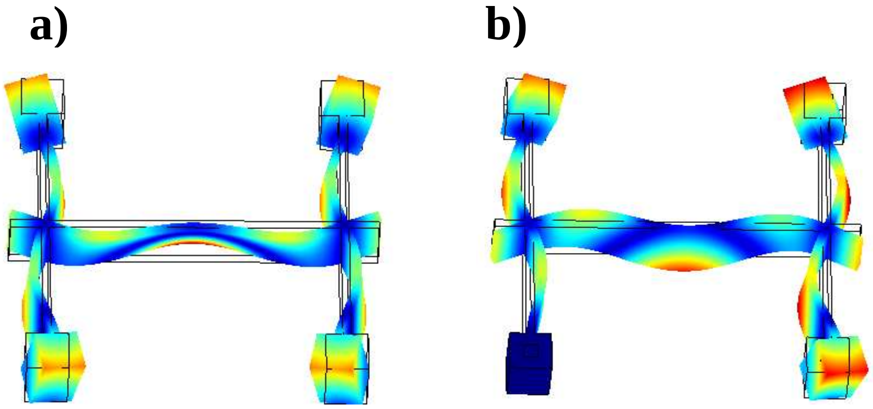

Figure 52: Mode shape of the fundamental mode of a FF3 resonator with nominal resonance frequency 10 MHz, from FEM simulations including anchors movements: a) all the supports ends are free (neglecting the effect the bias line); b) one supports end is blocked to take into account the effect the bias line.

2.6 The effect of the temperature and axial stress on the resonance frequency

Temperature variation can shift the resonance frequency of a flexural-beam resonator because it changes its material properties, but also because it produces a compressive or tensile stress on clamped-clamped beams: a tensile or compressive stress is created if the chip temperature drops or raises with respect to a reference temperature and the materials the resonator and substrate are made of are different. But the stress is still driven even if materials are equal, when there is a temperature difference between the resonator and the substrate, even if the materials.

Dilatation and reduction of width or length (in case of beams with at least one free end) are usually negligible if compared with other temperature effects.

The temperature dependence of the resonance frequency is fundamental to estimate the long term stability of the device resonance frequency, a very important feature especially if the resonator is used as frequency selective element in an oscillator.

With respect to material property changes, the Young's modulus E variation has the most important effect [15]. In a small range of temperature around the (reference) ambient temperature T_{ref}, E depends linearly on the temperature:

$$E = E_0 \left[1 + \alpha_E \left(T - T_{ref} \right) \right] \tag{48}$$

In (48), E_0 is the Young's modulus at reference temperature and α_E the temperature coefficient for the Young's modulus. Since α_E for polysilicon is very small (63 ppm/K according to [70]) its effect on resonance frequency of a beam resonator, can be model from (21) as:

$$\begin{aligned} f_m\left(E(T)\right) &= \frac{1}{2\pi}\left(\frac{\lambda_n}{L_b}\right)^2 \sqrt{\frac{E_0\left[1+\alpha_E\left(T-T_{ref}\right)\right]}{12\rho}} W_b \approx \\ &\approx \frac{1}{2\pi}\left(\frac{\lambda_n}{L_b}\right)^2 \sqrt{\frac{E_0}{12\rho}} W_b \left[1+\frac{\alpha_E}{2}\left(T-T_{ref}\right)\right] = f_0\left[1+\frac{\alpha_E}{2}\left(T-T_{ref}\right)\right] \end{aligned} \tag{49}$$

where f_0 is the resonance frequency when $T = T_{ref}$. Eq. (21) holds for any beam resonator, clamped-clamped, free-free or cantilever, because only the eigenvalues λ_n depends on boundary conditions [31]. Thus Eq. (49) holds for any kind of flexural-beam resonator, unless λ_n depends on E.

The effect of the temperature of Young's modulus can be considered linear and thus separately calculated and then superposed to other effect such as dilatation or axial stress induced by temperature.

In this section a model for the dependence of resonance frequency on an axial stress induced by the temperature is presented for clamped-clamped beams. For free-free resonator some attempts of modelling were done, but no satisfactory theoretical expression was found. Thus FEM simulations were carried out in order to make a comparison among clamped-clamped, FF1 and FF3 resonator, with respect to their resonance frequency sensitivity to the temperature/axial stress.

The axial stress can be induced not only by the temperature but also by residual stress induced by some fabrication process at high temperature which drives a different stress distribution on superposed layers of different materials (in a similar way as the already discussed bimorphic effect). Thus the model and the simulation proposed are useful also to estimate how much the resonance frequency of the fabricated devices can be different from the nominal one due to residual stress.

2.6.1 A theoretical model for clamped-clamped resonators

The analytical derivation of the resonance frequencies for axially loaded clamped-clamped beams has been already carried out in [84]. The approach presented in this thesis is slightly different and leads to a closed form for the resonance frequencies. The effect of temperature and/or residual stress on a clamped-clamped resonator can be modelled by supposing a uniform stress parallel to the beam axis, and by including its effect on the equation of motion of the beam. The total compressive axial stress σ_{eq} can be caused by the fabrication residual stress σ_R, by the temperature difference between the beam and the substrate, and by the difference between their respective thermal expansion coefficients. Consequently its expression can be written as:

$$\sigma_{eq} = \sigma_R + E\left[\alpha_m \Delta T + \left(T_m - T_{ref}\right)\Delta\alpha\right] \tag{50}$$

where α_m is the average value of the thermal expansion coefficients and $\Delta\alpha$ their difference; T_m is the mean temperature of the resonator and the substrate, ΔT their difference and T_{ref} a reference temperature; E is the Young's modulus of the material.

To obtain the resonance frequencies of a CC beam, the Euler-Bernoulli equation for a beam with rectangular section under axial load has to be solved. Such equation is:

$$EI\frac{\partial^4 u_y}{\partial x^4} + N\frac{\partial^2 u_y}{\partial x^2} + \mu\frac{\partial^2 u_y}{\partial t^2} = 0 \tag{51}$$

where N is a compressive axial load. If the stress σ_{eq} is considered as constant along the cross-section of the beam:

$$N = HW_b\sigma_{eq} \tag{52}$$

where W_b is the beam width, while H its thickness. The resonance frequencies of the structure are still given by Eq. (21), but the eigenvalues λ_n has to be calculated by solving the following equation [84]:

$$1 - \cos(\lambda_{1n})\cosh(\lambda_{2n}) = \frac{\lambda_{1n}^2 - \lambda_{2n}^2}{2\lambda_{1n}\lambda_{2n}}\sin(\lambda_{1n})\sinh(\lambda_{2n}) \tag{53}$$

where λ_{1n} and λ_{2n} are given by the expressions:

$$\begin{aligned}
\lambda_{1n} &= \sqrt{\frac{\sqrt{4\lambda_n^4 + \left(\frac{12\sigma_{eq}L_b{}^2}{EW_b{}^2}\right)^2} + \frac{12\sigma_{eq}L_b{}^2}{EW_b{}^2}}{2}} \\
\lambda_{2n} &= \sqrt{\frac{\sqrt{4\lambda_n^4 + \left(\frac{12\sigma_{eq}L_b{}^2}{EW_b{}^2}\right)^2} - \frac{12\sigma_{eq}L_b{}^2}{EW_b{}^2}}{2}}
\end{aligned} \tag{54}$$

where L_b is the beam length. If the axial stress is small enough, i.e. if $\sigma_{eq} << \lambda_n^2\left(EW_b{}^2/6L_b{}^2\right)$, and if its effect is small, i.e. $\lambda_n \approx \lambda_n^0$, where λ_n^0 is the n^th^ eigenvalue frequency of the unstressed structure and one of the solutions of (18), it is possible to find an approximation for the eigenvalue λ_n.

Once λ_n is known, after straightforward algebraic manipulation, it is possible to obtain the following expression for the resonance frequency:

$$f_n = f_n^0 \left[1 - \frac{3}{\pi W_b f_n^0} \frac{G\left(\lambda_n^0\right)}{\sqrt{12E\rho}} \sigma_{eq} \right] \tag{55}$$

where f_n^0 is the n$^{\text{th}}$ resonance frequency of the unstressed structure, and $G(\lambda_n^0)$ is a function only of the eigenvalue λ_n^0 and of the mode-shape of the unstressed structure:

$$G(\lambda_n^0) = \frac{\lambda_n^0 \left(\cosh\lambda_n^0 \sin\lambda_n^0 + \cos\lambda_n^0 \sinh\lambda_n^0 \right) - 2\sinh\lambda_n^0 \sin\lambda_n^0}{\lambda_n^0 \left(\cosh\lambda_n^0 \sin\lambda_n^0 - \cos\lambda_n^0 \sinh\lambda_n^0 \right)} \tag{56}$$

$G(\lambda_n^0)$ increases with n and it is nearly 1 for $n > 5$. For comparison, γ_n used in the model presented in [84] equals $-12G(\lambda_n^0)/\left(\lambda_n^0\right)^2$. A graph of function $G(\lambda_n^0)$ is represented in Figure 53: the value of the function increases if the order of the mode increases.

The *stability* of f_n descends at once from (55). For example, its value with respect to the temperature difference ΔT between resonator and substrate is:

$$S = \frac{1}{f_n^0} \frac{\partial f_n}{\partial \Delta T} = -\frac{3\alpha_m}{\pi W_b f_n^0} G\left(\lambda_0^n\right) \sqrt{\frac{E}{12\rho}} \tag{57}$$

According to (57) wider clamped-clamped beams are less sensitive to axial stresses, the stability is better for high resonance frequencies, but is worse for high order mode (S is proportional to $G(\lambda_n^0)$).

Eq. (57) is confirmed by FEM simulations in wide range of temperature and difference of temperature with respect to the substrate, as shown in 2.6.2. In order to isolate the effect of axial stress, E was taken constant in the FEM simulations presented in the next section. Indeed if $\sigma_{eq} << \lambda_n^2 \left(E{W_b}^2 / 6{L_b}^2 \right)$ the eigenvalue λ_n does not practically depend on E, even if according to (53) and (54) it generally does.

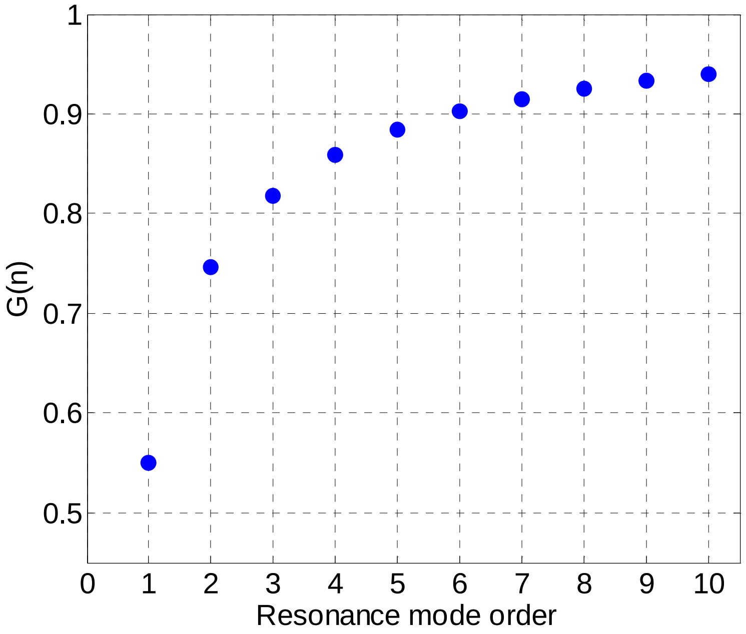

Figure 53: Dependence of function $G(\lambda^0_n)$ on the resonance mode order: it monotonically increases, approaching to 1 for $n \to \infty$.

. Thus considering Eq. (49) and what was said about it, it is possible to calculate the overall dependence on temperature, considering both the effect on Young's modulus and axial stress by:

$$f_n = f_n^0 \left[1 - \frac{3}{\pi W_b f_n^0} \frac{G\left(\lambda_n^0\right)}{\sqrt{12 E \rho}} \sigma_{eq} + \frac{\alpha_E}{2} \right] \tag{58}$$

2.6.2 FEM simulations for clamped-clamped and free-free resonators

Finite element simulations of the dependence of the resonance frequency on the temperature were performed. The analyses were focused on the effect of the axial stress caused by the temperature and neglected other temperature effects, like Young's modulus changes.

All the analyses were executed in FEMLAB: in a first step a temperature load was applied, a static nonlinear analysis was done and the consequent stress and strain configuration was stored; then this static solution was loaded for a pre-stressed modal analysis; the operation was repeated for different temperatures and for every kind of resonator in order to find in each case the resonance frequency at different temperatures/axial stresses, and for different width in the case of the clamped-clamped beam.

In Figure 54 a comparison between analytical model and simulations for a clamped-clamped resonator is shown: while the error is acceptable, it is shown to increase for increasing beam thickness, an effect which is not accounted for by the analytical model. In Figure 55, a comparison between the CC resonance frequency stability with respect to the beam width according to FEMLAB simulations and theoretical model in Eq. (57) respectively, is presented. The theoretical analysis for clamped-clamped resonators leading to Eq. (57) gives interesting suggestions for the design of clamped-clamped resonators: first, slender beams are more sensitive to axial loads (due to both temperature and/or residual stress) (Figure 55); moreover, resonators with higher resonance frequencies show a better stability; finally, because $G(\lambda_n^0)$ increases with increasing n, lower order clamped-clamped resonant modes are expected to be more stable than the upper ones.

The situation for FF1 and FF3 resonators is complicated by the presence of the supports, which are clamped-clamped beams (resonating on their second mode) themselves. A comparison between the simulation results for the three resonator types is shown in Figure 56. The resonance frequency was simulated for three devices with the same nominal resonance frequency (10 MHz) at 300 K, and the same width (2.2 μm). The average thermal expansion cofficient used was $\alpha_m = 4.5ppm$. The worst performance (largest Δf on the selected temperature range, or worst stability S) is that of a free-free resonator, namely the FF1 type. The FF3 resonator has the best performance, while the clamped-clamped beam resonating on its first resonance mode performs between the two. It is interesting that a higher order free-free mode is more stable that a lower order one: this is just the opposite of the behaviour predicted by Eq. (6) for clamped-clamped modes.

An interpretation of the results for free-free resonators is not straightforward: in particular, while the main beam in these two cases can be supposed to be axially unloaded (it can easily expand, discharging any axial stress), the frequency shift cannot be ascribed (at least not completely) to the frequency shift of the supports. This has been verified by separate simulations, which show that CC2 (clamped-clamped second mode) beams of the appropriate length have a much better stability when on their own, i.e. when not connected with the main beam. The main results of this activity about modelling of the effect of temperature and axial stress on resonance frequency are presented also in [76].

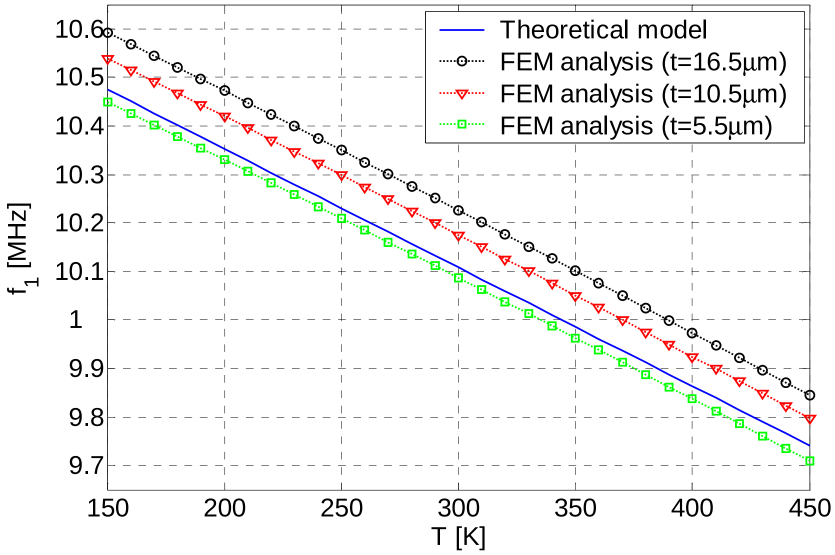

Figure 54: Simulated and theoretical dependence of the resonance frequency on the temperature for a clamped-clamped resonator (Substrate temperature T_{sub} = 300 K; α_m = 4.5 ppm/K) for different beam thicknesses.

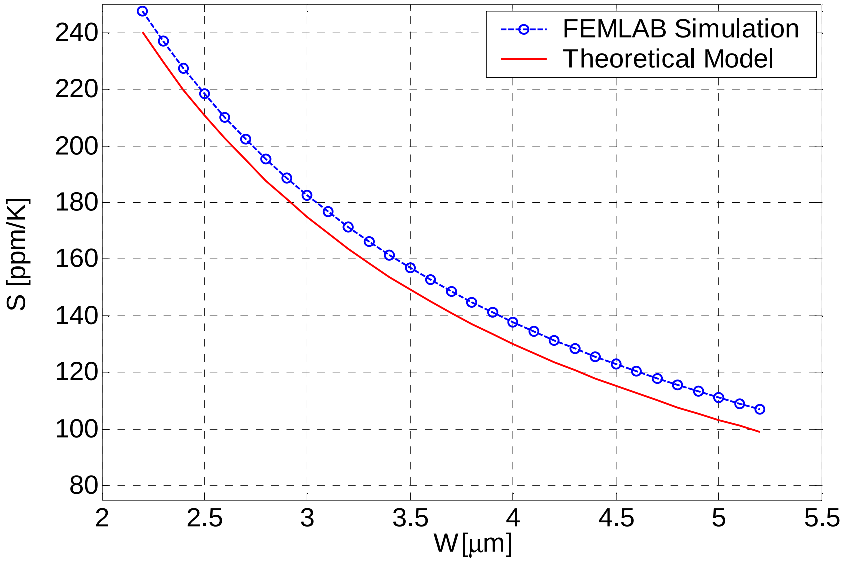

Figure 55: Simulated and theoretical stability of the resonance frequency of a clamped-clamped resonator (1st mode), with respect to the temperature difference between resonator and substrate for different beam widths (Substrate temperature T_{sub} = 300 K; α_m = 4.5 ppm/K); resonance frequency of the unstressed structure 10 MHz (resonator length is adjusted to obtain the same frequency at each width).

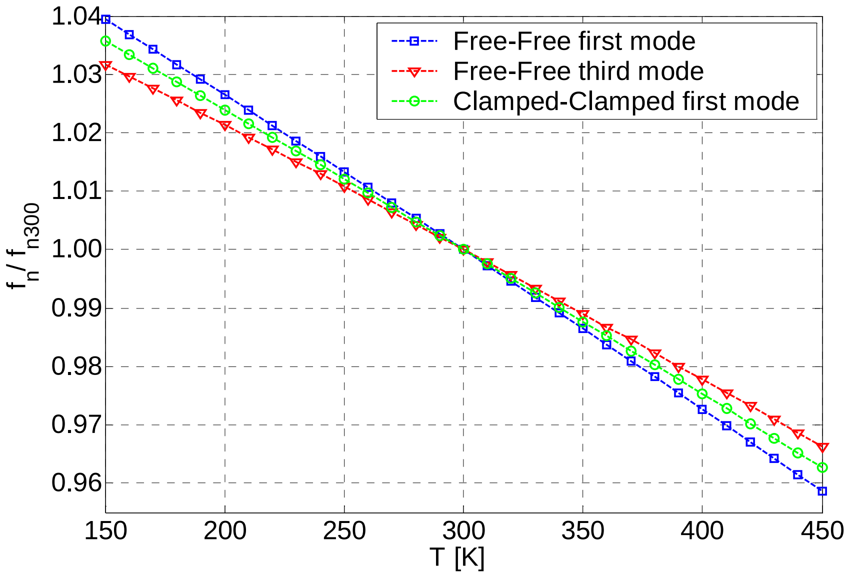

Figure 56: FEMLAB simulations of the dependence on the temperature of the normalized resonance frequencies for a clamped-clamped (first mode), an FF1 and an FF3 resonator (normalization is done with respect to the resonance frequency at T = 300 K). S = 269 ppm/K for the FF1 resonator, S = 244 ppm/K for the CC1 resonator and S = 218 ppm/K for the FF3 resonator. Substrate temperature T_{sub} *= 300 K;* α_m *= 4.5 ppm/K.*

2.7 Equivalent circuits for free-free resonators

Compact models for MEMS components, which operate on multiple physical domains, are required for efficient simulation of complex systems, including MEMS devices as well as analog and digital circuits. Consequently, a large amount of MEMS literature has been devoted to the development of such models (often based on a lumped-parameter approach) and to their integration in the flow of system simulation and design ([85],[86],[87]). In this respect, electrical lumped-parameter equivalent circuits are especially useful. They reduce the number of state variables of the model and they can be implemented in a language for behavioural modelling [87], but also on more established and conventional (from the point of view of the electronic design) circuit simulators.

This last aspect is relevant not only because circuit simulators are readily available in a design environment, but also because the equivalent circuit gives to the designer a quick insight into the component behaviour regardless of the underlying physical working principle, leading to a tighter interaction between the system-level and the device designer.

The equivalent circuit is a handy and quick analysis tool for device designer: as already discussed the equivalent circuit presented in [9] for single-beam resonators was fundamental also in the design of the flexural-beam resonators characterized in this thesis and proposed in [18], [74] and [76]. In the following an equivalent circuit for free-free resonators on the first mode (type FF1) is presented: the main beam is not considered as a stand-alone beam as in [18] and the effect of supports on it was included, so that equivalent components representing the supports are added with respect to the circuit used to design the free-free resonators presented in [18]. Both a general (or extended) and a simplified version of the circuit are presented.

The circuit predicts the behaviour of FF1 device with more accuracy than the circuit presented in [9], especially when the condition of supports matching is not completely satisfied, so that they do not exert any bending moment on the main beam, because for example they are too long or too short. The device behaviour was also compared with FEM simulations performed with FEMLAB: the agreement with the simulations is very good for both the simplified and the general form of the circuit, with respect to resonance frequency and quality factor[11], for both matched and unmatched supports. The agreement is acceptable with respect to the maximum resonator deflection (which is related to the output signal amplitude, and the linearity of the device) only when the extended equivalent circuit is used. Thus the circuit presented can be an accurate equivalent circuit for FF1 resonators and can also help to estimate how the performance of the device is worsened, when the condition of supports matching is not satisfied, due to some design error or process parameter dispersion.

Equivalent circuits can be extracted for free-free resonators with the main beam resonating on mode higher than the first (for example FF3 devices), by following a procedure similar to the one which will be presented for FF1 resonators. Besides the presented approach can be extended even to any resonator composed of multiple beams, each of which bends around the fundamental[12] resonance frequency of the device. More accurate equivalent circuits for FF1 and FF3 resonator could be a very important contribution to a future redesign of the device discussed in this chapter.

In the following first the extraction of the equivalent circuit and then its validation through FEM simulation will be presented.

---

[11] As camping mechanism only internal viscoelastic losses are included, but other damping source are anchor losses, can be included without changing the form of the circuit.

[12] In this case for “fundamental” it is not meant “the first”, but the one favoured by design with respect to both quality factor and electromechanical coupling.

2.7.1 Equivalent circuit for a free-free resonator resonating on the first resonance mode (FF1 type), including supports modelling

A FF1 resonator (Figure 57), can be decomposed into three beams, each of them obeying the Euler-Bernoulli beam equation, if they can be consider as slender (i.e. $W_b < L_b/10$ and $W_S < L_S/10$). The deflections $w(x, t)$ (for the main beam) and $u(y, t)$ (for the supports) can be written as a linear superposition of the equation solutions found by modal analysis [9], each of them corresponding to a different resonance frequency.

By calling $\Phi_n(x)$ and $\Psi_n(y)$ these solutions, i.e. the mode-shapes of the n^th^ resonance mode of the main beam and of the supports, respectively, the displacements are thus expressed as:

$$w(x,t) = \sum_{n=1}^{+\infty} \xi_n(t)\Phi_n(x) \qquad\qquad u(y,t) = \sum_{n=1}^{+\infty} \eta_n(t)\Psi_n(y) \tag{59}$$

where $\xi_n(t)$ and $\eta_n(t)$ are generalized displacements. A closed analytical form for each mode-shape can be calculated. Substitution of the first equation of (59) in the Euler-Bernoulli equation leads, for each resonance mode of the main beam Eq. (24), as seen in 2.1.2. Eq. (24) is formally equivalent to the one describing an RLC series circuit, once the mappings $r_n \rightarrow R_n$, $M_n \rightarrow L_n$, $1/K_n \rightarrow C_n$ are performed, where r_n, M_n and K_n are defined as in (25). The generalized force (generalized velocity $\dot{\xi}_n$) is then interpreted as a voltage (current). The input voltage V_s is coupled with the equivalent circuit of each mode by an ideal transformer of turn ratio Γ_n as defined in (25). The same can be done for the supports with the only difference that do not experiment any load due a driving voltage.

If the quality factor of the resonator is high enough, and the input voltage is narrowband around the first resonance frequency of the main beam (corresponding to the fundamental frequency of a FF1 resonator), it is possible to suppose that the first generalized displacement $\xi_1(t)$ is much larger than those of the higher modes. Consequently, only the first RLC series of the infinitely many implied by Eq. (24) will be included in the equivalent circuit. While this hypothesis greatly simplifies the equivalent circuit, it is not strictly necessary to the development of the following passages. The same assumption is not made for the supports, in order to model the behaviour of the device also if supports length is different from the optimum (matching) length.

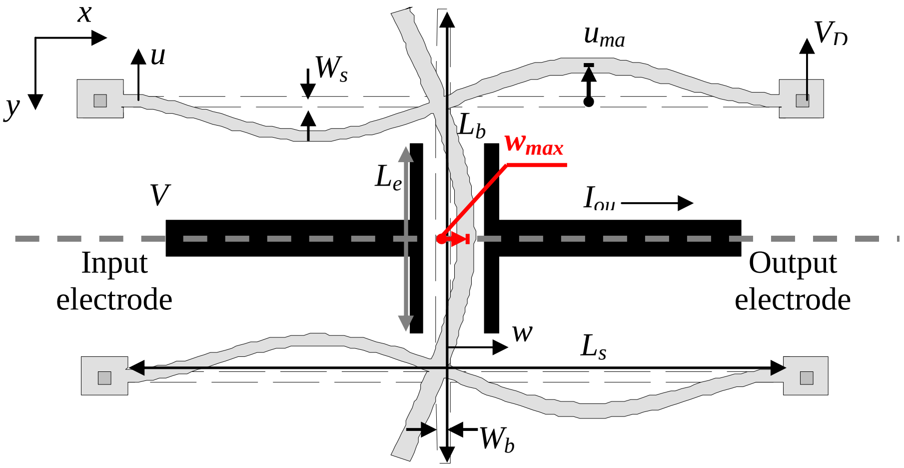

Figure 57: Schematic top view of a two-port free-free resonator with flexural support, with the main beam resonating on its first free-free mode, with the system of reference and displacement name used in section 2.7.1. The symmetry axis of the structure, parallel to y direction, is indicated by grey dashed line. Name of main beam deflection is w instead of u u_y*, as used previously, in order to make easier the writing of the maximum deflection* w_{max}

To model the dynamic properties of the full system, the behaviour of the nodal points (which are defined by the condition $\Phi_1(x) = 0$) has to be taken into account: a rigid connection is assumed, i.e., the angle between the main beam and the supports remains square during deflection. This hypothesis can be written simply as:

$$\left.\frac{\partial w(x,t)}{\partial x}\right|_{x=\hat{x}_i} = \left.\frac{\partial u(y,t)}{\partial y}\right|_{y=\hat{y}_i} \tag{60}$$

where $(\hat{x}_i, \hat{y}_i)$ are the coordinates of the nodal point. Substitution of Eqs. (59) into Eq. (60) gives:

$$\sum_{n=1}^{\infty} \Phi'_n(\hat{x})\xi_n(t) = \sum_{n=1}^{\infty} \Psi'_n(\hat{y})\eta_n(t)\,. \tag{61}$$

Solving for the first generalized displacement of the main beam it is possible to find:

$$\xi_1(t) = \frac{\sum_{n=1}^{\infty} \Psi'_n(\hat{y})\eta_n(t)}{\Phi'_1(\hat{x})} - \frac{\sum_{n=2}^{\infty} \Phi'_n(\hat{x})\xi_n(t)}{\Phi'_1(\hat{x})} . \tag{62}$$

Because of the above discussion, the second term in Eq. (62) can be neglected. Defining a coupling coefficient Π_n between the main beam and the nth mode of the support as:

$$\Pi_n = \frac{\Psi'_n(\hat{y})}{\Phi'_1(\hat{x})} \tag{63}$$

Eq. (62) becomes:

$$\xi_1(t) = \sum_{n=1}^{\infty} \Pi_n \eta_n(t) \tag{64}$$

Eq. (64) holds also for the first time derivative of the generalized displacements. This leads to a straightforward electrical representation: the equivalent RLC circuit of the nth mode of the support beams is coupled to the first mode of the main beam through an ideal transformer of turn ratio Π_n (Figure 58). This approach could be generalized to more complex systems of interconnected beams, although the resultant equivalent circuit could become so complex as to be impractical for many scopes. Considering the expressions for the first free-free mode from Eq. (17) and for the nth clamped-clamped mode from [31]:

$$\begin{gathered}
\Phi_1 = A\left\{\left[\cosh\left(\lambda_{f1}\frac{x}{L_b}\right) + \cos\left(\lambda_{f1}\frac{x}{L_b}\right)\right] + \right.\\
\left. + \frac{\cosh(\lambda_{f1}) - \cos(\lambda_{f1})}{\sinh(\lambda_{f1}) - \sin(\lambda_{f1})}\left[\sinh\left(\lambda_{f1}\frac{x}{L_b}\right) + \sin\left(\lambda_{f1}\frac{x}{L_b}\right)\right]\right\}\\
\Psi_n = B\left\{\left[\cosh\left(\lambda_{c2}\frac{y}{L_s}\right) - \cos\left(\lambda_{c2}\frac{y}{L_s}\right)\right] + \right.\\
\left. - \frac{\cosh(\lambda_{c2}) - \cos(\lambda_{c2})}{\sinh(\lambda_{c2}) - \sin(\lambda_{c2})}\left[\sinh\left(\lambda_{c2}\frac{y}{L_s}\right) - \sin\left(\lambda_{c2}\frac{y}{L_s}\right)\right]\right\}
\end{gathered} \tag{65}$$

it can be shown that the expression in Eq. (63) can be written also as:

$$\Pi_n = \frac{\lambda_{cn}}{\lambda_{f1}} \frac{L_b}{L_s} F\left(\lambda_{cn}, \lambda_{f1}\right) \tag{66}$$

where L_b, L_s are the lengths of the main beam and the support beam, λ_{cn}, λ_{f1} are the n^th^ eigenvalue of the support beam and the first eigenvalue of the main beam, respectively; the function $F(\lambda_{cn}, \lambda_{f1})$ can be easily derived from the analytical expressions of the mode shapes and if both Φ_1 and Ψ_n are normalized according to Eq. (19)[13], it can be written as:

$$F\left(\lambda_{cn}, \lambda_{f1}\right) = \\ = \frac{\left[\sinh\left(\frac{\lambda_{cn}\hat{y}}{L_s}\right) + \sin\left(\frac{\lambda_{cn}\hat{y}}{L_s}\right)\right] - \frac{\cosh\left(\lambda_{c2}\right) - \cos\left(\lambda_{c2}\right)}{\sinh\left(\lambda_{c2}\right) - \sin\left(\lambda_{c2}\right)}\left[\cosh\left(\frac{\lambda_{cn}\hat{y}}{L_s}\right) - \cos\left(\frac{\lambda_{cn}\hat{y}}{L_s}\right)\right]}{\left[\sin\left(\frac{\lambda_{f1}\hat{x}}{L_b}\right) - \sin\left(\frac{\lambda_{f1}\hat{x}}{L_b}\right)\right] + \frac{\cosh\left(\lambda_{f1}\right) - \cos\left(\lambda_{f1}\right)}{\sinh\left(\lambda_{f1}\right) - \sin\left(\lambda_{f1}\right)}\left[\cosh\left(\frac{\lambda_{f1}\hat{x}}{L_b}\right) + \cos\left(\frac{\lambda_{f1}\hat{x}}{L_b}\right)\right]} \tag{67}$$

and from (67) it can be shown that F is bounded for $\lambda_{cn} \rightarrow \infty$ ($n \rightarrow \infty$).

The existence of a nodal point at the centre of the support beams is compatible with their even resonance modes only; thus in Eq. (64) only even n are considered. Moreover, higher modes can be considered as quasi-statically driven in the considered frequency range, i.e. their only important mechanical properties is the generalized stiffness K_n defined as in (25)[14] their electrical equivalent reduces to a capacitance, whose value is:

$$C_n = \frac{1}{K_n} = \frac{L_s^3}{\lambda_{cc,n}^4} \frac{1}{EI_s} \tag{68}$$

where E is the Young's modulus of the material which the beams are made of and I_s is the moment of inertia of the support beam cross-section.

The circuit in Figure 58 can be further simplified by using the impedance transformation properties of ideal transformers, so that each

---

[13] With respect to the normalization of Ψ_n L_s substitutes L_b and the integral is done with respect to y instead of x.

[14] With Ψ_n and L_s which substitutes respectivelyΦ_n and L_b, while the integral is done with respect to y instead of x.

impedance is transferred to the first loop (Figure 59). The capacitance C_{up}, taking into account all the higher order modes of both supports, can be expressed as:

$$C_{up} = \sum_{n=1}^{\infty} \Pi_n^2 \frac{C_n}{2} = \frac{L_b^2 L_s}{2EI} \sum_{n=1}^{\infty} \frac{F(\lambda_{cn}, \lambda_{f1})}{\lambda_{cn}^2} \qquad (69)$$

Because of the boundedness of F, the terms of the series in Eq. (69) vanish as λ_{cn}^{-2}, so that only a limited number of higher modes of the support beam can be actually used to compute C_{up}.

A further simplification is possible by removing C_{up} altogether, leading to an equivalent circuit reduced to a single RLC series. In the next section, a comparison between FEM simulations and the results predicted by the circuits with C_{up} (extended) and without (simplified) will be presented.

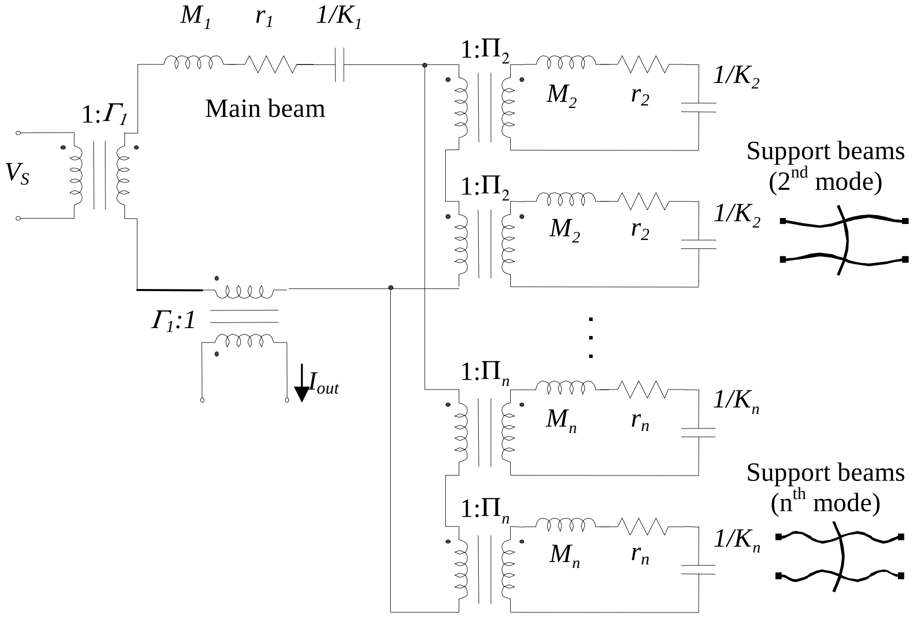

Figure 58: Full equivalent circuit for a FF1 resonator, including supports equivalent. The transform coupling the resonator with the output electrode is modelled as in 2.1.2 and the electromechanical coupling factor Γ_1 for the output port is defined as in (26).

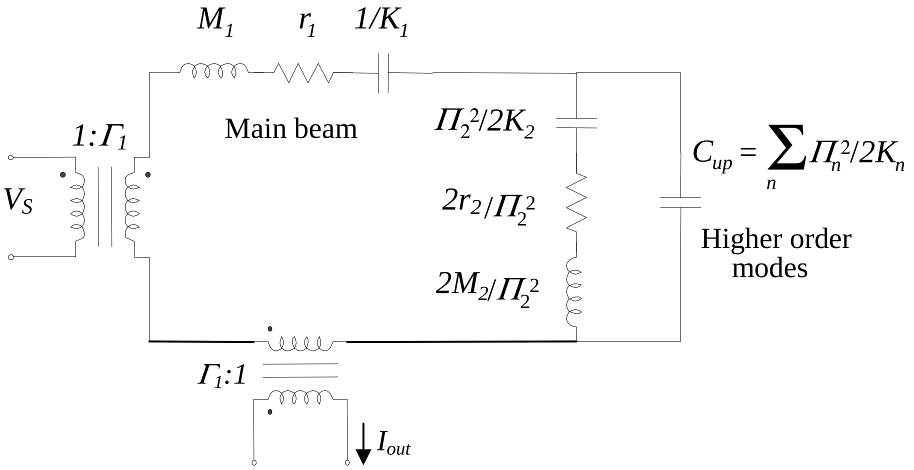

Figure 59: Reduced equivalent circuit for a FF1 resonator, including supports equivalents.

2.7.2 FEM Simulations

To validate the model, modal and frequency response simulations were performed using FEMLAB [43], and the results compared with the equivalent circuit predictions. The simulations were only mechanical and considered no electromechanical coupling, so that they do not validate the values of ideal transformers in Figures 58 and 59. In the calculation done using the equivalent circuits in Figures 58 and 59, the output port was considered as loaded by a short-circuit, while the voltage needed to obtain the mechanical load used in the simulation was given as an input.

Two types of simulations were implemented: the first one based on 1D beam elements (described by the Euler-Bernoulli theory), the second one with 2D elements. The simulated device was characterized by the following dimensions (as defined in Figure 57): $L_b = 42.2$ µm, $W_s = W_b = 2.2$ µm, while L_s was varied from 59.8 µm to 79.8 µm. The value $L_s = 69.8$ µm corresponds to the matched condition, where the main and support beams show resonance at the same frequency.

For each L_s, a modal simulation was carried out to extract the resonance frequency of the first mode. Subsequently, a frequency response simulation was performed in a narrow band around the resonance frequency, and the maximum deflection w_{max} of the main beam was extracted for each frequency (the maximum deflection occurs at the central point of the beam as shown in Figure 57). A uniform distributed mechanical load $p = \Gamma_1 V_s / L_e$ was used to mimic the electromechanical load applied by the electrode, L_e being the length of the electrode (see Figure 57). In the frequency response simulations, the damping was modelled as a bulk viscoelastic loss according to the Kelvin-Voigt model [34]. The same damping model was used to extract the equivalent resistances in the circuit.

Assuming a lumped-parameter second-order resonant system behaviour around the resonance frequency, the simulated frequency response was fitted against this function:

$$\left|W_{max}(f)\right| = \left| \frac{\frac{W_R}{Q}}{1 - \left(\frac{f}{f_0}\right)^2 + j\frac{f}{Qf_0}} \right| \tag{70}$$

where W_{max} is the Fourier transform of the deflection, f_0 the resonance frequency, W_R the deflection at resonance, and Q the quality factor. W_R and Q were used as fitting parameters, because f_0 is already known from the modal simulation. This can make the fitting more robust.

Simulations results for f_0, Q and W_R are compared with the corresponding values predicted by the extended and the simplified circuit (as defined at the end of the preceding section) in the graphs represented in Figures 60, 61 and 62. On the horizontal axis, the mismatch, i.e. the difference between the actual and the matched support length, is represented.

Resonance frequency and quality factor are more accurately predicted by the extended circuit model than by the simplified one (Figures 60 and 61), but the relative error is very small in both cases (less than 2.5% with respect to 2D simulations for a large relative mismatch of ±10 μm over 69.8 μm).

For the maximum deflection W_R (Figure 62) the error between theoretical and simulated curves is significantly larger, especially if the simplified model is considered. The maximum relative error with respect to the 2D simulations is nearly 13% for the extended model, and nearly 25% for the simplified one. The total error is contributed both by an offset and a higher slope of the curve. The offset is to be ascribed to the use of the Euler-Bernoulli equation in deriving the equivalent circuit, as the 1D simulations (which are based on the same model) are also affected by. Thus an equivalent circuit based on Timoshenko beam model [31] could solve the problem, but the procedure of extraction of an equivalent circuit would be very complicated if not impossible in that case.

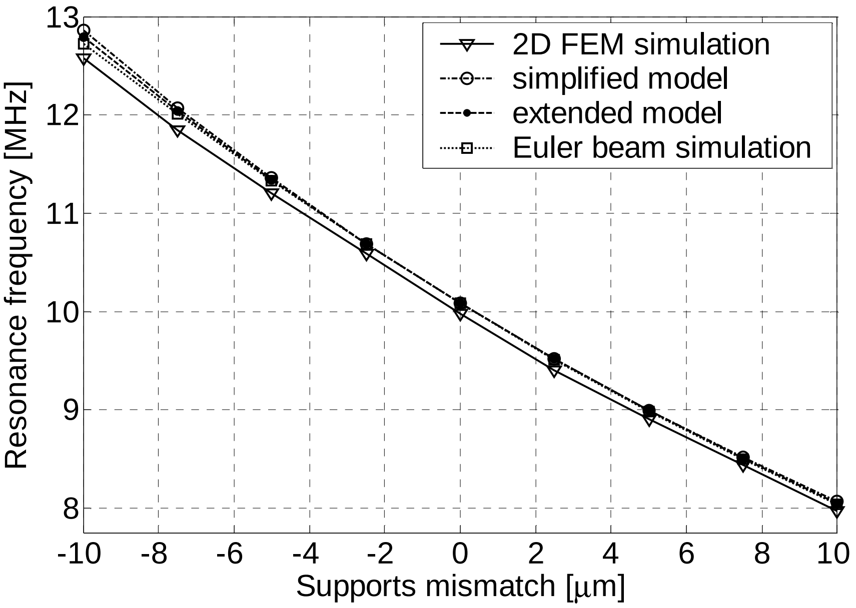

Figure 60: Frequency resonance f_0 as a function of support length mismatch: comparison between equivalent circuit and simulation results.

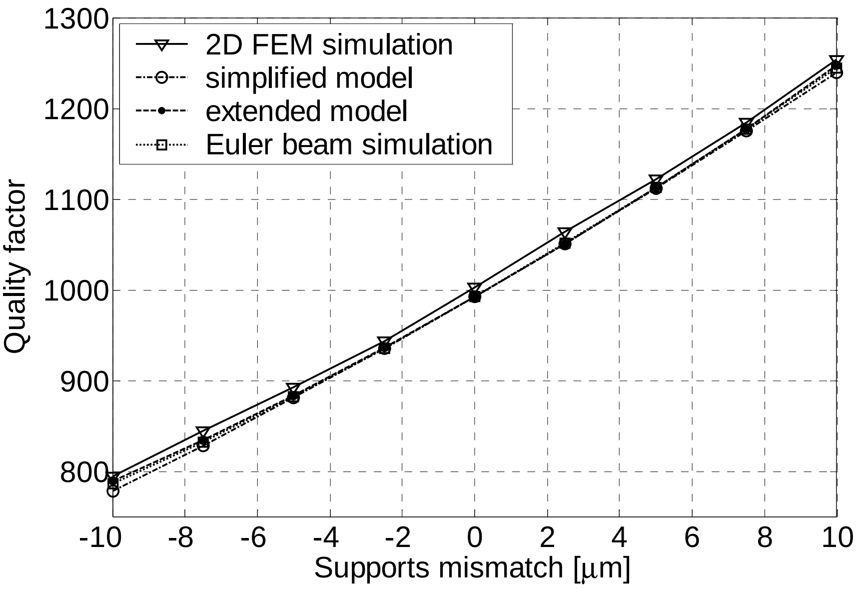

Figure 61: Quality factor Q as a function of support length mismatch: comparison between equivalent circuit and simulation results.

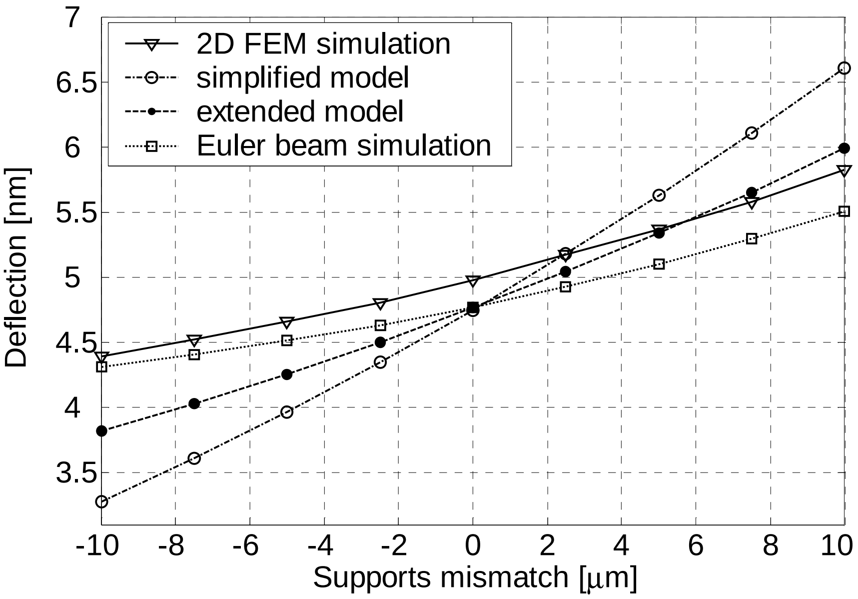

Figure 62: Maximum displacement W_R of the main beam as a function of support length mismatch: comparison between equivalent circuit and simulation results.

Results are nonetheless significant, and allow to use the presented equivalent circuit for simulations of the free-free resonator together with an electronic system or to exploit it as a synthesis tool, even if the inaccuracy of the value of W_R leads to an error on the estimated value of the ratio between output current and input voltage and consequently on the value of motional resistance.

The equivalent circuits proposed in this thesis are presented also in [75] and [77].

3. Design optimization of bulk-mode disk resonators

In this chapter design issues and solutions for bulk-mode disk resonators will be shown. As already said, bulk-mode resonators allows to reach higher resonance frequencies than flexural-beam resonators, retaining very high quality factor. For this reasons a research activity about MEM resonators for RF applications cannot avoid to consider the design and modelling of bulk-mode resonators.

The results shown in this chapter were obtained during a period of intensive collaboration with the international research laboratory IMEC (Interuniversity MicroElectronics Center) of Leuven in Belgium, where I spent several mounts, funded by a Marie Curie scholarship, in the framework of the project APROTHIN (Advanced PROcess Technologies for Horizontal INtegration). A small part of the achievements described in the following was presented in [88].

A huge number of bulk-mode disk resonators are under fabrication at IMEC: experimental data are expected soon, in order to validate the conclusions presented in the following.

3.1 Device description and design issues

The device, whose design was optimized, is a *contour mode disk resonator* and is represented in Figure 63: it is a disk connected to the substrate by a cylindrical *stem* or anchor; a couple of electrodes are used to electrostatically drive the disk into motion. The output current can be collected from the disk, in a one-port configuration; also a bias voltage (applied on the resonator or on the electrodes) is needed to linearize the relationship between the input voltage signal applied on the electrodes and the force actuated on the disk. The shape of the electrodes has to be properly chosen to actuate a force oriented in radial direction and constant on the lateral edge of the disk, so that only axisymmetric resonance modes and especially the so-called *contour modes* are stimulated: for this modes the disk, at least ideally, is only compressed and stretched alternatively, in radial direction, without any distortion of its circular shape and without any out-of-plane movement.

The ideal electrodes shape to reach this condition is a circular holed plate, with the hole concentric with the disk, so that the axisymmetry of the actuation is perfect. In the figure the electrodes are interrupted, essentially because it is necessary also to connect the disk to the reading electronics which is used to collect the output current due to the resonator movements. Even if the process allows to fabricate two or more different levels of connection, designing an electrode surrounding the entire disk will introduce parasitic capacitance between input and output. The shape schematically represented in Figure 63 is a possible a trade off between the necessity to increase the spectral purity of the device and to limit parasitic capacitance.

The two electrodes in Figure 63 can be also used as an input and an output electrode with the resonator grounded, in a two-port architecture, but in this case a lot of spurious modes which are not axisymmetric are stimulated. In particular there are Lame modes and some resonance modes at frequency lower than the contour mode, according to which the stem bends.

Thus for spectral purity reasons the resonator has to be used as one-port device, with all the disk surrounded by actuation electrodes, apart from regions where disk connection pass by. These regions have anyway to be kept as small as possible. Maximizing the region where the disk is surrounded by electrodes increases also the electromechanical coupling factor, which can be extracted in manner similar to what done in section 2.1.2 for flexural-beam resonator. Another way to maximize the electromechanical coupling is to reduce the gap between electrodes and disk: for this purpose a process to obtain gaps under 100 nm is going to be used to fabricate the devices at IMEC.

Considering the mechanical structure, there are two fundamental issues for the RF resonators design: first resonance frequency has to be chosen, second the mechanical losses has to be limited as much as possible, in order to maximize the quality factor.

The first parameter is essential in both filter and oscillation architecture, because it is the central frequency of the filter in the first case, while it is the frequency of the output oscillation in the second case. Nonetheless the quality factor is even more important, because the higher it is the higher the selectivity in filter architecture and, even more significant, the lower the phase noise in the oscillator architecture.

Thus to design a good RF MEM resonator, it is necessary both to set the resonance frequency and to maximize the quality factor.

These goals should be preferably reached by changing only layout parameters, such as lateral dimensions of the resonator or the size and the number of the anchors, without changing process parameters, such as layer thicknesses or material properties: of course it is not reasonable to change the process to optimize the device for each particular application, because it costs money and times. Nonetheless the effect of process parameters on the resonance frequency and quality factor has to be taken into account, because a variation of them due to process parameter dispersion can reduce the robustness of the design.

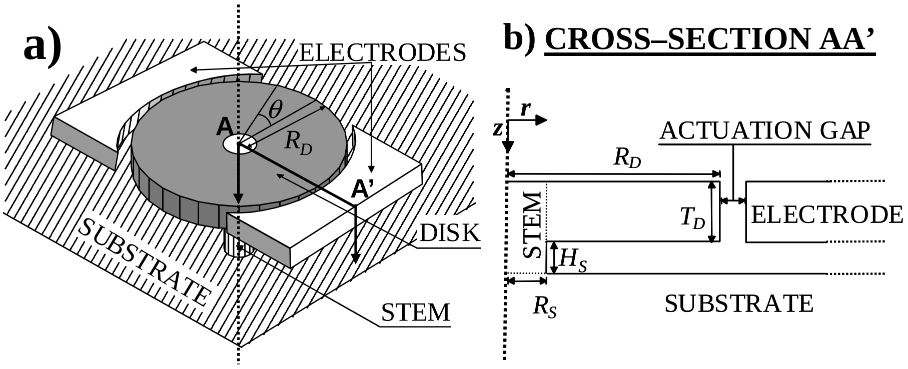

Figure 63: Schematic view of a contour mode disk resonator: a) 3D view; b) radial cross section (R_D is the disk radius, T_D the disk thickness, R_S the stem radius and H_S the stem height). The symmetry axis of the device is indicated by the dashed line.

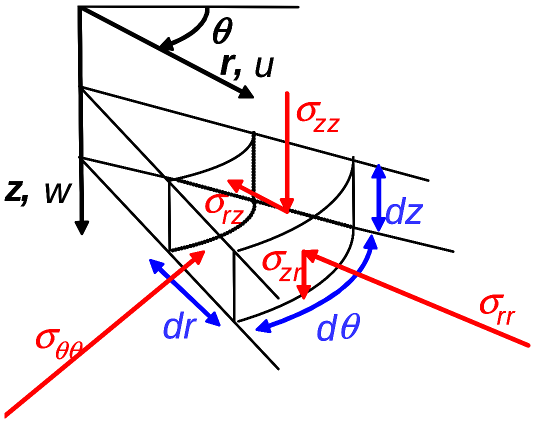

Figure 64: System of reference, displacements and stress components in cylindrical coordinates.

In particular, with respect to the cross-section of the device in Figure 63, the layout parameters are the radius of the disk R_D and the stem radius R_S, while process parameters are disk thickness T_D and the stem height H_S the material properties.

Due to the complexity of the estimation and optimization of quality factor (see also section 1.2.3) the main efforts concerning the design of contour mode disk resonators were concentrated in finding an accurate model to estimate the quality factor of the resonator.

3.1.1 Resonance frequency

The resonance frequencies of contour modes can be found starting from the equilibrium conditions. In cylindrical coordinates, if the problem is axisymmetric (i.e. assuming the mode shape does not depend on the angle θ indicated in Figure 63), the equilibrium conditions can be written as [89]:

$$\begin{cases} \dfrac{\partial \sigma_{rr}}{\partial r} + \dfrac{\partial \sigma_{rz}}{\partial z} + \dfrac{\sigma_{rr} - \sigma_{\theta\theta}}{r} = \rho \dfrac{\partial^2 u}{\partial t^2} \\ \dfrac{\partial \sigma_{zr}}{\partial r} + \dfrac{\partial \sigma_{zz}}{\partial z} + \dfrac{\sigma_{rz}}{r} = \rho \dfrac{\partial^2 w}{\partial t^2} \end{cases} \tag{71}$$

where u and w are the components of the displacement vector $\mathbf{u}$ in z and r direction, while σ_{ij} are the components of stress tensor ($i = r, \theta, z$ and $j = r, \theta, z$ where r, θ, z are the directions in cylindrical coordinates, as indicated in Figure 64). According to the assumption of axisymmetric mode shapes, the displacement in direction θ is zero as well as shear stress components $\sigma_{r\theta} = \sigma_{\theta r}$ and $\sigma_{z\theta} = \sigma_{\theta z}$.

If the assumption of plane stress is done it is possible to neglect also σ_{zz} and $\sigma_{zr} = \sigma_{rz}$, so that Eqs. (71) are reduced to the single equation:

$$\frac{\partial \sigma_{rr}}{\partial r} + \frac{\sigma_{rr} - \sigma_{\theta\theta}}{r} = \rho \frac{\partial^2 u}{\partial t^2} \tag{72}$$

Substituting then expression of stress in terms of displacements [89]:

$$\sigma_{rr} = \frac{E}{1-\nu^2}\left(\frac{\partial u}{\partial r} + \nu \frac{u}{r}\right) \qquad \sigma_{\theta\theta} = \frac{E}{1-\nu^2}\left(\frac{u}{r} + \nu \frac{\partial u}{\partial r}\right) \tag{73}$$

the following equation can be found:

$$\frac{E}{1-\nu^2}\left(\frac{\partial^2 u}{\partial r^2}+\frac{1}{r}\frac{\partial u}{\partial r}-\frac{u}{r^2}\right)=\rho\frac{\partial^2 u}{\partial t^2} \tag{74}$$

where E is the Young's modulus, ν the Poisson ratio and ρ the mass density of the disk.

Following the same approach described in 2.1.2 to find beams resonance frequency, the solution is assumed as a superposition of function $\xi_n(t)\Phi_n(x)$, with $\xi_n(t) = V\sin(2\pi f_n)$, and $\xi_n(t)\Phi_n(x)$ is substituted in (74), so that the following equation can be found for the nth mode shape $\Phi_n(x)$,

$$\left(\frac{\partial^2 \Phi_n}{\partial r^2}+\frac{1}{r}\frac{\partial \Phi_n}{\partial r}-\frac{\Phi_n}{r^2}\right)=\frac{\rho\left(1-\nu^2\right)}{E}\left(2\pi f_n\right)^2\Phi_n \tag{75}$$

where f_n is the resonance frequency of the nth contour mode. Eq. (75) is a Bessel equation, whose solution is:

$$\Phi_n = AJ_1\left(\frac{\lambda_n}{R_D}r\right)+BY_1\left(\frac{\lambda_n}{R_D}r\right)=AJ_1\left(\frac{\lambda_n}{R_D}r\right) \tag{76}$$

where J_1 is the Bessel function of first kind and first order, while Y_1 is the Bessel function of second kind and first order; $B = 0$, because Y_1 diverges for $r = 0$, so that if B was not zero the displacement would diverge for $r = 0$, but it cannot. λ_n is the nth eigenvalue. If the free condition, i.e. $\sigma_{rr} = 0$, is assumed at the ends of the disk, i.e. for $r = R_D$, the eigenvalue can be found by solving the following equation:

$$\lambda_n\frac{J_0(\lambda_n)}{J_1(\lambda_n)}=1-\nu \tag{77}$$

where J_1 is the Bessel function of first kind and zero order. Substituting (76) in (75), it can be shown that the resonance frequency f_n is given by the well known formula [37]:

$$f_n=\frac{1}{2\pi}\frac{\lambda_n}{R_D}\sqrt{\frac{E}{\rho(1-\nu^2)}} \tag{78}$$

Thus a very handy and compact formula can be used to choose the resonance frequency of a contour mode disk resonator. Once material properties are known and the resonance mode order *n* is chosen, the desired resonance frequency can be obtained by choosing the proper disk radius. It is important to notice that the only geometrical dimension, which the resonance frequency depend on, is the disk radius: it is strictly true only if the disk is thin, i.e. $T_D << R_D$, so that the plane stress assumption holds, and if the stem radius is much smaller than the disk, so that it is possible to neglect the effect of the stem on the contour mode resonance of the disk. However, for all the device geometries which will be discussed in this thesis, Eq. (78) holds, because it gives indications which agree with FEM modal simulations. Indeed FEM modal simulations confirm the independence of resonance frequency on T_D, R_S and H_S, for all geometries which were simulated.

3.1.2 The problem of quality factor estimation

Unlike the resonance frequency the quality factor of a contour mode disk resonator cannot be easily evaluated. As discussed in 1.2.3 the difficulty is due both to the great number of losses mechanisms which limit the quality factor and to the complexity of each mechanism.

The device analyzed in this thesis should work under vacuum, so that the air damping is removed. Thus the damping sources which limit the quality factor of the designed devices are anchor losses and internal dissipation. The first mechanism is generally considered as the fundamental for devices working in vacuum and consequently will be deeply investigated in this thesis. However, also a model for a particular internal loss, namely thermoelastic dissipation, was also considered in order to obtain a more accurate estimation of the quality factor of the devices.

In following sections first methods to estimate anchor losses through FEM simulation will be discussed and then theoretical models and simulations will be presented to obtain an estimation of thermoelastic losses in contour mode disk resonators. Each loss mechanism dissipates an amount of energy per cycle, and the overall energy dissipated per cycle (ΔW_L in Eq. (8)) is given by the sum of the energy dissipated by each mechanism. According to Eq. (8) if the Q_i is the quality factor calculated considering only the ith damping mechanisms, the overall quality factor Q is given by:

$$\frac{1}{Q} = \sum_i \frac{1}{Q_i} \tag{79}$$

Among all the mechanisms only anchor losses and thermoelastic losses will be considered, so that in the following the overall Q will be approximated by:

$$\frac{1}{Q}=\frac{1}{Q_{al}}+\frac{1}{Q_{thermo}} \tag{80}$$

where Q_{al} is the quality factor calculated considering only anchor losses, while Q_{thermo} is the quality factor calculated considering only thermoelastic dissipation. From the value of Q estimated as in (80) for different geometries, a strategy will be proposed to maximize the quality factor of contour mode disk resonators by properly choosing disk and stem radius, i.e. by only acting on layout parameters.

3.2 Anchor losses evaluation

In this section, three different strategies are presented to estimate anchor losses in a contour mode disk resonator, through FEM simulations. Even if a analytical models were proposed to evaluate anchor losses in beam resonators [36] and even in contour mode resonators [58], to obtain such models make very strong assumption were done by authors and at least in the case of contour mode disk resonators, they do not explain some results from simulations which will be discussed later.

The main problem in the evaluation of anchor losses in every MEM resonator is connected to the fact that the substrate has to be included in the simulations because according to the definition of anchor losses the substrate plays a very important role in this loss mechanism: the energy is lost through a wave which propagates from the resonator to the substrate (see also section 1.3.2) and of course the shape of this wave and the amount of energy lost are strictly connected to substrate properties. Furthermore, the presence of the substrate can also change the ideal mode shapes of a resonator: generally the anchor/substrate interface is assumed as still to extract mode shapes, but the substrate even if it is very rigid is not infinitely rigid and allows some movements at the interface. This can change a lot some resonance mode of the device as shown later.

But even if the whole substrate should be included in simulations to have accurate results it is not possible to do it: the substrate is practically “semi-infinite” with respect to the resonator and simulating the whole substrate means to simulate a so high number of element to make the problem unsolvable for even the most powerful calculator in the world, because it would need a too large amount of RAM and even if it had it, a too long time of computation would be necessary.

The problem can be solved in two different ways: substituting the substrate with a smaller domain which behaves like the substrate with respect to the wave driven by the resonator, or by removing the whole substrate and applying proper boundary conditions at the stem/substrate interface. Both the approach can be effective because to estimate the quality factor it is necessary that on the anchor/substrate interface there is something through which it is obtained the same configuration of stress and displacement as when there is the real substrate so that the work done by the resonator on the interface is the same as the job done to drive the wave in the substrate. In particular a smaller domain replacing the substrate has to absorb the whole wave coming from the substrate, without any spurious reflection and the wave driven in the smaller domain should be the same driven as when there is the entire substrate. The simplest idea to obtain such a smaller domain is to “cut” a portion of real substrate, large enough to totally attenuate any incoming wave. This idea cannot work because the needed portion is still too small, because the expected intrinsic dissipation of the substrate is expected to be low. Thus more complex approaches are necessary to find a proper substrate-equivalent domain.

Both using a substrate-equivalent element, it is possible to extract the quality factor by extracting the so-called “complex eigenvalue”. The extraction of complex eigenvalue is allowed by many FEM analysis tools. For example in Femlab [43] it is an option of the transient analysis and given the complex eigenvalue λ_n, the resonance frequency of the nth mode and its quality factor are given by:

$$f_n = \frac{1}{2\pi}\mathrm{Im}[\lambda_n] \qquad\qquad Q_n = \frac{\mathrm{Im}[\lambda_n]}{2\,\mathrm{Re}[\lambda_n]} \tag{81}$$

In the following, one strategy based on a substrate-equivalent element will be presented as well as a strategy based on proper boundary conditions applied at the stem/substrate interface, which are found by solving the equations ruling the propagation of an acoustic wave in the substrate.

First, a consideration on the axisymmetry of the geometry and of the mode shapes has to be done to simplify the simulations: each radial cross section as the one in Figure 63b shows at the resonance the same deformations and the same profile of stress as well as the same radial displacements as shown in (76), i.e. deformations does not depend on angle θ indicated in Figure 63a. If mode-shape is axisymmetric also the load driven on the substrate is axisymmetric and if the substrate is considered as isotropic or axisymmetric with respect to the material properties (i.e. E, ρ and ν do not depend on θ), also the propagating wave can be considered as axisymmetric. This allows to conclude that simulating the overall 3D structure is the same as simulating only a radial cross section (Figure 65): of course far from contour mode resonance the disk deformation could be not axisymmetric anymore, but if the quality factor is evaluated trough a complex eigenvalue associated to the respective resonance mode, the axisymmetry of the mode-shape is enough to allow the aforementioned simplification. On the other hand the hypothesis on the isotropy or axisymmetry of substrate material properties could be considered as very strong, but the simplification in Figure 65 allows to reduce very much the time of calculations.

The axisymmetry hypothesis of the overall problem will be fundamental also to extract the boundary conditions at the stem/substrate interface in the second simulation method presented.

3.2.1 Simulations based on a high damping substrate

In this section an element which can mimic the behaviour of the substrate is proposed: it is the *High Damping Substrate (HDS)*: the damping coefficients of the substrate are increased with respect to the real ones in order to obtain the total absorption of the incoming wave in small domain, but they cannot be augmented so much because if material properties are too much different from the real ones in the substrate, the wave propagating in the substrate is significantly different from the wave which propagates in the actual substrate. For example if both substrate and resonator are made of the same material characterized by a low intrinsic dissipation, a HDS substrate-equivalent element with damping coefficient too high would lead to spurious reflections, for the difference in the materials, which was introduced artificially.

HDS element can be implemented in Femlab [43], a FEM tool, capable of multi-physic simulations of structural, heat transmission, electrical and electromagnetic, fluid flows and micro fluidics, and chemical reactions. It is a complete and flexible tool which has been proved as useful for the analysis of many problems related to MEMS design, so that it could be interesting to exploit it also for anchor losses estimation. Another interesting peculiarity of Femlab, is the option of interfacing it with MATLAB, which increase the potentiality and the flexibility of Femlab, above all if parametric simulations are needed.

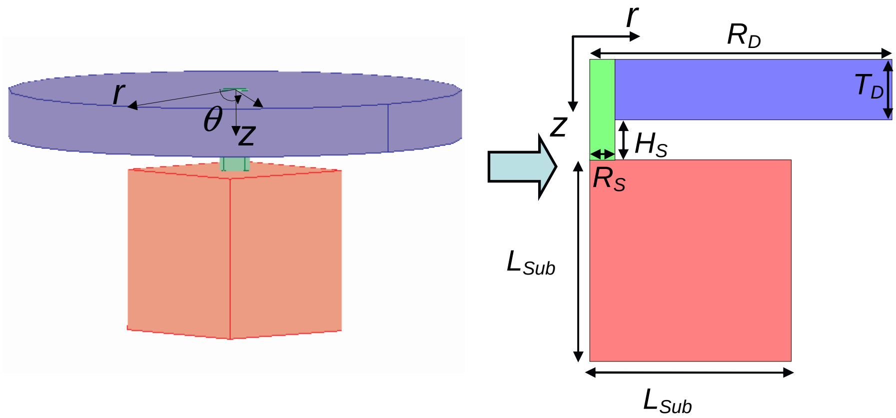

Figure 65: Due to the axisymmetry, the three dimensional problem (on the left) can be simplified in a bi-dimensional one (on the right) by simulating only one radial cross section. In blue it is represented the disk, in green the stem and in pink the HDS. Disk dimensions are indicated as well as the size L_{Sub} *of the HDS.*

As an example, the one-dimensional mass-spring-damper system is considered:

$$m\ddot{x} + c\dot{x} + kx = F \tag{82}$$

where m, k, c are respectively the mass, the stiffness and the damping coefficient, while F is the external applied force. According to the Rayleigh model:

$$c = \alpha m + \beta k \tag{83}$$

which leads to a quality factor:

$$Q = \frac{1}{\dfrac{\alpha}{\omega_0} + \beta\omega_0} \tag{84}$$

To obtain a HDS the two degrees of freedom α and β are too many: if the damping in the substrate depends on mass or stiffness, it does not matter, because the only important thing is that the damping factor c or better the elements of the damping matrix *[C]* are high enough to obtain that wave propagating in the substrate is completely absorbed in the finite domain.

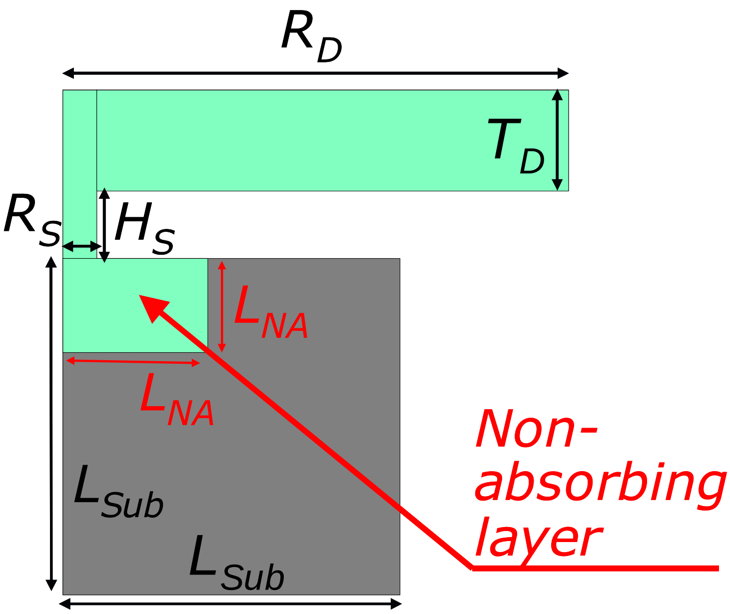

Figure 66: Geometry used in simulations, including non-absorbing layer (NAL), in the HDS. The regions with zero damping or the real low intrinsic damping of the material are represented in green, while the regions with a high damping are in green. L_{NA} is the non-absorbing layer size.

Thus it is assumed $\alpha = 0$, while β has to be increased until all the propagating wave was totally absorbed. Nonetheless, as already mentioned, it is not possible to increase too much the damping, because it would change too much the material properties of the substrate, leading to a change in propagating wave shape, with respect to what happens in the real substrate. Besides a decay of the acoustic wave in a too short area close to the anchor, should require a too fine mesh in order to avoid spurious reflection. It is necessary to choose carefully both β and the "size" of the HDS: in the simulations of disk resonators presented in this thesis, the HDS is a cylinder with radius equal to the height, so that its radial cross section is a square, whose side is the HDS size, indicated as L_{Sub} in Figure 65.

Both the two parameters have to be high to have the total absorption, but not too high the first to obtain the same wave propagating in the real substrate and to avoid spurious reflection at the interface between resonator and substrate, the second to avoid to simulate too many elements. On the other hand they are related because at least theoretically the higher β is the less substrate is needed to mimic the total absorption and vice versa. To obtain a more realistic behaviour at the stem/substrate interface, where the higher substrate deformation are expected to be higher, a “linear” model for the damping in the substrate could be used: β can set to 0, or at the low value expected in the real substrate, at the interface between substrate and resonator and increased linearly with the distance to the interface. As an alternative it is also possible to introduce a region around the interface with $\beta = 0$ or fixed to the low value expected for the substrate. This region, called also *non-absorbing layer (NAL)*, was chosen to be a cylinder with radius L_{NA} equal to the height, and consequently a square in the simulated cross-section (Figure 66).

In the following results from HDS-based simulations employing NAL will be presented as well as results HDS-based simulations which do not include NAL, while the model with linearly increased β was not tested.

Both the HDS-based simulations were compared with the results from simulations employing another substrate-equivalent element, the PML. Such element, similar to the homonymous element used in electromagnetic simulations [54], was used by a HiQLab, an open source FEM simulations tool, presented in [55] as a software to estimate anchor losses. The extraction of the quality factor can be done as in Femlab through the evaluation of complex eigenvalues.

The total absorption of energy is obtained through a complex-value change of coordinates. To explain this point, the one-dimensional example reported in [90] is considered. In that case the change of variable is defined as:

$$x \leftrightarrow \tilde{x} = \int_0^x \left(1 - j\sigma(s)/k\right) ds \tag{85}$$

where x is the Cartesian coordinate and $\tilde{x}$ the transformed coordinate; k is the wave number and $\sigma(s)$ a *stretch function*, which can be defined as:

$$\begin{cases} \sigma(s) = \sigma_0\left(s - L\right) & s > L \\ \sigma(s) = 0 & s \leq L \end{cases} \tag{86}$$

L is an offset length and σ_0 is a constant which can be related to the length of PML needed to dissipate the entire incident wave. Considering the equation for the propagation of an acoustic compressive wave in a bar:

$$E\frac{\partial^2 u}{\partial x^2} = \rho\frac{\partial^2 u}{\partial t^2} \tag{87}$$

where $u(x,t)$ is the displacement in x direction, E the Young's modulus and ρ the mass density of the material; if there is a boundary condition of no refection at one end of the bar, the time harmonic solutions can be expressed as:

$$u(x,t) = e^{j\omega t}\left(c_{out}e^{-jkx} + c_{in}e^{+jkx}\right) \tag{88}$$

where c_{out} is the amplitude of the outgoing wave from 0 to infinity, while c_{in} is the amplitude of the incoming wave from infinity to 0; the two amplitudes depend of course on the boundary conditions at the ends of the clamp, namely 0 and L_B; let us to assume that in L_B there is no reflected wave and that all the outgoing energy has to be absorbed; using a PML, it is possible to solve Eq.(87) for $x > L_B$ by substituting $x \leftrightarrow \tilde{x}$ as defined in (85), so that :

$$u(x,t) = e^{j\omega t}\left(c_{out}e^{-jkx}\exp\left(-\int_{L_B}^{x}\sigma(s)ds\right) + c_{in}e^{+jkx}\exp\left(\int_{L_B}^{x}\sigma(s)ds\right)\right) \qquad x > L_B \tag{89}$$

or using the expression for $\sigma(s)$ in (86), with $L = L_B$:

$$u(x,t) = e^{j\omega t}\left(c_{out}e^{-jkx}e^{-\sigma_0\frac{(x-L_B)^2}{2}} + c_{in}e^{+jkx}e^{+\sigma_0\frac{(x-L_B)^2}{2}}\right) \qquad x > L_B \tag{90}$$

Thus the change of coordinates introduces an attenuation of the propagating wave in PML region and σ_0 can be seen as an attenuation factor; by increasing σ_0 it is possible [90] to set the reflected wave (the second term in (90)) in L_B very close to zero, so that the condition of no reflection and total absorption of the propagating wave (perfect matching) is obtained. Of course to get the matching also the length of PML R_{PML} should be enough to have the entire outgoing wave absorbed.

The size of the PML cannot be too high to limit the number of simulated elements and then the simulation time. Also with respect to σ_0 it is necessary to choose a value high enough to have all the outgoing wave absorbed in the PML, but it should not be too high, because if the exponential function in the first term of (90) decrease in a too short length, the mesh used to numerically solve the problem, can become too coarse and there could appear some spurious reflection. Besides the complex-value of coordinates is equivalent to a change of material properties which can introduce a difference between the wave propagating in simulations and in the real substrate.

In HiQLab, a non-absorbing layer is also introduced between the anchor/substrate interface and the PML, in order to have a condition close to reality where deformation of the substrate is expected to be the highest.

HDS and PML are very similar: even the two models are different, the result is anyway a region where the wave is attenuated more than in the substrate. The problem in the choice of σ_0 and R_{PML} are the same as in the choice of β and L_{Sub}: a trade-off between the total absorption of the wave without any spurious reflection and the size. If the non-absorbing layer is included also the value of L_{NA} can change the results.

Thus several preliminary simulations were needed to evaluate the best values for β and L_{Sub} or for σ_0 and R_{PML}.

For HDS, different curves of the quality factor Q_{AL} only due to anchor losses as a function of β were extracted for different size of L_{Sub} and L_{NA}. Disk and stem material was polysilicon ($E = 160\ GPa$, $\rho = 2330\ Kg/m^3$, $\nu = 0.226$) and the substrate was assumed to be silicon with approximately the same material properties of the resonator. From such simulations if the NAL was not included (Figure 65) $\beta = 200\ ps$ and $L_{Sub} = 60\ \mu m$, were chosen because for all the substrate sizes simulated (from 30 μm to 80 μm) a minimum for Q_{AL} was found around $\beta = 200\ ps$ (even if the minimum position slightly decreases if L_{Sub} increases) and its value does not change for $L_{Sub} > 60\ \mu m$. This means that for $\beta < 200\ ps$ the attenuation inside HDS is not enough to absorb all the propagating wave, while for $\beta > 200\ ps$ the damping is too high and there are some spurious reflections at the interface between stem and substrate, confining greater amount of energy in the resonator where the intrinsic losses are neglected (i.e. $\beta = \alpha = 0$). Repeating the same analysis for a geometry including non-absorbing layer (Figure 66) leads to choose again 200 ps and 60 μm as optimum values respectively for β and. L_{Sub}, while for the NAL $L_{NA} = 10\ \mu m$ was chosen: Q_{AL} changes, generally increasing, if L_{NA} is changed from 0 to 10 μm, while if it is further increased results do not changes anymore.

The selected value for β, L_{Sub} and L_{NA} are the optimum choice for a silicon substrate and a contour mode disk resonator resonating around 200 MHz, if substrate material properties or device resonance frequency are too much different from the test case, the selected parameters could be no more the best one. The same hold in case of PML, because parameters σ_0, R_{PML} and L_{NA} has to be chosen in the same way.

3.2.2 Simulations based on analytical boundary conditions at the stem/substrate interface

Both PML and HDS lead to very fast simulations, at least in 2D, but give results dependent on the size of the simulated domain and on the damping parameter β in HDS or on the stretch parameter σ_0 in PML. Thus, in both cases, it is necessary to choose two parameters properly to obtain reliable results. Besides neither the PML nor the HDS is the real substrate; they are just an approximation of it.

Thus the possibility of totally eliminating the PML and the HDS was investigated, by replacing them with proper boundary conditions at the interface between anchor and substrate. These boundary conditions mimic the exact relationship between stress and displacements at the stem/substrate interface, due to the propagation of an acoustic wave in the substrate.

If the problem is axisymmetric as in the case of a contour mode disk resonator, a set of proper boundary conditions can be found in an analytical form by exploiting the solution for the propagation of an elastic axisymmetric wave in a semi-infinite space, in a similar way to what done in [58].

Fundamental conditions to use this model are:

a) The substrate is much higher than the resonator (the substrate behaves as a semi-infinite space).
b) The substrate is *isotropic*, or even if *anisotropic* it preserves the axial symmetry of the problem.

Due to the assumption b) Eq. (71) holds in the substrate considering the system of reference in Figure 64.

Defining the Lame coefficients λ, μ, stress tensor components can be expressed as functions of strain tensor components:

$$\sigma_{ij} = 2\mu\varepsilon_{ij} + \delta_{ij}\lambda\sum_{k}\varepsilon_{kk} \tag{91}$$

where δ_{ij} is the Kronecker delta (it is 1 if $i = j$, else 0), and Lame coefficients can be expressed as functions of Young's modulus E and Poisson ratio v as:

$$\lambda = \frac{E\nu}{(1-2\nu)(1+\nu)} \qquad \mu = \frac{E}{2(1+\nu)} \tag{92}$$

Neglecting the non-linear terms, the strain tensor components in axisymmetric coordinates can be expressed as [91]:

$$\begin{array}{lll} \varepsilon_{rr} = \dfrac{\partial u_r}{\partial r} & \varepsilon_{\theta\theta} = \dfrac{u_r}{r} & \varepsilon_{zz} = \dfrac{\partial u_z}{\partial z} \\ \varepsilon_{rz} = \dfrac{1}{2}\left(\dfrac{\partial u_z}{\partial r} + \dfrac{\partial u_r}{\partial z}\right) & \varepsilon_{r\theta} = 0 & \varepsilon_{z\theta} = 0 \end{array} \tag{93}$$

so that, substituting the Eqs. (93) in (92) and then (93) in (71), after some straightforward calculations it is possible to find two equations in dependence on the displacements *u* and *w*:

$$\begin{cases} c_L^2\left(\dfrac{\partial^2 u}{\partial r^2} + \dfrac{1}{r}\dfrac{\partial u}{\partial r} - \dfrac{u}{r^2} + \dfrac{\partial^2 u}{\partial z^2}\right) + \left(c_L^2 - c_T^2\right)\dfrac{\partial}{\partial z}\left(\dfrac{\partial w}{\partial r} - \dfrac{\partial u}{\partial z}\right) = \dfrac{\partial^2 u}{\partial t^2} \\ c_L^2\left(\dfrac{\partial^2 w}{\partial r^2} + \dfrac{1}{r}\dfrac{\partial w}{\partial r} + \dfrac{\partial^2 w}{\partial z^2}\right) + \left(c_L^2 - c_T^2\right)\left[\dfrac{\partial}{\partial r}\left(\dfrac{\partial u}{\partial z} - \dfrac{\partial w}{\partial r}\right) + \dfrac{1}{r}\left(\dfrac{\partial u}{\partial z} - \dfrac{\partial w}{\partial r}\right)\right] = \dfrac{\partial^2 w}{\partial t^2} \end{cases} \tag{94}$$

where c_L and c_T are the velocities of the longitudinal and transverse wave, defined as:

$$c_L = \sqrt{\frac{\lambda + 2\mu}{\rho}} \qquad c_T = \sqrt{\frac{\mu}{\rho}} \tag{95}$$

If **u** is the displacements vector, the rotation vector $\boldsymbol{\Omega}$ and the dilatation Δ are given by [89]:

$$\boldsymbol{\Omega} = \nabla \times \mathbf{u} \qquad \Delta = \nabla \cdot \mathbf{u} \tag{96}$$

If the problem is axisymmetric, $\boldsymbol{\Omega}$ and Δ can be expressed in cylindrical coordinates as:

$$\boldsymbol{\Omega} = \begin{pmatrix} 0 \\ \dfrac{\partial u}{\partial z} - \dfrac{\partial w}{\partial r} \\ 0 \end{pmatrix} = \begin{pmatrix} 0 \\ \Omega_\theta \\ 0 \end{pmatrix} \qquad \Delta = \frac{\partial u}{\partial r} + \frac{u}{r} + \frac{\partial w}{\partial z} \tag{97}$$

so that from (94) it is possible to find the following equations for Ω_θ and Δ:

$$\begin{cases} c_L^2\left(\dfrac{\partial^2\Delta}{\partial r^2}+\dfrac{1}{r}\dfrac{\partial\Delta}{\partial r}+\dfrac{\partial^2\Delta}{\partial z^2}\right)=\dfrac{\partial^2\Delta}{\partial t^2} \\ c_T^2\left(\dfrac{\partial^2\Omega_\theta}{\partial r^2}+\dfrac{1}{r}\dfrac{\partial\Omega_\theta}{\partial r}-\dfrac{\Omega_\theta}{r^2}+\dfrac{\partial^2\Omega_\theta}{\partial z^2}\right)=\dfrac{\partial^2\Omega_\theta}{\partial t^2} \end{cases} \tag{98}$$

The dilatation and the rotation are associated to the geometrical characteristics of the wave: the first can be related with a dilatation wave, which retains the shape of any infinitesimal element of the domain, changing only its volume, while the second can related to a distortion wave, which maintains the volume but alters the shape of any infinitesimal element of the domain.

Then the solutions for the rotation and the dilatation can be assumed to be respectively $\Omega_\theta=\overline{\Omega}(r,z)\cdot e^{j\omega t}=\overline{\Omega}\cdot e^{j\omega t}$ and $\Delta=\overline{\Delta}(r,z)\cdot e^{j\omega t}=\overline{\Delta}\cdot e^{j\omega t}$, i.e. they can be obtained by multiplying a part only dependent on the time and another one only dependent on r and z. Furthermore, it is possible also to make the hypothesis that the part dependent only on the time is a sinusoidal function. According to these assumptions Eq. (98) becomes:

$$\begin{cases} c_L^2\left(\dfrac{\partial^2\overline{\Delta}}{\partial r^2}+\dfrac{1}{r}\dfrac{\partial\overline{\Delta}}{\partial r}+\dfrac{\partial^2\overline{\Delta}}{\partial z^2}\right)=-\omega^2\overline{\Delta} \\ c_T^2\left(\dfrac{\partial^2\overline{\Omega}}{\partial r^2}+\dfrac{1}{r}\dfrac{\partial\overline{\Omega}}{\partial r}-\dfrac{\overline{\Omega}}{r^2}+\dfrac{\partial^2\overline{\Omega}}{\partial z^2}\right)=-\omega^2\overline{\Omega} \end{cases} \tag{99}$$

Eqs. (99) can be solved by applying to the first one the Hankel transform (or Bessel-Fourier transform) of zero order and to the second one the Hankel transform (or Bessel-Fourier transform) of first order. Given a function F, its zero order Hankel transform F_0 and its first order Hankel transform F_1, transforms and inverse transforms are defined as [92]:

$$F_0(q,z)=\int_0^\infty rF(r,z)J_0(qr)dr \qquad F(r,z)=\int_0^\infty qF_0(q,z)J_0(qr)dq$$

$$\text{and} \tag{100}$$

$$F_1(q,z)=\int_0^\infty rF(r,z)J_1(qr)dr \qquad F(r,z)=\int_0^\infty qF_1(q,z)J_1(qr)dq$$

where J_0 and J_1 are the Bessel functions of the first kind of zero and first order respectively.

According to the properties of the Hankel transform, if F and its first derivative with respect to r are bounded for $r \to \infty$ (see appendix A)):

$$\begin{aligned} &\int_0^\infty r\left(\frac{\partial^2 F}{\partial r^2}+\frac{1}{r}\frac{\partial F}{\partial r}\right)J_0(qr)dr=-q^2F_0 \\ &\int_0^\infty r\left(\frac{\partial^2 F}{\partial r^2}+\frac{1}{r}\frac{\partial F}{\partial r}-\frac{F}{r^2}\right)J_1(qr)dr=-q^2F_1 \end{aligned} \qquad (101)$$

Thus, by applying the Hankel transforms as defined in (100) to (99) and exploiting the properties defined in (101), the following equations can be found:

$$\begin{cases} \dfrac{\partial^2\overline{\Delta}_0}{\partial z^2}=\left(q^2-\dfrac{\omega^2}{c_L^2}\right)\overline{\Delta}_0 \\ \dfrac{\partial^2\overline{\Omega}_1}{\partial z^2}=\left(q^2-\dfrac{\omega^2}{c_T^2}\right)\overline{\Omega}_1 \end{cases} \qquad (102)$$

and solving Eq. (102) the following expression for the dilatation wave can be found:

$$\begin{aligned} &\overline{\Delta}_0(q,z)=A(q)e^{-\gamma_L z}+C(q)e^{+\gamma_L z} \\ &\gamma_L=\sqrt{q^2-\frac{\omega^2}{c_L^2}} \end{aligned} \qquad (103)$$

while and for the rotation wave it is obtained:

$$\begin{aligned} &\overline{\Omega}_1(q,z)=B(q)e^{-\gamma_T z}+D(q)e^{+\gamma_T z} \\ &\gamma_T=\sqrt{q^2-\frac{\omega^2}{c_T^2}} \end{aligned} \qquad (104)$$

Considering that for $z \to \infty$ the amplitude of the wave cannot diverge, or assuming in a equivalent way as negligible the regressive wave, because of the hypothesis of total absorption of the wave propagating in the substrate (no reflection), it is necessary that $C = 0$ and $D = 0$.

Assuming also for the displacement vector components $u = U(r,z) \cdot e^{j\omega t} = U \cdot e^{j\omega t}$ and $w = W(r,z) \cdot e^{j\omega t} = W \cdot e^{j\omega t}$, it is possible to find the following relations between displacement, dilatation and rotation wave, by properly combining Eqs. (94) and (97):

$$\begin{cases} U = -\dfrac{1}{\omega^2}\left(c_L^2 \dfrac{\partial \bar{\Delta}}{\partial r} + c_T^2 \dfrac{\partial \bar{\Omega}}{\partial z} \right) \\ W = -\dfrac{1}{\omega^2}\left[c_L^2 \dfrac{\partial \bar{\Delta}}{\partial z} - c_T^2 \left(\dfrac{\partial \bar{\Omega}}{\partial r} + \dfrac{\bar{\Omega}}{r} \right) \right] \end{cases} \tag{105}$$

If the Hankel transform of first order is applied to the first equation in (105) and the Hankel transform of zero order to the second one, Eq. (105) becomes:

$$\begin{cases} U_1 = -\dfrac{1}{\omega^2}\left[\left(c_L^2 \displaystyle\int_0^\infty r \dfrac{\partial \bar{\Delta}}{\partial r} J_1(qr)dr \right) + c_T^2 \dfrac{\partial \Omega_1}{\partial z} \right] \\ W_0 = -\dfrac{1}{\omega^2}\left\{ c_L^2 \dfrac{\partial \Delta_0}{\partial z} - c_T^2 \left[\displaystyle\int_0^\infty r \left(\dfrac{\partial \bar{\Omega}}{\partial r} + \dfrac{\bar{\Omega}}{r} \right) J_0(qr)dr \right] \right\} \end{cases} \tag{106}$$

Since the following relations hold if F is bounded for $r \to \infty$ (as shown in appendix A):

$$\begin{aligned} &\int_0^\infty r\left(\frac{\partial F}{\partial r} \right) J_1(qr)dr = \int_0^\infty rF J_0(qr)dr = -qF_0 \\ &\int_0^\infty r\left(\frac{\partial F}{\partial r} + \frac{F}{r} \right) J_0(qr)dr = \int_0^\infty rF J_1(qr)dr = +qF_1 \end{aligned} \tag{107}$$

Eq. (106) becomes:

$$\begin{cases} U_1 = -\dfrac{1}{\omega^2}\left(c_T^2 \dfrac{\partial \Omega_1}{\partial z} - q c_L^2 \Delta_0 \right) \\ W_0 = -\dfrac{1}{\omega^2}\left(c_L^2 \dfrac{\partial \Delta_0}{\partial z} - q c_T^2 \Omega_1 \right) \end{cases} \tag{108}$$

To find a proper set of boundary conditions, the displacement at the interface between anchor and substrate has to be found. If the interface is at *z = 0*, the transform of the displacements components at the interface can be expressed as:

$$\begin{cases} U_1(q, z=0) = U_{10} = \dfrac{1}{\omega^2}\left(c_T^2\gamma_T B + qc_L^2 A\right) \\ W_0(q, z=0) = W_{00} = \dfrac{1}{\omega^2}\left(c_L^2\gamma_L A + qc_T^2 B\right) \end{cases} \tag{109}$$

where the expression for the dilatation and rotation in (103) and (104) have been substituted.

It is then necessary to express *A* and *B* as functions of the stress components in order to find an expression which relates the displacements to the stress in the transformed domain. The stress components which act on the stem/substrate interface are σ_{zz} and σ_{rz}, because the interface stem/substrate is perpendicular to z as shown in Figure 63b and the problem is axisymmetric. They can be expressed as functions of the displacements components by the following expressions, which can be found combining (91),(93) and (95):

$$\begin{aligned} \sigma_{zz} &= \rho c_L^2 \frac{\partial u_z}{\partial z} + \rho\left(c_L^2 - 2c_T^2\right)\left(\frac{\partial u_r}{\partial r} + \frac{u_r}{r}\right) \\ \sigma_{rz} &= \rho c_T^2 \left(\frac{\partial u_z}{\partial r} + \frac{\partial u_r}{\partial z}\right) \end{aligned} \tag{110}$$

or, given the expressions for dilatation and rotation in (97), stress components can be written as:

$$\begin{cases} \sigma_{zz} = \rho c_L^2 \Delta - 2\rho c_T^2 \left(\dfrac{\partial u_r}{\partial r} + \dfrac{u_r}{r}\right) \\ \sigma_{rz} = \rho c_T^2 \Omega_\theta - 2\rho c_T^2 \dfrac{\partial u_z}{\partial r} \end{cases} \tag{111}$$

Then, $\sigma_{zz} = S_Z(r,z) \cdot e^{j\omega t} = S_Z \cdot e^{j\omega t}$ and $\sigma_{rz} = S_R(r,z) \cdot e^{j\omega t} = S_R \cdot e^{j\omega t}$ are assumed to find:

$$\begin{cases} S_Z = \rho c_L^2 \overline{\Delta} - 2\rho c_T^2 \left(\dfrac{\partial U}{\partial r} + \dfrac{U}{r} \right) \\ S_R = \rho c_T^2 \overline{\Omega} + 2\rho c_T^2 \dfrac{\partial W}{\partial r} \end{cases} \tag{112}$$

so that, if the Hankel transform of zero order is applied to the first equation in (112) and the Hankel transform of first order to the second one, it is possible to extract, by the Hankel transforms properties defined in (107):

$$\begin{cases} S_{Z0} = \rho\left(c_L^2 \Delta_0 - 2c_T^2 q U_1 \right) \\ S_{R1} = \rho c_T^2 \left(\Omega_1 - 2qW_0 \right) \end{cases} \tag{113}$$

Eqs. (113) can be evaluated in z = 0 to find an expression for *A* and *B* as functions of stress and displacement components at the stem/substrate interface:

$$A = \frac{S_{Z00}}{\rho c_L^2} + \frac{2c_T^2 q U_{10}}{\rho c_L^2} \quad ; \quad B = \frac{S_{R10}}{\rho c_T^2} + \frac{2qW_{00}}{\rho} \tag{114}$$

where $S_{Z00} = S_{Z0}(q, z=0)$ and $S_{R10} = S_{R1}(q, z=0)$. Substituting the expressions for *A* and *B* in (114) into (109), it is possible to find two expressions which relates the Hankel transforms of the displacement components to the transforms of the stress components. After straightforward calculations these expressions are:

$$\begin{cases} U_{10} = \dfrac{1}{\rho c_T^2} \cdot \dfrac{\left\{ \dfrac{\gamma_T \omega^2}{c_T^2} S_{R10} - q\left[\left(q^2 + \gamma_T^2 \right) - 2\gamma_L \gamma_T \right] S_{Z00} \right\}}{\left(q^2 + \gamma_T^2 \right)^2 - 4q^2 \gamma_L \gamma_T} \\ W_{00} = \dfrac{1}{\rho c_T^2} \cdot \dfrac{\left\{ \dfrac{\gamma_L \omega^2}{c_T^2} S_{Z00} - q\left[\left(q^2 + \gamma_T^2 \right) - 2\gamma_L \gamma_T \right] S_{R10} \right\}}{\left(q^2 + \gamma_T^2 \right)^2 - 4q^2 \gamma_L \gamma_T} \end{cases} \tag{115}$$

Finally, it is possible to apply the inverse transform as defined in (100) to Eqs. (115), in order to find the following boundary conditions:

$$\begin{cases} u = \int_0^{\infty} q \left\{ A_{RR}(q) \left[\int_0^{Rs} r\sigma_{zr}(r) J_1(qr)dr \right] + A_{RZ}(q) \left[\int_0^{Rs} r\sigma_{zz}(r) J_0(qr)dr \right] \right\} J_1(qr)dq \\ w = \int_0^{\infty} q \left\{ A_{ZR}(q) \left[\int_0^{Rs} r\sigma_{zr}(r) J_1(qr)dr \right] + A_{ZZ}(q) \left[\int_0^{Rs} r\sigma_{zz}(r) J_0(qr)dr \right] \right\} J_0(qr)dq \end{cases} \tag{116}$$

where functions A_{IJ} are defined as:

$$\begin{aligned} A_{RR}(q) &= \frac{1}{\rho c_T^4} \cdot \frac{\gamma_T \omega^2}{\left(q^2+\gamma_T^2\right)^2 - 4q^2\gamma_L\gamma_T} \\ A_{ZZ}(q) &= \frac{1}{\rho c_T^4} \cdot \frac{\gamma_L \omega^2}{\left(q^2+\gamma_T^2\right)^2 - 4q^2\gamma_L\gamma_T} \\ A_{RZ}(q) = A_{ZR}(q) &= \frac{1}{\rho c_T^2} \cdot \frac{-q\left[\left(q^2+\gamma_T^2\right) - 2\gamma_L\gamma_T\right]}{\left(q^2+\gamma_T^2\right)^2 - 4q^2\gamma_L\gamma_T} \end{aligned} \tag{117}$$

Eqs. (116) and (117) can be implemented in Femlab as boundary conditions at the stem/substrate interface, avoiding to include any substrate-equivalent element.

Coefficients A_{IJ} are dependent only on the wave frequency and on the material properties of the substrate (velocities c_L and c_T of the longitudinal and transversal waves and mass density ρ). They do not depend on the resonator dimensions and material properties.

The problem with the coefficients A_{IJ} is that each of them has a discontinuity, due to the presence of a real positive zero q_0 in the denominator. This discontinuity results in a divergence of the value of each A_{IJ} (Figure 67).

The value of q_0 can be found by substituting γ_T and γ_L from (103) and (104) in the expression of the denominator of all the coefficients A_{IJ} in Eqs. (117), leading to the equation:

$$\left(2q_0^2 - \frac{\omega^2}{c_T^2}\right)^2 - 4q_0^2\sqrt{q_0^2 - \frac{\omega^2}{c_L^2}} \cdot \sqrt{q_0^2 - \frac{\omega^2}{c_T^2}} = 0 \tag{118}$$

Eq. (118) can be numerically solved. For a silicon substrate and a propagating wave with frequency 200 MHz the value of q_0 is about 2.6×10^5 m^{-1} (0.26 μm^{-1}).

The physical meaning of this discontinuity can be found considering the sense of applying Hankel transform to stress components and displacements: the operation is equivalent to write the wave as a superposition of infinite waves $B(z)J_n(qr)$ (with n = 0, 1 depending on the transform order). Thus q^{-1} can be considered a sort of "wavelength" in radial direction, even if, being Bessel functions not periodic, it is not possible to talk about wavelength; due to this reason q^{-1} will be called "pseudo-wavelength" in the following. According to this interpretation the singularity in the coefficients A_{IJ} for q_0 means that stresses, with pseudo-wavelength q_0^{-1} in radial direction, produce very high displacements, i.e. the wave with this radial pseudo-wavelength is better propagating than all the other waves (for silicon q_0^{-1} at 200 MHz is about 3.8 μm).

The discontinuity results in a great difficulty in numerical calculating the outer integrals in (116): they cannot converge, due to the discontinuity .

Thus it is necessary to remove this discontinuity, by introducing a substrate model more realistic: in the previous calculations the intrinsic losses of the substrate were neglected and this resulted in an infinite ratio between each displacement components and each stress component at the interface for a particular pseudo-wavelength. Introducing a viscoelastic damping in the substrate the discontinuity becomes a sharp peak and the integrals in (116) can be numerically evaluated if the grid of q-space is fine enough around the peak. The introduction of the viscoelastic damping can be done by defining a new Young's modulus E' for the substrate, according to Kelvin-Voigt representation [34]:

$$E' = E(1 + j\omega\tau) \tag{119}$$

where E is the Young's modulus considered till this point and τ is the relaxation time of the material. Reasonable values for τ can be evaluated from thermoelastic and phonon-phonon dissipations in the substrate. Using the expression for the attenuation of a longitudinal plane wave due to thermoelastic dissipation in [93] and due phonon-phonon interaction in [94], values for τ about 1 fs can be found for silicon (see appendix B). Of course other internal damping mechanisms can increase the estimated value for τ, thus in the following simulations considering also higher value for τ will be presented.

Another interesting observation about graphs in Figure 67 is that coefficients A_{IJ} are complex and their imaginary part produces a component of each displacement with a phase shift of 90° with respect to the stress acting in the same direction. As an example, the imaginary part of A_{ZZ} introduces a component of w with a 90 degrees of phase shift with respect to σ_{zz}. This results in a dissipation of energy and it is interesting to notice that it occurs also without considering any intrinsic losses in the material (in Figure 67 it is assumed $\tau = 0$).

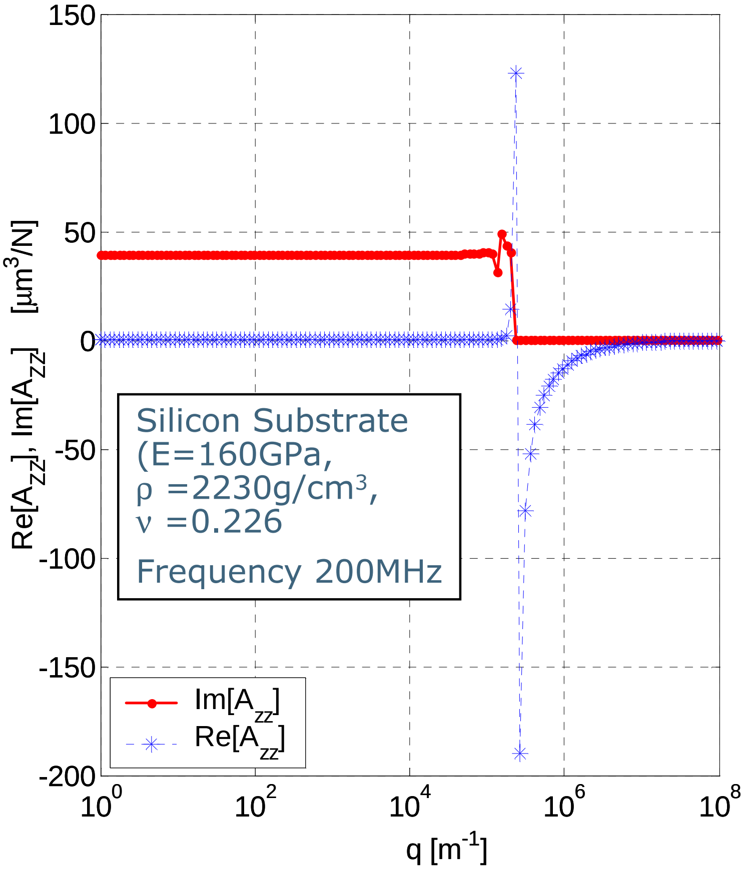

Figure 67: Real (blue curve) and imaginary (red curve) part of coefficient A_{ZZ} for a silicon substrate and a propagating wave at 200 MHz. It is possible to see the pseudo-wavelength where the real part diverges and the cut-off pseudo-wavelength (wave components with a pseudo-wavelength higher than the cut-off one are attenuated). A similar behaviour has been found also for the other coefficients A_{IJ}.

The imaginary parts of A_{IJ} are zero for high value of q (for example $Im[A_{ZZ}] = 0$ for $q^{-1} > c_l/\omega$), which means that components of displacement with higher pseudo-wavelength are attenuated, i.e. they are evanescent wave; c_l/ω can be considered as a cut-off pseudo-wavelength for displacements in z direction generated by the compressive stress σ_{zz}. Of course this is true only if other losses are neglected: if an intrinsic damping is introduced as in (119), the wave is attenuated for all the pseudo-wavelength.

The previous observation is very important to give a physical explanation of the anchor loss dissipation: it occurs just because the resonator movements produce a wave propagating in the substrate, with some evanescent components and thus a part of the energy stored in the device is dissipated during each cycle to sustain these attenuated waves.

3.3 Comparison between three methods to evaluate anchor losses

Several simulations were done in order to compare the performance of the two methods proposed in this thesis with PML-based simulations, which were performed using the version of HiQLab downloadable from [95]. Also a comparison with some experimental data from [37] was done in order to validate the simulation approaches. In all the simulations presented in the following internal damping of stem and disk was neglected.

PML and HDS based simulations give very similar results if they both include a non-absorbing layer or if they do not include it, as shown in Figure 68. In both simulations, whose results are shown in Figure 68, the NAL size L_{NA} is chosen large enough so that a change of it does not affect anymore the results as discussed in 3.2.1

On the other hand the presence or the absence of the non-absorbing layer in the simulations can change a lot the value of the estimated quality factor only due to the anchor losses: considering for example a disk resonator, resonating at about 184 MHz on its first contour mode the dependence of Q_{al} on the stem radius R_S show a very huge and sharp peak if the non-absorbing layer is considered, while if NAL is not included in the simulations the peak is less sharp and its value is smaller (Figure 69).

The model with NAL included should be better than the one with NAL excluded, because considers the real substrate material properties close to the stem/substrate interface, where the higher substrate deformations are expected, but a comparison with experimental data from [37] seems to demonstrate a better agreement of simulation without non-absorbing layer, as shown in Figure 70.

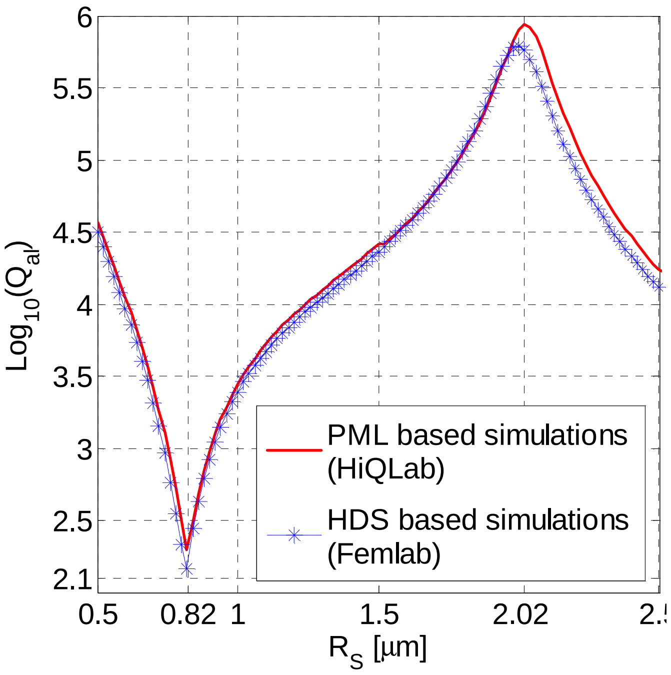

Figure 68: Comparison between the HDS-based and PML-based simulations with respect to the quality factor dependence on stem radius, with non absorbing layer included. R_D = 15 μm, T_D = 3 μm and H_S = 0.5 μm; disk and stem material Polysilicon (E = 160 GPa, ρ = 2230 Kg/m^3, ν = 0.226) for a resonance frequency of the first contour mode about 184 MHz, independently on R_S. Substrate material was assumed to be silicon, with material properties equal to the ones of stem and substrate.

The agreement between experimental data from [37] and HDS/PML-based simulations is anyway acceptable and this could be a validation of these two strategies both with and without NAL included.

On the other hand the quality factor from experimental data can be due not only on anchor losses but also on other damping mechanisms, while in the simulations only anchor losses are considered. Even if anchor losses are expected to be the dominant damping mechanism, if there are some other significant dissipation sources and if they were considered in simulations the quality factor given by estimating anchor losses with NAL included could be lowered and it could match better with measurements, while the quality factor obtained by evaluating anchor losses without including NAL could become smaller than the measured one.

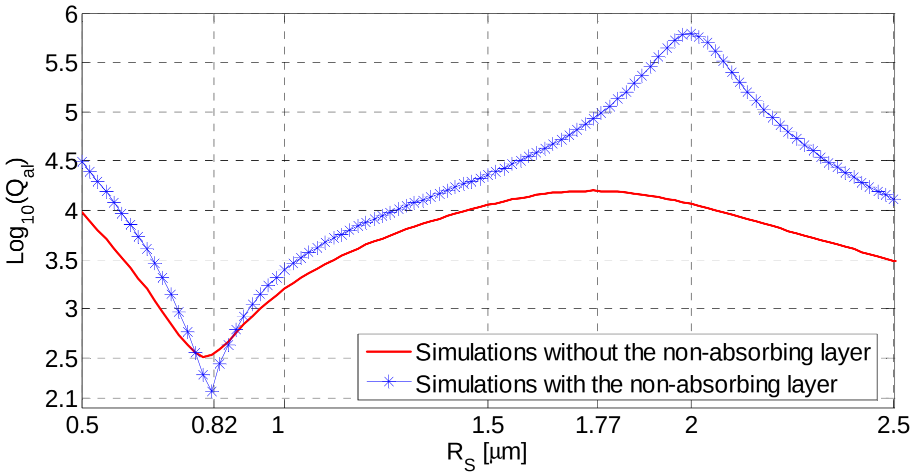

Figure 69: Comparison between HDS-based simulations with and without the non absorbing layer included. R_D = 15 μm, T_D = 3 μm and H_S = 0.5 μm; disk and stem material is Polysilicon (E = 160 GPa, ρ = 2230 Kg/m^3, ν = 0.226) for a resonance frequency of the first contour mode about 184 MHz, independently on R_S. Substrate material was assumed to be silicon, with material properties equal to the ones of stem and substrate

Thus the comparison between simulations and measurements from [37] does not lead to any clear solution about the necessity of including or not the non-absorbing layer. Something more about it can be concluded by comparing HDS/PML-based simulation with the simulation model employing theoretical boundary conditions (THBC) at the stem/substrate interface, but first it is mandatory to consider the effect of the relaxation time τ defined in (119) on the results of THBC-based simulations.

It is again important to notice that unlike the parameters β and σ used in HDS and PML strategies, the parameter τ corresponds to the *actual* substrate damping, if the intrinsic damping of the substrate can model as a viscoelastic dissipation according to Kelvin-Voigt model as in Eq. (119). It is not an artificial parameter included to obtain the total absorption of the wave propagating in the substrate, using a finite domain and it can be measured or theoretically evaluated. More complicated model than Kelvin-Voigt's can be used employing more time constants [34], to obtain a more accurate model of substrate intrinsic damping.

In order to evaluate the effect of τ on the curve $Q_{al}(R_S)$ simulations with different τ were performed for a polysilicon (E = 160 GPa, ρ = 2230 Kg/m^3, ν = 0.226) disk resonator with fixed disk radius R_D = 15 μm, disk thickness T_D = 3 μm, and stem height H_S = 0.5 μm, changing the stem radius R_S from 0.5 µm to 3 µm. The substrate material is assumed to be homogenous silicon with material properties approximately equal to the polysilicon used to fabricate the disk and stem. Resonance frequency is about 184 MHz.

Parameter τ was varied in the range 10-200 fs even if an evaluation of this parameter suggests a τ about 1 fs, if thermoelastic and phonon-phonon dissipation are considered according to formulas in [93] and [94]. This choice can be justified because there could be some other mechanisms contributing to internal losses, which can increase τ, thus the estimated relaxation time is probably a "best case". Second for very small τ, lower than 1 fs, some numeric instability affect the results, and can be only removed by taking more mesh point to calculate the integral in (116), resulting in very long time of computation.

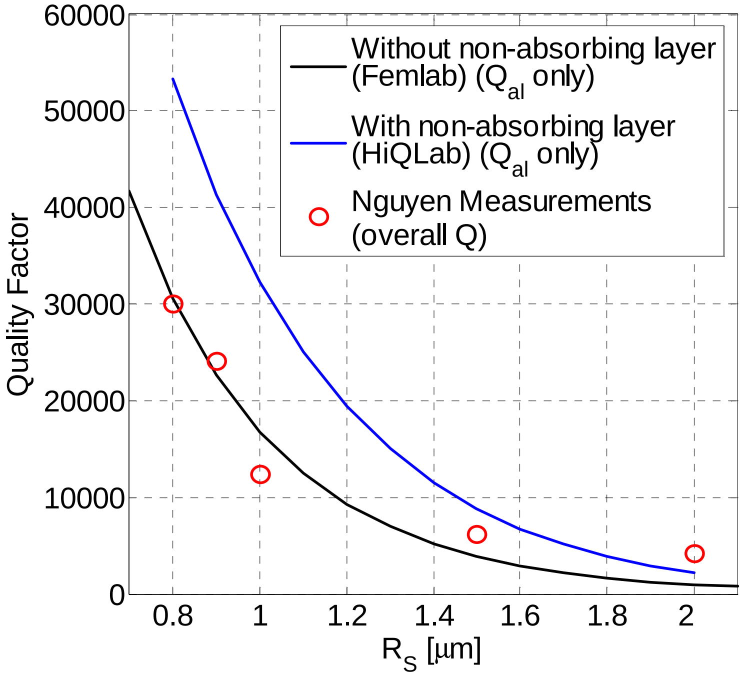

Figure 70: Comparison between experimental data from [37] and both HDS-based simulations without the non-absorbing layer and PML-based simulations with NAL included. R_D = 18 μm, T_D = 2.1 μm and H_S = 0.35 μm; disk and stem material is Polysilicon (E = 150 GPa, ρ = 2300 Kg/m^3, ν = 0.226) for a resonance frequency of the first contour mode about 150 MHz, independently on R_S. Substrate material was assumed to be silicon, with material properties equal to the ones of stem and substrate.

On the other hand, according to the simulations in Figure 71, for $\tau < 100\ fs$ the curves $Q_{al}(R_S)$ do not change anymore if the relaxation time is decreased. It means that for value of τ lower than 100 fs the substrate damping does not affect the simulations results, or, in other words, the only mechanism which influences the quality factor is the dissipation through anchor losses. If τ is 1 fs, as estimated considering thermoelastic and phonon-phonon dissipation in the substrate, the device works in a condition of anchor losses-dominated energy dissipation.

If a comparison between the THBC-based simulations and PML/HDS based simulations is carried out, the value of substrate relaxation time results fundamental to affirm the need of including or not the non-absorbing layer.

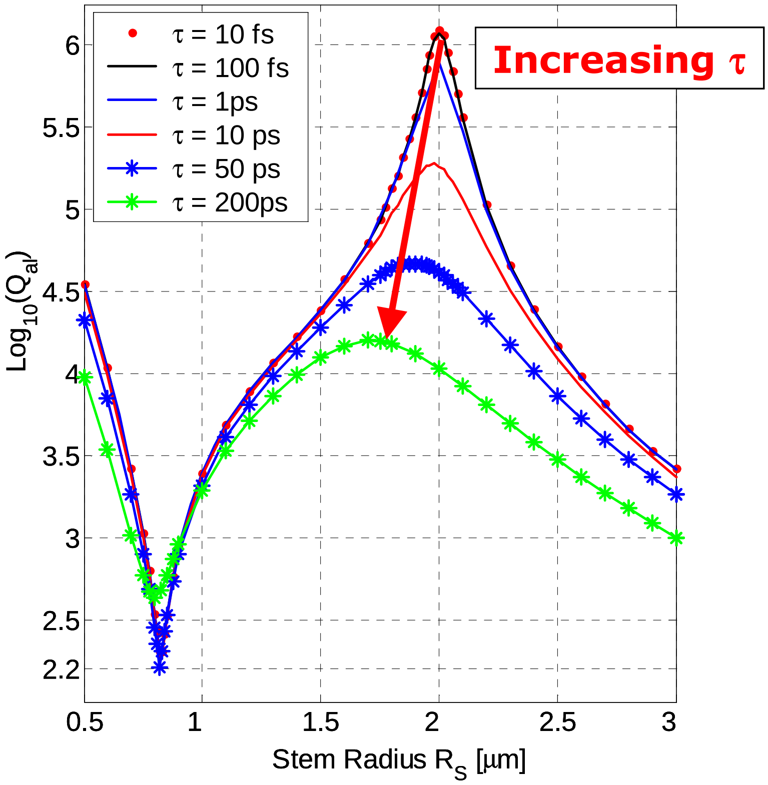

Figure 71: Dependence of quality factor only due to anchor losses on stem radius with parametric viscoelastic relaxation time τ, varying from 10 fs to 200 ps. Disk and stem material was considered to be polysilicon (E = 160 GPa ρ = 2230 Kg/m^3 and ν = 0.226), while the substrate was assumed to be made of homogeneous silicon (approximately with the same material properties of polysilicon). Disk radius is fixed to 15 μm, disk thickness to 3 μm and stem height to 0.5 μm, resulting in a resonance frequency of about 184.5 MHz. All the simulations were carried out implementing the THBC-based method in Femlab.

Considering again a disk with radius R_D = *15 μm*, thickness T_D = *3 μm*, and stem height H_S = *0.5 μm*, made of polysilicon, it was found that until $\tau > 50$ *ps* results for the dependence of Q_{al} on the stem radius R_S, given by the simulations based on THBC model, agree with results obtained employing HDS/PML model, without non-absorbing layer (NAL) included (Figure 72). Specifically for the HDS model the agreement is obtained if $\tau = \beta$. The result is not surprising because it is possible to find that β and τ represent exactly the same kind of intrinsic damping, i.e. a viscoelastic damping increasing with the material stiffness. The only difference is that while τ can be considered as the real relaxation time of the structure, β was a relaxation time increased to a value high enough to obtain the total absorption of energy in the simulated portion of substrate, but not to high in order to avoid spurious reflections.

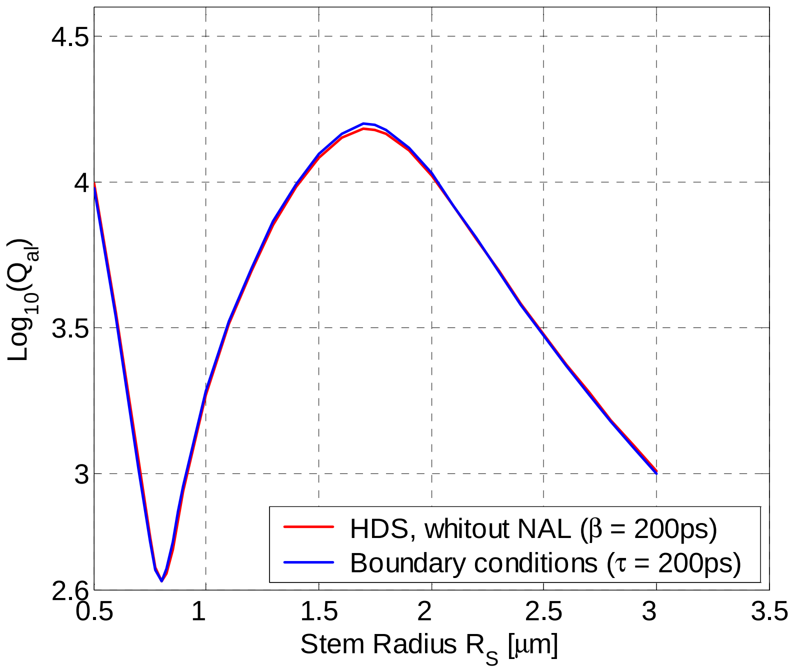

Figure 72: Comparison between THBC-based model (blue line) and HDS-based model without non-absorbing layer included (red line), with respect to the dependence of Q_{al} on the stem radius, with $\tau = \beta = 200$ ps. Disk and stem material was considered to be polysilicon (E = 160 GPa ρ = 2230 Kg/m^3 and ν = 0.226), while the substrate was assumed to be made of homogeneous silicon (approximately same material properties of polysilicon). Disk radius is fixed to 15 μm, disk thickness to 3 μm and stem height to 0.5 μm, resulting in a resonance frequency of about 184.5 MHz.

Thus the equivalence between the results in Figure 72, can be interpreted as a proof that when the relaxation time of the material the substrate is made of is higher than 50 ps a propagating acoustic wave at 184.5 MHz (resonance frequency of the simulated device) is totally absorbed in a portion of substrate equal to the portion of substrate included in the HDS based simulations (i.e. a cylinder of radius 60 μm and height 60 μm, with respect to results in Figure 72).

But if $\tau < 1\ ps$ THBC model agrees with HDS/PML with non-absorbing layer included (Figure 73). It can be reasonable because in this case it is necessary to set a damping much higher than the real one (i.e. $\beta >> \tau$) to obtain the total absorption in a small domain, using HDS/PML model. But this damping has to be raised to high value gradually to avoid spurious reflections and to have a more accurate model for the substrate where the higher deformation are expected, that is, close to the stem/substrate interface.

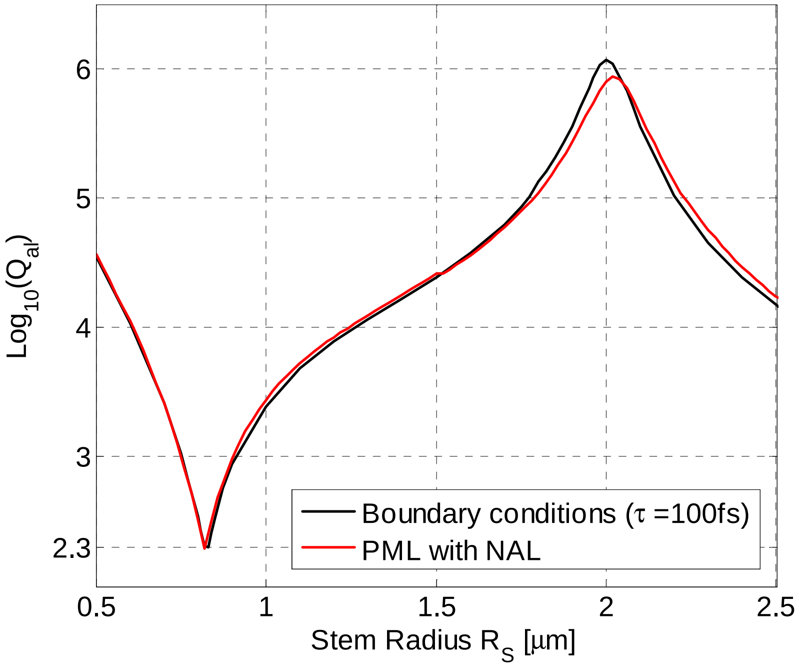

Figure 73: Comparison between THBC-based model (blue line) with $\tau = 100$ fs and PML-based model with non-absorbing layer included (red line), with respect to the dependence of Q_{al} on the stem radius. Disk and stem material was considered to be polysilicon ($E = 160$ GPa, $\rho = 2230$ Kg/m^3 and $\nu = 0.226$), while the substrate was assumed to be made of homogeneous silicon (approximately same material properties of polysilicon). Disk radius

is fixed to 15 μm, disk thickness to 3 μm and stem height to 0.5 μm, resulting in a resonance frequency of about 184.5 MHz.

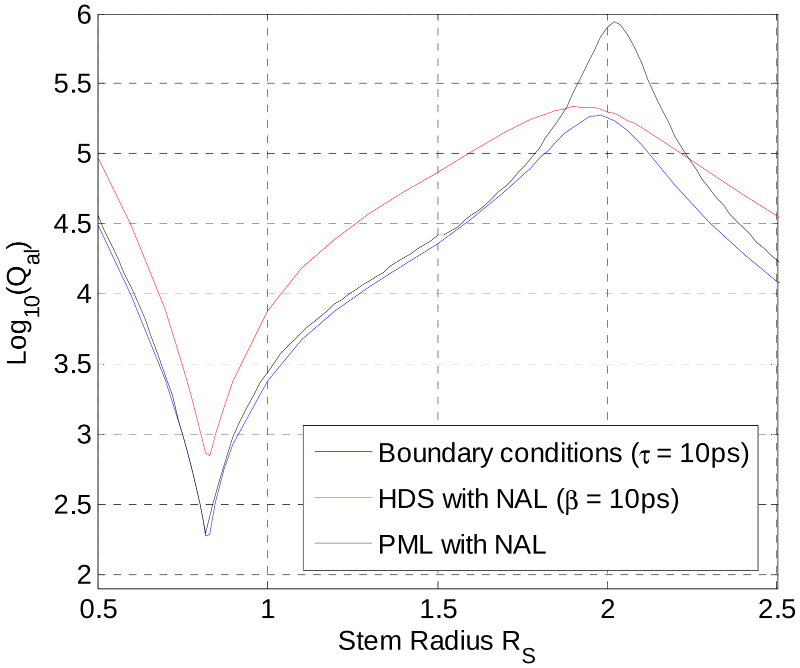

Figure 74: Comparison among THBC-based model(blue line), HDS-based model without non-absorbing layer included (red line) and PML with non-absorbing layer included (black line), with respect to the dependence of Q_{al} on the stem radius, with τ = β = 10 ps. Disk and stem material was considered to be polysilicon (E = 160 GPa, ρ = 2230 Kg/m^3 and ν = 0.226), while the substrate was assumed to be made of homogeneous silicon (approximately same material properties of polysilicon). Disk radius is fixed to 15 μm, disk thickness to 3 μm and stem height to 0.5 μm, resulting in a resonance frequency of about 184.5 MHz.

Finally, for *1 ps* < τ < *50 ps*, the HDS/PML model is different from the THBC one if both non-absorbing layer is included or not (Figure 74).

Thus THBC-based model solve the problem about the opportunity of including or not NAL in HDS/PML-based model in order to obtain the more accurate results. By the comparisons between HDS/PML-based model and THBC model it is now clear that non-absorbing layer is necessary when the substrate damping is low, while it can be removed when the damping is high. Besides, there is a relaxation time interval where the HDS/PML cannot give the same results as THBC model, neither with nor without non-absorbing layer. THBC model (with $\tau = 100\ fs$) was compared also with HDS/PML model (non-absorbing layer included) for some SiGe disks ($E = 137\ GPa$, $\rho = 3430\ Kg/m^3$, $\nu = 0.23$) with disk thickness $T_D = 2\ \mu m$ and disk height $H_S = 1\ \mu m$ (the substrate is assumed to be made of silicon). This values correspond to the one obtained by particular process flow used to fabricate the devices at IMEC. In Figure 75, the dependence of Q_{al} stem radius is represented with disk radius $R_D = 10\ \mu m$ (resonance frequency about 207 MHz). In this case the agreement between THBC and HDS model with non-absorbing layer included, is still good even if there is a little difference in the curve $Q_{al}(R_S)$ around the maximum. This could be due to the fact that the maximum amplitude is very huge according to HDS, which means probably that for $\tau = 100\ fs$ the intrinsic damping is still important and limits the maximum amplitude. On the other hand the mismatch could be also due to some numeric error in THBC and/or HDS model for such low damping.

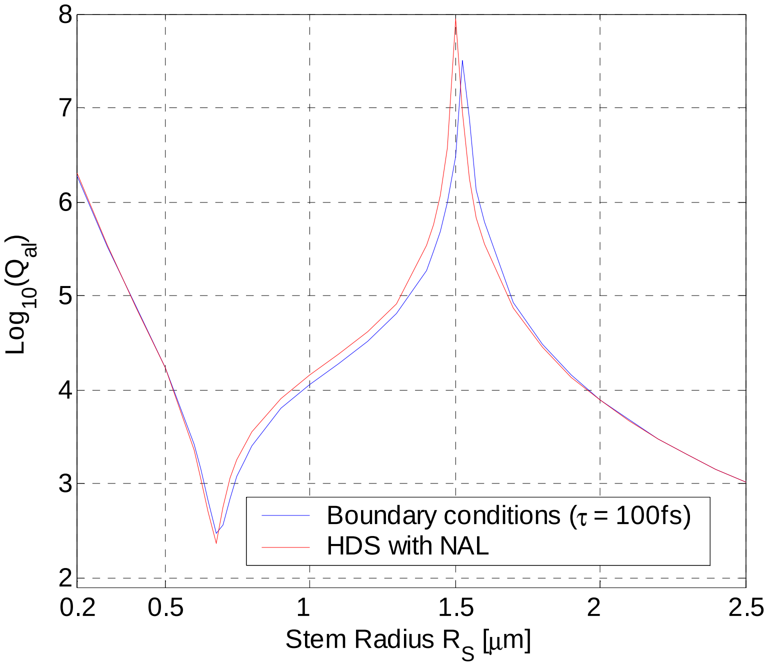

Figure 75: Comparison between THBC-based model (blue line) with $\tau = 100$ fs and HDS-based model with non-absorbing layer included (red line), with respect to the dependence of Q_{al} on the stem radius. Disk and stem material was considered to be SiGe ($E = 137$ GPa $\rho = 3430\ Kg/m^3$ and $\nu = 0.23$), while the substrate was assumed to be made of homogeneous silicon (approximately same material properties of polysilicon). Disk radius is fixed to 10 μm, Disk thickness to 2 μm and stem height to 1 μm, resulting in a resonance frequency of about 207 MHz.

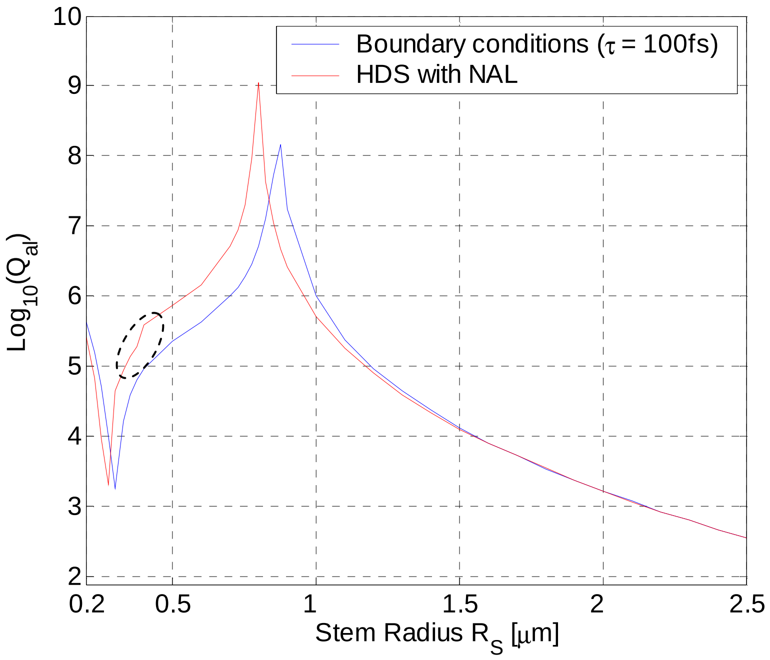

Figure 76: Comparison between THBC-based model (blue line) with τ = 100 fs and HDS-based model with non-absorbing layer included (red line), with respect to the dependence of Q_{al} on the stem radius. Disk and stem material was considered to be SiGe (E = 137 GPa, ρ = 3430 Kg/m^3 and ν = 0.23), while the substrate was assumed to be made of homogeneous silicon (approximately same material properties of polysilicon). Disk radius is fixed to 9 μm, Disk thickness to 2 μm and stem height to 1 μm, resulting in a resonance frequency of about 230 MHz. A sharp change of slope in the HDS simulation with NAL is circled by a black dashed line.

In Figure 76 the difference is even higher ($R_D = 9\ \mu m$ for a resonance frequency about 230 MHz), with even a shift in the minimum position, but in this case it is possible to conclude that the wrong results come from the HDS model: first because of the sharp step (almost a discontinuity), circled in the figure, second because including in the simulation the thermoelastic damping (see section 3.6.4), the agreement between HDS and THBC is complete. In the specific if the thermoelastic damping is included in the HDS model the minimum position shifts, which is a nonsense, because as it will be shown in the following the minimum is due to the superposition between resonance frequencies of the contour mode and a parasitic bending mode, and according to the theory the intrinsic damping of the resonator material should not influence the resonance frequency of the bending mode (see section 3.5).

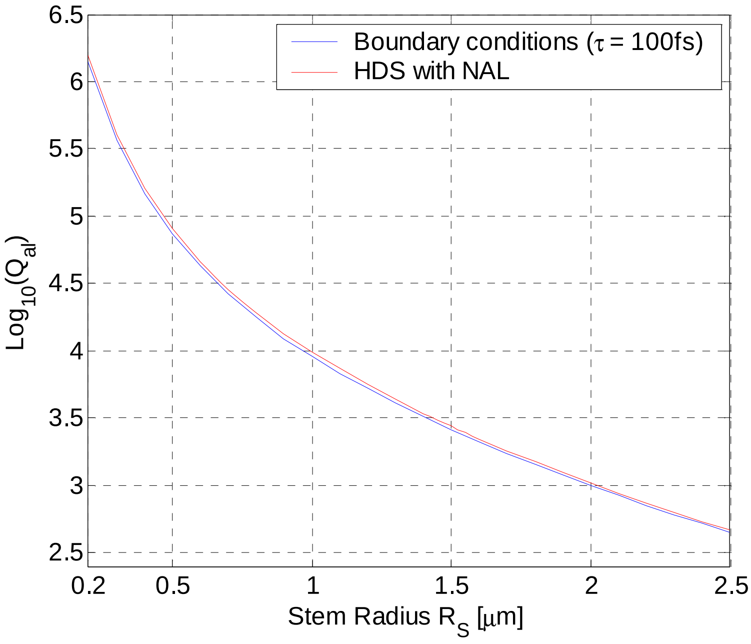

Figure 77: Comparison between THBC-based model(blue line) with $\tau = 100$ *fs and HDS-based model with non-absorbing layer included (red line), with respect to the dependence of* Q_{al} *on the stem radius. Disk and stem material was considered to be SiGe (E = 137 GPa,* $\rho = 3430$ *Kg/m*^{3} *and* $\nu = 0.23$*), while the substrate was assumed to be made of homogeneous silicon (approximately same material properties of polysilicon). Disk radius is fixed to 10* μm*, disk thickness to 4* μm *and stem height to 1* μm*, resulting in a resonance frequency of about 207 MHz.*

A last comparison between HDS and THBC method is presented in Figure 77 (disk material SiGe, substrate material Silicon, $T_D = 4\ \mu m$, $H_S = 1\ \mu m$, $R_D = 10\ \mu m$, R_S variable from 0.2 µm to 2.5 µm (resonance frequency about 207 MHz). The agreement this time is perfect, and it is always very good when there is neither a maximum nor a minimum in the curve $Q_{al}(R_S)$: in this case it is possible to conclude that there are no accuracy problems for both the HDS-based and THBC model.

Besides the greater accuracy shown with respect to HDS/PML methods, the model based on the theoretical boundary conditions allow also a deep insight of the anchor loss mechanism: as shown in the previous section it can be used to explain anchor losses with the creation of evanescent waves in the substrate. Besides it could be used to evaluate which stress component is the more important to evaluate the anchor losses, among the stress components acting on the interface. These components are the shear stress $\sigma_{rz}(r,0)$ and the compressive stress $\sigma_{zz}(r,0)$. To evaluate their respective effect on the anchor losses, results of a complete THBC-based simulation are compared with the results given by the same simulation performed by setting $A_{RR} = A_{ZR} = 0$, so that simulation results become independent on $\sigma_{rz}(r,0)$. The comparison is shown in Figure 78: the difference is small but very important because excluding shear stress changes significantly the maximum position which is a fundamental results of the simulation, since identify the stem radius which can be chosen to minimize the anchor losses. Anyway apart from the maximum region the contribution of shear stress is negligible.

To summarize the comparison between the three discussed simulations mode it is possible to say that PML-based simulations and HDS-based simulations basically agree. Also their agreement with some measurements from [37] is good.

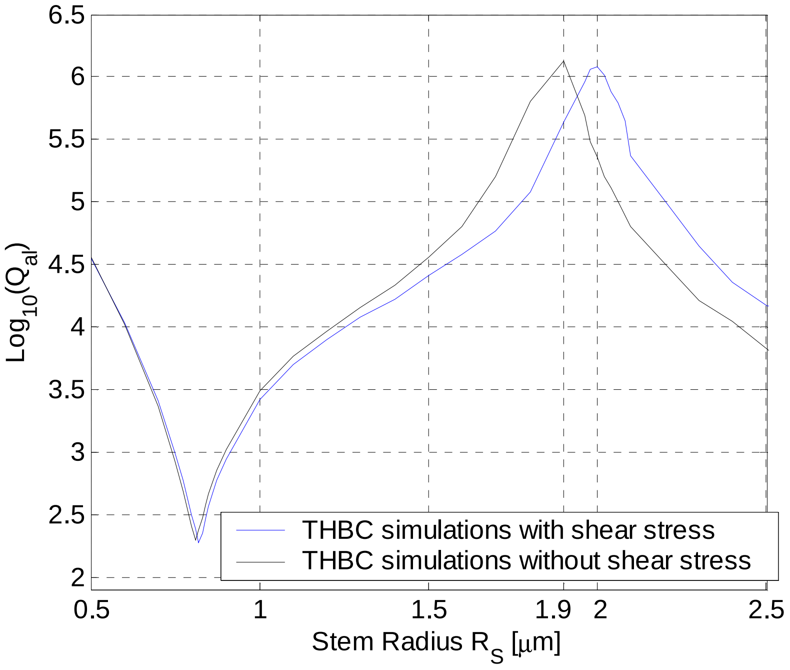

Figure 78: Dependence of Q_{al} on the stem radius according to THBC-based simulations compete, when the effect of the shear stress at the stem/substrate interface is considered (blue line) and when it is neglected (black line); $\tau = 100$ fs in both the cases. Disk and stem material was considered to be Polysilicon ($E = 160$ GPa, $\rho = 2230$ Kg/m^3 and $\nu = 0.226$), while the substrate was assumed to be made of homogeneous silicon (approximately the same material properties of polysilicon). Disk radius is fixed to 15 μm, disk thickness to 3μm and stem height to 0.5 μm, resulting in a resonance frequency of about 184 MHz. The curves are less regular than in the previous figure because a rougher mesh is used for both the FEM analysis both to calculate the integrals in (116).

THBC-based model confirm substantially results form HDS-based method and PML-based method, allowing to draw the conclusion that non-absorbing layer is necessary if the real damping of the substrate is small.

The main advantage provided by THBC-model is the great insight and consequently the chance of a better understanding of the physical mechanism which determine the anchor losses

Besides THBC model avoids spurious parameters as PML/HDS size, parameters β and σ, or the size of the size of non-absorbing layer. It introduces the real relaxation time τ of the substrate, which can be fundamental parameter to evaluate the quality factor of the device and can be even measured and/or estimated.

Moreover in some cases, it seems that THBC-based simulations give more accurate results than HDS/PML-based model, as in the case of results in Figure 76, or for a substrate relaxation time neither too small nor too high.

The main drawback of THBC-based method is unluckily given by the velocity of simulations: while to calculate the quality factor for a specified geometry the HDS/PML-based model needs 15-30 sec., the THBC-based model needs 50 seconds when a rough mesh is used (Figure 78) and even 4 minutes, when a fine mesh is used (all the other figures). This is due to the sharp peak in the coefficient A_{IJ}, which leads to the necessity of using a very large amount of points around the peak, in order to evaluate numerically the integrals in (116). Maybe a more efficient algorithm to find the inverse Hankel transform is needed to obtain faster simulations with THBC method.

Due to this last drawbacks in the following HDS-based or PML-based simulations will be generally presented. THBC-method can be still used to verify results from the other two methods when results are suspected to be inaccurate as in the case of results in Figure 76.

3.4 Dependence of quality factor due to anchor losses on disk and stem dimensions

In this section results about the dependence of anchor losses on stem radius and height as well as on disk radius and thickness, will be discussed for a contour mode disk resonator, resonating on its first mode. The dependence on the disk thickness has not been investigated too much, because a discussion about it was already done in [55].

All the results presented in this section were extracted from PML-based or HDS-based simulations, with non-absorbing layer included, i.e. the relaxation time of the substrate was assumed to be small (less than 1 ps according to the THBC-based simulations presented in the previous section).

3.4.1 Dependence on the stem radius (or anchor size)

As shown by the results in the previous section curves $Q_{al}(R_S)$ can monotonically decrease (Figures 70 and 77) or can have a minimum and a maximum for particular values of stem radius (Figures 68, 75 or 76). It is an unexpected behaviour, which was never observed by measurements, but which seems to be very probable because it is predicted by all the three different simulation strategies compared in the previous section.

Generally it is assumed that curves $Q_{al}(R_S)$ should monotonically decrease because the larger is the stem/substrate interface, the larger amount of energy can be lost through the anchor [37]. Also the theoretical model presented in [58] seems to confirm this observation, but the assumptions made on the stress distribution at the anchor are very strong and could exclude some cases.

The presence of the minimum is due to the superposition of a parasitic bending mode to the contour mode as it can be found by in the deflected shape of the disk at the resonance, when the quality factor is minimum (Figure 79). Indeed the disk bends whatever is the stem radius, but at the minimum the bending is maximum, because probably the resonance frequency of the bending mode equals the resonance frequency of the contour mode for that particular stem radius. The resonance frequency of the contour mode does not depend on stem radius as shown by Eq. (78) and by results from FEM modal simulations (Figure 80), but the resonance frequency of bending modes does. The dependence of resonance frequency of the bending mode, even if not straightforward can be modelled as shown in section 3.5. Anyway it is possible to observe that a higher stem radius makes the disk more rigid with respect to the bending: from FEM simulations bending mode resonance frequency increases if stem radius increases (Figure 80). The interference of the bending mode with the contour mode was discussed also in [55], where a minimum was observed in the dependence of the quality factor on the disk thickness. The model in [58] cannot predict the minimum because neglect the possibility of disk bending. The strict connection with the parasitic bending mode is confirmed by the small influence of shear stress at the stem/substrate interface on the anchor losses, as shown in 3.3. The compressive stress and the consequent compressive wave is the main source of anchor losses and both compressive stress and wave are very high when the disk bending is high, because when the disk bends the stem goes up and down (Figure 79) and subsequently drives a high compressive stress at the stem/substrate interface.

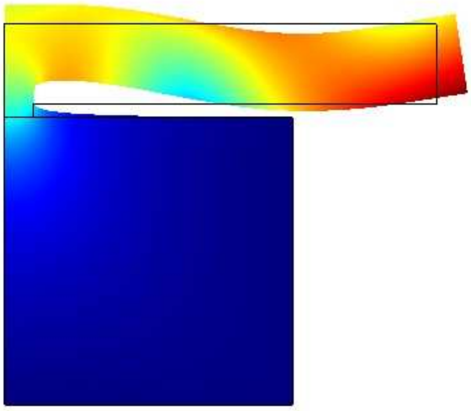

Figure 79: *Typical coupling of a contour mode with a bending mode, near to the minimum of a curve* $Q(R_S)$*. The simulation was done in Femlab, using the geometrical dimensions and material properties by which the minimum in Figure 68 is obtained.*

The maximum in the curves $Q_{al}(R_S)$ is probably due to the equilibrium by the two different effects of an increase of the stem radius, for values higher than the minimum: increasing the stem the difference between the resonance frequency of the contour mode and of the bending mode increases, but also the section through which the energy can be lost enlarges.

The first effect leads to a raise of Q_{al}, while the second would decrease it. Thus Q_{al} increases as long as the first effect prevails on the second, then, after the maximum, it decreases. The maximum occurs when the two effect are equals.

The presence of a maximum and a minimum in the curves $Q_{al}(R_S)$ is not only a novelty with respect to what is generally believed, but it is also very important for the design of the device: it is possible to maximize the quality factor by choosing a proper stem radius. The stem radius should be not necessary as small as possible to maximize the quality factor, so that there is no need to complicate the technological process in order to reduce the minimum stem radius which can be obtained.

Stem radius is a layout parameter and thus it can be changed by simply change the device layout without modifying the process: this is very important because as it will be shown in the following the maximum position in the curve $Q_{al}(R_S)$ depends on the disk radius, and consequently on the resonance frequency of the device, according to (78). Thus for each resonance frequency a different stem radius is needed to maximize the quality factor and it is consequently very important the possibility of changing it by layout.

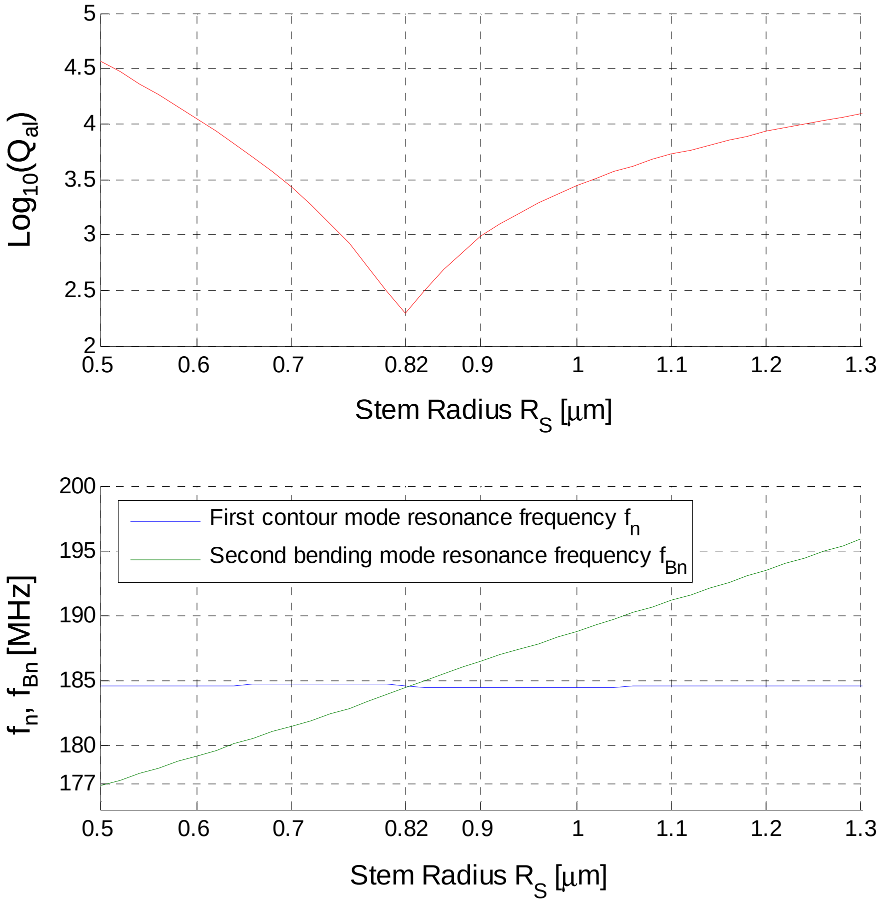

Figure 80: *Simulation of the quality factor dependence on stem radius (upper chart) and simulation of the dependence of the resonance frequencies on stem radius of the first contour mode and of the second bending mode (lower chart).* $R_D = 15\ \mu m$, $T_D = 3\ \mu m$ *and* $H_S = 0.5\ \mu m$; *disk, stem and substrate material Polysilicon (*$E = 160$ GPa, $\rho = 2230$ Kg/m^3, $\nu = 0.226$*).*

3.4.2 Dependence on the stem height

The stem can be in first approximation considered as beam, which is alternately compressed and extended when the disk bends (Figure 79). Since the coupling of the contour mode with a bending one has been identified as the main cause of anchor losses increase, it is possible to choose a proper value of the stem height H_S in order to obtain an acoustical impedance transformation, so that the energy transferred from the stem to the substrate is minimized; this “impedance matching” can be achieved by transforming the condition of free end (zero acoustical impedance) at a distance H_S from the substrate, i.e. where the stem is connected to the disk, to a condition of clamped end (infinite acoustical impedance) at the stem/substrate interface.

While changing stem radius is possible to reduce the bending of the disk, by avoiding the contour and the bending mode resonate at the same frequency, a change in the stem height does not hinder the bending resonance, but avoid the transfer of energy. From the equation of acoustic wave propagation in bar under compression:

$$\rho \frac{\partial^2 w}{\partial t^2} = E \frac{\partial^2 w}{\partial x^2} \tag{120}$$

it is possible to find that the length to obtain that the bar resonates on its first clamped-free mode, at same frequency f_1 of the disk is [31]:

$$L_m = \frac{1}{4 f_1} \sqrt{\frac{E}{\rho}} \tag{121}$$

where E is the Young’s modulus and ρ the mass density of the stem material. Eq. (121) represents a $\lambda/4$ adaptation: a bar under compression is indeed ruled by a law analogous to the one ruling electrical transmission lines, if the compressive force replaces the voltage and the velocity the current ($\sqrt{E/\rho}$ is the velocity of the wave).

The main limit of this strategy is that the stem height is given by a layer thickness and thus is process parameter: it means that for each resonance frequency the process should be changed in order to maximize the quality factor only due to anchor losses.

Furthermore, another big problem is that the needed L_m is generally too high: considering a polysilicon stem ($E = 160\ GPa$, $\rho = 2230\ Kg/m^3$) L_m has to be 4.24 μm for f_1 = 500 MHz and 21.12 μm for f_1=100 MHz. More reasonable values can be obtained for resonance frequency higher than 1 GHz: in this case L_m becomes lower than 2 μm. For lower resonance frequencies anyway it seems that the stem height should be to be as high as possible in order to as close as possible to L_m. Alternatively according to Eq. (121) the $\lambda/4$ adaptation can be used for low-frequency resonators if materials stiffer and/or lighter than polysilicon are used for the stem.

According to the simulations the solution is not so easy. In Figure 81 a simulation of Q_{al} dependence on the stem height H_S with parametric stem radius is represented, for a contour mode resonator made of polysilicon and with disk radius R_D = *15 μm*, disk thickness T_D = *3 μm* (resonance frequency 184.5 MHz, not dependent on stem height). From the theory the quality factor is expected to increase monotonically until the maximum, which is obtained if $H_S = L_m$ (about 11.5 μm). According to the simulation the curve for R_S = *0.5 μm* is almost like the one expected monotonically increasing and reaching a maximum for value very close to L_m. For higher values of R_S the maximum still occurs for $H_S = L_m$, but Q_{al} is not monotonic anymore: there is first and unexpected minimum (for H_S = *1.35 μm*). For R_S = *2.02 μm* there is even a very high maximum before the minimum and the theoretical maximum for $H_S = L_m$ disappears. These unexpected behaviours occur because the beam cannot be considered slender anymore if its height is comparable with is base radius and because also stem height affects the resonance frequency of the parasitic bending mode (see section 3.5).

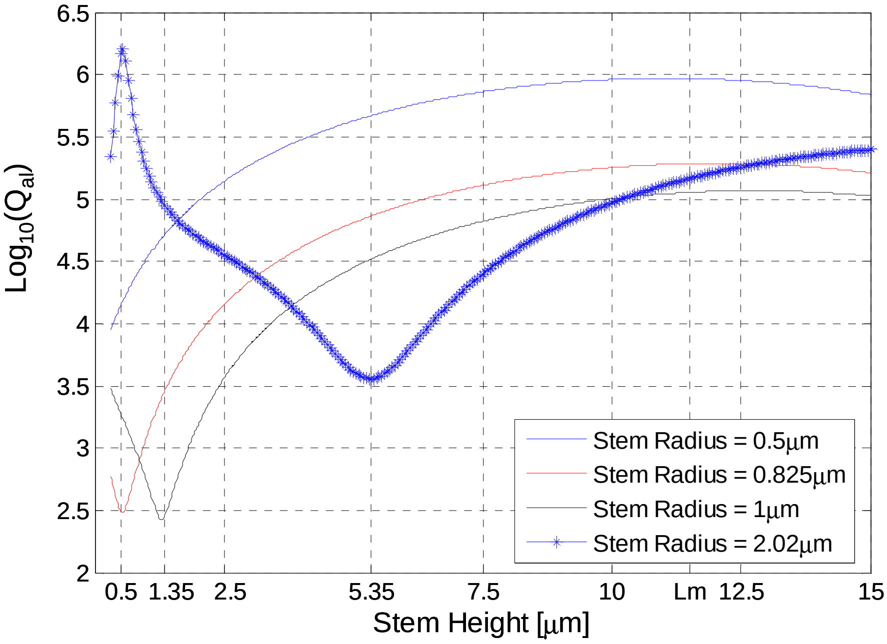

Figure 81: HDS-based *simulations of the dependence of* Q_{al} *on the stem height with parametric stem radius for a contour mode disk resonator, resonating on its first contour mode with parametric stem radius; non absorbing layer is included,* R_D *= 15 μm,* T_D *= 3 μm; disk, stem and substrate material Polysilicon (E = 160 GPa, ρ = 2230 Kg/m*^{3}*, ν = 0.226).*

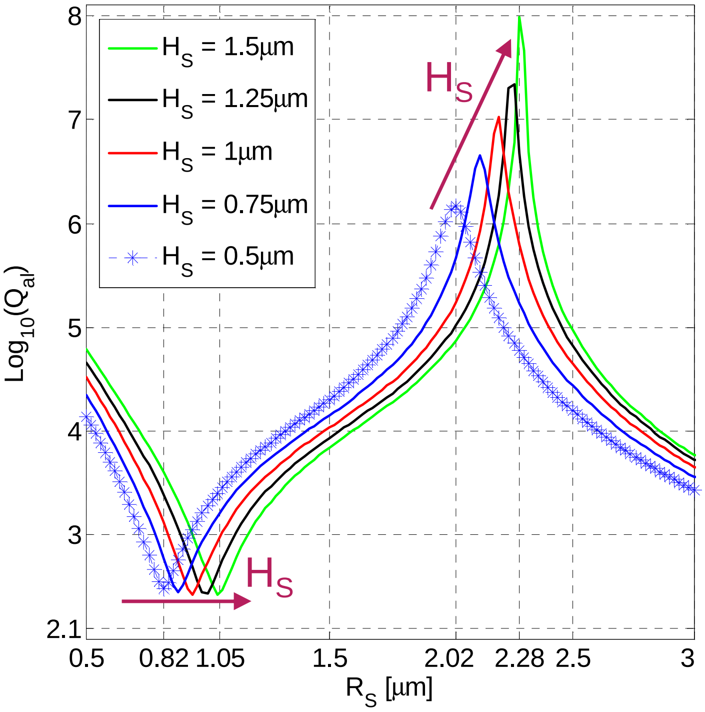

Figure 82: HDS-based simulations of the dependence of Q_{al} on the stem radius for a contour mode disk resonator, resonating on the first mode, with parametric stem height; non-absorbing layer is included, R_D = 15 µm, T_D = 3 µm; disk, stem material is polysilicon (E = 160 GPa, ρ = 2230 Kg/m^3, ν = 0.226), while the substrate is considered as made of silicon with properties similar to the polysilicon.

Other simulations have been carried out to see the influence of a stem height change on the curves $Q_{al}(R_S)$. The goal of these simulation was to consider the influence of a variation of stem height on the position of the maximum $Q_{al}(R_S)$: the stem radius which give the maximum in curve $Q_{al}(R_S)$ can be chosen to maximize the quality factor only due to anchor losses, but the choice could be not the best one if there is variation of disk thickness, stem height and/or material properties of both stem and disk, which can change from chip to chip, or inside the same chip, due to a dispersion in process parameters. Thus, if the change of maximum position in a the curve $Q_{al}(R_S)$ due to a change of H_S is evaluated, it is possible to estimate the "robustness" of the anchor losses minimization with respect to stem height variations.

In Figure 82 some curves $Q_{al}(R_S)$ with different stem height H_S and extracted by HDS-based simulations with NAL included are plotted, while in

Figure 83 the same curves with are evaluated by a HDS-based simulation without non-absorbing layer: apart from the different shape of the curves, in both the cases the effect of an increase in stem height is both on the position of the minimum, which shift towards higher values of the stem radius R_S, and on the position and on the value of the maximum, which shift also towards higher R_S and increases its value. The most important information from Figures 82 and 83 is that choosing R_S in order to maximize Q_{al} with a nominal H_S for example equal to 1 µm, the validity of this choice holds enough even if there are a great dispersion of the process ($\pm 0.5\mu m$) on the value of H_S; furthermore, an error on the value of H_S leads to a decrease of the Q much smaller than the same error on R_S, so that it is possible to conclude that stem height is not a too critical parameter.

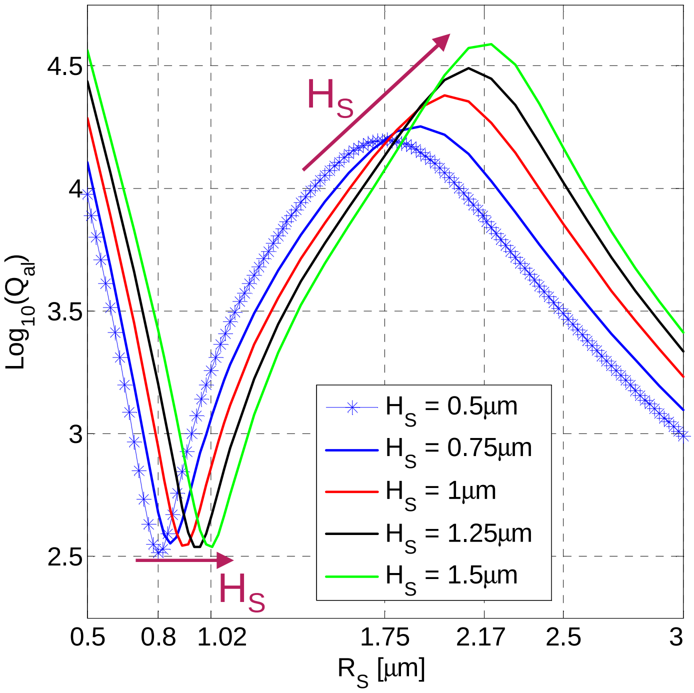

Figure 83: HDS-based simulations of the dependence of Q_{al} on the stem radius for a contour mode disk resonator, resonating on the first mode, with parametric stem height; non absorbing layer is not included, R_D = 15 μm, T_D = 3 μm; disk and stem material is polysilicon (E = 160 GPa, ρ = 2230 Kg/m^3, ν = 0.226), while the substrate is considered as made of silicon with properties similar to the polysilicon.

3.4.3 Dependence on the disk radius and thickness

Like a stem height variation also a change of disk radius and/or disk thickness can change the profile of curves $Q_{al}(R_S)$. If the radius and/or the thickness of the disk in the fabricated device are different from the nominal ones, their variation can affect the maximum position in curves $Q_{al}(R_S)$.

An investigation into the effect of the thickness on Q_{al} in contour mode disk resonator has been already presented in [55], where it was shown by PML-based simulations that there was a minimum in the dependence of Q_{al} on the thickness. This minimum is due to a parasitic bending mode which interferes with the contour mode. Changing the disk thickness the contour mode resonance frequencies do not change according to (78) if the disk is thin, while the resonance frequencies of the bending modes are affected by the disk thickness. Considering a free disk, i.e. neither connected to a substrate through a stem nor at the end, the resonance frequencies of bending modes is found by solving the following equation [96]:

$$\rho \frac{\partial^2 w}{\partial t^2} = \frac{E \cdot T_D^2}{12\left(1-\nu^2\right)\rho} \nabla_c^2 \left(\nabla_c^2 w\right) \tag{122}$$

where w is the deflection in z direction while E is the Young's modulus, ρ is the material density and ν the Poisson; T_D is the thickness of the disk and ∇_c^2 is the scalar Laplacian in cylindrical coordinates:

$$\nabla_c^2 w = \frac{\partial^2 w}{\partial r^2} + \frac{1}{r}\frac{\partial w}{\partial r} + \frac{1}{r^2}\frac{\partial^2 w}{\partial \theta^2} + \frac{\partial^2 w}{\partial z^2} \tag{123}$$

If the disk is thin enough it is possible to consider the deflection as constant and equal to the deflection of the neutral plane (similar to the assumption done to find the Bernoulli equation for slender beam), so that $\partial^2 w / \partial z^2 = 0$. Furthermore, if the resonance mode is axisymmetric (as for the bending mode coupled with our contour mode), also $\partial^2 w / \partial \theta^2 = 0$ is satisfied. If these assumptions hold it is possible to find the resonance frequency of the bending disk from (122), in a similar way to what done to find the resonance frequency of disk contour modes or bending beams:

$$f_{Bn} = \frac{1}{2\pi}\left(\frac{\lambda_{Bn}}{R_D}\right)^2 \sqrt{\frac{E}{12\left(1-\nu^2\right)\rho}} \cdot T_D \tag{124}$$

where λ_{Bn} is the nth eigenvalue, which depends on the boundary conditions on the edge of the disk ($r = R_D$); if the disk is free at its ends, the radial bending moment M_r, as well as the shear transverse force Q_r, has to be zero at the edge. The expressions for M_r and Q_r can be found in many mechanics book, for example in [97]:

$$M_r = \frac{ET_D^3}{12\left(1-\nu^2\right)}\left(\frac{\partial^2 w}{\partial r^2}+\frac{\nu}{r}\frac{\partial w}{\partial r}\right) \qquad Q_r = \frac{ET_D^3}{12\left(1-\nu^2\right)}\frac{\partial}{\partial r}\left(\frac{\partial^2 w}{\partial r^2}+\frac{1}{r}\frac{\partial w}{\partial r}\right) \tag{125}$$

Using the boundary conditions of free end the equation to find the eigenvalues λ_{Bn} is:

$$\frac{\lambda_{Bn} I_1\left(\lambda_{Bn}\right)}{\lambda_{Bn} I_0\left(\lambda_{Bn}\right)+2\nu I_1\left(\lambda_{Bn}\right)} = \frac{J_1\left(\lambda_{Bn}\right)}{J_2\left(\lambda_{Bn}\right)} \tag{126}$$

where J_1 and J_2 are the Bessel functions of first kind, of first and second order respectively, while I_1 and I_0 are the modified Bessel functions of first kind, of first and zero order.

According to Eq. (124) it is clear that the resonance frequency of bending modes is proportional to the thickness, thus changing it the resonance frequency of the parasitic bending mode can be forced to be close or far from the resonance frequency of the contour mode. Due to this effect also a maximum is expected in curves $Q_{al}(T_D)$, because there is probably one minimum for each parasitic bending mode and evidently a maximum should be between two consecutive minima.

Anyway maximizing the quality factor by choosing the optimum thickness is not efficient, because such optimum change if the contour mode resonance frequency changes and changing the process parameters each time to obtain different thickness of the disk layer is not a practical solution.

Also the disk radius affect the quality factor, because a certain value of disk radius can lead to a matching between the resonance frequencies of a contour mode and a bending mode, while another value can lead to a great difference to the two frequencies: according to (78) the resonance frequency of the contour mode is proportional to $1/R_D$ while the according to (124) f_{Bn} is proportional to $1/R_D^2$.

The disk radius cannot be used to separate the two resonance frequencies, because it has to be fixed in order to obtain the target resonance frequency, according to Eq. (78). Thus, the quality factor only due to anchor losses can be maximized in a contour mode disk resonator only choosing the proper value of the stem radius.

Nonetheless the value of disk radius can affect the curve $Q_{al}(R_S)$: an increase of the disk radius results in a shift of the minimum and of the maximum position towards higher values of stem radius. According to Eqs. (78) and (124), if the disk radius is enlarged, the resonance frequency of the contour mode is reduced less than the resonance frequency of the bending mode, so that for $R_S = 0$ the difference between the two resonance frequencies is higher and the stem radius has to be increased more than with a smaller disk radius to obtain the matching between the two resonance frequencies; in other words, as a consequence of the disk radius raise the curves in Figure 80 are both translated towards smaller frequencies, but the line corresponding to the bending mode shifts more than the other.

On the other hand due to the a big increase of the disk radius a higher order bending mode can shift to a frequency lower than the contour mode for $R_S = 0$ and a new couple minimum/maximum can be added to the curve $Q_{al}(R_S)$ for small stem radii.

A similar reasoning can be done for the thickness which has an important effect on the curve $Q_{al}(R_S)$, because as the disk radius affects the coupling between contour mode and bending mode and thus position of minimum and maximum in curves $Q_{al}(R_S)$.

3.5 A theoretical model to find the minimum in the curves $Q_{al}(R_S)$

Even if the estimation the stem radius which gives the maximum in curves $Q_{al}(R_S)$, is more important than the evaluation of the minimum position in order to optimize the layout of a disk resonator, it was not possible to find analytical formula to find the maximum, due to the complexity of the problem. Thus the maximum position can be estimated only by simulations.

On the other hand also the knowledge of the position of the minimum in curves $Q_{al}(R_S)$ gives some indications for the design: it allows to exclude from the possible design choice an interval of stem radii around the minimum; besides as shown in the previous section, a minimum in the curve $Q_{al}(R_S)$ has to be necessarily followed by a maximum, thus if the minimum position is known also a rough indication about the maximum position is available, reducing the number of simulations needed to find the maximum.

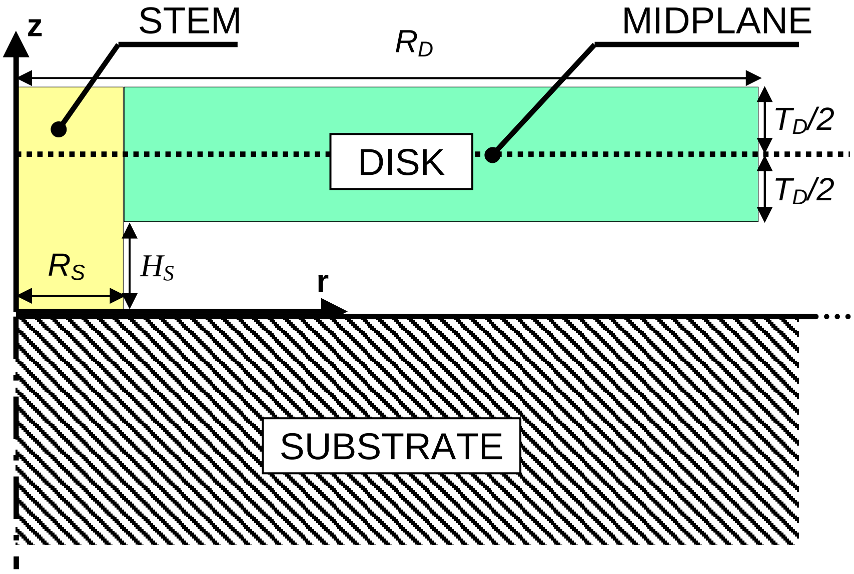

Figure 84: Radial cross section of the resonator, emphasizing the division in 3 domains of the device, made in order to estimate the resonance frequencies of the bending modes: the 'disk' in green, the 'stem' in yellow, the substrate in black and white.

Nonetheless also the evaluation of the minimum position is not easy, mainly due to the complexity of the calculation of the resonance frequencies of the disk bending modes, which are dependent not only on disk dimensions and material properties, but also on the stem and the substrate behaviour.

The minimum is obtained if the resonance frequencies of parasitic bending mode and contour mode are exactly equal. Thus the stem radius R_{Smin}, which leads to a minimum in the curves $Q_{al}(R_S)$, can be found by forcing the condition of equality between the two resonance frequencies. But according to (78) the resonance frequency of the contour mode is independent from stem radius. Eq. (78) is confirmed for FEM simulations, for stem radius smaller than $0.2R_D$: the maximum error found between results predicted by (78) and simulations is less than 1%, with respect to this range of stem radii.

Thus the problem is to find the dependence of resonance frequencies of the bending modes on the stem radius.

To find an approximated solution of the problem the disk, the stem and the substrate are first modelled separately as indicated in Figure 84 and then they are put together, by using proper boundary conditions at the interfaces between different domains. The “disk” is considered as a cylinder with a circular hollow of radius R_S in the centre (green region in Figure 84).

If the disk is moderately thick, its dynamic behaviour can be described by the following system of differential equations better than by (124) [98]:

$$\begin{cases} D\dfrac{\partial}{\partial r}\left(\dfrac{\partial \psi}{\partial r}+\dfrac{\psi}{r}\right)-\kappa^2 G T_D\left(\psi+\dfrac{\partial w}{\partial r}\right)+\omega_{mb}^2\rho I\psi=0 \\ \kappa^2 G\left[\dfrac{\partial}{\partial r}\left(\psi+\dfrac{\partial w}{\partial r}\right)+\dfrac{1}{r}\left(\psi+\dfrac{\partial w}{\partial r}\right)\right]+\omega_{mb}^2\rho w=0 \end{cases} \tag{127}$$

where $w(r,t)$ is the transverse deflection of the disk midplane, while $\psi(r,t)$ is the bending rotation perpendicular to the midplane; T_D is the disk thickness, $I = T_D^3/12$ is the inertia moment per unit of length and $\kappa = \pi^2/12$ the shear correction factor. Finally, $\omega_{mb} = 2\pi f_{mb}$, where f_{mb} is one of the resonance frequencies of the structure, while the flexural rigidity D and the shear modulus G are defined as:

$$D=\frac{ET_D^3}{12\left(1-\nu^2\right)} \qquad G=\frac{E}{2\left(1+\nu\right)} \tag{128}$$

Theory of moderately thick disk was introduced because it was generally found not enough accurate to estimate resonance frequency of bending modes of the disk considered in this thesis (contour mode disk resonators with resonance frequency higher than 100 MHz), even if the disk was completely free, i.e. not connected to substrate through a stem.

The differential equations in (127) can be used to find the eigenfrequency of the holed disk, applying as boundary conditions:

a) *free* conditions at the external end of the disk ($r = R_D$), that is, both the bending moment M_r (bending the cross-section of the disk perpendicular to the radius) and the shear force V directed along z are zero at this boundary:

$$\begin{gathered} M_r\big|_{r=R_D}=D\left(\frac{\partial \psi}{\partial r}+\frac{\nu}{r}\psi\right)\bigg|_{r=R_D}=0 \\ V\big|_{r=R_D}=\kappa^2 G T_D\left(\psi+\frac{\partial w}{\partial r}\right)\bigg|_{r=R_D}=0 \end{gathered} \tag{129}$$

b) Boundary conditions fixed by the stem at the internal end ($r = R_S$). Some hypothesis are made on the stem movements:
   1. Stem is assumed as extremely rigid with respect to the rotation of the section perpendicular to the radius, which is reasonable if the height ($T_D + H_S$) is higher than stem radius. This assumption leads to the condition:

$$\psi\left(R_S, t\right) = 0 \qquad (130)$$

   2. The only movement allowed for the stem is a compression up and down in *z* direction.
   3. The resonance frequencies of the stem, considered as separated from the disk, are generally higher than the resonance frequencies of the devices studied in this thesis (according to theory and FEM simulations the first resonance frequency of a 'stand-alone' stem with height $H_S + T_D = 4\ \mu m$ and stem radius 1 µm is higher than 2 GHz). Thus the behaviour of the stem around the resonance frequency of the disk can be considered as quasi-static.
   4. According to ii. and iii. the stem can be considered as a lumped spring of stiffness *K*, which opposes the movements of the disk up and down at its inner end. The last boundary condition is thus:

$$V + Kw\Big|_{r=R_S} = Kw - \kappa^2 G T_D \left(\psi + \frac{\partial w}{\partial r} \right)\Bigg|_{r=R_S} = 0 \qquad (131)$$

If the beam is considered as a one-dimensional bar under compression the compressive stress σ_{zz} can be written as a function of the strain ε_{zz} and consequently of the displacement w_1[15] in *z* direction, as:

$$\sigma_{zz} = E\varepsilon_{zz} = E\frac{\partial w_1}{\partial z} \qquad (132)$$

---

[15] The name is chosen to avoid confusion with the displacement *w* of the disk midplane.

whose solution is, according the frame of reference in Figure 84:

$$w_1(z,t) = \frac{1}{E}\int_0^z \sigma_{zz}\,dz + w_1(0,t) \tag{133}$$

The displacement at the stem/substrate interface *w₁(0,t)*, can be estimated by the boundary conditions in Eq. (116). Such boundary conditions can be simplified a lot if the shear stress is neglected, which reasonable according to what was observed in section 3.3, if the compressive stress is assumed as constant on the stem/substrate interface and if the displacement $w_1(0,t)$ is assumed as constant on the interface. If the displacement all over the interface is approximated with its value for $r = 0$ and if the compressive stress at the interface is called $\sigma_{zz}(0,t)$:

$$w_1(0,t) = \sigma_{zz}(0,t)\,R_S\int_0^\infty A_{ZZ}(q)\,J_1(qR_S)\,dr = c_{zz}\sigma_{zz}(0,t) \tag{134}$$

with the coefficient c_{zz} defined as:

$$c_{zz} = R_S\int_0^\infty A_{ZZ}(q)\,J_1(qR_S)\,dr \tag{135}$$

A more accurate approximation can be obtained if $w_1(0,t)$ is considered still constant, but equal to its mean value. In this case, if shear stress is neglected and compressive stress is assumed as constant, it is possible to obtain from Eq. (116):

$$w_1(0,t) = \frac{2}{R_S^2}\int_0^{R_S} \sigma_{zz}(0,t)\,R_S\left[\int_0^\infty A_{ZZ}(q)\,J_1(qR_S)\,dq\right]dr \tag{136}$$

with the coefficient c_{zz} defined as:

$$c_{zz} = \frac{w(0,t)}{\sigma_{zz}(0,t)} = \frac{2}{R_S}\int_0^{R_S}\left[\int_0^\infty A_{ZZ}(q)\,J_1(qR_S)\,dq\right]dr \tag{137}$$

Apart from neglecting the shear stress, assumptions are strong but at least allow to approach the problem in analytical way, without using simulations. Besides for small stem radius the error introduced by assuming displacement and stress constant should be not too large. Substituting (134) or (136) in (133), the following expression is obtained:

$$w_1(z,t) = \frac{1}{E}\int_0^z \sigma_{zz}\,dz + c_{zz}\sigma_{zz}(0,t) \tag{138}$$

In order to find K in (44) it is necessary to write w, and consequently σ_{zz}, in terms of V. V is defined inside the disk as [89]:

$$V(r,t) = \int_{H_s}^{T_D+H_S} \sigma_{zr}(r,z,t)\,dz \tag{139}$$

Due to the symmetry of stress tensor $\sigma_{rz} = \sigma_{zr}$, so that if the shear stress σ_{rz} is assumed linear for $0 < r < R_S$:

$$\sigma_{rz}(r,z,t) = \sigma_{rz}(R_S,z,t)\frac{r}{R_S} = \sigma_{zr}(R_S,z,t)\frac{r}{R_S} \qquad \text{for} \qquad 0 < r < R_S \tag{140}$$

On the other hand, because of the force equilibrium in r direction on the element Ω of the stem, represented in Figure 85, σ_{rz} can be written as a function of the compressive stress σ_{rr}. Given that the upper surface of the disk for $z = H_S + T_D$ can be considered as unloaded, the equilibrium of forces on Ω leads to:

$$2\pi\int_0^{R_S} \sigma_{rz}(r,z,t)\,r\,dr = 2\pi R_S \int_z^{H_S+T_D} \sigma_{rr}(R_S,z,t)\,dz \tag{141}$$

If $\sigma_{rr}(R_S,z,t)$ is assumed linear and zero in midplane of the disk, according to the theory of moderately thick disk, used also to find (127):

$$\sigma_{rr}(R_S,z,t) = S\left[z - \left(H_S + \frac{T_D}{2}\right)\right] \tag{142}$$

where S is the maximum for $\sigma_{rr}(R_S,z,t)$, which is obtained for $z = H_S$ and $z = H_S + T_D$.

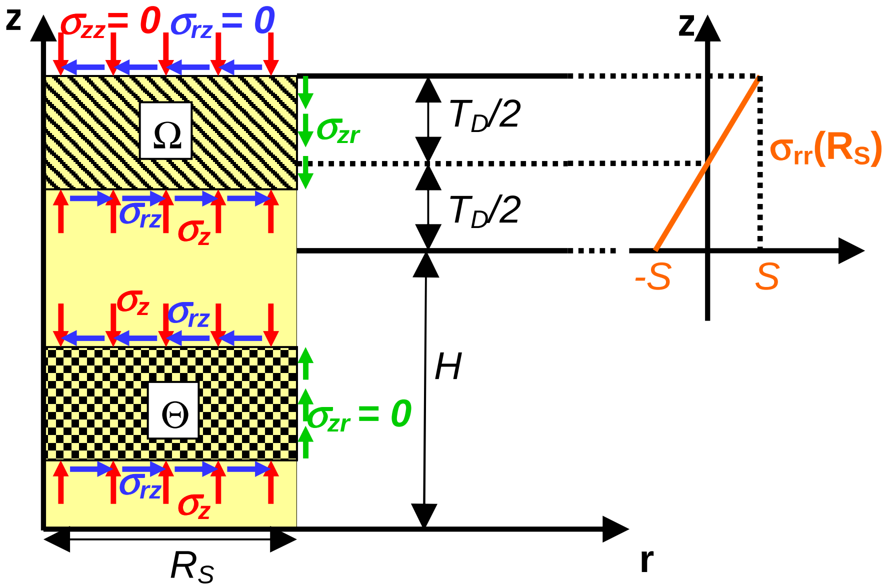

Figure 85: Zoom of the stem with the disk only partially drawn: in the figure the domains Ω and Θ are represented together with the stress components loading them, in order to show how the force balances are done. On the top right of the figure the profile along z of compressive stress in radial direction inside the disk and in the specific at the interface disk/stem, is represented.

Thus, it is possible to find $\sigma_{zr}(R_S,z,t)$, by combining (141) with (140) and (142):

$$\sigma_{zr}\left(R_S,z,t\right)=\frac{3}{2R_S}S\left(H_S-z\right)\left(H_S+T_D-z\right) \tag{143}$$

and from (139) and (143), $V(R_S,t)$ can be written as a function of S:

$$V\left(R_S,t\right)=\int_{H_S}^{T_D+H_S}\sigma_{zr}\left(R_S,z,t\right)dz=\frac{ST_D^3}{4R_S} \tag{144}$$

According to the equilibrium of force in *z* direction on the element Ω in Figure 85, the compressive stress in z direction *σ_{zz}(,z,t)*, considered as constant inside the stem can be written as function of $\sigma_{zr}(R_S,z,t)$:

$$\begin{aligned}\sigma_{zz}(z,t) &= \frac{2}{R_S}\int_{z}^{T_D+H_S}\sigma_{zr}(R_S,z,t)dz = \\ &= \frac{S}{2R_S^2}\left[2z-\left(2H_S+T_D\right)\right]\left(H_S+T_D-z\right)^2 = \\ &= \frac{V}{R_S T_D^3}\left[2z-\left(2H_S+T_D\right)\right]\left(H_S+T_D-z\right)^2\end{aligned} \tag{145}$$

$$\text{for} \qquad 0<r<R_S \qquad \text{and} \qquad H_S<z<H_S+T_D$$

For $0 < z < H_S$, $\sigma_{zr}(R_S,z,t) = \sigma_{rz}(R_S,z,t) = 0$, because the external surface of the stem is unloaded, thus the compressive stress has to be constant along *z*, according to the equilibrium of force in *z* direction on the domain Θ in Figure 85. The constant value of σ_{zz} can be found by fixing the continuity condition for $z = H_S$:

$$\sigma_{zz}(z,t) = \sigma_{zz}(H_S,t) = \frac{2V}{R_S} = \sigma_{zz}(0,t) \tag{146}$$

$$\text{for} \qquad 0<r<R_S \qquad \text{and} \qquad H_S<z<H_S+T_D$$

At this point the whole profile of compressive stress $\sigma_{zz}(z,t)$ along all the stem can be written as a function of *V* from Eqs. (145) and (146). Thus applying (145) and (146) to (138), it is possible to find a relation between displacement along *z* direction w_1 and *V*:

$$\begin{aligned}&w_1(z,t) = \left(\frac{z}{E}+c_{zz}\right)\frac{2V}{R_S} \qquad \text{for} \quad 0<z<H_S \\ &w_1(z,t) = \frac{2V}{R_S}\left\{\frac{1}{E}\left[H_S+\left(H_S-z\right)\left(\frac{H_S^3+2T_D\left(H_S^2-T_D^2\right)}{2T_D^3}+\right.\right.\right. \\ &\left.\left.\left.-\frac{H_S\left(3H_S+4T_D\right)z+\left(3H_S+2T_D\right)z^2-z^3}{2T_D^3}\right)\right]+c_{zz}\right\} \qquad \text{for} \quad H_S<z<H_S+T_D\end{aligned} \tag{147}$$

But to find the stem stiffness K, as defined in (131), the displacement w of the disk midplane for $r = R_S$ is needed. For continuity it can be found as:

$$w(R_S, t) = w_1\left(H_S + \frac{T_D}{2}, t\right) = \frac{2}{R_S E}\left(H_S + \frac{13}{32}T_D + c_{zz}E\right)\cdot V \tag{57}$$

In Eq. (57) there are three terms which are summed and they can be seen as three compliance in series: the first takes in account the stem for $0 < z < H_S$ ($c_1 = 2H_S/(R_S E)$), the second the stem for $H_S < z < H_S + T_D$ surrounded by the disk ($c_2 = 13T_D/(16R_S E)$) and the third the substrate ($c_3 = 2c_{zz}/R_S$). Thus the overall K is:

$$K = \frac{R_S E}{2\left(H_S + \frac{13}{32}T_D + c_{zz}E\right)} \tag{148}$$

Eqs. (127), can be solved by applying the boundary conditions defined in (129), (130) and (131), using the method used in [99] to find the bending resonance frequencies for a thick beam, which can be applied also to thick bending disk problem. This method was used instead of the numerical method in [98], because it gives an exact analytical solution for the mode shape, without doing any approximation, and because it is more flexible, so that it was more straightforward to use it.

Thus Eqs. (127) were first manipulated to have a two-equation system with the first equation dependent on w but not on ψ and the second one dependent on ψ but not on w, so that, defining $\xi = r/R_D$, Eqs. (127) becomes:

$$\begin{cases} \dfrac{\partial}{\partial \xi}\left\{\dfrac{1}{\xi}\dfrac{\partial}{\partial \xi}\left[\xi\dfrac{\partial}{\partial \xi}\left(\dfrac{1}{\xi}\dfrac{\partial(\xi\psi)}{\partial \xi}\right)\right]\right\} + \lambda_{mb}^4\left(z^2 + s^2\right)\dfrac{\partial}{\partial \xi}\left(\dfrac{1}{\xi}\dfrac{\partial(\xi\psi)}{\partial \xi}\right) - \lambda_{mb}^4\left(1 - \lambda_n^4 z^2 s^2\right) = 0 \\ \dfrac{1}{\xi}\dfrac{\partial}{\partial \xi}\left\{\xi\dfrac{\partial}{\partial \xi}\left[\dfrac{1}{\xi}\dfrac{\partial}{\partial \xi}\left(\xi\dfrac{\partial w}{\partial \xi}\right)\right]\right\} + \lambda_{mb}^4\left(z^2 + s^2\right)\dfrac{1}{\xi}\dfrac{\partial}{\partial \xi}\left(\xi\dfrac{\partial w}{\partial \xi}\right) - \lambda_{mb}^4\left(1 - \lambda_n^4 z^2 s^2\right) = 0 \end{cases} \tag{149}$$

where λ_{mb} is the eigenvalue corresponding to the m^{th} resonance mode of the bending disk.

From Eq. (127), the resonance frequency f_{mb} can be written in terms of eigenvalue λ_{mb}:

$$f_{mb} = \frac{1}{2\pi}\left(\frac{\lambda_{mb}}{R_D}\right)^2 \sqrt{\frac{E}{12\left(1-\nu^2\right)\rho}} \cdot T_D \tag{150}$$

Coefficients z and s are defined as:

$$z^2 = \frac{I}{T_D R_D^2} = \frac{1}{12}\left(\frac{T_D}{R_D}\right)^2 \qquad s^2 = \frac{D}{\kappa T_D G R_D^2} = \frac{2}{\left(1-\nu^2\right)\pi^2}\left(\frac{T_D}{R_D}\right)^2 \tag{151}$$

Eq. (150) is formally the same as Eq. (124) for the thin disk, but according to Eqs. (59) and (61), λ_n is generally not constant as in the case of thin disk, but it depends on $(T_D/R_D)^2$. On the other hand, if $(T_D/R_D) \to 0$, $z \to 0$ and $s \to 0$, Eqs. (149) become equivalent to Eq. (122) for a thin disk.

Before solving Eqs. (149), it is necessary to observe that going from (127) to (149) the system order was increased from 2 to 4, thus not all the solutions of (149) are solutions of (127). Consequently to delete the wrong solutions given by (149), the general solution of (149) was substituted back in (127), so that 4 of the 8 arbitrary constant in the general solution of (149) were fixed in order to make it to be a general solution also for (127). Defining:

$$\begin{aligned}
A_m &= \sqrt{\frac{z^2+s^2}{2} - \sqrt{\left(\frac{z^2-s^2}{2}\right) + \frac{1}{\lambda_{mb}^4}}} = \\
&= \frac{T_D}{R_D}\sqrt{\frac{24+(1-\nu)\pi^2}{24(1-\nu)\pi^2} - \sqrt{\left(\frac{24-(1-\nu)\pi^2}{24(1-\nu)\pi^2}\right)^2 + \left(\frac{R_D}{\lambda_{mb}T_D}\right)^4}} \\
B_m &= \sqrt{\frac{z^2+s^2}{2} + \sqrt{\left(\frac{z^2-s^2}{2}\right)^2 + \frac{1}{\lambda_{mb}^4}}} = \\
&= \frac{T_D}{R_D}\sqrt{\frac{24+(1-\nu)\pi^2}{24(1-\nu)\pi^2} + \sqrt{\left(\frac{24-(1-\nu)\pi^2}{24(1-\nu)\pi^2}\right)^2 + \left(\frac{R_D}{\lambda_{mb}T_D}\right)^4}}
\end{aligned} \tag{152}$$

the general solution of (149) for w and ψ, was found to be:

$$\begin{aligned}\psi &= d_1 J_1\left(\lambda_{mb}^2 A_m \xi\right) + d_2 Y_1\left(\lambda_{mb}^2 A_m \xi\right) + d_3 J_1\left(\lambda_{mb}^2 B_m \xi\right) + d_4 Y_1\left(\lambda_{mb}^2 B_m \xi\right) \\ w &= \frac{A_m R_D}{\left(A_m^2 - s^2\right)\lambda_{mb}^2}\left[d_1 J_0\left(\lambda_{mb}^2 A_m \xi\right) + d_2 Y_0\left(\lambda_{mb}^2 A_m \xi\right)\right] + \\ &\qquad + \frac{B_m R_D}{\left(B_m^2 - s^2\right)\lambda_n^2}\left[d_3 J_0\left(\lambda_{mb}^2 B_m \xi\right) + d_4 Y_0\left(\lambda_{mb}^2 B_m \xi\right)\right]\end{aligned} \tag{153}$$

with J_0 and Y_0 Bessel functions of zero order, respectively of first kind and of the second kind, while J_1 and Y_1 are Bessel functions of first order, respectively of first kind and of the second kind.

The fourth arbitrary constant d_i can be found by applying the boundary conditions defined in (145) and (146) to (138), rewritten considering the change of coordinates by which r was replaced with ξ:

$$\begin{aligned} &M_r\big|_{\xi=1} = \frac{D}{R_D}\left(\frac{\partial \psi}{\partial \xi} + \frac{\nu}{\xi}\psi\right)\Bigg|_{\xi=1} = 0 \qquad V\big|_{\xi=1} = \kappa^2 G T_D\left(\psi + \frac{1}{R_D}\frac{\partial w}{\partial \xi}\right)\Bigg|_{\xi=1} = 0 \\ &\psi\left(\xi = \frac{R_S}{R_D}\right) = 0 \qquad \left(V + Kw\right)\Big|_{\xi=\frac{R_S}{R_D}} = \left[Kw - \kappa^2 G T_D\left(\psi + \frac{1}{R_D}\frac{\partial w}{\partial \xi}\right)\right]\Bigg|_{\xi=\frac{R_S}{R_D}} = 0 \end{aligned} \tag{154}$$

Defining $\alpha_m = \lambda_n^2 A_m$, $\beta_m = \lambda_{mb}^2 B_m$, $h = R_S/R_D$ and the vector $\mathbf{d} = (d_1, d_2, d_3, d_4)^T$, the application of the boundary conditions in (154) leads to the linear system of equations:

$$\begin{pmatrix} \dfrac{\alpha_m J_0(\alpha_m)}{(1-\nu)} - J_1(\alpha_m) & \dfrac{\alpha_m Y_0(\alpha_m)}{(1-\nu)} - Y_1(\alpha_m) & \dfrac{\beta_m J_0(\beta_m)}{(1-\nu)} - J_1(\beta_m) & \dfrac{\beta_m Y_0(\beta_m)}{(1-\nu)} - Y_1(\beta_m) \\ \dfrac{J_1(\alpha_m)}{A_m^2 - s^2} & \dfrac{Y_1(\alpha_m)}{A_m^2 - s^2} & \dfrac{J_1(\beta_m)}{B_m^2 - s^2} & \dfrac{Y_1(\beta_m)}{B_m^2 - s^2} \\ J_1(\alpha_m h) & Y_1(\alpha_m h) & J_1(\beta_m h) & Y_1(\beta_m h) \\ \dfrac{J_0(\alpha_m h) + \dfrac{J_1(\alpha_m h)}{A_m K_m^*}}{B_m\left(A_m^2 - s^2\right)} & \dfrac{Y_0(\alpha_m h) + \dfrac{Y_1(\alpha_m h)}{A_m K_m^*}}{B_m\left(A_m^2 - s^2\right)} & \dfrac{J_0(\beta_m h) + \dfrac{J_1(\beta_m h)}{B_m K_m^*}}{A_m\left(B_m^2 - s^2\right)} & \dfrac{Y_0(\beta_m h) + \dfrac{Y_1(\beta_m h)}{B_m K_m^*}}{A_m\left(B_m^2 - s^2\right)} \end{pmatrix} \cdot \mathbf{d} = 0 \tag{155}$$

Eq. (155) can be solved only if the determinant of the matrix which multiplies **d** is zero:

$$\left|\begin{pmatrix} \frac{\alpha_m J_0(\alpha_m)}{(1-\nu)} - J_1(\alpha_m) & \frac{\alpha_m Y_0(\alpha_m)}{(1-\nu)} - Y_1(\alpha_m) & \frac{\beta_m J_0(\beta_m)}{(1-\nu)} - J_1(\beta_m) & \frac{\beta_m Y_0(\beta_m)}{(1-\nu)} - Y_1(\beta_m) \\ \frac{J_1(\alpha_m)}{A_m^2 - s^2} & \frac{Y_1(\alpha_m)}{A_m^2 - s^2} & \frac{J_1(\beta_m)}{B_m^2 - s^2} & \frac{Y_1(\beta_m)}{B_m^2 - s^2} \\ J_1(\alpha_m h) & Y_1(\alpha_m h) & J_1(\beta_m h) & Y_1(\beta_m h) \\ \frac{J_0(\alpha_m h) - \frac{J_1(\alpha_m h)}{A_m K_m^*}}{B_m\left(A_m^2 - s^2\right)} & \frac{Y_0(\alpha_m h) - \frac{Y_1(\alpha_m h)}{A_m K_m^*}}{B_m\left(A_m^2 - s^2\right)} & \frac{J_0(\beta_m h) - \frac{J_1(\beta_m h)}{B_m K_m^*}}{A_m\left(B_m^2 - s^2\right)} & \frac{Y_0(\beta_m h) - \frac{Y_1(\beta_m h)}{B_m K_m^*}}{A_m\left(B_m^2 - s^2\right)} \end{pmatrix}\right| = 0 \tag{156}$$

where K_m^* is defined as:

$$K_m^* = \frac{1}{s^2 \lambda_{mb}^2} \frac{K}{\kappa G} \frac{R_D}{T_D} \tag{157}$$

Given the material properties of the resonator, R_D, T_D, H_S, and R_S, it is possible to find the λ_{mb}, and the resonance frequencies f_{mb} of each bending mode, by solving Eq. (156). But in order to find the stem radius which gives the minimum in the curves $Q_{al}(R_S)$ it is possible also to set $\lambda_{mb} = \lambda^*$ so that the resonance frequency of the m^{th} bending mode is equal to the resonance frequency of the n^{th} contour mode, and find the stem radius R_{Smin} (or better the ratio $h_{min} = R_{Smin}/R_D$), which satisfy (156) if $\lambda_{mb} = \lambda^*$ (material properties as well as T_D, R_D and H_S are fixed). Combining (78) and (150), λ^* is:

$$\lambda^* = \sqrt[4]{12}\lambda_n \frac{R_D}{T_D} \tag{158}$$

To evaluate R_{Smin}, Eqs. (156) have to be solved numerically, for example with Matlab. In dependence of the values of R_D, T_D and λ^*, A_m can be imaginary. This can lead to problem for the numerical solver.

To avoid it, defining $\bar{A}_m = |A_m|$, $\bar{\alpha}_m = |\alpha_m|$, the solutions can be written as:

$$\begin{aligned}
\psi &= d_1 I_1\left(\lambda_{mb}^2 \bar{A}_m \xi\right) + d_2 K_1\left(\lambda_{mb}^2 \bar{A}_m \xi\right) + d_3 J_1\left(\lambda_{mb}^2 B_m \xi\right) + d_4 Y_1\left(\lambda_{mb}^2 B_m \xi\right) \\
w &= \frac{\bar{A}_m R_D}{\left(\bar{A}_m^2 + s^2\right)\lambda_{mb}^2}\left[-d_1 I_0\left(\lambda_{mb}^2 \bar{A}_m \xi\right) + d_2 K_0\left(\lambda_{mb}^2 \bar{A}_m \xi\right)\right] + \\
&\quad + \frac{B_m R_D}{\left(B_m^2 - s^2\right)\lambda_n^2}\left[d_3 J_0\left(\lambda_{mb}^2 B_m \xi\right) + d_4 Y_0\left(\lambda_{mb}^2 B_m \xi\right)\right]
\end{aligned} \tag{159}$$

leading to the following eigenvalue equation:

$$\left|\begin{pmatrix}
\frac{\bar{\alpha}_m I_0(\bar{\alpha}_m)}{(1-\nu)} - I_1(\alpha_m) & -\frac{\bar{\alpha}_m K_0(\bar{\alpha}_m)}{(1-\nu)} - K_1(\bar{\alpha}_m) & \frac{\beta_m J_0(\beta_m)}{(1-\nu)} - J_1(\beta_m) & \frac{\beta_m Y_0(\beta_m)}{(1-\nu)} - Y_1(\beta_m) \\
-\frac{I_1(\bar{\alpha}_m)}{\bar{A}_m^2 + s^2} & -\frac{K_1(\bar{\alpha}_m)}{\bar{A}_m^2 + s^2} & \frac{J_1(\beta_m)}{B_m^2 - s^2} & \frac{Y_1(\beta_m)}{B_m^2 - s^2} \\
I_1(\bar{\alpha}_m h) & K_1(\bar{\alpha}_m h) & J_1(\beta_m h) & Y_1(\beta_m h) \\
\frac{-J_0(\bar{\alpha}_m h) - \frac{J_1(\bar{\alpha}_m h)}{\bar{A}_m K_m^*}}{B_m\left(\bar{A}_m^2 + s^2\right)} & \frac{\frac{Y_1(\bar{\alpha}_m h)}{\bar{A}_m K_m^*} - Y_0(\bar{\alpha}_m h)}{B_m\left(\bar{A}_m^2 + s^2\right)} & \frac{J_0(\beta_m h) + \frac{J_1(\beta_m h)}{B_m K_m^*}}{\bar{A}_m\left(B_m^2 - s^2\right)} & \frac{Y_0(\beta_m h) + \frac{Y_1(\beta_m h)}{B_m K_m^*}}{\bar{A}_m\left(B_m^2 - s^2\right)}
\end{pmatrix}\right| = 0 \tag{160}$$

Results predicted by the method described in the previous section were compared with the value of the minimum in curves $Q_{al}(R_S)$ for some disks of SiGe, with a different radii ($9\ \mu m < R_D < 20\ \mu m$) and consequently different resonance frequencies ($103.5\ MHz < f_1 < 230\ MHz$) of the first contour mode. Disk thickness was fixed to 2 μm and stem height to 1 μm. This comparison is represented in Figure 86. Even if the theoretical model agree in a qualitative way with the dependence of R_{Smin} on R_D given by the simulations, relative error can be as high as 40%, while the absolute error can be higher than 1 μm (for value of R_{Smin} higher than 4 μm). A behaviour similar to the one in Figure 86 was found for other simulated geometries.

Especially for high stem radius, the more important causes of inaccuracy of the model can be assumed to be the condition of no rotation for $r = R_S$, as shown by deformed shape of the resonance modes from FEM simulations.

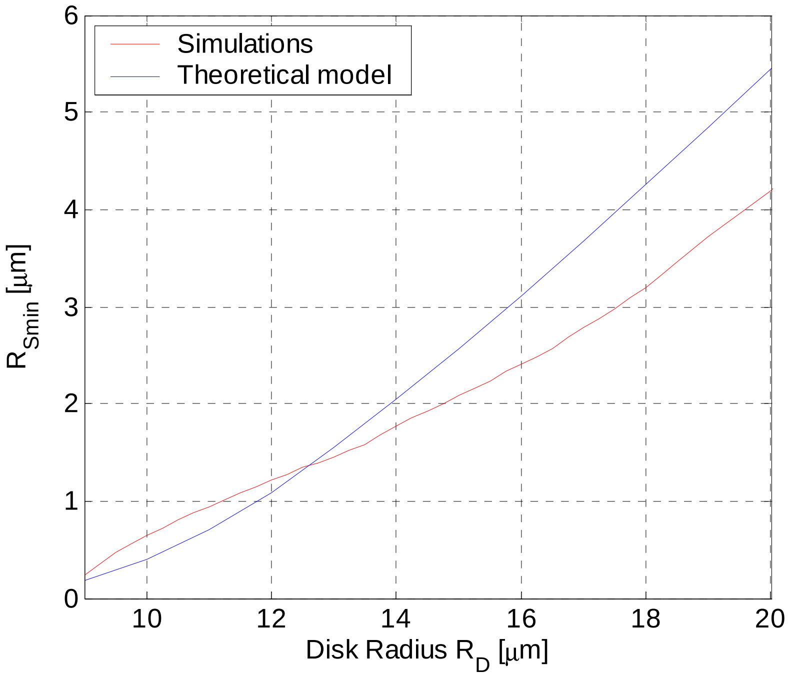

Figure 86: Value of the stem radius which leads to a minimum in curves $Q_{al}(R_S)$, according to the presented theoretical model (blue line) and to FEM simulations, for a disk radius R_D varying from 9 to 20 μm. Disk and stem material was considered to be SiGe (E = 137 GPa, ρ = 3430 Kg/m^3 and ν = 0.23), while the substrate was assumed to be made of homogeneous silicon. Disk thickness is fixed to 2 μm and stem height to 1 μm, resulting in a resonance frequency varying from 230 to 103.5 MHz, in dependence on disk radius.

Also the schematization of the stem as one-dimensional bar, which removes the effect above all of displacement *u* in radial direction inside the stem can be important. Such assumption cancels also the effect of shear stress σ_{rz}, but this can be considered as less important, because, as shown in section 3.3, at least its effect on the acoustic wave propagating in the substrate is negligible.

Finally, the hypothesis of quasi-static motion of the stem should not affect too much the results, given that according to FEM simulations results the resonance frequencies of the stand-alone stem are much higher than the resonance frequency of the devices the simulations in Figure 86 are about.

3.6 Thermoelastic losses

In this section thermoelastic losses in a disk resonator are evaluated, in the simple case of a totally free disk, not connected to a substrate through the stem. Initially only the thermoelastic dissipation due only to contour mode was considered, because it was expected that internal losses played an important role only if anchor losses are minimized, that is, if the energy stored in the bending mode are minimum. It should allow to neglect the coupling with the bending mode produced by the stem. But from both theory and simulations it was found that thermoelastic losses in the parasitic bending mode are much higher than in the contour mode, so that even a small amount of energy stored in a bending movements produced a large increase of the overall thermoelastic losses in the device.

Thus also the thermoelastic losses in the bending mode were evaluated, but having no clue about the exact distribution of energy between bending and contour mode around the minimum of anchor losses (maximum of quality factor), it was not possible to estimate analytically the effect of thermoelastic losses on the quality factor of anchored disk. Also in this case the solution was to include this mechanism in FEM simulations.

3.6.1 Thermoelastic dissipation in contour modes of a free disk

The interaction between elastic deformation and temperature gradient is the source of thermoelastic damping. Referring to the structure and the frame of reference in Figure 87, for a contour mode disk resonator this interaction is ruled by the following system of partial differential equations:

$$\begin{cases} \dfrac{E}{1-\nu^2}\dfrac{\partial}{\partial r}\left(\dfrac{\partial u}{\partial r}+\dfrac{u}{r}\right)-\dfrac{E\alpha_T}{1-\nu}\dfrac{\partial T}{\partial r}=\rho\dfrac{\partial^2 u}{\partial t^2} \\ \nabla\cdot\left(K_{th}\nabla T\right)-\dfrac{E\alpha_T\left(T+T_0\right)}{1-2\nu}\dfrac{\partial}{\partial t}\displaystyle\sum_{i=1}^{3}\varepsilon_{ii}=C_P\dfrac{\partial T}{\partial t} \end{cases} \tag{161}$$

where K_{th} is thermal conductivity, C_P the thermal capacitance and α_T the coefficient of thermal expansion (CTE) of the disk; T_0 is the equilibrium or ambient temperature, while T is the temperature variation with respect to T_0 inside the disk and u the displacement in radial direction of points inside the disk. Generally $T << T_0$, so that it is possible to neglect T, when it is added to T_0, leading to a linear PDE system.

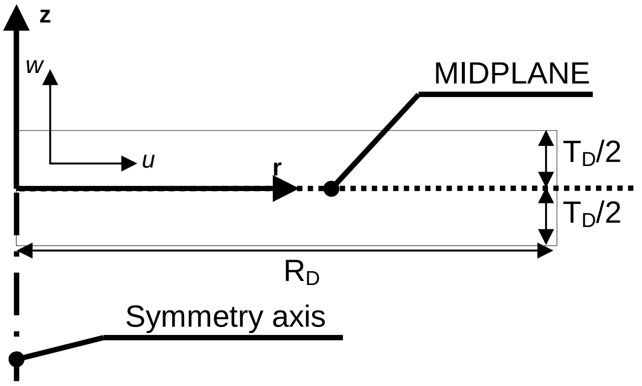

Figure 87: Axisymmetric system of reference used to model thermoelastic losses in contour and bending modes of a disk resonator not anchored to a substrate

The two equations are expressed in cylindrical coordinates. The first one [89] is the differential equation for a disk expanding in radial direction with an added term $\left(E\alpha_T\right)/\left(1-\nu\right)\cdot\left(\partial T/\partial r\right)$, due to the thermal expansion. The second one is the heat transfer equation with an heat generation q_e due to disk vibrations [35]. For a contour mode, exploiting the axisymmetry of the problem and assuming the plane stress condition ($\sigma_{zz} = 0$, which is reasonable if the plate is thin enough), q_e can be written as:

$$q_e = \frac{E\alpha_T T_0}{1-2\nu}\frac{\partial}{\partial t}\sum_{i=1}^{3}\varepsilon_{ii} = \frac{E\alpha_T T_0}{1-\nu}\frac{\partial}{\partial t}\left(\frac{\partial u}{\partial r}+\frac{u}{r}\right) \tag{162}$$

It is important to observe that the heat generation occurs only if there is a time-variant deformation (it does not take place if the deformation is static) and if there is a dilatation, that is, if the trace of strain tensor is different from zero (i.e. there is no strain-dependent heat generation if the there is a pure rotation wave without a dilatation component). Substituting Eq. (162) in (161), writing the term $\nabla\cdot\left(K_{th}\nabla T\right)$ for an axisymmetric geometry and assuming the thermal conductivity K_{TH} as constant all over the disk, Eqs. (161) become:

$$\begin{cases} \dfrac{E}{1-\nu^2}\dfrac{\partial}{\partial r}\left(\dfrac{\partial u}{\partial r}+\dfrac{u}{r}\right)-\dfrac{E\alpha_T}{1-\nu}\dfrac{\partial T}{\partial r}=\rho\dfrac{\partial^2 u}{\partial t^2} \\ K_{th}\left(\dfrac{\partial^2 T}{\partial r^2}+\dfrac{1}{r}\dfrac{\partial T}{\partial r}\right)-\dfrac{E\alpha_T T_0}{1-\nu}\dfrac{\partial}{\partial t}\left(\dfrac{\partial u}{\partial r}+\dfrac{u}{r}\right)=C_P\dfrac{\partial T}{\partial t} \end{cases} \tag{163}$$

Eqs. (163) can be solved if the following simplifying assumptions hold:

1. *Weak coupling*: the coupling term $\left(E\alpha_T\right)/\left(1-\nu\right)\cdot\left(\partial T/\partial r\right)$ is very small, so that disk mode shapes, calculated by the first equation are approximately the same as the mode shapes found when thermal effect is not considered.
2. *In any instant and in any point internal to the disk, the thermal gradient follows the profile of dilatation*: solution of the second equation it is assumed to be the solution forced by the heat source q_e. This is equivalent to the assumption of resonance frequencies much smaller than $1/\tau_T$, where τ_T is the characteristic time needed to end a thermal transitory in the system. According to the simulations such approximation works fine if the disk is thermally insulated, while the agreement between theoretical result and simulation is worse when a temperature or some kind of heat transmission as convection or radiation are allowed at the disk external interfaces. This is reasonable because a fixed external temperature increase the thermal inertia of the system, above all close to the boundaries.

Besides, the following hypotheses have been already made in order to obtain Eqs. (163):

3. Not only the mode shapes but also the thermal gradient is axisymmetric: they both depend only on radial direction r and not on the rotation angle around the symmetry axis θ.
4. There are not out plane movements, such as the bending which is introduced by a stem which anchor the centre of the disk to the substrate. Thus in (163) u and T are independent on z direction and the displacement in z direction is neglected.

According to the presented approach the first equation in (163) is simplified because of the first assumption and solved. Then its solution is substituted in the second equation and exploiting the second assumption T is found. Finally T is substituted back in the first equation to find the part dependent on the time of the solution.

The first assumption is verified because adding the term $\left(E\alpha_T\right)/\left(1-\nu\right)\cdot\left(\partial T/\partial r\right)$ only the part dependent on the time of the displacement changes and not the part dependent on the radius, i.e. the mode shape. Consequently the only hypotheses of the model are practically only the second the third and the fourth (the first automatically holds if the others holds).

According to the first hypothesis it is possible to find the displacement u by solving:

$$\frac{E}{1-\nu^2}\frac{\partial}{\partial r}\left(\frac{\partial u}{\partial r}+\frac{u}{r}\right)=\rho\frac{\partial^2 u}{\partial t^2} \tag{164}$$

whose solution can be found by separating variables as:

$$u = Ae^{j2\pi f_n t} J_1\left(\frac{\lambda_n}{R_D}\right) \tag{165}$$

where λ_n is the n$^{\text{th}}$ eigenvalue for the contour mode, which can be calculated as in (77), while f_n is the eigenfrequency, which will be different from the one given in (78), because of the thermal effect. R_D is the disk radius.

According to the second assumption the second equation in (163) can be solved if u is written as in (165). The temperature profile found in such a way is:

$$T = -Ae^{j2\pi f_c t}\eta(f_c)\frac{\lambda_n}{R_D}J_0\left(\frac{\lambda_n}{R_D}\right) = -Ae^{j2\pi f_n t}\eta(f_n)\left(\frac{\partial u}{\partial r}+\frac{u}{r}\right) \tag{166}$$

with:

$$\eta(f_n) = \frac{\alpha_T E T_0}{1-\nu}\frac{j2\pi f_n}{j2\pi f_n C_P + K_{th}\left(\frac{\lambda_n}{R_D}\right)^2} \tag{167}$$

In (166) no thermal boundary conditions are included, thus the temperature profile found in this way is different from the real one, but simulations confirm, at least for polysilicon and SiGe resonator, that (166) give a good approximation of the temperature profile at least when the resonator is almost or totally thermally insulated from the external environment.

Substituting the expression for T in (166) back in the first equation of (163) the following equation is obtained:

$$\frac{E}{1-\nu^2}\frac{\partial}{\partial r}\left(\frac{\partial u}{\partial r}+\frac{u}{r}\right)\left[1+\alpha_T\left(1+\nu\right)\eta\left(f_n\right)\right]=\rho\frac{\partial^2 u}{\partial t^2} \tag{168}$$

which gives the same solution as in (165), but leads to the following expression for f_n, which is different from (78):

$$f_n=\frac{1}{2\pi}\frac{\lambda_n}{R_D}\sqrt{\frac{E\left[1+\alpha_T\left(1+\nu\right)\eta\left(f_n\right)\right]}{\rho\left(1-\nu^2\right)}} \tag{169}$$

Assuming $\alpha_T\left(1+\nu\right)\eta\left(f_n\right)<<1$, and substituting the expression for $\eta\left(f_n\right)$ in (167):

$$f_n\approx\frac{1}{2\pi}\frac{\lambda_n}{R_D}\sqrt{\frac{E}{\rho\left(1-\nu^2\right)}}\left[1+\frac{1}{2}\frac{\left(1+\nu\right)}{\left(1-\nu\right)}\frac{j2\pi f_n\alpha_T^2 E T_0}{j2\pi f_n C_P+K_{th}\left(\frac{\lambda_n}{R_D}\right)^2}\right] \tag{170}$$

Defining f_0 as the resonance frequency of the device when there is no thermoelastic effect (i.e. calculated as in (78)) and assuming $f_n\approx f_0$, f_n can be written as:

$$f_{cn}=f_0\left[1+\frac{1}{2}\frac{\left(1+\nu\right)}{\left(1-\nu\right)}\frac{j2\pi f_0\alpha_T^2 E T_0}{j2\pi f_0 C_P+K_{th}\left(\frac{\lambda_{nc}}{R_D}\right)^2}\right] \tag{171}$$

The eigenfrequency f_n is a complex number, thus the resonance frequency f_n^* is defined as [35]:

$$f_n^* = \mathrm{Re}\left[f_n \right] = f_0 \left[1 - \frac{1}{2} \frac{(1+\nu)}{(1-\nu)} \frac{4\pi^2 f_0^2 \alpha_T^2 E T_0}{4\pi^2 f_0^2 C_P^2 + K_{th}^2 \left(\frac{\lambda_n}{R_D} \right)^4} \right] \tag{172}$$

which generally leads to a resonance frequency $f_n^* \approx f_0$: for example for a Polysilicon disk (*E = 160 GPa*, ρ = *2230 Kg/m*^{3}, ν = *0.226*, K_{TH} = *30 W/(K*m)*, C_P = *1.63 MJ/(K*m*^{3}*)*, α_T = *2.6x10*$^{-6}$ *K*$^{-1}$) resonating on the first contour mode, with ambient temperature T_0 = *300 K* and R_D = *15* μ*m* (f_0 = 184.5 MHz), $f_n^* = f_0 \left(1 + 9.7\text{x}10^{-11} \right)$.

While with respect to the hypothesis $\alpha_T (1+\nu)\eta(f_n) << 1$, substituting the value of f_n from (172), $\alpha_T (1+\nu)\eta(f_n) = 3\text{x}10^{-4} + j8\text{x}10^{-8}$ can be found, which is safely negligible with respect to the unity. Generally at least for polysilicon resonator under the GHz, $\alpha_T (1+\nu)\eta(f_n) << 1$ is largely satisfied.

Finally, the thermoelastic losses can be estimated by defining the quality factor only due to thermoelastic effect Q_{TH}, which can be calculated by the complex eigenfrequency f_n^* as [35]:

$$Q_{TH}^{-1} = 2\frac{\mathrm{Im}\left[f_n \right]}{\mathrm{Re}\left[f_n \right]} = \frac{(1+\nu)}{(1-\nu)} \frac{E\alpha_T^2 T_0}{C_P} \frac{2\pi f_0 \tau_R}{1 + \left(2\pi f_0 \tau_R \right)^2} \tag{173}$$

where τ_R is a time constant defined as:

$$\tau_R = \frac{K_{th}}{C_P} \frac{\rho\left(1 - \nu^2 \right)}{E} \tag{174}$$

while $E\alpha_T^2 T_0 / C_P$ is equal to the relaxation strength of the Young's modulus $\Delta_E = \left(E_{ad} - E_{is} \right) / E_{is}$, where E_{ad} is the unrelaxed or *adiabatic* Young's modulus and E_{is} the relaxed or *isothermal* Young's modulus [35]. According to Eq. (173) the higher the CTE, the temperature, the Poisson ratio and the Young's modulus, the lower Q_{TH}, while high capacitance material are good to have a high Q_{TH}. Eq. (173) can be further simplified considering that for the material generally used for MEMS (mono crystalline silicon, polysilicon and SiGe) $0.15\ ps < \tau_R < 1.25\ ps$, so that $(2\pi f_0 \tau_R)^2 << 1$, at least for $f_0 < 40\ GHz$. Thus Eq. (173) can be safely approximated to:

$$Q_{TH}^{-1} \approx \left(1+\nu\right)^2 \frac{\alpha_T^2 T_0}{C_P^2} 2\pi f_0 K_{th} \rho \qquad (175)$$

where the dependence on E disappears and there is a linear dependence on thermal conductance K_{TH}: this means that the worse the thermal conductivity the lower thermoelastic losses, so that polycrystalline material as SiGe and polysilicon performed better than mono crystalline silicon (even if SiGe performance is decreased by the high CTE and high mass density). Finally, it is important to observe in (173) and (175) that Q_{TH} is independent on R_D and on all the other geometrical dimension of the disk, as well as it is independent on the order of the resonance mode. It depends only on material properties and on resonance frequency. Thermoelastic dissipation in a contour mode disk resonator can be even modelled as a viscoelastic Kelvin-Voigt damping according to (175) [34].

Thermoelastic damping is extremely low for a completely free contour mode disk: for a disk designed to resonate at a frequency of 200 MHz Q_{TH} calculated from (173) and (175) is about 10 million if the material is polysilicon and about 8.5 million if the material is SiGe. But as shown in the following, when the disk is connected to the substrate through a stem, part of the energy is stored in a bending movement, whose thermoelastic losses are much higher.

3.6.2 Thermoelastic dissipation in bending modes of a free disk

According to FEM simulations, if the anchor losses are minimized (i.e. in correspondence of a local maximum in curves $Q_{al}(R_S)$), the quality factor considering both anchor and thermoelastic losses is generally limited to a value much smaller than both the result given by the simulation including only anchor losses and the Q_{TH} calculated in section 3.6.1, even if such model is confirmed by the simulations if the disk is not connected to the substrate by a stem (see section 3.6.3). This can be explained by the fact that, due to the presence of the stem, if the anchor losses are minimized, a part of energy is anyway stored in a parasitic bending mode, even if this amount of energy is very small due to separation between the resonance frequencies of the two modes. In this section a model for the thermoelastic losses in a disk resonating on a bending mode is extracted, in order to demonstrate that they are much more important than in the disk contour modes. So that, even if a very small portion of the overall energy of the resonator is stored in a bending mode, it can affect very much the whole Q.

Thermoelastic losses of a disk bending mode can be evaluated through the same approach used in [35] to evaluate thermoelastic losses in a beam resonator.

Considering thermal dilatation, and making the hypothesis of thin disk[16], the equation for a bending disk is slightly modified with respect to Eq. (122), in order to include thermal stress effects:

$$\rho T_D \frac{\partial^2 w}{\partial t^2} = \frac{1}{r}\frac{\partial}{\partial r}\left\{ r\frac{\partial}{\partial r}\left[D\frac{1}{r}\frac{\partial}{\partial r}\left(r\frac{\partial w}{\partial r}\right) + \frac{E\alpha_T I_T}{1-\nu}\right]\right\} \tag{176}$$

where w is the deflection of the midplane in z direction, T_D disk thickness, ρ the mass density, D the flexural rigidity of the plate, E the Young's modulus, ν the Poisson ration α_T the coefficient of thermal expansion and I_T a parameter dependent on the temperature which can be defined as:

$$I_T = \int_{-T_D/2}^{T_D/2} Tzdz \tag{177}$$

where T is the temperature variation with respect to the ambient temperature. The heat transfer equation can be found by making the same assumptions made in [35]: only the temperature gradient in z direction (i.e. in the bending direction) is considered, neglecting thermal gradients in other direction; then it is assumed $T << T_0$, to obtain a linear PDE equation as in (163).

Finally, the dilatation is written exploiting the axisymmetric condition and assuming a plane stress condition ($\sigma_{zz} = 0$, reasonable if the plate is thin enough), in the same way as in the case of the contour mode. The heat transfer equation found in such way is:

$$K_{th}\frac{\partial^2 T}{\partial z^2} - \frac{E\alpha_T T_0}{1-\nu}\frac{\partial}{\partial t}\left(\frac{\partial u}{\partial r} + \frac{u}{r}\right) = C_P\frac{\partial T}{\partial t} \tag{178}$$

---

[16] The model for the thick disk is more accurate, but using such model make only more complex the demonstration, while it can be shown that the only thing that it changes, is the value of the eigenvalue λ_{mb} in the expression for Q presented in the following.

Considering that, according to the model for thin disks, $u = z\psi$ and $\psi = \partial w/\partial r$, where ψ is the rotation angle perpendicular to radial direction, Eq. (178) becomes:

$$K_{th}\frac{\partial^2 T}{\partial z^2} - \frac{E\alpha_T T_0 z}{1-\nu}\frac{\partial}{\partial t}\left(\frac{\partial^2 w}{\partial r^2} + \frac{1}{r}\frac{\partial w}{\partial r}\right) = C_P\frac{\partial T}{\partial t} \tag{179}$$

Fixing boundary condition of disk thermally insulated and assuming a temperature profile $T = e^{-j\omega t}T'(r)$ the solution of Eq. (178) is:

$$T = -\frac{E\alpha_T T_0}{1-\nu}\left[z - \frac{\sin(gz)}{g\cos\left(\frac{T_D g}{2}\right)}\right]\frac{1}{r}\frac{\partial}{\partial r}\left(r\frac{\partial w}{\partial r}\right)e^{j\omega t} \tag{180}$$

with:

$$g = (1+j)\sqrt{\frac{\omega C_P}{2K_{th}}} \tag{181}$$

This expression for T can be substituted back in (177) and then the result of (177) can be placed in (176). Assuming $w = e^{-j\omega t}\overline{w}(r)$ Eq. (176) becomes:

$$-\rho T_D \omega_m{}^2 = D\left\{1 + \frac{(1+\nu)}{(1-\nu)}\frac{E\alpha_T^2 T_0}{C_P}\left[1 + F(\omega_m)\right]\right\}\frac{1}{r}\frac{\partial}{\partial r}\left\{r\frac{\partial}{\partial r}\left[\frac{1}{r}\frac{\partial}{\partial r}\left(r\frac{\partial w}{\partial r}\right)\right]\right\} \tag{182}$$

where, defining $\xi = T_D g = (1+j)T_D\sqrt{\frac{\omega C_P}{2K_{th}}}$:

$$F(\omega_m) = F(\xi) = \frac{24}{\xi^3}\left[\frac{\xi}{2} - \mathrm{Tan}\left(\frac{\xi}{2}\right)\right] \tag{183}$$

Solving (182) it is possible to find the complex eigenfrequency $f_m = \omega_m/2\pi$, given by:

$$\begin{aligned} f_{mb} &= \frac{1}{2\pi}\left(\frac{\lambda_{mb}}{R_D}\right)^2 \sqrt{\frac{E}{12\left(1-\nu\right)^2\rho}}\sqrt{1+\frac{\left(1+\nu\right)}{\left(1-\nu\right)}\frac{E\alpha_T^2T_0}{C_P}\left[1+F\left(\xi\right)\right]} = \\ &= f_{mb0}\sqrt{1+\frac{\left(1+\nu\right)}{\left(1-\nu\right)}\frac{E\alpha_T^2T_0}{C_P}\left[1+F\left(\xi\right)\right]} \cong \\ &\cong f_{mb0}\left\{1+\frac{1}{2}\frac{\left(1+\nu\right)}{\left(1-\nu\right)}\frac{E\alpha_T^2T_0}{C_P}\left[1+F\left(\xi\right)\right]\right\} \end{aligned} \tag{184}$$

where it is assumed also $\frac{\left(1+\nu\right)}{\left(1-\nu\right)}\frac{E\alpha_T^2T_0}{C_P}\left[1+F\left(\omega_m\right)\right] << 1$, which is generally satisfied and where f_{mb0} is the eigenfrequency as calculated in (124), that is, when there is no thermoelastic damping.

Generally such hypothesis is verified: the resonance frequency is $f_{bm}^* = \mathrm{Re}\left[f_m\right] \approx f_0$ also when the thermoelastic effect is considered. From (184) it is possible to find the quality factor only due to thermoelastic losses for a bending mode as:

$$Q_{TH}^{-1} = 2\frac{\mathrm{Im}\left[f_{cn}\right]}{\mathrm{Re}\left[f_{cn}\right]} = \frac{\left(1+\nu\right)}{\left(1-\nu\right)}\frac{E\alpha_T^2T_0}{C_P}\left[\frac{6}{\xi^2}-\frac{6}{\xi^3}\frac{\sin\left(\xi\right)+\sinh\left(\xi\right)}{\cos\left(\xi\right)+\cosh\left(\xi\right)}\right] \tag{185}$$

which is the same result found in [35] multiplied by the factor $\left(1+\nu\right)/\left(1-\nu\right)$, the beam thickness is replaced by the disk thickness: Because of $\left(1+\nu\right)/\left(1-\nu\right) > 1$, a bending disk suffer thermoelastic damping even more than a bending beam, whose Q is anyway lowered very much by thermoelastic effect ([35],[36]).

It is possible to show that considering a thick disk, the same formal result as in (185) is obtained: the only difference between thin and thick disk is in the eigenvalue λ_{mb} and thus in the resonance frequency calculated neglecting thermoelastic effect f_{mb0}, which can be calculated using the methods in [98] or in [99].

3.6.3 FEM Validation of the models for a free disk

The models described in sections 3.6.1 and in 3.6.2 can be validated by FEM simulations: this is possible through a transient analysis with eigenvalue extraction performed by the Femlab coupled thermal-structural module. The quality factor is extracted as for the anchor losses simulations, by using the formula in (81). In all the simulations presented in the following the disk is considered as thermally insulated.

The agreement is very good for both the model, as shown in Figures 88 and 89, even if for the bending mode there is an error around the minimum value for Q_{TH}. Furthermore, in the case of the bending mode, calculating the frequency f_{mb0} with the model for thick disk, improves only slightly the agreement for high value of the ratio T_D/R_D (small disk radius in Figure 89).

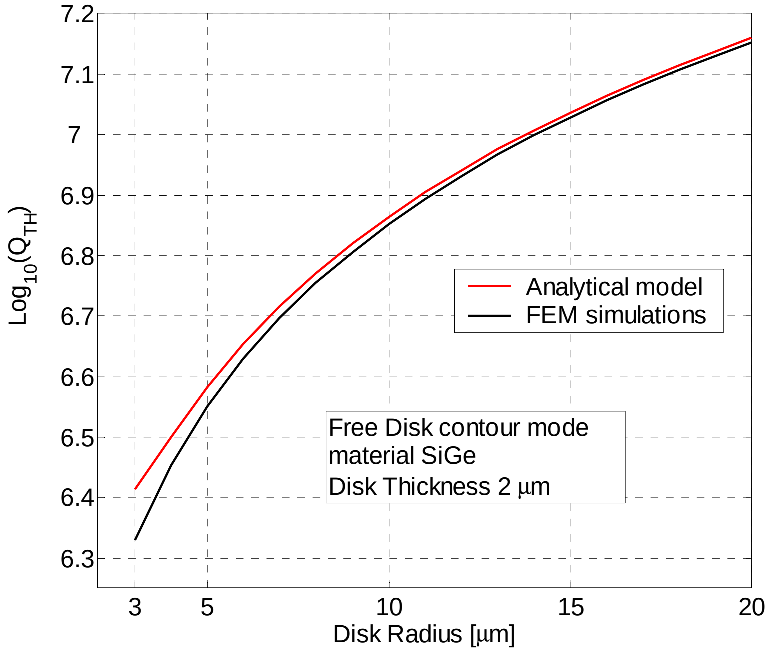

*Figure 88: Quality factor Q_{TH} only due to thermoelastic losses for the first contour mode for a SiGe disk (E = 137 GPa, ρ = 3430 Kg/m^3, ν = 0.23, K = 9.8 W/(K*m), C_P = 1.57 MJ/(K*m^3), α_T = 4.18x10^{-6} K^{-1}) with thickness 2 μm and radius varying from 3 μm to 20 μm (resonance frequency varying from nearly 600 MHz to 103 MHz). The red curve represents Q_{TH} according to the analytical model, the black curve according to Femlab simulations. In simulations the disk is considered as thermally insulated.*

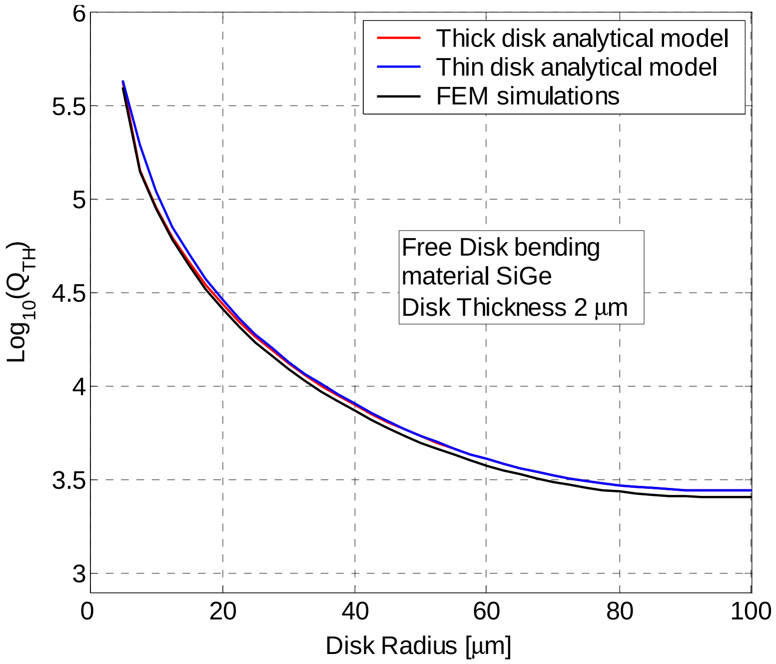

Figure 89: Quality factor Q_{TH} *only due to thermoelastic losses for the second bending mode for a SiGe disk (*$E = 137$ *GPa,* $\rho = 3430$ *Kg/m*^{3}*,* $\nu = 0.23$*,* $K = 9.8$ *W/(K*m),* $C_P = 1.57$ *MJ/(K*m*^{3}*),* $\alpha_T = 4.18\mathrm{x}10^{-6}$ *K*$^{-1}$*) with thickness 2* μ*m and radius varying from 5* μ*m to 100* μ*m (resonance frequency varying from nearly 900 MHz to 2 MHz). The blue curve represents* Q_{TH} *according to the analytical model for a thin disk, the red curve according to the analytical model for a thick disk, the black curve according to Femlab simulations. In simulations the disk is considered as thermally insulated*

As anticipated, thermoelastic damping for the bending mode is much higher than in the case of contour mode for the same range of frequencies: indeed depending on the disk radius, the resonance frequency of contour mode whose Q_{TH} simulation is represented in Figure 88, belongs to the interval [103 MHz; 609 MHz], which is, if $R_D < 20\ \mu m$, the same more or less for the bending mode whose Q_{TH} simulation is shown in Figure 89. In the same resonance frequencies interval, for the contour mode Q_{TH} varies from 1 million to 10 millions, while for the bending mode from nearly 30,000 to almost 400,000, which makes a large difference. Furthermore, for R_D around 10 μm, the resonance frequencies of the two modes are very close and thus they can be coupled if the disk is anchored to the substrate, through a central stem: in this region Q_{TH} is about 100,000 for the bending mode and about 7 millions for the contour mode, that is, almost 2 order of magnitude of difference. It means that when modes are coupled, even if the energy stored in the bending mode is only 1% percent of the energy stored in the contour mode, thermoelastic losses due to the bending mode are comparable to the ones due to contour mode.

3.6.4 Simulations of the quality factor of a contour mode disk resonator, including both anchor losses and thermoelastic damping

The evaluation of the overall thermoelastic dissipation in a contour mode of a disk anchored to a substrate through a central stem is very difficult because, if the device is anchored in the centre, the overall energy stored in the resonator is divided between a contour and a bending movement in a way which is difficult to predict. This is also one of the reason which makes difficult to find completely analytical models for the anchor losses, including the coupling with the bending mode. Thus, the only way to evaluate thermoelastic losses in a disk resonator is to include it in a FEM simulation which includes also both stem and substrate. Then thermoelastic effect was included in HDS simulation by making HDS simulations using Femlab thermal-structural module.

In all the simulations presented in the following disk boundaries are considered as thermally insulated, as well as the boundaries of the HDS.

In Figure 90 results are shown from HDS-based simulations of the quality factor due to both anchor loss and thermoelastic effect for a SiGe resonator, with stem height 1 µm, disk thickness 2 µm, disk radius 10µm and a stem radius varying from 0.2 to 2.5µm. The resonance frequency is about 207 MHz, according to both theory and simulations. These results are compared with both HDS and THBC simulations including only anchor losses. The effect of thermoelastic dissipation is a decrease of the quality factor around the maximum of the curve $Q(R_S)$. The maximum is about 1.3 million, lower than the value obtained when the thermoelastic losses are not included, but also lower than 7.3 million, the thermoelastic limit expected by Eq. (173), which evaluates thermoelastic losses for a pure contour mode. This can be explained only assuming that a small part of the energy is anyway stored, even around the maximum, in a bending mode. Such hypothesis is confirmed also by mode shapes extracted form FEM simulations.

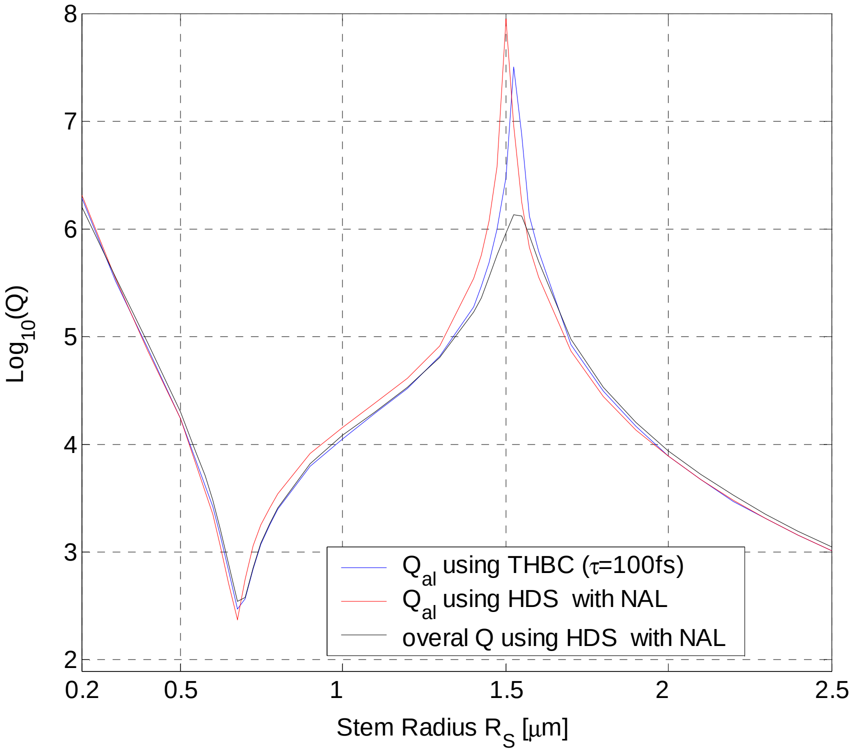

*Figure 90: Comparison between HDS-based simulations of the quality factor due to both anchor loss and thermoelastic effect (black curve) and both HDS-based (red line) and THBC-based (blue line) simulations including only anchor losses, with respect to the dependence of the quality factor on stem radius. Disk and stem material is considered to be SiGe (E = 137 GPa, ρ = 3430 Kg/m^3, ν = 0.23, K = 9.8 W/(K*m), C_P = 1.57 MJ/(K*m^3), α_T = 4.18x10^{-6} K^{-1}), while the substrate is assumed to be made of homogeneous silicon. Disk radius is fixed to 10 μm, Disk thickness to 2 μm and stem height to 1 μm, resulting in a resonance frequency of about 207 MHz.*

Assuming that it is possible to neglect anchor losses around the maximum (which reasonable according to results in Figure 90), it is possible to calculate the ratio between energy stored in the bending mode E_B and the energy stored in the contour mode E_C as:

$$\frac{E_B}{E_c}=\left(1-\frac{Q_M}{Q_{THC}}\right)\Bigg/\left(\frac{Q_M}{Q_{THB}}-1\right) \qquad (186)$$

where Q_M is the overall Q at the maximum, while Q_{THC} is the quality factor due only to thermoelastic losses related to the contour mode (Eq. (173)) and Q_{THB} is the quality factor due only to thermoelastic losses related to the bending mode (Eq. (185)). With respect to the case shown in Figure 90, the ratio expressed in (186) is about 0.0685. In spite of only 6.4% of the energy stored in the bending mode, thermoelastic losses due to the bending mode gives the limit of the quality factor. From Figure 90 it is also possible to observe that around the minimum of the curve, thermoelastic losses does not change results given by simulations including only anchor losses, as expected because around the minimum anchor losses are much higher than thermoelastic dissipation of both contour and bending mode.

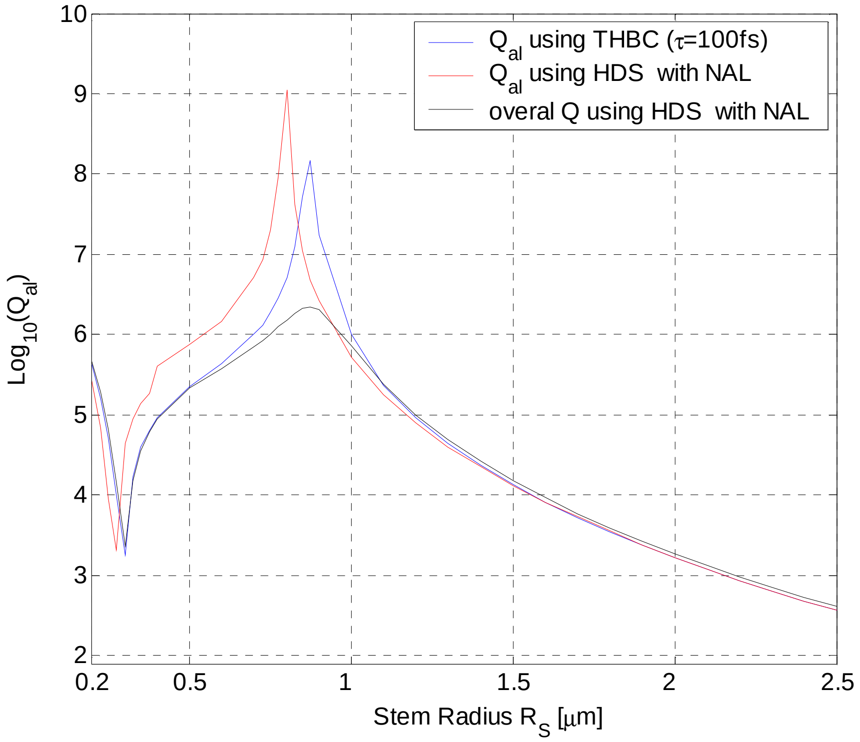

*Figure 91: Comparison between HDS-based simulations of the quality factor due to both anchor loss and thermoelastic effect (black curve) and both HDS-based (red line) and THBC-based (blue line) simulations including only anchor losses, with respect to the dependence of the quality factor on stem radius. Disk and stem material is considered to be SiGe (E = 137 GPa, ρ = 3430 Kg/m^3, ν = 0.23, K = 9.8 W/(K*m), C_P = 1.57 MJ/(K*m^3), α_T = 4.18x10^{-6} K^{-1}), while the substrate is assumed to be made of homogeneous silicon. Disk radius is fixed to 9 μm, Disk thickness to 2 μm and stem height to 1 μm, resulting in a resonance frequency of about 230 MHz.*

In Figure 91 the same simulation is presented for a SiGe resonator with $H_S = 1\ \mu m$, $T_D = 2\ \mu m$, $R_D = 9\ \mu m$ and a stem radius R_S varying from 0.2 to 2.5 µm (resonance frequency about 230 MHz). Also in this case thermoelastic damping results in lowering the maximum, but, as already said, simulation results in Figure 90 confirm also the low accuracy of HDS-based simulations without thermoelastic losses included with respect to THBC model: results for HDS-based simulation, including thermoelasticity matches with THBC for any stem radius apart form the maximum region, while it disagree with HDS-based simulation neglecting thermoelasticity, even around the minimum. But thermoelastic dissipation cannot affect either the minimum amplitude, because it is negligible if the anchor losses are maximum, or the minimum position, because the minimum is due to the fact that for a particular stem radius the resonance frequency of a parasitic bending mode equals the resonance frequency of the fundamental contour mode and both resonance frequencies are independent on the disk intrinsic damping unless it is too high.

Thus HDS-based simulations including thermoelasticity show that the introduction of this intrinsic loss is necessary to obtain a more realistic curve $Q(R_S)$ around the maximum, but also to improve the overall accuracy of the simulation.

3.7 A design strategy for high-Q contour mode disk resonator

In this section all the observations from the simulations discussed in this chapter will be summarized and exploited to synthesize a strategy to optimize the design of a contour mode disk resonator for RF applications.

The goal is to obtain a target resonance frequency and a quality factor as high as possible, by choosing properly the layout parameters, i.e. the disk radius and the stem radius. Also an evaluation of the robustness of the strategy is provided.

3.7.1 From theory and simulations to a design recipe

An optimum design of a contour mode disk resonator can be easily achieved starting from the following observation: while according to simulations the quality factor Q_{al} only due to the anchor losses is affected by both R_D and R_S, according to both theory and simulations the resonance frequency f_n of a contour mode disk resonator is dependent only on the disk radius ($\propto 1/R_D$, according to (78)). Thus the following strategy is a good option:

1. Chose the disk radius in order to obtain the resonance frequency given by the simulations.
2. Chose the optimum stem radius to maximize the quality factor.

While there is an analytical expression to calculate the disk radius to obtain a target resonance frequency, the choice of the optimum stem radius is more complicated.

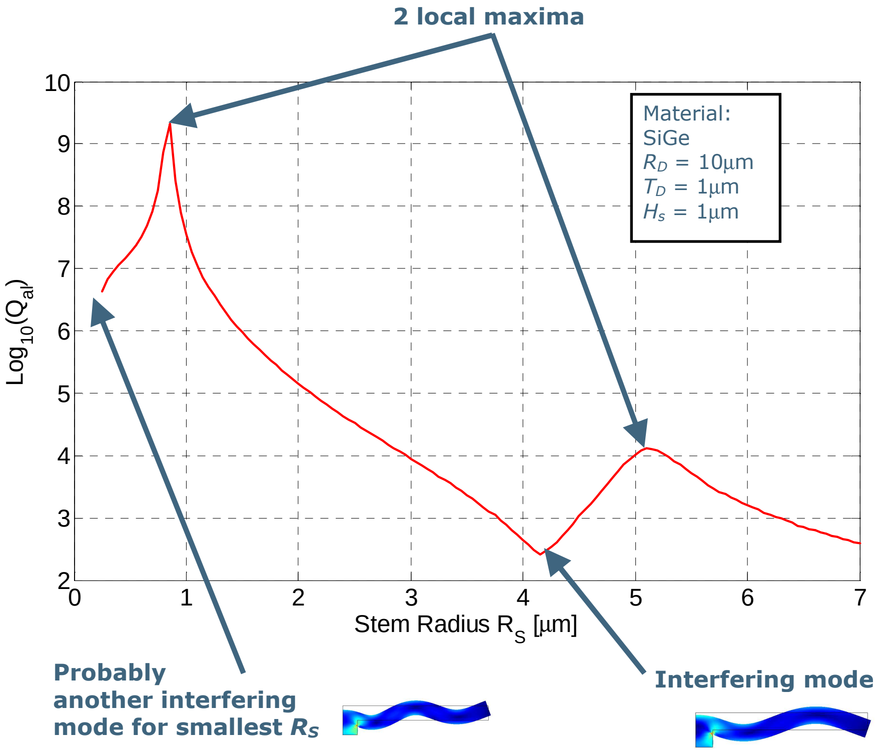

2 local maxima

Probably another interfering mode for smallest R_S

Interfering mode

Figure 92: HDS-based simulations of the quality factor only due to the anchor losses in a SiGe resonator (E = 137 GPa, ρ = 3430 Kg/m^3 and ν = 0.23), with disk radius R_D = 10 μm (resonance frequency 207 MHz) and disk thickness T_D = 1 μm, while stem height H_S is 1 μm and stem radius varies from 0.2 μm to 7 μm. The substrate material is silicon. In the figure the shapes of the interfering modes are included: the second minimum is due to the interference with the second bending mode, while the first is due to the interference with the third one. The first minimum cannot be seen in the figure because it occurs for very small values of R_S, but has to exist, because of course for R_S = 0, there is no stem and thus no anchor losses, so that $Q_{al} \to \infty$.

The quality factor generally monotonically decreases if the stem radius increases (Figures 70 and 77), unless an interfering bending mode is superposed to the desired contour mode (watch for example at Figures 68, 75 or 76), for a certain stem radius. In this case there is a minimum for the quality factor corresponding to this particular stem radius. The minimum has to be followed by a maximum, because for high stem radius is anyway expected a quality factor decreasing towards zero, due to the great area the energy can flow through.

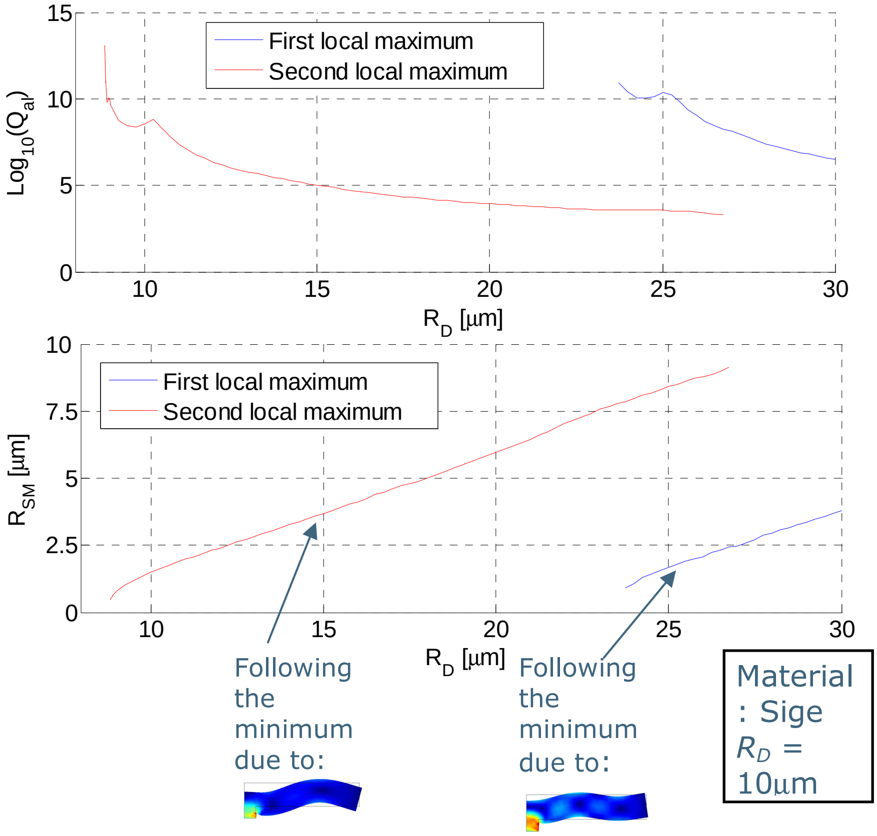

Figure 93: Bottom graph: simulation of the dependence on the disk radius R_D of the stem radius R_{SM2} which gives the local maximum in the curve $Q_{al}(R_S)$ following the minimum due to the interference with the second bending mode (red curve) and of stem radius R_{SM3} which gives the local maximum following the minimum due to the interference with the third bending mode (blue curve). Top graph: quality factor obtained by choosing $R_S = R_{SM2}$ (red curve), and by fixing $R_S = R_{SM2}$ (blue curve). Disk and stem material is SiGe, $T_D = 2$ µm, $H_S = 1$ µm and R_D varies from 9 µm to 30 µm (resonance frequency from 230 MHz to 70 MHz).

Thus the maximum quality factor can be obtained choosing the stem radius equal to the minimum value which can be designed according the layout rules, or equal to the stem radius R_{SM} which leads to the maximum following to the minimum due the interference of the bending mode.

But the situation is sometimes complicated by the presence of more than one maximum because of the interference with more than one bending mode (Figures 92 and 93). Nonetheless simulations show that the higher the stem radius value which gives the maximum, the lower the obtained quality factor (Figures 92 and 93). This reduces the choice between only the first maximum and the minimum layout value for R_S. Besides, if the position of the first maximum is higher than $R_D/4$ (Figure 93) the value for the quality factor corresponding to the maximum is generally too low to be taken in consideration and this further reduce the region where it is needed to look for the maximum.

A possible strategy to find the optimum value for R_S is:

1. Looking for the first local maximum in the region $R_S \in [R_S^*, R_D/4]$, where R_S^* is the minimum layout value for the stem radius
2. Compare the quality factor in the local maximum with the quality factor for the minimum stem radius and choose the stem radius which gives the maximum one.

This strategy can be used for an automatic design tool which gives the value for R_D and R_S to obtain a target resonance frequency (given as input) and the maximum quality factor only due to the anchor losses, once material properties disk thickness and stem height are fixed by the process. Some results of this algorithm, including also thermoelastic losses will be discussed in 3.7.2.

A better criterion in the choice of the optimum R_S could be looking for the maximum which assures not only a high value for the maximum Q_{AL}, but also the robustness of it. The designed values for R_S could be different from its value in the real device, and also disk thickness and disk radius, stem height and/or material properties could vary with respect to the nominal ones, leading to a quality factor lower than expected.

Thus, given the expected maximum variation for each parameter, simulations should be carried out to estimate if R_{SM} leads to a more robust maximum than R_S^* or vice versa (i.e. in which case the maximum is less affected by parameters perturbations).

The choice of this second optimization method has to be recommended also because if another damping source limits the quality factor (Figures. 90 and 91) the difference between the overall quality factor in R_S^* and R_{SM} becomes smaller and less significant.

Furthermore, as shown in 3.7.4, the smaller R_{SM} is, the more it is affected by the value of the disk radius R_D. In particular the distance between minimum and maximum decreases a lot for small value of R_{SM} (Figure 94) leading to the possibility of obtaining a minimum quality factor even choosing it to get the maximum, because of some perturbation in the value of process parameters.

The problem can be limited, considering that curves $Q(R_S)$ are not symmetric around R_{SM} and this asymmetry becomes higher if R_{SM} decreases (Figure 94). Thus, in order to minimize the influence of a stem radius fluctuation on the quality factor, for small R_{SM} should be chosen as an optimum value $R_{SM} + \delta R$ in order to reduce the maximum decrease of the quality factor with respect to the expected value, when there is the maximum variation (given the maximum stem variation ΔR_S this could be reached by choosing δR so that $Q(R_{SM} + \delta R + \Delta R_S)= Q(R_{SM} + \delta R - \Delta R_S))$. This approach can be used also for high value of R_{SM}, even if in that case is less important, at least if ΔR is not very high.

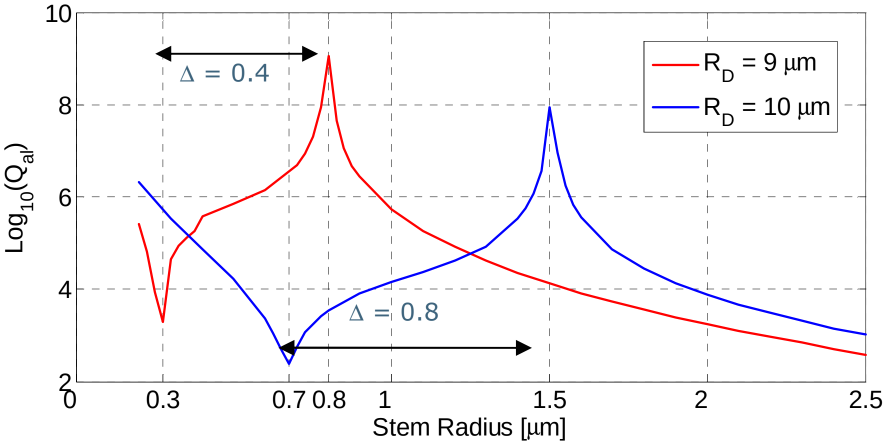

Figure 94: Quality factor only due to the anchor losses in a SiGe resonator (E = 137 GPa, ρ = 3430 Kg/m^3 and ν = 0.23), with radius R_D = 10 μm and thus resonance frequency 207 MHz (blue curve) and in a SiGe disk with radius R_D = 9 μm and thus resonance frequency 230 MHz (red curve). Disk thickness T_D is 1 μm, while stem height H_S is 1 μm and stem radius varies from 0.2 μm to 2.5 μm for both the curves. The substrate material is silicon. Both the simulations were performed using a HDS element to mimic the substrate. Indeed THBC method is more accurate especially for the curve with R_D = 9 μm, because of the small values of the stem radii which gives the minimum and the maximum, but with respect to the effect the figure want to show, that is, the decreasing of the distance between minimum and maximum for small values of the stem radius, using THBC would not change the conclusions.

The final design recipe to obtain high quality factor, with the smallest sensitivity to stem radius variation is:

1. Chose the disk radius in order to obtain the resonance frequency given by the simulations.
2. Looking for the first local maximum R_{SM} in the region $R_S \in [R_S^*, R_D/4]$, where R_S^* is the minimum layout value for the stem radius.
3. Find δR which leads to $Q(R_{SM} + \delta R + \Delta R_S) = Q(R_{SM} + \delta R - \Delta R_S))$, where ΔR_S is the maximum stem variation.
4. Given the maximum stem radius variation ΔR_S compare $Q(R_S^* + \Delta R_S)$ with $Q(R_{SM} + \delta R + \Delta R_S)$:
    a. If $Q(R_S^* + \Delta R_S) > Q(R_{SM} + \delta R + \Delta R_S)$ choose $R_S = R_S^*$.
    b. If $Q(R_S^* + \Delta R_S) < Q(R_{SM} + \delta R + \Delta R_S)$ choose $R_S = R_{SM} + \delta R$.

The third step which can be optional, because if R_{SM} is high enough (approximately, higher than $1/10R_D$), it does not improve the robustness of the Q (in this case δR is fixed to zero).

The algorithm assures not the lowest anchor losses but the lowest anchor losses when the variation of R_S is the highest expected (better value in the worst case). Besides it can be easily implemented, for example in Matlab.

Of course also the effect other parameter variation should be done to verify the validity of this choice (see 3.7.4).

3.7.2 Effect of thermoelastic damping on the strategy for quality factor maximization

As observed in section 3.6, thermoelastic damping decreases a lot the amplitude of the quality factor around the local maximum, while it does not affect too much the value for small R_S, that is, close to R_S^*. It is reasonable if it is assumed that for small stem radii the coupling with bending mode is smaller: if it holds, for smaller stem radius the thermoelastic limit should be due only to the to the contour mode (Eq. (173)), being extremely small the energy stored in the bending mode. On the other hand for $R_S = 0$, the disk is free, i.e. not connected to the substrate, and thus there is no coupling at all between contour and bending mode. Furthermore, the decreasing of the coupling between contour and bending mode for small R_S is confirmed by the fact that value of the minimum quality factor is higher when it occurs for smaller stem radius (Figure 94).

Thus the thermoelastic damping smoothes the difference between the quality factor obtained for the minimum radius R_S^* allowed by layout and the quality factor obtained for the first local maximum R_{SM}, and sometimes even can change the choice of the optimum stem radius: it is just what happen in the case shown in Figure 90, at least if the first algorithm proposed is considered, i.e. the algorithm which chooses the value of stem radius which maximizes Q without considering the robustness.

Finally, the effect of the thermoelastic damping indicates that is better to choose a most robust maximum instead of highest, because if the value of $Q(R_S^*)$ and $Q(R_{SM})$ are similar there is no great advantage in choosing the criterion of the higher quality factor. Besides being it so important around the local maximum, it is mandatory to include it in the simulations used to find the maximum.

3.7.3 Results from algorithm for the synthesis of contour mode disk resonators

In Figure 95 results of a synthesis algorithm which chooses as stem radius the one which gives the maximum Q are shown, while in Figure 96 it is possible to observe the results from a synthesis algorithm which chooses as stem radius the one which gives the most robust maximum Q. This second algorithm is the one discussed in 3.7.1, forcing $\delta R = 0$, even if it can be fixed from the algorithm to improve the robustness of the local maximum. This choice was done only to increase the velocity of the algorithm. The maximum error ΔR_S between the designed and the obtained value of the stem radius is fixed to 0.1 μm. Both the algorithms are based on HDS Femlab simulations, including thermoelastic effect and are implemented in Matlab, exploiting the possibility of interfacing Femlab and Matlab [43].

From results in Figures 95 and 96, it is possible to observe that by the presented synthesis algorithm it is possible to obtain the target frequency with a good accuracy and very high quality factors: in the worst case, when there is no dispersion on the stem radius it is possible to obtain a Q about 1 million, while if a dispersion of ±0.1 μm is assumed, Q is nearly two hundred thousands in the worst case. For low frequencies resonators (around 60-70 MHz) it is possible even to reach 10 millions. Of course the limit of the described approach is that only two damping source are considered: other intrinsic losses or surface effects can further limit the quality factor if anchor losses are minimized. Nonetheless if such losses are independent or weakly dependent on the stem radius the choice made to optimize the quality factor is still valid.

Besides there can be also a dispersion on the value of stem height, disk thickness and radius which can lower a lot the value of the quality factor in the worst case (i.e. if the difference between the designed or nominal value and the effective one is the maximum expected).

Finally, it is evident that if the value or the robustness of the maximum quality factor is considered, the chosen R_{Sopt} can be a lot different: for example considering the robustness, the region at low frequencies where the first local maximum is preferable with respect to R_S^* (around 90 MHz) increases with respect to the case when only the value of the quality factor is consider. The opposite happens for the region at high frequencies where the first local maximum is preferable than R_S^* (around 215 MHz)

3.7.4 Robustness of the choice with respect to variation o stem height, disk radius and disk thickness

A variation even high on the stem height value affect only slightly the position of a local maximum, following a minimum due to a parasitic bending mode (Figures 82 and 83 in 3.4.2). Thus the choice of the optimization strategy presented in this section is robust with respect to stem height variation.

On the other hand variation of disk radius and thickness are more important.

Given the material properties, stem height and disk thickness, the relation between R_{SM} and R_D is almost linear in a very big region, so that it is to verity easily the effect of a difference between the real and the nominal disk radius on the position of a local maximum (Figure 97).

The dependence on the disk radius in the linear region is significant but not too large: an increase of 1 μm in the value of disk radius leads to an increase of about 0.4 μm of the maximum position, even if with respect to this value, there are small differences among the different curves shown in Figure 97. The situation is significantly worse for small values of R_{SM}, where the curves $R_{SM}(R_D)$ are not linear anymore: small changes in the value of disk radius leads to large variations in the position of the maximum. This non-linear region is very important because the smaller R_{SM}, the higher the quality factor obtained by designing the stem radius equal to R_{SM}. The choice of a stem radius slightly higher than R_{SM} can improve the robustness also with respect to a variation of R_D, because reduces the risk to obtain a minimum instead a maximum due to a disk radius higher than the nominal one.

A careful control of the disk radius is necessary for the robustness of design not only with respect to the quality factor, but also with respect to the resonance frequency.

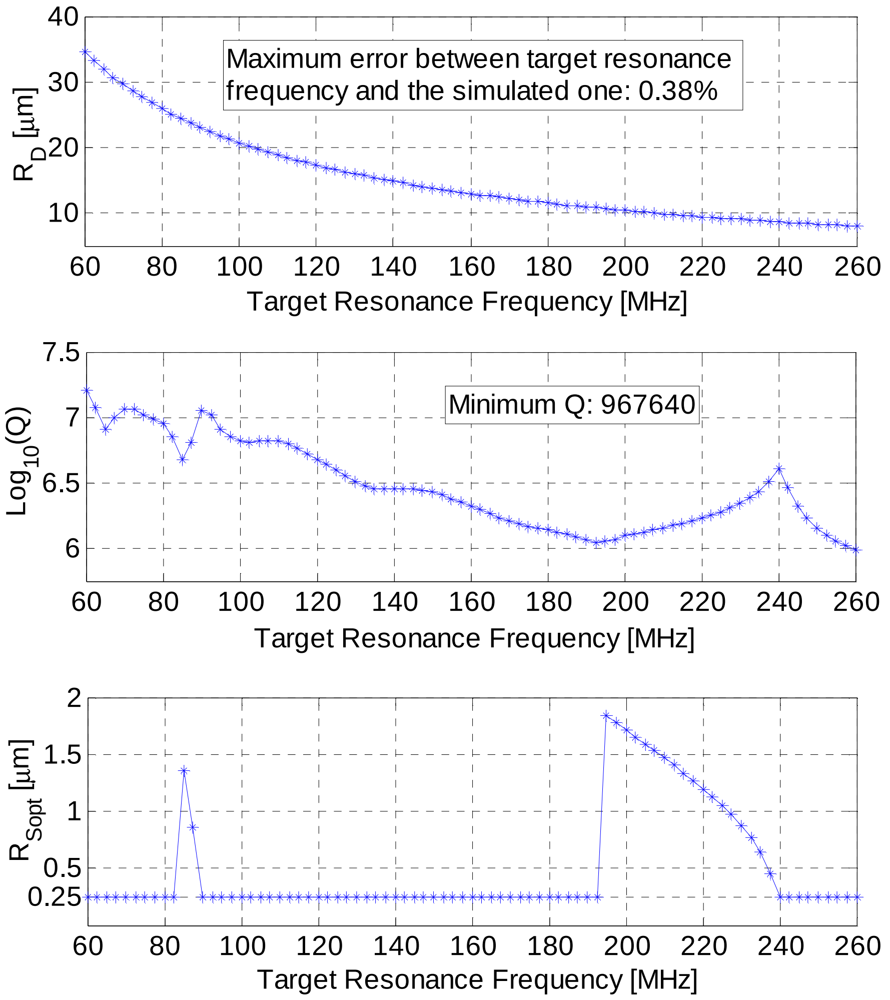

*Figure 95: Results of the algorithm of automatic synthesis considering no spread of the value of stem radius ($\Delta R_S = 0$), for a SiGe ($E = 137$ GPa, $\rho = 3430$ Kg/m^3, $\nu = 0.23$, $K = 9.8$ W/(K*m), $C_P = 1.57$ MJ/(K*m^3), $\alpha_T = 4.18\text{x}10^{-6}$ K^{-1}) resonator, with $T_D = 2$ μm, $H_S = 1$ μm. The upper graph represents the disk radius R_D chosen to obtain the target resonance frequency. The lower graph shows the optimum value for stem radius R_{Sopt} to obtain the maximum quality factor, given the target resonance frequency. Finally, the remaining graph represents the quality factor expected given the chosen R_D and R_{Sopt}, in dependence of the target resonance frequency. The maximum relative error between the target frequency and the resonance frequency according to the simulations is shown as well as the quality factor obtained in the worst case by the algorithm (minimum of the curve in the second graph). The algorithm exploits HDS-based simulations including thermoelastic losses.*

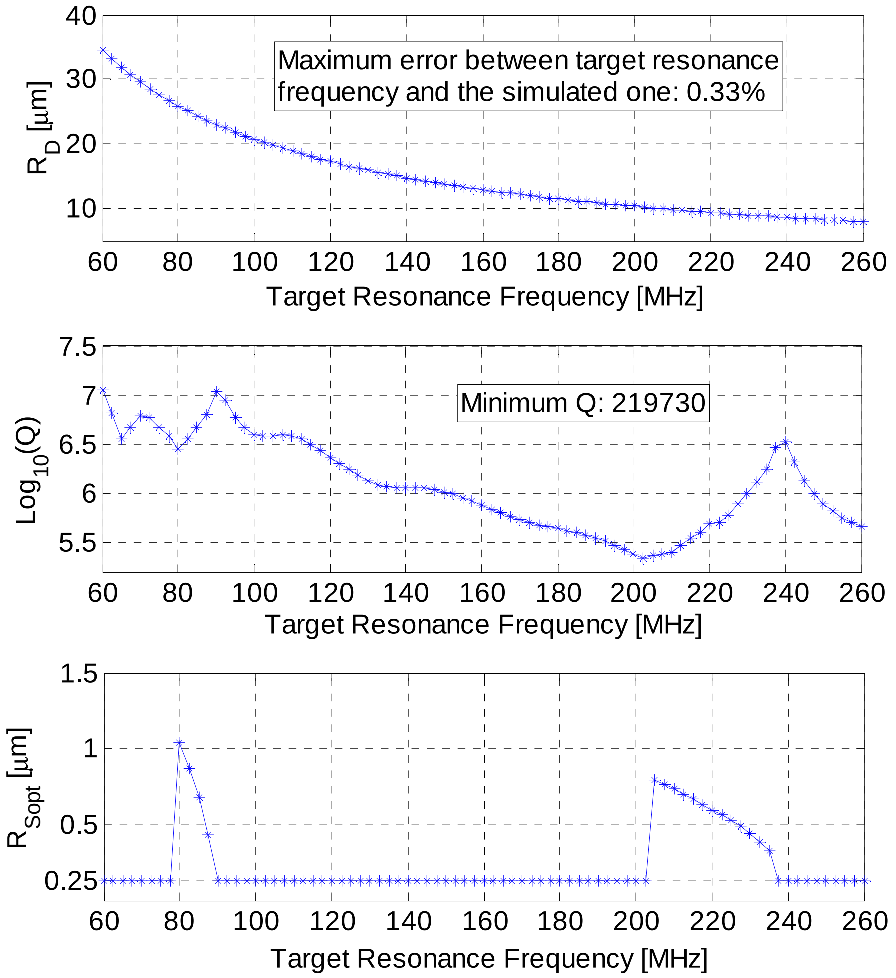

Figure 96: Results of the algorithm of automatic synthesis considering a maximum spread on the value of stem radius $\Delta R_S = 0.1\ \mu m$*, for a SiGe (*$E = 137$ *GPa,* $\rho = 3430\ Kg/m^3$*,* $\nu = 0.23$*,* $K = 9.8\ W/(K*m)$*,* $C_P = 1.57\ MJ/(K*m^3)$*,* $\alpha_T = 4.18x10^{-6}\ K^{-1}$*) resonator, with* $T_D = 2\ \mu m$*,* $H_S = 1\ \mu m$*. The upper graph, represents the disk radius* R_D *chosen to obtain the target resonance frequency. The lower chart shows the optimum value for stem radius* R_{Sopt} *to obtain the most robust maximum for the quality factor, given the target resonance frequency. Finally, the remaining graph represents the quality factor expected in the worst case in dependence of the target resonance frequency, given the chosen* R_D *and* R_{Sopt}*,. The worst case occurs if the variation of* R_S *is maximum and thus if* $R_S = R_{Sopt} \pm \Delta R_S$*. The maximum relative error between the target frequency and the resonance frequency according to the simulations is shown, as well as the quality factor obtained in the worst case by the algorithm (minimum of the curve in the second graph). The algorithm exploits HDS-based simulations including thermoelastic losses.*

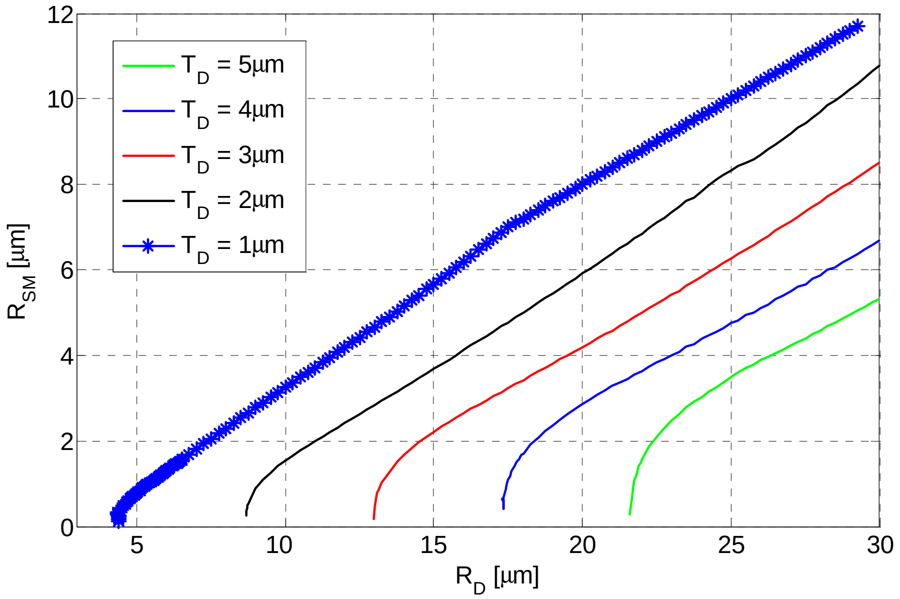

Figure 97: *Simulation of the dependence on the disk radius R_D of the stem radius which gives the local maximum R_{SM} in the curve $Q_{al}(R_S)$ following the minimum due to the interference with the second bending mode of the disk. The thickness is parametrically changed from 1 to 5 µm. Disk and stem material is considered to be SiGe (E = 137 GPa, ρ = 3430 Kg/m^3 and ν = 0.23), while the substrate was assumed to be made of homogeneous silicon. Stem height is fixed to 1 µm, resonance frequency varies from about 70 MHz to nearly 500 MHz. All the simulations were performed extracting R_{SM} from PML-based simulations (HiQLab) of the quality factor only due to anchor losses.*

Results in Figure 97 suggest also a way to find the local maximum for every value of R_D by making few simulations to extract the two coefficients which define the curve Of course this method fails in the region with low values for R_{SM}, where the curve shape is not linear.

Besides, Figure 97 shows the importance of disk thickness on the position of the maximum: it was expected because the resonance frequency of the bending mode is affected by T_D as shown in section 3.4.3. The effect of T_D on a local maximum following a minimum due to the interaction of a certain bending mode seems to be easily predictable by curves in Figure 97: if the thickness increases, they are translated towards right-down, that is, the maximum occurs for smaller stem radius and for larger disk radius.

The effect of the disk thickness is even more important than the one of the disk radius: maximum position shifts even of 2 µm if the thickness increases/decreases of 1 µm.

Thus also the thickness is a parameter which has to be carefully controlled in order to obtain a robust design according to the strategy presented in this thesis.

Finally, some simulations were done to verify the effect of small variation in disk and or substrate material properties but their effect is very small. The material properties become important only if the material is completely changed.

4. Magnetically actuated MEM microbalances

In this chapter the idea, the design, the fabrication and a preliminary characterization of a novel MEM microbalance is presented. As discussed in chapter 1, MEM microbalances are generally resonators covered by a sensitive layer in order to adsorb or adsorb some particular molecule form the environment. The resonance frequency of the device decreases if the resonator adsorbs a mass, thus if it is included in an oscillator as frequency-selective element, the shift of the output oscillation can be used to estimate the weight of the adsorbed mass.

The device presented in this thesis has still to be functionalized with a proper sensitive layer and potentially it can be used for any application involving the measure of an adsorbed mass: it can be employed as a chemical sensor, a DNA sensor or even to measure the thickness of a deposited layer in a process to fabricate electronics or MEMS. Given that the device has not been yet functionalized only a characterization of its performance as resonator has been carried out, as well as a verification of the effect of humidity of its resonance frequency.

A previous experience in modelling chemical sensors based on resonant cantilever was fundamental to start these activities. Such experience was developed during a collaboration with PEL (Physical Electronics Laboratory) of ETH Zurich, but is not included in this thesis. Details about it can be found in [100] and [101].

On the other hand the activity presented in this thesis about design, fabrication and characterization of MEM microbalances is partially described in [102] and [103], while the first idea of the device was presented in [104].

4.1 Device description and basic working

The microbalance proposed in this thesis is a torsional resonator with magnetic actuation and sensing (Figure 98). To the author’s knowledge, the only other resonator which implements magnetic actuation and sensing is the resonant cantilever proposed in [6] for scanning probe microscope applications, which is, however, based on a completely different mechanical structure. Also, the mechanical structure of a torsional resonator is quite unusual: something similar was proposed only in [16] for a magnetic sensor.

The device was designed in order to obtain the best performance, with the less expensive CMOS-compatible process.

In the following first a description of the proposed device and its basic working will be given, then the reasons of the choice of the actuation and sensing mechanisms will be discussed, as well as the choice of the mechanical structure.

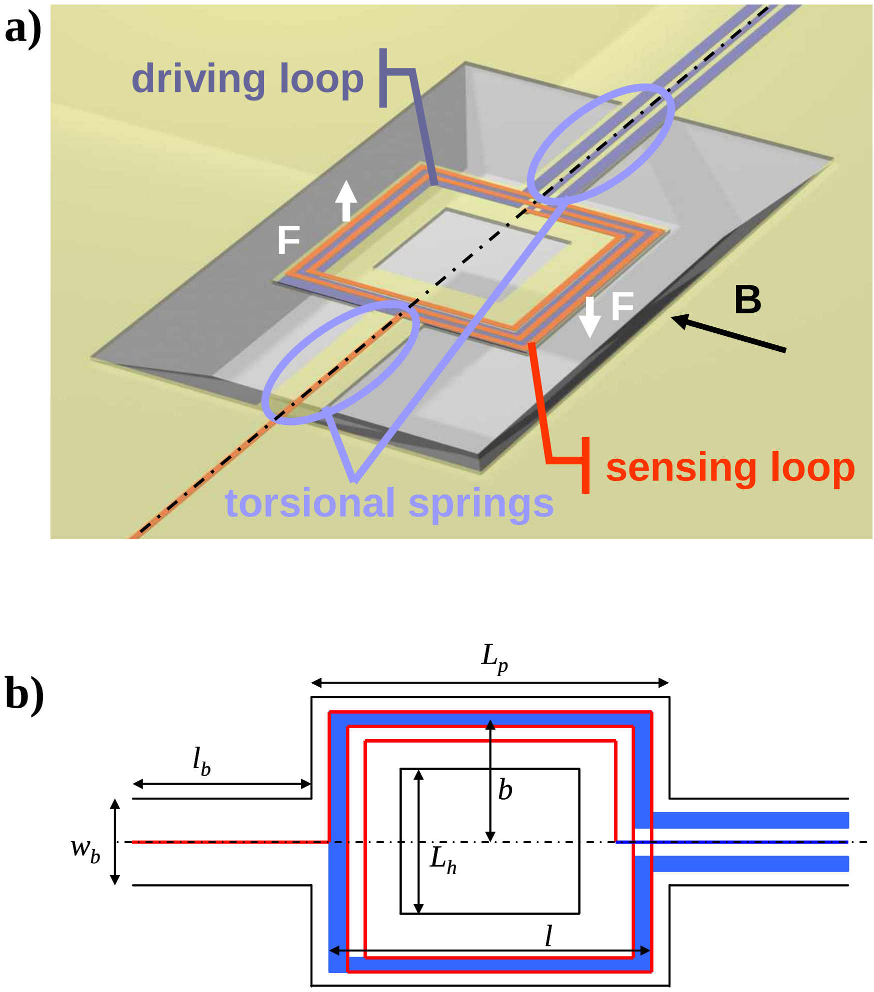

Figure 98: a) 3D sketch of the torsional microbalance proposed in this thesis. The black dash-dotted line represents the symmetry axis of the device. b) Top-view of the device.

Nonetheless, In spite of all the reasons examined in the following the novelty of the device, was the fundamental motivation, which led to investigate the possibility to fabricate the presented device.

The mechanical structure proposed is a torsional resonator composed of a central square holed suspended by two lateral beams, as shown in Figure 98. The hole in the central square is required only for the release of the device and its necessity will be detailed in section 4.4. It has only a slight influence on the device performance as shown in the following.

Two inductive loops are integrated in the plate. The first loop (in blue in Figure 98) is used to actuate the device, while the second one (in red in Figure 98) senses the movements of the rotor.

Both actuation and sensing work because of an external magnetic field **B**, directed as in Figure 98. **B** can be generated by a couple of small permanent magnets which can be included in the package: for example there are NdFeB magnets smaller than 1 mm^3, which can generate magnetic fields about 0.1 T in a region close enough to the magnets.

If the input loop carries the input signal current I, on each side of the loop the well known Lorentz Force **F** is exerted:

$$\mathbf{F} = l \cdot I \cdot \mathbf{i} \wedge \mathbf{B} \tag{187}$$

where l is the length of the loop side and **i** a vector, with unitary module and direction parallel to the wire. The force is zero on the sides of resonator central square which are parallel to the magnetic field **B**, while it is directed in z direction on the perpendicular sides as indicated in Figure 98. If the mechanical structure is symmetric with respect to an axis parallel to the lateral beams and crossing the centre of the central square, the total force in z direction is zero, avoiding at least theoretically the bending of the structure, while there is a twisting moment $\boldsymbol{\tau}$ which drives a rotation of the central square around the symmetry axis:

$$\boldsymbol{\tau} = \sum_i \mathbf{F}_i \wedge \mathbf{b}_i \tag{188}$$

where $\mathbf{F}_i$ is the force acting on the ith side of the loop, while $\mathbf{b}_\mathrm{i}$ is the moment arm, i.e. the distance between the ith loop side and the device symmetry axis.

Considering only the driving port as composed by only one loop the moment is due only to the force equal and opposite acting on two symmetric sides of the loop.

With respect to the direction of the vectors indicated in Figure 98, the magnitude τ of the moment $\boldsymbol{\tau}$ is obtained combining Eqs. (187) and (188):

$$\tau = 2blIB = A_{in}IB \tag{189}$$

where A_{in} is the area embedded by the input loop equal to the length l of one side of the loop multiplied by $2b$ which is equal to the perpendicular side of the loop (Figure 98b). B is the magnitude of the magnetic field.

Assuming as linear the relation between actuated moment and rotation of the plate, the plate rotates at a frequency equal to the frequency of the input current I because of the linearity of Eq. (189), while the lateral beams work as torsional springs.

If the frequency of the input signal is equal to the resonance frequency of the torsional plate the amplitude of the rotation is maximum, while aside from this frequency the resonator movements are much smaller if the quality factor is high. A high quality factor is expected even at atmospheric pressure, if the gap between the structure and the substrate is high enough to neglect squeeze film damping.

The rotation of the plate is detected by the output loop according to the Faraday-Lance law: if the resonator rotates the flow of the magnetic field **B** trough the output loop increases, leading to an electromotive force at the ends of the output loop, which opposes the change of flow. If the plate rigidly rotates around the symmetry axis, i.e. it does not bend, the output voltage V_{emf} is thus:

$$V_{emf} = -\frac{\partial \Phi_B}{\partial t} = A_{out}B\frac{\partial \sin(\theta)}{\partial t} \tag{190}$$

where Φ_B is the flow of the external magnetic field, A_{out} the area embedded by the output loop and θ the rotation angle. If the rotation amplitude is small:

$$V_{emf} \approx A_{out}B\frac{\partial \theta}{\partial t} \tag{191}$$

The resonance frequency of the excited torsional mode can be estimated considering the resonator as lumped-parameter system [10], composed of a mass and a spring: the lateral beams are considered as pure torsional springs, without any inertial properties, while the central plate is assumed to be extremely rigid in comparison with the springs, so that it rigidly rotates without bending. These assumptions introduce a small error with respect to the value given by FEM modal simulations as shown in section 4.3.2. and lead to the following easy formula for the resonance frequency f_0 of a torsional mode:

$$f_0 = \frac{1}{2\pi}\sqrt{\frac{2K_t}{J_p}} \tag{192}$$

where K_t is the torsional spring constant of each beam, which act in parallel so that their spring constant are added; J_p is the inertia moment of the plate. These parameters can be found by [105]:

$$K_t = \frac{GJ_0}{l_b} \qquad\qquad J_p = \frac{1}{12}\rho t\left(L_p^4 - L_h^4\right) \tag{193}$$

where l_b is the length of the lateral beams and G the material shear modulus ($G = E\big/\left[2\left(1+\nu\right)\right]$, with E Young's modulus and ν the Poisson ration); ρ is the material mass density, t the plate thickness, L_p the side of the square plate and L_h the side of the square hole inside plate. The expression for the inertia moment of the plate in (193) holds for thin plates ($t << L_p$) which is the case of the device in this thesis. Besides, L_h does not affect to much the inertia moment and consequently the resonance frequency: for example, if L_h is a half than L_p, J_p is only 1/16 smaller than if the resonator was not holed. Finally, J_0 is the polar moment of inertia of the beam cross-section. If the thickness t[17] of the cross section is much smaller than the width w_b, according to [105] J_0 can be calculated as:

$$\begin{aligned} J_0 &= \frac{1}{3}\cdot w_b\cdot t^3\cdot\left[1-\frac{192}{\pi^5}\frac{t}{w_b}\cdot\left(\sum_{n=1,3,5,\ldots}^{\infty}\frac{1}{n^5}\tanh\left(\frac{n\cdot\pi\cdot w_b}{2t}\right)\right)\right]\approx \\ &\approx (w_b - 0.6t)\cdot\frac{t^3}{3} \end{aligned} \tag{194}$$

At this point the basic working of the device as a resonator is known. To use the device as a microbalance it is necessary also to estimate how much mass adsorption from the outside can change the resonance frequency of the device. Assuming that no mass is adsorbed by the lateral beam, or that if any is adsorbed it neither changes K_t nor the inertial properties of the overall

---

[17] It is called as the thickness of the plate because they are equal due to the process chosen to fabricate the device (see section 4.4).

devices, if a mass δm is adsorbed by the surface of the central plate, the inertia moment of the plate is increased by an additional quantity δJ_p, while the spring constants of the beams remains unvarying. Thus the resonance frequency becomes:

$$f_{\delta m} = \frac{1}{2\pi}\sqrt{\frac{2K_t}{\left(J_p + \delta J\right)}} = f_0\sqrt{\frac{J_0}{\left(J_p + \delta J\right)}} \tag{195}$$

If $\delta J_p << J_p$ the new resonance frequency can be approximated as:

$$f_{\delta m} \approx f_0\left(1 - \frac{\delta J_p}{2J_p}\right) \tag{196}$$

Defining the frequency shift Δf as:

$$\Delta f = \frac{\delta J_p}{2J_p} f_0 \tag{197}$$

the sensitivity of the resonance frequency to a change of inertia moment can be defined as:

$$S = \frac{\Delta f}{f_0} = \frac{\delta J_p}{2J_p} \tag{198}$$

If the adsorbed mass δm is considered as uniformly distributed on the central plate, writing δJ_p as a function of δm and substituting to J_p its expression in (193), it is possible to write the sensitivity of the resonance frequency to the adsorbed mass as:

$$\begin{aligned} S = \frac{\Delta f}{f_0 \delta m} = \frac{1}{\delta m}\frac{\delta J_p}{2J_p} = \frac{\frac{1}{12}\delta\sigma\left(L_p^4 - L_h^4\right)}{\frac{2}{12}\rho t\left(L_p^4 - L_h^4\right)} = \\ = \frac{\delta\sigma}{2\rho t\delta m} = \frac{1}{2\rho t\left(L_p^2 - L_h^2\right)} \end{aligned} \tag{199}$$

where it is defined also $\delta\sigma$, as the variation of area mass density due to the mass adsorption.

Sometimes, it can be also interesting to evaluate the maximum shift of resonance frequency, which can be obtained. For example if the resonator is covered with a sensitive layer which allows the adsorption of molecules whose molar mass is m and if the maximum area density of adsorbed molecules (i.e. the area density of adsorption sites) is σ_S, the maximum frequency shift can be found from (197) as:

$$\Delta f_{MAX} = \frac{m\sigma_S}{2N_A\rho t} f_0 \tag{200}$$

4.1.1 Choice of the actuation and sensing mechanisms

In this section the motivation to use magnetic sensing and driving will be given, comparing them with other actuation and sensing mechanisms.

Electrostatic actuation generally widely in MEMS, anyway it needs not need small gaps between electrodes and rotor, so that it had no problem of stiction if the device is plunged in solution to sense for example DNA or proteins. Furthermore, if it is used in a device working in air for example a gas sensor, it experiences the decrease of the quality factor due to squeeze film damping, which is very important in electrostatically actuated devices, where the rotor vibrates in direction perpendicular to the electrodes and the gap is small.

Magnetically driven resonators are not affected by either stiction or squeeze film damping because they do not require small gaps.

Finally, magnetic actuation can be implemented with a bulk micromachining process, without any additional wafer bonding as in [16]. Apart from few examples [16], due to the small gaps required, electrostatic actuation generally is implemented using surface micromachining process, which can be CMOS-compatible only using new materials as SiGe [28], and are anyway more complex and expansive than bulk micromachining process, even if they allow to fabricate more complex MEMS structure. Indeed as shown in section 4.4, employing bulk micromachining techniques, it is possible to fabricate the proposed device by a single-mask CMOS-compatible post process, which can be performed at the end of a standard CMOS process.

With respect to the piezoelectric actuation it was discarded because it need a deposition and the lithography of a piezoelectric layer, made of material generally not used in standard CMOS fabrication. The goal of reducing the complexity and the cost of the technological process leads to prefer magnetic actuation to piezoelectric actuation.

Finally, magnetic actuation was also preferred to thermal actuation, which is used generally if the mechanical structure is a cantilever made of different layers with different CTE (coefficient of thermal expansion): magnetic actuation requires only the metal wires and the intermetallic dielectrics, which embed it, while to exploit bimorphic effect it is required to save part of the silicon under the oxide. Thus, using thermomechanical actuation, the overall mass of the device is higher if the area occupied by the device is the same, so that the ratio between the adsorbed mass (or the mass adsorbed per unit area) and the resonator mass (or the resonator mass per unit area) is lower than using magnetic actuation. In other words, the resonator magnetically actuated if adsorbs the same mass (or mass per unit area) as a thermomechanically actuated resonator with the same resonance frequency, the shift of resonance frequency is higher in the magnetic resonator, so that it works better as microbalance. The situation can be improved using the metallic layer to exploit the bimorphic effect, but also in this case the overall mass is anyway increased, because to control the effect the metal should occupy an area larger than the wires used for magnetic actuation.

Besides thermomechanical actuation is non-linear: the heat generated by current-carrying wire is proportional to RI^2, where R is the wire resistance and I the signal current. Last but not least, thermomechanical actuation is sensitive to temperature drifts: indeed the change of temperature can be due to the input signal current, but also to temperature variation of the environment or to the heating due other device on the chip.

A magnetic sensing was chosen, basically because to exploit also for the sensing the external magnetic field provided by NdFeB magnets. For the same reasons discussed about the magnetic actuation, magnetic sensing is preferable to electrostatic and piezoelectric sensing. Another mechanism is widely used for MEM microbalance, i.e. the piezoresistive sensing [101]. It is efficient but it requires or a potion of silicon substrate where fabricate diffused resistors (or piezo-transistors) [101], or polycrystalline resistors. The first solution implies a higher mass of the resonator and consequently a smaller sensitivity of the device as microbalance, as discussed about thermomechanical actuation. On the other side, piezoresistive properties of polycrystalline materials are not predictable and depend on the technological process used. Besides piezoresistive sensing is plagued by thermal drifts, which can vary the resistivity in the same way as a mechanical stress.

A resonant cantilever similar to the one proposed in [101], with polycrystalline piezoresistances, is fabricated on the same chip of the novel devices proposed in this thesis, in order to compare the performance of the two kinds of devices. Unluckily no measurements of the resonant cantilever are now available.

The bigger limit of the magnetic actuated and sensed devices is their bad scalability: the smaller the device the smaller the driving and sensing loops have to be, decreasing. according to Eqs. (189) and (191), the efficiency of both actuation and sensing. This bad scalability prevents also to reach high resonance frequencies, but this is not a big problem in the use of the resonator as microbalance: the higher the resonance frequency the higher the shift of frequency due to a mass adsorption according to Eq.(197), but at high frequency the quality factor decreases, increasing the effect of phase noise [19] and consequently reducing the minimum change of resonance frequency due to mass adsorption which can be distinguished from the noise. Besides the sensitivity to the adsorbed mass can be increased by scaling the device according to Eq. (199), but scaling also the surface where the particles can be adsorbed, cancelling this effect when a limited number of adsorption sites per unit area allowed, as in the case modelled by Eq. (200). Finally, at high frequency also the complexity of the driving and sensing electronics is complicated.

Another problem of magnetic sensing and actuation is that the package of the devices is more complex than for microbalance actuated in other way because of the magnets. Nonetheless magnetic actuation and sensing have significant advantages with respect to other actuation mechanisms, which largely justify their employ in MEM microbalances.

4.1.2 Choice of the mechanical structure

The mechanical structure of the presented resonator is chosen to exploit the magnetic sensing better other typical mechanical structure often used in MEM microbalances, as bending cantilevers (or clamped-free beams) and clamped-clamped beams. In the specific clamped-free and clamped-clamped beam has to be indeed “plates”, if their movements are magnetically sensed, because loop of metal with a significant area A_{out} has to be integrated on them to obtain a good sensing according to Eq. (191).

Basically a torsional structure has to be preferred to bending plates because a movement of the torsional resonator, as the one in Figure 98, produces a change of the flow constant along all the central plates, while in a flexural plate there are regions where the flow variation is zero. Thus there are parts of s bending plates where the presence of the sensing loop is useless.

The flexural-plates resonators in Figure 99 can be used as an example. For both the cantilever and the clamped-clamped plates the output electromotive force is given by:

$$V_{emf} = -\frac{\partial \Phi_B}{\partial t} = B\int_{-W/2}^{W/2}\int_{L_1}^{L_2} \frac{\partial \sin(\varphi)}{\partial t} dxdy \approx \int_{-W/2}^{W/2}\int_{L_1}^{L_2} \frac{\partial \xi_n}{\partial t}\frac{\partial \Phi_n}{\partial x} dxdy \qquad (201)$$

where W is the width of the loop, while L_1 and L_2 define the interval along x where the sensing loop is integrated (according to Figure 99 this interval is different for the two flexural resonators); ξ_n and Φ_n, are the part only dependent on the time and the mode shape of the nth resonance mode of the plate and can be defined as in section 2.1.

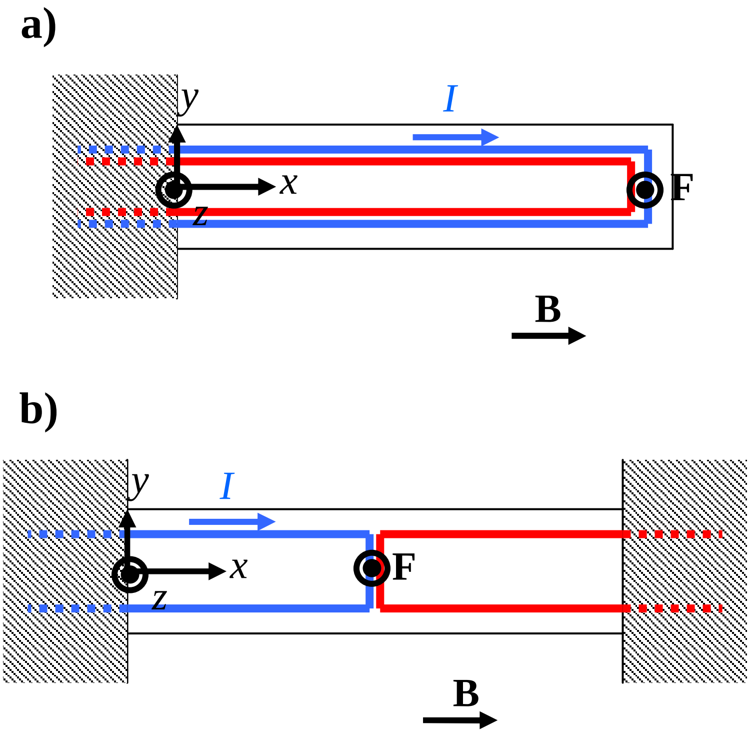

Figure 99: a) A hypothetical cantilever with magnetic sensing and actuation. b) A hypothetical clamped-clamped plate with magnetic sensing and actuation. In both cases the driving loop is in blue, the sensing loop in red.

Given that the mode shapes of bending plates and beams are equals, if the boundary conditions are equal [101], for the first mode of a cantilever Φ_{1cf} and for the first mode of a clamped-clamped beam Φ_{1cc} it is possible to write from [31]:

$$
\begin{aligned}
\frac{\partial \Phi_{1cf}}{\partial x} = \frac{\lambda_{1cc}}{L} \Bigg\{ & \left[\sinh\left(\lambda_{1cf} \frac{x}{L} \right) + \sin\left(\lambda_{1cf} \frac{x}{L} \right) \right] + \\
& - \frac{\cosh(\lambda_{1cf}) + \cos(\lambda_{1cf})}{\sinh(\lambda_{1cf}) + \sin(\lambda_{1cf})} \left[\cosh\left(\lambda_{1cf} \frac{x}{L} \right) - \cos\left(\lambda_{1cf} \frac{x}{L} \right) \right] \Bigg\} \\
\frac{\partial \Phi_{1cc}}{\partial x} = \frac{\lambda_{1cc}}{L} \Bigg\{ & \left[\sinh\left(\lambda_{1cc} \frac{x}{L} \right) + \sin\left(\lambda_{1cc} \frac{x}{L} \right) \right] + \\
& - \frac{\cosh(\lambda_{1cc}) - \cos(\lambda_{1cc})}{\sinh(\lambda_{1cc}) - \sin(\lambda_{1cc})} \left[\cosh\left(\lambda_{1cc} \frac{x}{L} \right) - \cos\left(\lambda_{1cc} \frac{x}{L} \right) \right] \Bigg\}
\end{aligned}
\tag{202}
$$

where the mode shapes are both normalized according to Eq. (19), L is the plate length as indicated in Figure 99, while λ_{1cf} and λ_{1cc} are respectively the first eigenvalue for a clamped-free plate and for a clamped-clamped plate ($\lambda_{1cf} = 1.87$ and $\lambda_{1cc} = 4.73$ according to [31]). The derivatives in (202) are represented in Figure 100, normalized with respect to the length: in the cantilever the region close to the end is useless because the derivative of the mode shape is close to zero, while at the free end there is a region with constant derivative, where the flow variation is maximum (Figure 100a). Thus the region, where the flow of **B** changes, is small and it is not possible to exploit the whole area covered by the sensing loop in Figure 99. The situation is even worse (Figure 100b) for the clamped-clamped plate, whose mode-shape first derivative has a zero at the anchor and one even in the middle.

Furthermore, this derivative changes its sign and this reduce the area where the output loop can be place to a half, because according to Eq. (201), the mode-shape derivative should have constant sign in the interval $[L_1, L_2]$, in order to maximize the output signal.

Bending plates and beams are thus less efficient than the torsional resonator, in order to obtain a good magnetic sensing.

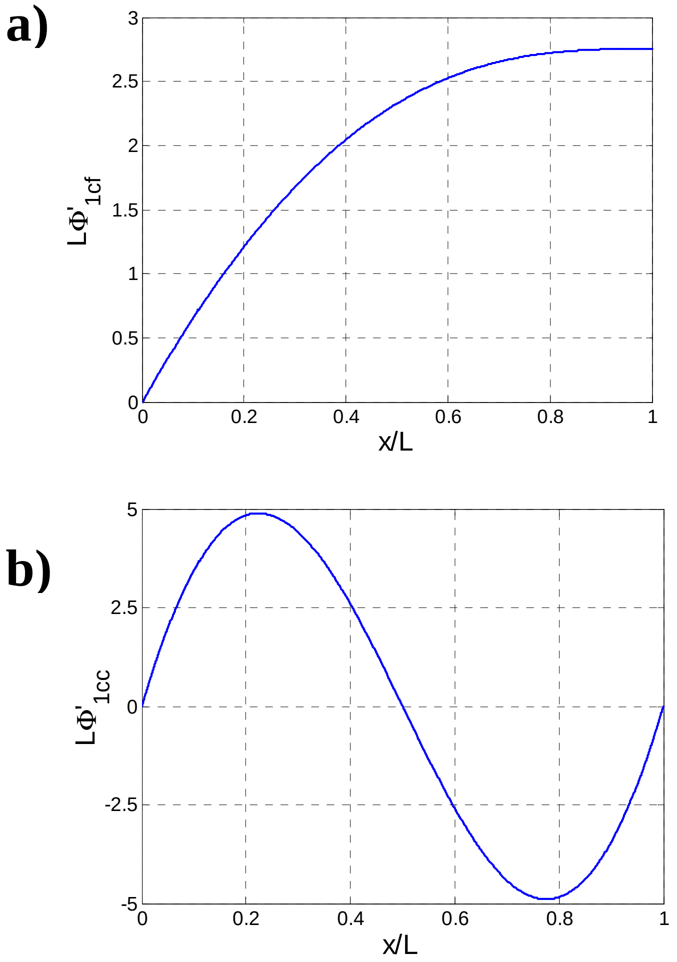

Figure 100: a) Graph of the first derivative of the mode-shape of a cantilever (Figure 99a). b) Graph of the first derivative of the mode-shape of a clamped-clamped beam (Figure 99b). In both cases the derivative is multiplied for the beam length L and the function is plotted with respect to the normalized length x/L.

4.2 Equivalent circuit

Before the discussion about the choice of the dimensions of the device and the layout design, an electrical circuit equivalent to the proposed microbalance is presented. This circuit was important during the design to optimize the sensing and the actuation of the resonator, also in dependence on the electronics of driving and sensing. Thus equivalent circuit can also used what is the best configuration of driving and sensing electronics. Furthermore, it can be used to evaluate the frequency response of the device. The equivalent circuit can be found in a way similar to what done in [10]. The device can be considered as a second-order lumped-parameter system with an inertia moment variable, due to the plate mass adsorption, so that its dynamic behaviour is ruled by the following equation:

$$\left(J_p + \delta J_p\right)\ddot{\theta} + D\dot{\theta} + 2K_t\theta = \tau \tag{203}$$

If τ is considered as a current and $\dot{\theta}$ as a voltage, $(J_P + \delta J_P)$ as a variable capacitance, $1/(2K_t)$ as an inductance and D as a conductance, Eq. (203) is the same as the equation following from the Kirchhoff's first law for a RLC parallel. Defining, from Eqs. (189) and (191), the coupling factors Γ_{in} and Γ_{out} as:

$$\Gamma_{in} = A_{in}B \qquad\qquad \Gamma_{out} = A_{out}B \tag{204}$$

it is possible to find the equivalent circuit in Figure 101. In the circuit also the electrical resistances R_i and R_o of the input and output port are included. T_1 and T_2 are ideal transformers, mimicking the electromechanical coupling at the input and output port, while $1/\Gamma_{in}$ and Γ_{out} are their respective turn ratios.

If the output port is loaded by an impedance Z_L the relationship between the voltage V_L on the load and the input current (i.e. the transimpedance) as a function of the frequency, is given by:

$$\frac{V_L}{I} = \frac{Z_L}{R_o + Z_L}\frac{\dfrac{\Gamma_{in}\Gamma_{out}}{2K_t}j2\pi f}{1 + 2\pi f\left(\dfrac{D}{2K_t} + \dfrac{\Gamma_{out}^2}{2K_t\left(R_o + Z_L\right)}\right) - \left(\pi f\right)^2\left[\left(J_P + \delta J_P\right)/\left(2K_t\right)\right]} \tag{205}$$

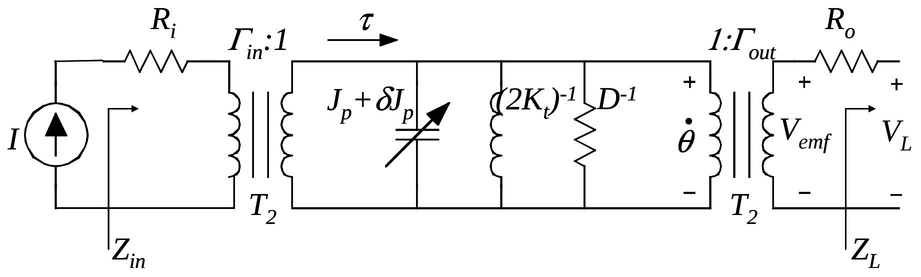

Figure 101: Equivalent circuit of the presented torsional microbalance.

To minimize the partition ratio $Z_L/\left(R_0+Z_L\right)$ in Eq. (205) it is necessary to obtain $Z_L >> R_o$. Besides if $Z_L >> \left(D/\Gamma_{out}^2\right)$ Eq. (205) can be written as:

$$\frac{V_L}{I}=\frac{\frac{\Gamma_{in}\Gamma_{out}}{K_t}j\pi f}{1+\frac{f}{f_{\delta m}Q}-\left(\frac{f}{f_{\delta m}}\right)^2} \tag{206}$$

where Eq. (195) is exploited and the quality factor of the resonator is defined as:

$$Q=\sqrt{2K_t\left(J_p+\delta J_p\right)}\Big/D\approx\sqrt{2K_tJ_p}\Big/D \tag{207}$$

Thus, if the electronics used to collect the output signal has very big input impedance, the load and the resistance R_o does not affect the transimpedance. This very important because a from (205) if Z_L is resistive the quality factor is decreased, while if the impedance has a significant reactive component, another pole is added to transimpedance function and it is possible to have a resonance frequency of the overall system (MEMS and electronics) different from the mechanical resonance frequency of the resonator. Therefore the best way of collecting the output signal is to use a voltage amplifier as output stage (Z_L very high).

On the other hand, in Eqs. (205) and (206) the device was assumed to be driven by an ideal current generator: indeed if the output impedance Z_O of the driving stage is not much higher than the input impedance of the device Z_{in}, the driving current partly flows in Z_O, leading to a transimpedance:

$$\frac{V_L}{I}=\frac{Z_O}{R_i+Z_O}\frac{\frac{\Gamma_{in}\Gamma_{out}}{2K_t}j2\pi f}{1+2\pi f\left(\frac{D}{2K_t}+\frac{\Gamma_{in}^2}{2K_t\left(R_i+Z_O\right)}\right)-\left(\pi f\right)^2\left[\left(J_P+\delta J_P\right)/\left(2K_t\right)\right]} \tag{208}$$

where Z_L was considered higher enough than both R_o and D/Γ_{out}^2 . Thus, repeating the same analysis done about Z_L, the best working condition for the device (i.e. the smallest input partition $Z_O/\left(R_i+Z_O\right)$, and transimpedance the closest to the ideal Eq. (206)) is obtained if it is driven by an ideal current generator. As the maximum input impedance ($R_{in}+D/\Gamma_{in}^2$ at the resonance) is generally very low, Z_O has a small effect, even if the value of this impedance is not so high.

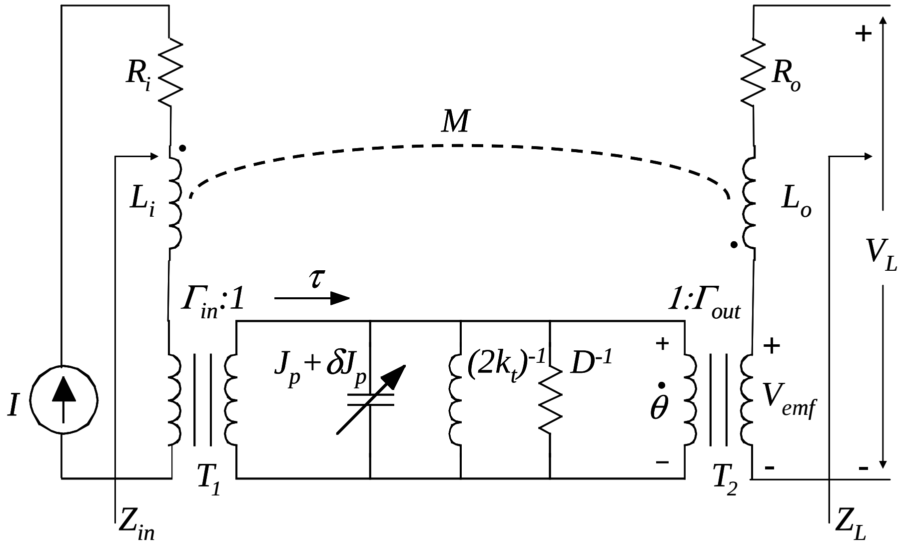

Figure 102: Equivalent circuit of the presented torsional microbalance, with parasitic inductances and mutual inductance.

A fundamental parameter is the transresistance R_T at the resonance, which has to be as high as possible to allow the highest output voltage at the resonance. In the ideal conditions, from Eq. (206), it is give by:

$$R_T = \left.\frac{V_L}{I}\right|_{f=f_{\delta m}} = \frac{\Gamma_{in}\Gamma_{out}}{K_t}\pi f_{\delta m} Q = \frac{\Gamma_{in}\Gamma_{out} Q}{\sqrt{2K_t\left(J_p + \delta J_p\right)}} \approx \frac{\Gamma_{in}\Gamma_{out} Q}{\sqrt{2K_t J_p}} \tag{209}$$

where it is assumed $\delta J_p << J_p$.

The circuit in Figure 101 can be further refined by considering the electrical inductance of the input and output loop, as well as the mutual inductance between the two ports (Figure 102). The effect of these parasitic elements was initially neglected due to the low resonance frequencies of the devices. Among these elements, the mutual inductance M is important because it leads to a couple of complex zeros in the transimpedance function. From the circuit in Figure 102, if Z_O and Z_L are large enough the transimpedance becomes:

$$\begin{aligned} \frac{V_L}{I} &= jM2\pi f + \frac{\dfrac{\Gamma_{in}\Gamma_{out}}{K_t}\pi f}{1 + \dfrac{f}{f_{\delta m}Q} - \left(\dfrac{f}{f_{\delta m}}\right)^2} = \\ &= jM2\pi f\,\frac{\left(1 + \dfrac{\Gamma_{in}\Gamma_{out}}{2K_t M}\right) + \dfrac{f}{f_{\delta m}Q} - \left(\dfrac{f}{f_{\delta m}}\right)^2}{1 + \dfrac{f}{f_{\delta m}Q} - \left(\dfrac{f}{f_{\delta m}}\right)^2} \end{aligned} \tag{210}$$

The couple of zeros occur at the frequency f_z:

$$f_z = \frac{f_{\delta m}}{\sqrt{1 + \dfrac{\Gamma_{in}\Gamma_{out}}{2K_t M}}} \tag{211}$$

The optimal condition is $M << \Gamma_{in}\Gamma_{out}/(2K_t)$, so that the frequency of the zeros goes to infinity and consequently the separation between poles and zeros is very high. On the other hand if $M >> \Gamma_{in}\Gamma_{out}/(2K_t)$, $f_z \approx f_{\delta m}$ cancelling the frequency selectivity of the resonator.

The overall mutual inductance M cannot be easily predicted because is due not only the two facing loop in Figure 98 but also by the mutual inductance between wires carrying the input and output. Besides, if the chip is measured using a PCB board, out-of-chip components and connections introduce additional parasitic elements which have the same effect of the mutual inductance between the two facing loop.

As shown by measurement results in section 4.6, the parasitic signal due to the mutual inductance is never large enough to cancel the frequency selective behaviour of the device.

4.3 Design

In this section the criteria used for the microbalances dimensioning will be discussed. The design choices are mainly driven by the necessity of fixing the resonance frequency and optimizing the magnetic actuation and sensing. According to Eq. (199), the mass sensitivity of the microbalance can be optimized by minimizing the area of the central plate, but such area reduction leads to a decrease of the area embedded by the input and output loop. Besides if the area where the mass can be adsorbed is reduced, it is expected for many application that the maximum shift of the resonance frequency is reduced if the plate area decreases, because the number of adsorption sites is lowered. Anyway according to Eq. (200) the higher the resonance frequency, the higher the maximum shift of the resonance frequency, which increases if the device dimensions decrease. But if the resonance frequency increases the quality factor could decrease, reducing the minimum change of resonance frequency which can be detected.

The design choice is to optimize the sensing and the actuation of the resonator, instead of optimizing its performance as microbalance, basically because if actuation and sensing are not efficient the resonator cannot even work: indeed the novelty of the device leads to be careful in this respect. Besides it is not certain whether the performance of the resonator as microbalance increases if its dimensions are scaled: basically it depends on how the quality factor changes if dimensions are scaled.

However, the sensitivity is estimated after the choice of layout parameters in order to verify the performance of the device as microbalance.

4.3.1 Layout

Two different devices were designed, one (type A) with a central plate as large as possible, in order to obtain a very efficient magnetic and actuation sensing, the other (type B) with a central plate smaller, in order to verify the effect of scaling on the device and to obtain an higher resonance frequency and consequently better performance with respect to the mass sensitivity (Eq. (199)) and to maximum resonance frequency shift, when the area density of the adsorption sites is limited (Eq. (200)).

The maximum dimensions of the central plate are limited in order to avoid the so-called *buckling* of the structure [70]. The buckling is mechanical instability which occurs in clamped-clamped structure, because of the residual compressive stress on the released device. If the stress is too high or if the structure from anchor to anchor is too long the resonator can break just after the release. According to [70] the maximum length L_{MAX} of a clamped-clamped beam under a compressive stress σ is given by:

$$L_{MAX} = \frac{1}{2\pi}\sqrt{\frac{EI}{A\sigma}} = \frac{1}{\pi t}\sqrt{\frac{E}{3\sigma}} \tag{212}$$

where A is the cross-section area, I the inertia moment of the beam and t its thickness. For beam longer than L_{MAX} a clamped-clamped beam cracks because of the buckling. Eq. (212) of course does not hold for the device proposed in this thesis, but can be used as a rough to evaluate approximately the maximum overall length (length of plate plus length of lateral beams) allowed for the device. The problem is that the residual stress is unknown because it is the first time that the proposed technological process is used to fabricate MEMS. If the overall length of the structure is 600 μm and if the thickness is about 3.5 μm (the same thickness of the fabricated devices according to process data and measurements performed with a profilometer) according to Eq. (212) a residual stress about 7.8 MPa is needed to make a clamped-clamped beam to crack (the device is made mainly of Silicon oxide whose Young's modulus is 70 GPa). A higher length leads to a smaller residual stress for the buckling. A maximum length of 600 μm was chosen for the device in order to reduce the probability of buckling of the structure. Nonetheless this possibility cannot be excluded until data about the residual stress are known.

The type A device was designed with a square central plate with a side length $L_p = 400\ \mu m$. The plate hole is a square with side $L_h = 200\ \mu m$, in order to obtain the correct release of the resonator (section 4.4.2). In this way each beam is long 100 μm. Each "beam" is wide 70 μm, because as explained in the following it has to be large enough to allow to the signal-carrying metals to reach the central plate through the “beam” and to obtain a distance between metals and “beam” sides large enough to prevent metal damages during the release process (section 4.4.2). Thus such “beams” are indeed plates. Anyway in the following they will be sometimes called beams to avoid confusion with the central plate. The length of the torsional springs is designed to be 100 μm because given the width a lower length could totally invalidate the approximations used in section 4.1 to find the device resonance frequency. Indeed if the beam is too short and too wide is behaviour is too far from the behaviour of a beam to assume for its spring constant the expression in Eq. (194). Besides if the beam is too short and large, its rigidity becomes comparable with the plate rigidity, invalidating the hypothesis of lumped-parameter system. Finally, according to Eq. (209), the higher the beam spring constant K_t, the lower the transimpedance at the resonance R_T, so that it is important to have long lateral beam to obtain a small K_t.

On the other hand, the central plate of type B device is smaller than the plate of type A microbalance: it is a square with side $L_p = 200\ \mu m$, with a central square hole with side $L_h = 100\ \mu m$. The beam width is approximately same as in the case of type A device (63 μm), while the beam length is 190 μm, higher than the length of type A device in order to obtain a behaviour closest to the working of a torsional beam, and a high R_T. As shown in section 4.4, the device is mainly made of BPSG (borophosphosilicate glass), layers, which have approximately the same mechanical properties of silicon oxide. Considering thus the device as completely made of silicon oxide ($E = 70\ GPa$, $\rho = 2200\ Kg/m^3$, $\nu = 0.17$) and assuming oxide plate and beam thickness $t = 3.5\ \mu m$, according to Eqs.(192), (193) and (194), the resonance frequency of type A device is 30.9 kHz, while for the type B resonator is almost three times higher, i.e. 84.92 kHz. The mass sensitivity is 0.54 μg^{-1} for type A device, leading to a shift of resonance frequency about 17 Hz/ng, while the mass sensitivity of type B is 2.08 μg^{-1}, resulting in a shift of the resonance frequency of 182 Hz/ng.

The maximum resonance frequency shift has been evaluated with respect to one of the possible applications of the devices: considering the device as covered by DNA filaments and consequently as a DNA sensors, the molecule molar mass in Eq. (200) can be assumed to be 1.5 Mg/mol while a reasonable value for the density of the adsorption sites is $\sigma_S = 10^{12}\ cm^{-2}$ [106]. Substituting these value in Eq. (200), a maximum resonance frequency shift $\Delta f_{MAX} = 50\ Hz$ for type A sensor and $\Delta f_{MAX} = 136\ Hz$ for type B device.

Magnetic sensing and actuation can be maximized not only by increasing the area of the central plate but also by increasing the number of loops, as for the output port in Figure 98. If the number of loops is increased, the area embedded by the output port augments, while with respect to the input port a high number of loops means a high number of element perpendicular to the magnetic field, and thus an increase of the actuated moment. As shown in section 4.2 the best performance of the device is obtained if it is driven by an ideal current generator, but if the resonator is driven by forcing a current in the input port, a high number of loops of the input port could not be the optimum choice: a high number of loops means that the width of the metal has to be smaller and consequently the maximum current the metal can carry has to be reduced in order to avoid metals damages, because of a too high density of current.

Current density in metals is generally by electromigration [107], a well known physical mechanism which shortens the lifetime of the metals and whose velocity increases if the current density carried by the metal or the temperature are increased. Thus in process data the highest current that the metal can safely carry at a certain temperature is generally specified.

Thus current flowing in input port should has to be limited to a certain value, given the width and the thickness of the metal, and consequently also the twisting moment τ is limited (Eq. (189)). But if the actuated moment is too small also the output signal could be too small to be discerned by noise, parasitic or interfering signal. Thus in the final design the input port of both type A and type B device is composed of only one loop, with a metal width $W_{min} = 20\ \mu m$. This is optimum width because a higher width would decrease too much the embedded area. Besides the larger the width of the input loop the larger the lateral beams has to be, so that if the input metal is too wide it possible to obtain R_T too low or to invalidate the formula used to estimate the resonance frequency and the frequency response at the resonance.

For the same reasons, the input loop is fabricated with the second level of metal: the process chosen to fabricate the device has three level of metals with different thickness and thus different maximum current per metal width. The thicker level is the third, but it is not used to fabricate the input port because is used as protective layer for the oxide layers underneath, during the some steps of the fabrication process (see section 4.4). Thus the second level is chosen because it is thicker and thus can carry more current than the first level. With this dimensioning the maximum current allowed at ambient temperature, according to the process data, is 20 mA. To maximize the embedded area the metal is designed as close as possible to the external edge of the plate. A space of 10 µm between the metal and the edge is anyway needed to avoid damages of the metal during the release (see section 4.4.2).

A wide and thick input metal reduces also the electrical resistance R_i of the port reducing the overall input resistance and lowering the input current partition if the output impedance Z_O of the current generator is not infinite. If the input port is fabricated using the metal 2 and $W_{min} = 20\ \mu m$, R_i is nearly 5 Ω for the type A device and nearly 8 Ω for type B device.

On the other hand the output port has not the problem of carrying current: according to what said in section 4.2 the optimum way to collect the output signal is using a voltage amplifier with very high input impedance ($Z_L \to \infty$), so that the output metal has not to be wide and can be fabricated with a width $W_{mout} = 1\ \mu m$ (minimum width allowed by layout rules) and with the first layer of metal the thinner one. Furthermore, also the resistance R_o is not critical if a voltage amplifier is used to collect the output signal: it can be easily neglected with respect to the typical input impedance of a voltage amplifier, even if it reaches some kΩ. Thus it is possible to design a lot of windings in the output port: 27 windings are designed for output port of type A microbalance and 14 for the output port of type B device. The final layout of a type A device is represented in Figure 103: the metal loops are indicated as well the layer of metal 3 covering the MEM structure to protect it during some fabrication. Also the area where the passivation and the intermetallic dielectrics are opened, is indicated. Such opening is important to help the release.

It is not easy to evaluate how much the multi-winding configuration is better than single-winding configuration, because at each turn of the metal the area added to the overall embedded area decreases and the exact calculation of the area embedded by each turn is not straightforward. Nonetheless, as shown in Figure 104, an approximated estimate of the overall embedded area can be carried out: the area embedded by the first turn is considered to be given by the product of the length of the first two consecutive sides after the first (the second and the third), then the following two sides are not considered, so that the area of the second turn is approximated with the product of the lengths of fifth and sixth sides; the area of the remaining windings is calculated in the same way. If the number of windings is N, the length of the first side L_1, the metal width W_{mout} and the space between two metal s, the area A_{out} embedded by the output loop can be thus approximated as:

$$\begin{aligned} A_{out} &= \sum_{i=1}^{N} \left[L_1 - 2(n-1)(s+W_{mout}) \right] \left[L_1 - (2n-1)(s+W_{mout}) \right] = \\ &= N \left[L_1^2 - (2N-1)(s+W_{mout}) + \frac{(N-1)(4N+1)}{3}(s+W_{mout})^2 \right] \end{aligned} \tag{213}$$

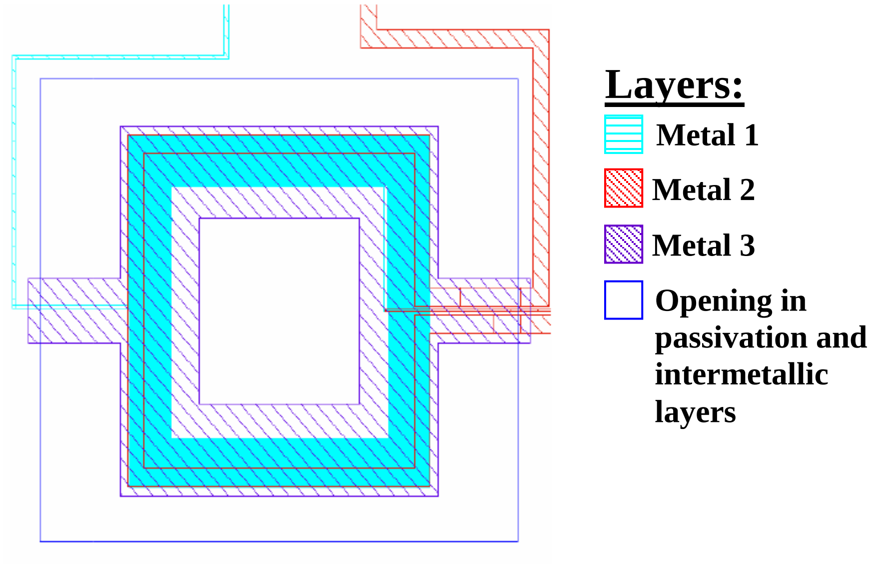

Figure 103: Layout of a type A microbalance (central plate 400x400 μm).

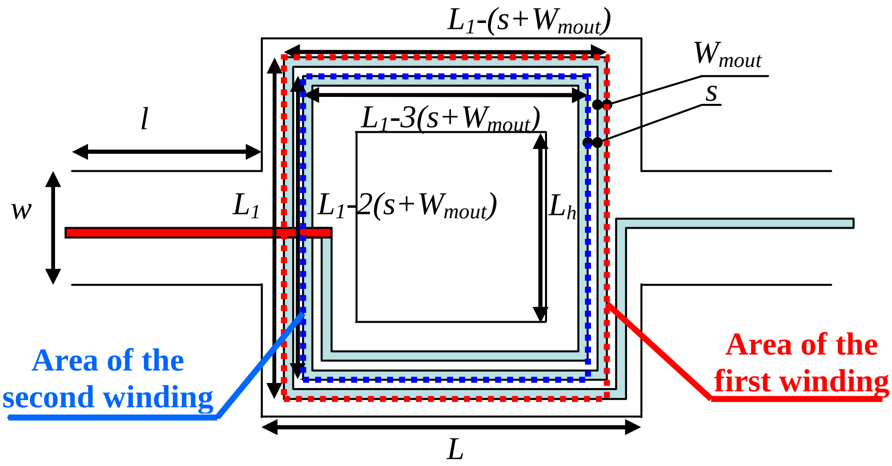

Figure 104: Output port with the more than one winding: the red dashed line surrounds the area approximately embedded by the first loop, while the blue dashed lines approximately surrounds the area embedded by the first loop.

	Type A	**Type B**
L_b	100 μm	190 μm
W_b	70 μm	63 μm
L_p	400 μm	200 μm
L_h	200 μm	100 μm
t	3.5 μm	3.5 μm
f_0	30.9 kHz	84.9 kHz
A_{in}	0.13 mm^2	0.026 mm^2
A_{out}	2.90 mm^2	0.33 mm^2
$\Delta f/\delta m = f_0 S_{\delta m}$	17 Hz/ng	182 Hz/ng
J_p	$1.54\cdot10^{-17}$ Kg·m^2	$9.62\cdot10^{-19}$ Kg·m^2
$2K_t$	$5.81\cdot10^{-7}$ N·m	$2.74\cdot10^{-7}$ N·m
R_i	5 Ω	7.9 Ω
R_o	7.9 kΩ	700 Ω
R_T	125.5 mΩ (B = 100 mT, Q = 100)	16.3 mΩ (B = 100 mT, Q = 100)

Table 1: List of the nominal dimensions and expected some main features of the devices, such as the resonance frequency, mass sensitivity, transimpedance at the resonance and port electrical resistances.

According to Eq. (213) the area embedded by a type A device is about 2.9 mm^2 (nearly 20 times the area of a single-winding output loop), while A_{out} is 0.33 mm^2 for a type B device (nearly 10 times the area of a single-winding output loop). Given that A_{in} is 0.13 mm^2 for type A microbalance and 0.026 mm^2 for type B device, if the external magnetic field is 100 mT and the quality factor 100, according to Eq. (209) the transimpedance at the resonance R_T is 125.5 mΩ for type A and 16.3 mΩ for type B device. In Table 1 the dimensions and the expected performances of the two designed devices are summarized.

4.3.2 Post-layout FEM simulations

To verify the resonance frequencies of the designed devices some FEM modal simulations were carried out with Femlab[43]. The high ratio between structure plate side L_p and the thickness t as well as between the width W_b and the length l_b of the lateral beams and the thickness t, makes difficult to perform a 3D simulations of the structure. Thus the device was modelled with shell elements, i.e. 2D elements fit to simulate thin solids. In a first approximated simulation, the resonator was assumed to be made entirely by silicon oxide silicon ($E = 70\ GPa,\ \rho = 2200\ Kg/m^3,\ \nu = 0.17$), i.e. the metal loops are neglected. Metals are made of aluminium which has material properties not much different for the silicon dioxide properties, in particular the Young’s modulus is almost the same. Material properties of the aluminium are $E = 70\ GPa,\ \rho = 2700\ Kg/m^3,\ \nu = 0.35$. Thus the effect of aluminium metals should be small, considering also that they do not cover the whole resonator. In particular their presence should reduce the device resonance frequency, because of the higher mass density and Poisson’s ratio with respect to the silicon oxide.

Femlab simulation considering the whole resonator as made of oxide predict a resonance frequency $f_0 = 27.6\ kHz$ for type A device and $f_0 = 82.4\ kHz$ for type B device. Both the resonance frequencies are lower than the calculated one, essentially because the rigidity of the plate is not much higher than lateral beams, so that the central plate stiffness cannot be neglected and the device cannot be considered as a lumped-parameter system. The contribution of the plate is to decrease the overall stiffness of the structure and consequently its resonance frequency.

The previous observation is confirmed by the fact that the percentage error is higher for the type A device (error 12%) than for type B device (error 3%): lateral springs of type A devices are shorter and thus stiffer than in type B.

Besides the central plate is larger in type A than in type B, so that at the resonance it can be slightly bended in direction perpendicular to the lateral beams instead of rigidly rotating, introducing a further discrepancy with respect to the lumped-parameter model.

Modal simulations gives also information with respect to the other resonance modes of the structure: for type A device the torsional mode is the fundamental and it is followed by a bending mode at 33 kHz (Figure 105a), which cannot be anyway stimulated by the designed actuation, which results in a twisting moment but not in a force perpendicular to the plane where the device lies. The following mode is the third at 83 kHz (Figure 105b), i.e. at a frequency far enough from the resonance frequency of the fundamental mode to affect the spectral purity of an oscillator using the device as a frequency selective element (even a rough low-pass filter can remove this interfering mode). With respect to the type B device, the fundamental mode resonates at about 47 kHz and is a bending mode similar to the second mode of type A device and consequently cannot be excited by the actuated moment. The torsional mode is the second mode, the third is at 136 kHz and is again a bending mode, while the fourth, at 294 kHz, is similar to the third mode of type A device and is at frequency high enough to be neglected.

The effect of the metals was estimated still performing a FEM modal simulation using shell elements, but defining three different regions one with two, the second with one and the third with no metal layers. Such regions can be defined by importing the layout of the device (Figure 103). If the thickness of each metals and intermetallic layer are known, it is possible to determine different material properties for each region, by extracting a mean value of the material properties of all intermetallic and metal layers, weighted by their respective thicknesses.

Such simulation was performed only for type A device, leading to a simulated resonance frequency about 27.0 kHz. As expected, the difference with the result from the simulation carried out with the whole resonator made of silicon oxide is very small (relative error about 2%) and the effect of the metal loop is to decrease the resonance frequency as they make heavier the structure. A similar effect is expected for type B device. In Figure 106 the deflected shape of the device according to this last simulation is shown. Further simulations carried out also using Ansys, gives the same results as Femlab.

The idea and the design of the resonator were the subject of a master degree thesis [104], and were proposed at an international conference [102].

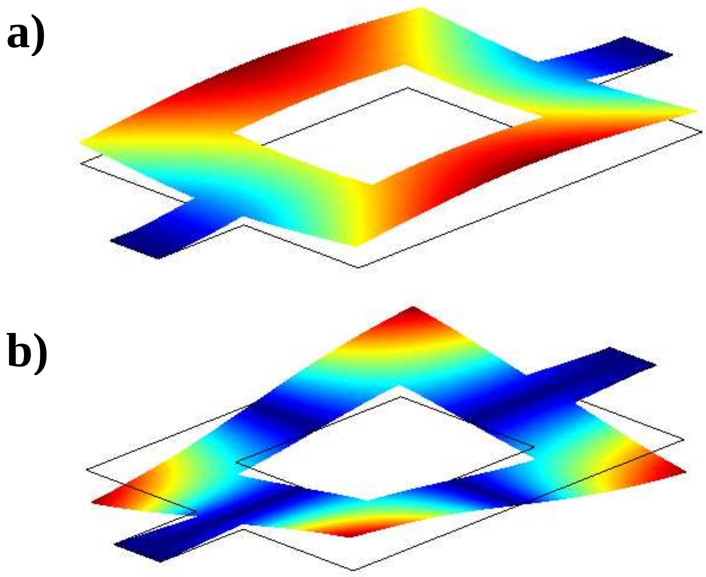

Figure 105: Deformed shape of two parasitic resonance modes of a type A device: a) Second mode at 33 kHz; b) fourth mode at 83 kHz. Colours close to the red represent regions where the displacement is highest, colder colours (blue) the region where the displacement is smallest.

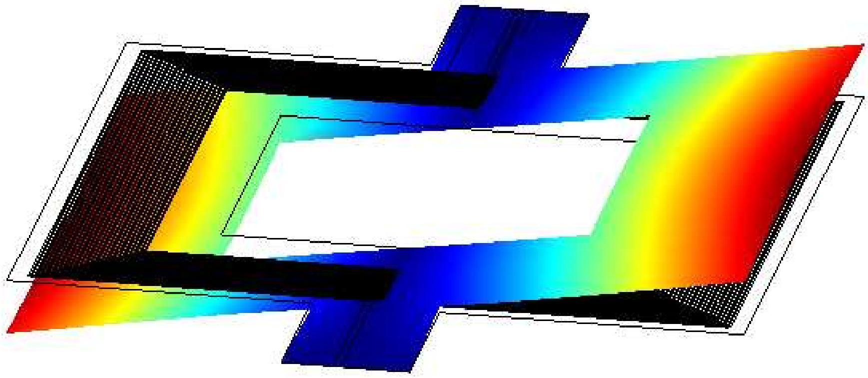

Figure 106: Deformed shape of the fundamental resonance mode of a type A device. Colours close to the red represent regions where the displacement is highest, colder colours (blue) the region where the displacement is smallest. The figure comes from FEM modal simulation including metal loops and performed with Femlab.

4.4 Fabrication: a CMOS-compatible process flow

The fabrication of the device was carried out by two separate flows: first fabrication steps were performed in STMicroelectronics Agrate plant, using *BCD6* process. On the processed chips there was not only the sensor, but also some integrated electronic circuit. After that, in the laboratory of Information Department of the University of Pisa, a CMOS-compatible post-processing was carried out to release the mechanical structure.

4.4.1 First process steps in a CMOS standard technology

The initial part of the sensor fabrication was fulfilled using BCD6 process, a standard mixed technology including BJT, CMOS and DMOS (MOS for power application). In this thesis only the process features, which are strictly connected to the fabrication of the device, will be given.

The foundry makes available two options for the process, one with 5 levels of metal, the second with 3 levels of metal. To fabricate the proposed device 3 levels are enough, besides a higher number of metal implies also more level of intermetallic layers leading to a thicker and thus less sensitive microbalance, as shown in Eq. (199). Besides more intermetallic layers means a thicker oxide layer in the region where it has to be removed in order to release the device, and consequently a more difficult post-processing: as shown in 4.4.2 the more critical step in the post-processing is just the removal of this oxide layers. The intermetallic layers are made of BPSG.

The first stage the fabrication is accomplished according to the mask defined by the layout in Figure 103: the input and output loops are fabricated using respectively the first and the second level of metal. The third level of metal overlap the whole region which will be the future released structure. This layer protects the structure by the fabrication step indicated by the fourth masks indicated in Figure 103, i.e. the opening of passivation and intermetallic layers, obtained by plasma etch. This plasma etch anyway does not remove all the intermetallic dielectrics, so that, the first task of the post-processing is to remove the residual silicon oxide which surround the resonator.

4.4.2 A CMOS-compatible post-processing to release the MEMS

In the post-processing, first a selective removal of the silicon oxide around the device is performed. Then the metal 3 protective layer is eliminated and finally the crystalline silicon substrate under the plate is etched by a tetra-methyl ammonium hydroxide (TMAH) to release the resonating structure. All these three steps are CMOS-compatible, because require no high temperature step and does not damage CMOS devices. In particular the TMAH anisotropic etch allows a high compatibility with standard microelectronics technologies, primary because it does not contain metallic ions detrimental to CMOS reliability, as for example the ions K^+ released by KOH etchings. Besides it can be specifically tailored to avoid the etching of the metal layers, basically made of aluminium) used for electrical connections as demonstrated by [108] and [109]. Only two lithographies and one mask are needed for the complete release of the structure.

A schematic section of the device along the plate immediately before post-processing (i.e. as obtained from the foundry) is given in Figure 107a.

The post-processing, used to release the plate and springs, requires two lithographic steps. Initially, during the first lithography, the photoresist is used to protect the plate and springs areas, and is removed in the areas where the silicon substrate has to be etched; practically the area covered by the photoresist is given by the inverse of the union of the metal 3 and oxide openings masks in Figure 103.

Later on it was observed that the metal 3 protection is enough to protect the springs and the central plate during a following buffered HF (BHF) wet etch, used to remove the oxide where they are not protected by the photoresist or the metal 3. BCD6 metal 3 is an alloy mainly composed by aluminium and BHF etch remove partially also aluminium, but the part of metal 3 which is removed during the BHF etch is negligible because the thickness of such metal layer very high and because according to experimental observation the etch rate of BCD6 metal 3 in a BHF solution is much slower than oxide etch rate. Thus the first lithographic step can use a mask equal to the mask defined by the layer for the oxide opening in Figure 103, i.e. the photoresist can be removed both on the resonator and where the oxide should be open. It allows to use in this first lithographic step the same mask used to remove the metal 3 protection in the second step.

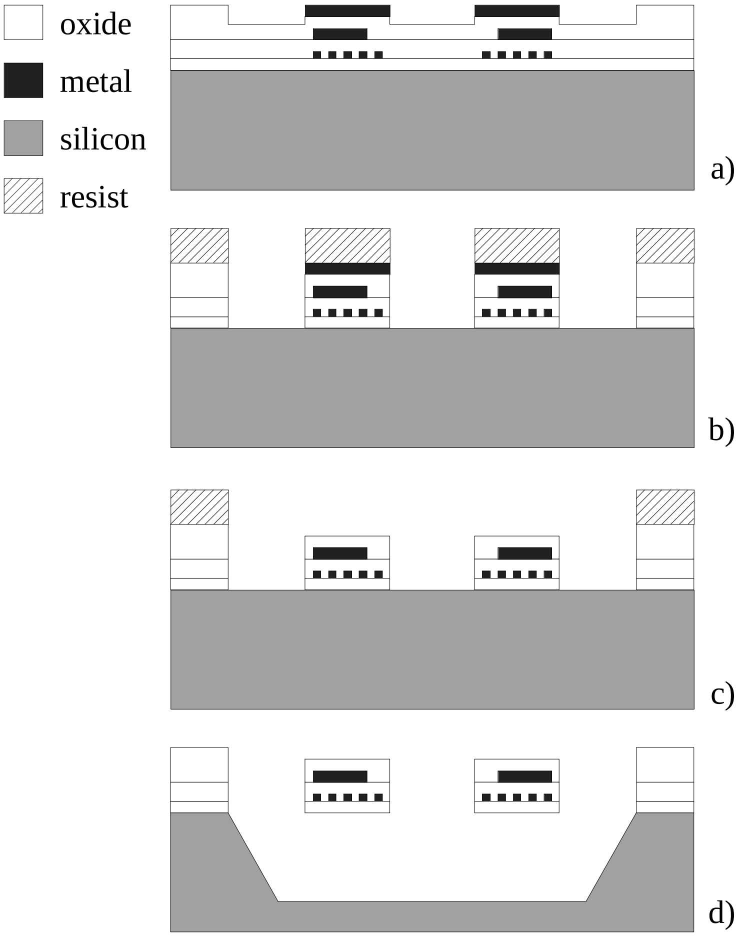

Figure 107: Cross-sections of the plate at different times during post-processing: a) as received from the foundry, b) immediately after the BHF etch, c) immediately after the aluminium etch (the protective metal has been removed), and d) after the TMAH etch.

After the removal of photoresist the BHF etch is performed to remove approximately 2.5 µm of oxide to expose the silicon surface (Figure 107b). Composition of the BHF solution is approximately 6.8% of HF, 34.6% of NH_4F and 58.6% of deionised water. This step is the most critical in the process, because the initial non-planarity of the sample impairs the photoresist coverage of the plate, and also because, due to the large thickness to be removed and the nature of the wet etch, a significant overetch takes place, and the metal loops, embedded in the oxide plate, can be exposed. To avoid to expose metal loops and thus their damage during the subsequent aluminium etch, the metals of each device are designed at a distance of at least 10 μm from the structure edges.

On the other hand, the bad photoresist coverage and thus the bad adhesion of the photoresist to the surfaces facilitates the removal of some portion of photoresist during the etch. To avoid it the photoresist adhesion is improved by using a *primer*, a polymer which can be deposed with a spinner like the photoresist. Besides, after the photoresist development, a *hard post baking* follows instead of a standard post baking: the chip is exposed to UV for 3 minutes and after is baked at a higher temperature than the standard (140°C instead of 115°C). Because of the higher temperature the photoresist is harder to remove. On the other hand the preliminary UV exposition is necessary to partially break the polymeric links of the photoresist, allowing to remove it with acetone at the end of the BHF etch. The primer and the hard post-baking allow the photoresist to not be damaged for 30 minutes, i.e. the time needed to remove 2.5 μm of oxide around the resonator. However, at the end of the BHF etch the photoresist is too damaged to be used as a mask also for the aluminium etch.

Thus, a second lithography is performed to expose the plate and silicon area, while the outer areas and pads are protected. The same mask employed in the first lithography can be used.

An aluminium wet etch is used to remove the protective metal layer on top of the plate. The composition of the solution is about 71.6% H_3PO_4, 3.4% CH_3COOH and 25% of deionised water. The time needed for the complete removal of the metal is 12 minutes at 40°C.

After the etch of the metal 3 a stylus profilometer can be used to evaluate the thickness of the oxide layers where they were not removed, in order to estimate the resonator thickness *t*. The value of *t* was found to be generally around 3.5 μm, confirming what estimated by process data.

The removal of the protective layer is necessary because after the BHF is protective function is no needed anymore, and if it was retained, the final devices would very thick and the mass sensitivity of the microbalance very low. Besides the devices are resonator moving in a magnetic field and some parasitic currents could be generated in a thick metal plate on them. Such parasitic currents would oppose to the movement which had generated it by driving a magnetic field acting in opposition to the external one.

At this point, before the TMAH etch, a layer of about 500 nm of aluminium is deposited by evaporation on the back of the chip, because during the following etch the back of the chip would be greatly etched as well, leading to the reduction of the velocity and efficiency of the etch. Besides a too large reduction of the chip thickness could also make easier to break the chip during the following manipulations.

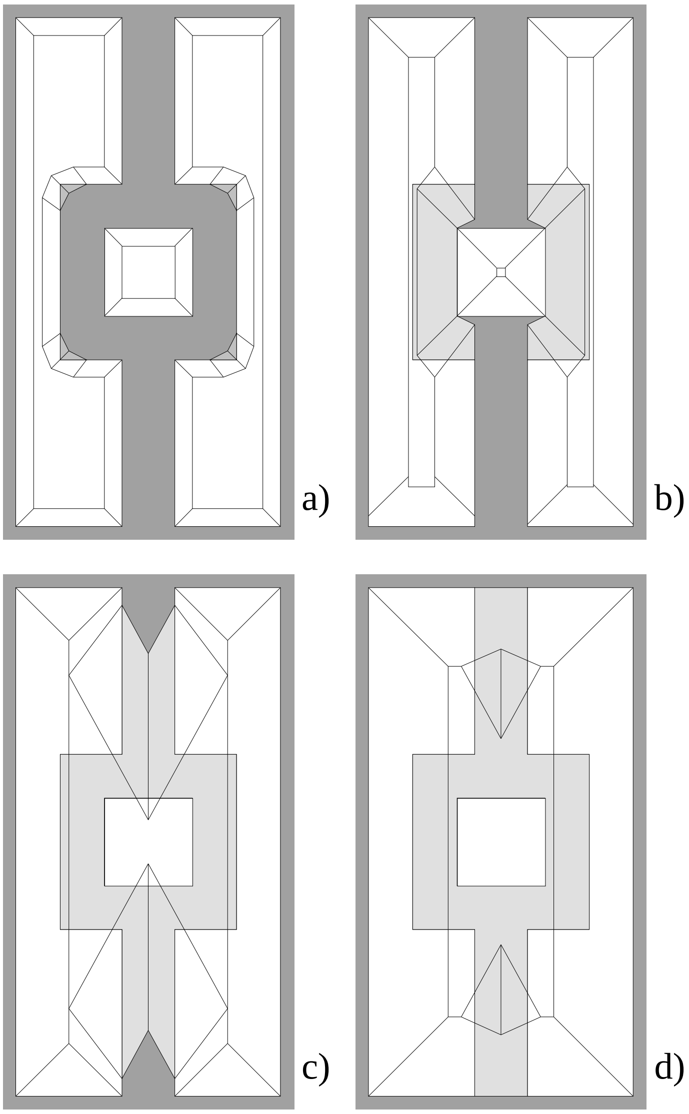

Figure 108: Top view of the evolution of the TMAH etch at four subsequent times (from a to d). Dark grey indicates areas where the oxide stack is still anchored on the silicon substrate, light grey areas where it is released. In d) the residual silicon wedges on the bottom of the cavity are visible.

After the deposition of aluminium at the back of the chip, the sample is ready for the TMAH etch (Figure 107c). During the etch, the metal pads are exposed to the etching solution. To reduce the etch rate of aluminium, TMAH is often added with dissolved silicon ([108],[109]) or silicic acid [110]. These are known to reduce the etch rate of aluminium, but the silicon etch rate is also greatly reduced, and the surface roughness is impaired by the appearance of pyramidal hillocks. Silicic acid is often preferred because it is more quickly dissolved but, as a result of its tendency to adsorb large amounts of humidity, the actual quantity of silicon added to the solution is more difficult to control.

To recover an adequate etch rate for silicon, an oxidising agent is commonly added to the solution. In our case, the selected compound was ammonium peroxodisulphate (AP). Unfortunately, such TMAH-based solutions are known to be susceptible to rapid aging, and, unless periodically replenished of AP at very short intervals [111], their etching speed drops considerably. For this reason, all the solutions for the etching were prepared immediately before use and never used for longer than one hour.

Preparation of the solution is as follows: 80% weight of deionised water is added to 20% weight of a 25% TMAH solution (Fluka chemicals code 87731) to obtain a 5% TMAH solution in weight. Afterwards the solution is heated to 50°C and 20 g/l of silicic acid hydrate (Fluka chemicals 60780) are added. The solution is stirred to allow the complete dissolution of the silicic acid, revealed by the clear appearance of the solution. The dissolution would take between 30 and 60 min. The solution was then heated to 80°C (the etching temperature) and, immediately before use, 6 g/l of AP (Fluka chemicals 09915) were added and again allowed to completely dissolve (a step requiring 2 minutes at most).

At this point, the silicon chip carrying the microbalances was introduced and the etch carried out. During the etch, the solution was not stirred. After 60 min of etch, the chip was moved to a second batch of solution, prepared in exactly the same way, for as many times as was required to completely release the plate from the silicon substrate. As the pH of the solution is believed to influence the etch rate and selectivity [112], it was periodically monitored during the etch: its value typically remained between 12.1 and 12.4. The whole procedure proved to be reliable and insure a reasonably constant and predictable etch rate.

The same stylus profilometer employed to estimate resonator thickness can be used to measure the {1 0 0} silicon etch rate. Its average value was evaluated to be about 35 μm/h. To completely release the resonator, 2 h 45 minutes of etch were required. Consequently, three batches of fresh solution have to be used for every sample. SEM and optical microscopy observation of the samples did not detect any appreciable damage of the metal pads. The total depth etched into the substrate was about 100 μm. Such depth is not required for operation of the plate, but because of the nature of the etch.

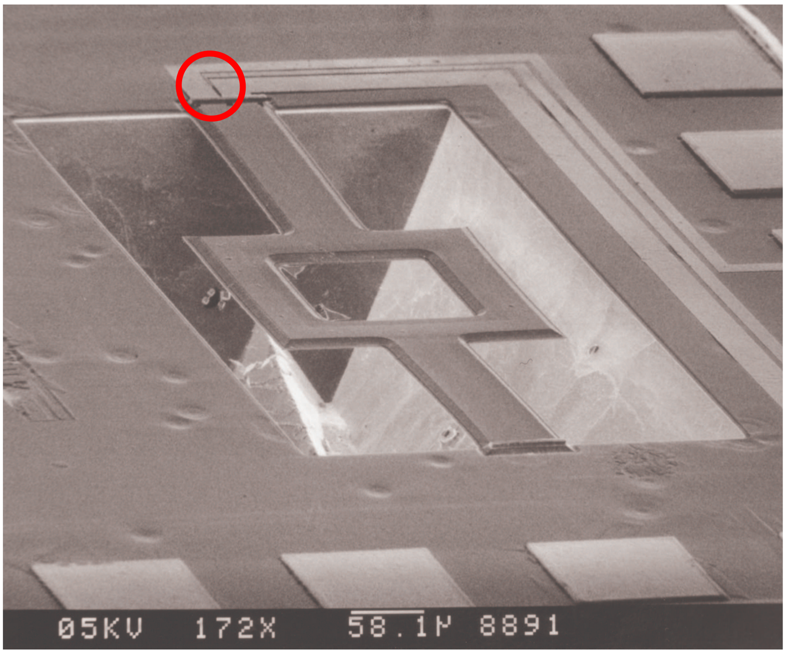

Figure 109: SEM photograph of a type B device after TMAH etch. One of the silicon wedges is visible on the bottom. The tiny output metal is circled in red where it can be damaged by the aluminium etch.

Actually, the torsional beams are released only after the corners of the plate are completely underetched, and convex corners (which are preferential etching points) at the end of the beams are exposed. The evolution of the etch at four different times is sketched in Figure 108. For the same reason, two residual silicon wedges are present at the bottom of the cavity (Figure 108d). One of them is visible also in Figure 109, showing a SEM picture of a typical sample.

Although the complete release of the plate is achieved, the aforementioned oxide overetch problem can result in a damage to the metal structures. In particular, the thin output loop connections to the pads is exposed during the BHF and subsequently damaged during the aluminium etch. The metal can be damaged in the point indicated in Figure 109 and in the picture at the optical microscope in Figure 110, where the metal loops are more recognizable than in the SEM picture in Figure 109.

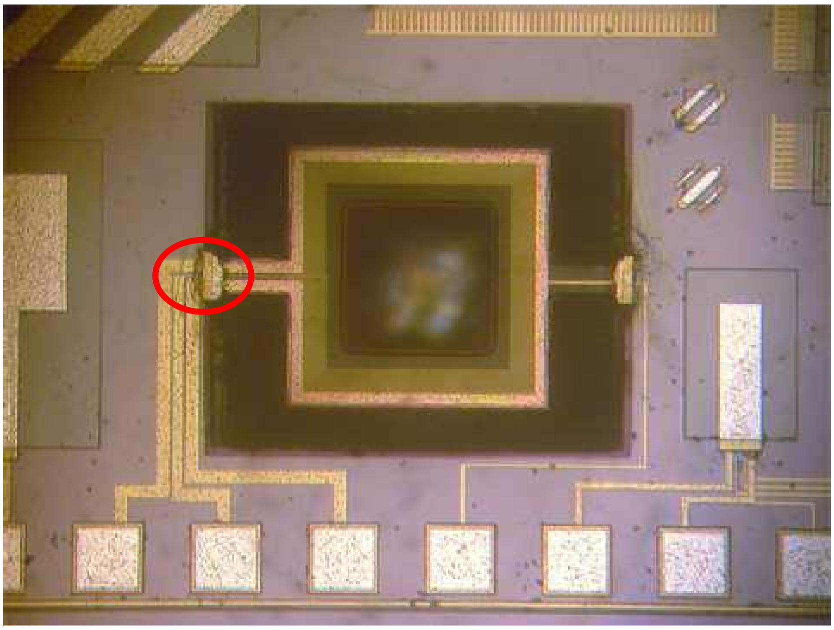

Figure 110: Top-view of a type A device after TMAH etch, observed through an optical microscope. This view show the metal loops better the SEM picture. The tiny output metal is circled in red where it can be damaged by the aluminium etch.

Initially the metal was so damaged that it could not allow the electrical connectivity. The problem was reduced by using a mask 20 µm smaller in direction parallel to the length of the lateral springs. With this mask reduction the electrical connectivity of the output loop is now obtained for the large majority of the processed devices.

The main features of the post-processing described in this section are also published in [103]. Some small differences between what said in this thesis and in such paper are due to some process improvements accomplished after the paper publication.

4.5 Experimental setup

To evaluate the performance of the proposed microbalance, three different setups are used: first the electrical resistance R_i and R_o are evaluated by a four contact measurement, carried out using a multimeter. This measure is done to detect preliminary the device with input and/or output loops damaged: a damaged metal results a R_i or R_o much higher than usual. They can be even so high that the electrical connectivity is not guaranteed. A completely broken input loop is very unusual, as well as a high R_i, while sometimes the output loop is sometimes interrupted due to damages in the region circled in red in Figures 109 and 110. After the reduction of the size of the mask used for BHF and aluminium etch, the occurrence of this problem is low. The value of the resistances R_i and R_o of working devices are respectively around 5.5 Ω and 2.9 kΩ for type A device and about 7.9 Ω and 680 Ω for type B device. Such measured values practically agree with the expected values (see Table 1).

After the preliminary verification of electrical connectivity the mechanical working of the device can be checked by extracting the mechanical frequency response of the resonator, through an optical measurement setup. Then the frequency response of the overall device is performed with an electrical measurement. The acquisition of the frequency response is long as shown in the following, thus the preliminary screaming of the devices with damaged input or output loop, allow to save a lot of time. The setup for electrical measurements can be also slightly modified to allow the evaluation of the effect of humidity on the resonance frequency of the device.

The measurements presented in this thesis characterize the working of the device as resonator and not as microbalance, as no attempts to cover the device with a sensitive layer were performed.

In the following of this section a description of the optical and electrical setup to acquire the device frequency response will be discussed.

4.5.1 Setup for optical measurements

This first measurement setup exploits the principle of the optical leverage: a laser beam is pointed on the central plate, almost perpendicular to it. A screen is placed perpendicular to the laser ray at about 2 meters far from the device to collect the flicker reflected by the plate (Figure 111a). If the resonator rotates around its symmetry axis parallel to the lateral springs, the reflected ray is rotated of an angle 2θ, if θ is the angle of rotation of the resonator (Figure 111b).

The distance L of the screen from the device amplifies the displacements of the light spot on the screen due to the reflected ray rotation, allowing to detect even very small rotation of the device central plate. If the microbalance static rotation is θ the light spot on the screen moves at a distance d with respect to the position of the spot when the microbalance is still, according to the following equation, which can be found by the geometric construction in Figure 111b:

$$d = L\tan\left(2\theta\right) \approx 2\theta L \tag{214}$$

where the angle θ is considered small enough to assume $\tan\left(2\theta\right) \approx 2\theta$, as generally is, according to the results shown in next section. If the resonator oscillates at a frequency around the resonance frequencies of the presented devices, human eyes are not able to follow the spot movements on the screen, and actually a dilatation of the spot is observed, with a decreasing on its intensity, because the time the spot stays in a certain position is reduced if the movements amplitude is increased. The spot becomes approximately an ellipse with its major axis increasing as the movements amplitude increases. If the rotation of the central plate of the microbalance is given by a sinusoidal function $\theta = |\theta|\sin\left(\theta\right)$, calling *R* the length of the spot major axis, following again Figure 111b, the amplitude of the central plate rotation can be found as:

$$|\theta| = \frac{R-r}{4L} \approx \frac{R}{4L} \tag{215}$$

where *r* the radius of the spot when the device is immobile, which has to be much smaller than *R* to guarantee the measurement accuracy.

This kind of optical measurement is affected by errors for both small and high value of θ: for small value of $|\theta|$, *R* is too close to *r* to have an accurate measure, so that reliable values of the measure can be taken only if *R* is at least twice or three times as high as *r*. On the other hand for high value of $|\theta|$ the intensity of the spot decreases so much, that is difficult to detect the borders of the spot, even in a dark room.

The external magnetic field is provided by two facing macroscopic magnets whose size is about 12x20 cm, placed at a distance of about 5 cm from each other; the magnetic field varies from 70 to 80 mT for B inside the space between the two magnets, according to measurements carried out with a Hall sensor (A SS94A by Honeywell). As for the large part of the electrical measurements macroscopic magnets are used instead of NdFeB micro-magnets, because despite their high magnetization, the generated magnetic field decreases very quickly with the distance. If a surface of the NdFeB magnets, the magnetic field can be as high as 200 mT, at a distance of less than 1 cm it can be smaller than 30 mT.

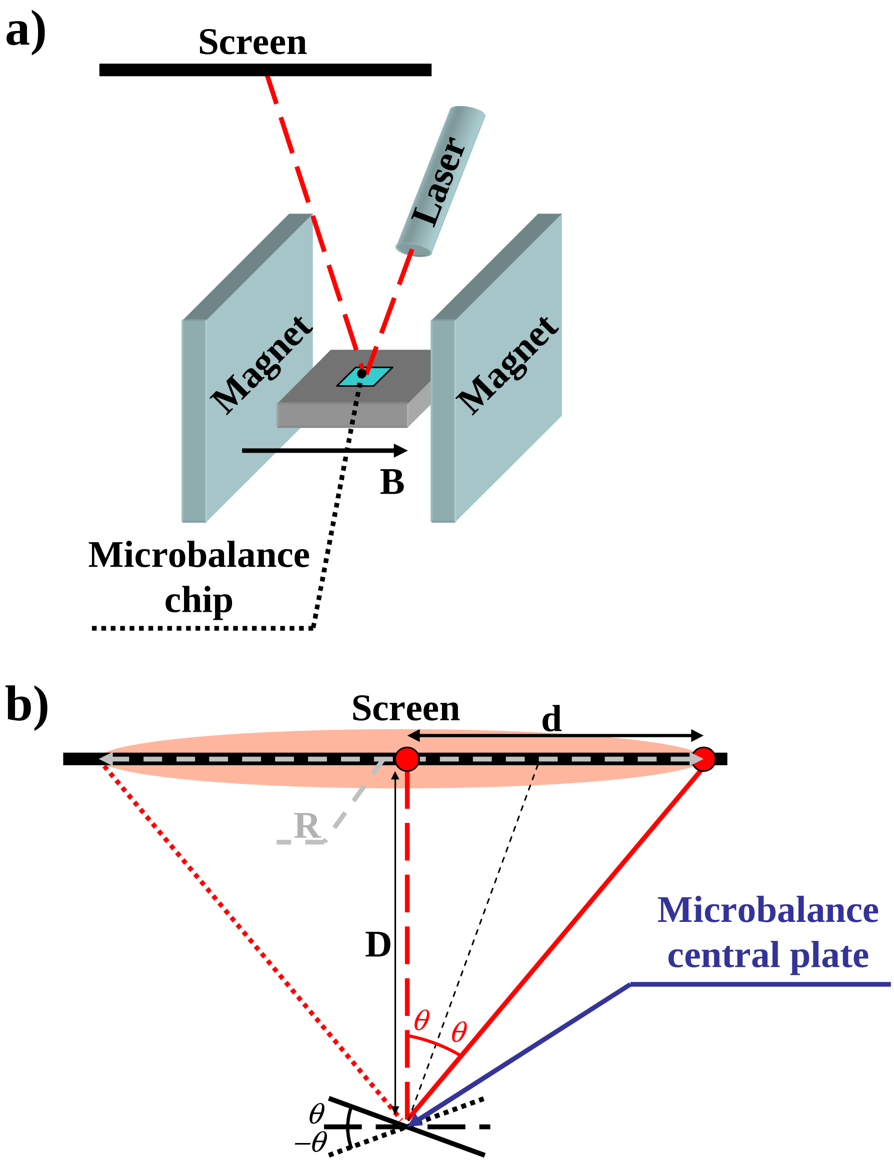

Figure 111: Setup for the optical measurements: a) Schematic 3D view with magnets, chip laser and screen; b) a sketch representing the deviation of the incident laser beam (red dashed line) if the microbalance is rotated of an angle θ *(red solid line) and if it is rotated of an angle of* $-\theta$ *(red dotted line). Red dots on the screen indicate the light spot when the microbalance is still and when it is statically rotated of an angle* θ*. The pink ellipse is what is seen on the screen when the resonator moves close to the device resonance frequency with amplitude of the rotation angle equal to* θ*.*

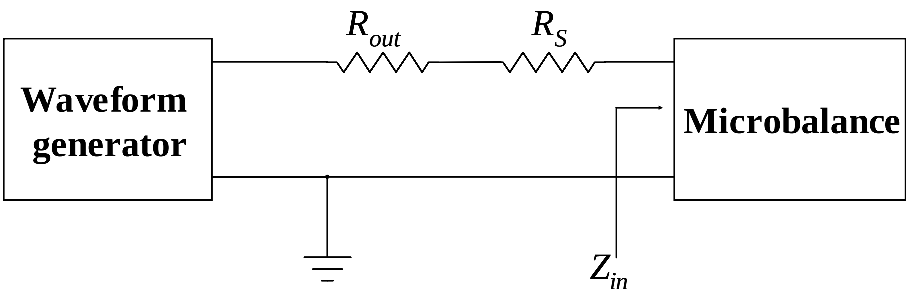

Figure 112: Driving stage for both the optical and the electrical measurements.

Thus the positioning of the micro-magnet should be very accurate to guarantee the repeatability of the measurement. Such accuracy is not possible with the facility of laboratory of the Information Department of University of Pisa. Besides the positioning of micro-magnets close to the device is very difficult and can be damage the chip if it is not done without particular care.

For all this reason micro-magnets were not used to characterize the device. Anyway in the next section some measurements will be presented for the electrical frequency response of devices on chip where a micro-magnet were glued onto, in order to demonstrate the possibility of using micro-magnets.

All the optical measurements were performed at atmospheric pressure, given than it is not possible to insert all the described optical sensing system in a vacuum chamber.

The device is driven with a waveform generator with a $R_S = 100\ \Omega$ series resistance as shown in Figure 112, where the output impedance of the waveform generator is R_{out} and the device is indicated with its input impedance Z_{in}. This is not the optimal driving according to what said in section 4.2, but it works fine for the device characterization because it both allows an easy evaluation of the input current, given the voltage provided by the voltage generator and assures that input current does not exceed the maximum 20 mA allowed by the process data, if the input voltage is low enough.

The input current I is, according to the circuit in Figure 112:

$$I = \frac{V_s}{R_{out} + R_S + Z_{in}} \tag{216}$$

where V_s is the voltage signal provided by the waveform generator. *I* is a function of the frequency through Z_{in} but according to the equivalent circuit in Figure 101, if the output loop is open (i.e. unloaded), the input impedance Z_{in} is, neglecting the mass loading:

$$Z_{in} = R_i + \frac{j2\pi f \dfrac{\Gamma_{in}^2}{2K_t}}{1 + j\dfrac{f}{f_0 Q} - \left(\dfrac{f}{f_0}\right)^2} < R_i + \pi f_0 \frac{\Gamma_{in}^2}{K_t} Q = R_i + \frac{\Gamma_{in}^2}{\sqrt{J_P K_t}} Q \qquad (217)$$

because the RLC parallel mimic the device mechanical resonance is maximum at the resonance. But with a reasonable $Q = 100$ and $B = 80\ mT$, according to the expected values in Table 1 $\Gamma_{in}^2 Q \big/ \sqrt{J_P K_t}$ should be around 3.6 mΩ for type A device and 0.8 mΩ for type B device.

Thus in both cases $Z_{in} \approx R_i$ and the input current is at each frequency:

$$I = \frac{V_s}{R_{out} + R_S + R_i} \qquad (218)$$

The resistance R_S is inserted in the circuit to limit the input current: given that the minimum value for V_s is 100 mV and the waveform output resistance $R_{out} = 50\ \Omega$, the minimum input current is about 1.8 mA for type device and 1.7 mA for type B device. $R_S = 100\ \Omega$ allow to drive also smaller currents which stress less the device both from a mechanical and electrical point of view. Besides including R_S, the minimum current is almost the same, 0.6 mA, for both type A and type B device. Also for higher values the driven current is independent from the device input impedance Z_{in}, but is function only of the input voltage. Such observations were confirmed by measuring the current driven into the resonator, with an amperometer.

In the calculations of the input current the parasitic inductances and the mutual impedences in the equivalent circuit in Figure 102 can be safely neglected: *M* and L_o have no effect because no current flow in the output open loop, while it is possible to demonstrate that $\omega L_i << R_i$. Indeed according to the expressions for a square inductance in [113], L_i is at most 1 nH for the type A device and 0.36 nH for type B device, resulting in an impedance module ωL_i around 0.2 mΩ for both type A and type B devices around their respective resonance frequencies. Thus in both cases L_i can be neglected with respect to R_i at the working frequencies of both the devices. FEM magnetic simulations carried out with Femlab slightly underestimate the values calculated with the formulas in [113], practically confirming the previous observations.

Thus, according to Eqs. (203), (204) and (189) the angle amplitude of the angle θ, measured according to Eq. (215), can be written as a function of the frequency as:

$$|\theta| = \left| I \frac{\frac{\Gamma_{in}}{2K_t}}{1 + j\frac{f}{Qf_0} - \left(\frac{f}{f_0^2}\right)} \right| = \left| \frac{V_s}{R_{out} + R_S + R_i} \frac{G_S}{1 + j\frac{f}{Qf_0} - \left(\frac{f}{f_0^2}\right)} \right| \tag{219}$$

where the mass loading is neglected ($\delta J_P = 0$) and was defined the static gain $G_S = \Gamma_{in} / 2K_t$ which is the angle of rotation in mrad driven by a static current of 1 mA, if such current could be carried by the input loop. $f_0 = \sqrt{2K_t / J_P} / 2\pi$ is the resonance frequency of the device if it is not mass loaded, while $Q = \sqrt{2K_t J_p} / D$ is the quality factor and they are equal to the resonance frequency and the quality factor in Eq. (206), if there is no mass loading ($\delta J_P = 0$).

Eq. (219) can be used as a fitting function to extract the static gain, the resonance frequency and the quality factor of the resonator (fitting parameters) from the measurements.

The frequency response is extracted by manually changing the frequency of the sinusoidal input provided by the waveform generator and reading at each frequency the major axis of the light spot on the screen, which is graduated. The process of acquisition is a bit long and the accuracy of the results is low as already said, but the extraction of the mechanical frequency response gives a first demonstration of the device operation and let to estimate the static gain and the maximum amplitude of rotation ($= G_S QI$) which cannot be extracted from electrical measurements.

Besides, optical measurements can give a confirmation of the value for resonance frequency and quality factor extracted from electrical measurements.

4.5.2 Setup for electrical measurements

Electrical measurements can be performed to extract the overall frequency response of the device: the resonator is inserted in the gap between two facing macroscopic magnets, providing a 70-80 mT[18] magnetic field, as the ones used for the optical measurement. The magnetic field can be measured through a Hall sensor. The microbalance can be driven with the same input stage used for optical measurements shown in Figure 112 and providing an input current I fixed according to Eq. (216). The sensor output voltage is thus amplified by a voltage amplifier fabricated on PCB board, with high input impedance and gain A.

From Eq. (210) it is possible to find the output voltage after the amplification V_{out}:

$$V_{out} = jM2\pi f \frac{AV_s}{R_{out} + R_S + R_i} \frac{\left(1 + \frac{\Gamma_{in}\Gamma_{out}}{2K_t M}\right) + \frac{f}{f_0 Q} - \left(\frac{f}{f_0}\right)^2}{1 + \frac{f}{f_0 Q} - \left(\frac{f}{f_0}\right)^2} \tag{220}$$

where $f_{\delta m} = f_0$, because no sensitive layer is deposited onto the resonator, so that no mass loading is expected. The effect the mutual inductance was included, first because of its important role as feed-through parasitic element, introducing two complex zeros in the system transfer function, second because it is fundamental to explain the shape of the frequency responses from measurements. The inductance L_i is neglected because $\omega L_i << R_i$ at the working frequencies of the devices, as shown in the previous section, while L_o can be neglected because only an extremely small current flows in the output loop because of the high input impedance of the voltage amplifier. Anyway according to expressions in [113] L_o is about 551 nH for type A device and 60 nH for type B device, resulting in an impedance module ωL_o around 100 mΩ and 30 mΩ, for type A and type B devices close to their respective resonance frequencies. In both cases thus $\omega L_o << R_o$, so that the inductance of the output loop is anyway negligible with respect to the loop resistance, at the operating frequency of the proposed device, whatever the input impedance of the amplifier stage is.

The amplified output voltage V_{out} and the input signal V_s are respectively the input and the external reference for a lock-in amplifier, which filters all components at a different frequency from the one of V_s, cleaning V_{out} from noise and harmonics due to amplifier distortions.

---

[18] This value holds only for the measurements at atmospheric pressure: smaller magnets were used for the measurements at different vacuum levels, because of the need of put inside both device and magnets in a vacuum chamber.

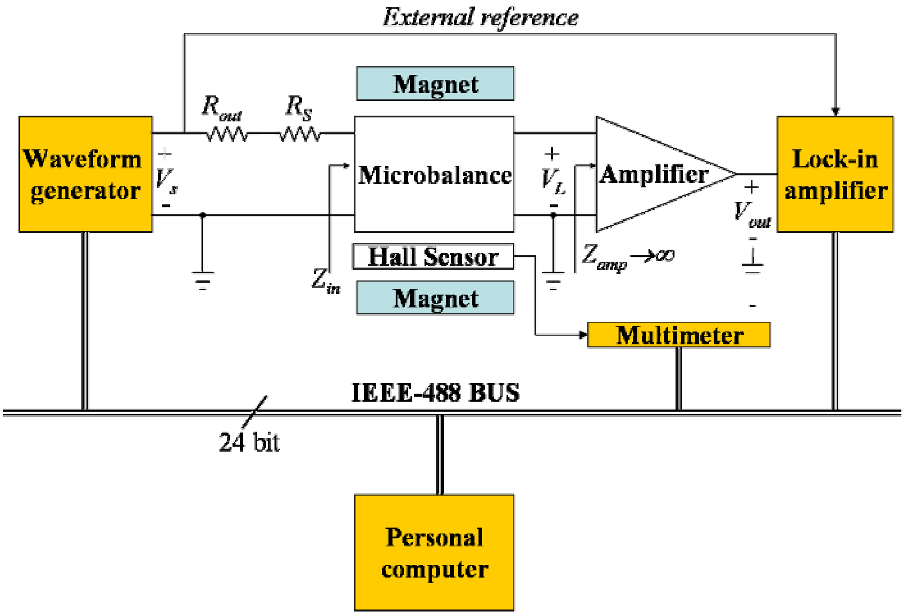

Figure 113: Setup for electrical measurements.

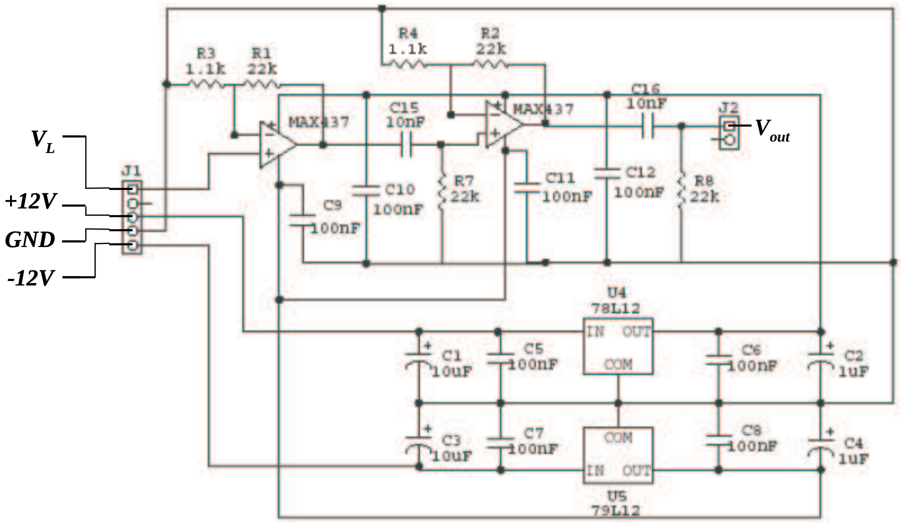

Figure 114: Amplifier stage collecting the sensor output signal V_L and feeding the lock-in amplifier with the signal V_{out}.

An IEEE-488 card, driven by PC, is used to drive the waveform generator and to collect the output of the lock-in amplifier, so that the acquisition of the frequency response can done automatically, driving both the waveform generator and the lock-in amplifier with Labview [83]. A Hall sensor is placed close to the device and its output terminals are connected to a multimeter (the sensor output signals is a voltage), so that at the beginning of each acquisition the PC can read also the magnetic filed through the IEEE-488 card.

The possibility of automating the measurements is a great advantage with respect to the optical measurements, because it both save the time of the operator, and remove all the errors which can be induced by the operator.

In Figure 113 the block diagram of the setup for the electrical measurements is represented, while in Figure 114 the detailed scheme of the voltage amplifier collecting the sensor output signal is represented.

The amplification of the voltage V_L is required because according to the expected value for R_T (see Table 1 for B = 100 mT and Q = 100), an input current of some mA results in some hundreds of μV for type A device and in some tens of μV for type B device. The amplifier is composed of two non-inverting voltage amplifier based on op-amp MAXIM437. The gain of each stage is theoretically 21[19], while the bandwidth is 2.9 MHz, given the high GBP[20] (= 60 MHz) of the op-amps (the bandwidth is given by the ratio between the GPB and the amplification). The overall amplification of the amplifier is thus 441, while the bandwidth is enough with deal with the frequencies which devices operate at. Measurements of the amplification in a bandwidth from 20 kHz to 100 kHz, confirm this expectation, giving a constant amplification $A = 450$, slightly higher than the expected one.

In the scheme in Figure 114 also two voltage regulators are inserted (regulators LM78L12 and LM79L12), in order to provide supply voltages minimally affect by disturbs to the amplifiers.

Finally, a CR high-pass filter follows each amplifier to reject op-amp offsets, flicker noise and 50 Hz interfering signal from the supply voltages.

As shown in the next section, the problem of electrical measurements is the parasitic feed-through due to the mutual inductance M. In particular it forces sometimes to use Eq. (220) to fit measurements results, leading to a four-parameter fitting, which not too much robust, given the high number of parameters. A possible solution is to acquire first a resonance frequency without the magnets and after the resonance frequency with the magnets.

---

[19] Using the names of the resistances in Figure 114, the amplification of each stage is $1+R_3/R_1$ for the first stage and $1+R_4/R_2$ for the second stage, according to the well-known formula.

[20] *Gain Bandwidth Product*.

During the first acquisition the device is not actuated because $B = 0$ and subsequently $\tau = 0$. Thus the component of V_P output voltage V_{out} only due to the parasitic feed-through is acquired. Such component is given by:

$$V_P = j2\pi fMA\frac{V_s}{R_{out} + R_S + R_i} \tag{221}$$

During the second measurement the device is actuated and V_{out} is given by the sum of the parasitic and the "mechanical" (i.e. due to the plate movements) component, according to Eq. (220). If the frequency response acquired in the measurement without magnets was stored by the PC, can be now subtracted to the second measurement giving:

$$\begin{aligned} V_{out} - V_P = V_{out} &= \frac{AV_s}{R_{out} + R_S + R_i}\frac{j2\pi f\dfrac{\Gamma_{in}\Gamma_{out}}{2K_t}}{1 + \dfrac{f}{f_0 Q} - \left(\dfrac{f}{f_0}\right)^2} = \\ &= \frac{AV_s}{R_{out} + R_S + R_i}\frac{j\dfrac{f}{f_0 Q}R_T}{1 + \dfrac{f}{f_0 Q} - \left(\dfrac{f}{f_0}\right)^2} \end{aligned} \tag{222}$$

which can be used to extract f_0, Q and R_T by a measurements fitting (Q and f_0 should be equal to the one extracted by the optical measurements). On the other hand the mutual inductance M can be extracted by fitting the frequency response from the measurement without magnets, using as a fitting function Eq. (221).

Electrical measurements thus add the value of the transresistance at the resonance R_T and the value of mutual inductance M to the parameters already extracted by optical measurements. Besides electrical measurements can be carried out both at atmospheric pressure and in vacuum, because they do not require a bulky screen at a distance of 2 meters as the optical measurements. Thus they allow a characterization of the device at different level of vacuum.

This characterization was done by putting the device in a vacuum chamber. In the chamber two facing magnets smaller, which generates a magnetic field $B = 28\ mT$ were also placed to allow the characterization in vacuum. Such magnets are smaller than the ones used for optical measurements, which are used also for electrical measurements at atmospheric pressure, just because they have to enter in the vacuum chamber.

The vacuum was obtained by a system based on a combined membrane pump/turbomolecular pump, while the pressure was measured with a standard thermocouple gauge. Measurements at low pressure can be done also without removing the parasitic signal with the two-measurements system aforementioned, because the high Q obtained under vacuum raises a lot the value of R_T, so that the parasitic signal is negligible in region around the resonance large enough to extract resonance frequency, quality factor and R_T by using as fitting curve the frequency response described by Eq. (222).

Through electrical measurements also the working of devices packaged with NdFeB micro-magnets was demonstrated. Finally, the effect of the humidity on the resonance frequency of the device were demonstrated, by putting the device under test in a chamber filled by a flow of drying air varying from 500 to 600SCCM[21]. Due to the small size of this chamber it was not possible to use any macroscopic magnets, so that these measurements were performed on devices packaged with a NdFeB micro-magnet.

4.6 Measurements results

In this section the results obtained by all the measurements described in the previous section will be shown and discussed. Several of these measurements were carried out during a master thesis activity [114].

4.6.1 Results from optical measurements

Many measurements with different driving currents were done on a type A and a type B device, using the setup for optical measurements previously described. For all the measurements B is about 75 mT. In Figure 115 results for type A device are represented for driving currents from 2.28 mA to 6.66 mA (peak amplitude), with the amplitude of the rotation angle at the resonance varying from 7.9 mrad (0.45 degrees) to 22.7 mrad (1.30 degrees). Results fro type B devices are shown in Figure 116: in this case the input current is varied from 4.8 mA to 12.18 mA, resulting in amplitudes of the rotation angle at the resonance from 9.4 mrad (0.53 degrees) to 24.7 mrad (1.41 degrees).

For type B device high driving currents are needed to obtain a rotation of the central plate similar to the one achievable with a type A device with

---

[21] *Standard Cubic Centimeter per Minute*

smaller currents. The minimum angle of rotation which can be measured is in both the cases 1.3 mrad (0.07 degrees), equivalent to a dilatation of 0.5 cm on the screen which collects the laser beam reflected by the microbalance. All the angles measured are small enough, so that Eq. (214) holds. The dependence of the maximum amplitude of the rotation angle on the input current amplitude is practically linear as expected.

Each curve in Figures 115 and 116 is fitted, using the curve described by Eq. (219), in order to find the resonance frequency f_0, the quality factor Q and the static gain G_S (or the gain at the resonance QG_S). An example of these fittings is given for type A device in Figure 117a and fro type B device in Figure 117b. The mean value for the resonance frequency is 30.32 kHz for type A device, while for type B device is 89.82 kHz. The maximum percentage difference between the resonance frequency from one measurement and the mean value is 1.3% for type A device and 0.3% for type B device. Anyway there is a difference of some kHz between the measured resonance frequencies and the ones expected according to both measurements and simulations. In particular is between the two for type A device and higher than for both type B device. This disagreement is confirmed by electrical measurements shown in the following and can be probably attribute to the overetch of the oxide layers during BHF etch. Moreover this overetch changes very likely from chip to chip as demonstrated by electrical measurements on devices on other chip. Indeed the repeatability of the post-processing has to be increased in this respect.

Quality factor varies from 135 to 160 for type A device with respect to measurements in Figure 115. Anyway the quality factor given by the other two measurements is 137, leading to discard the results of 160. A mean value of 136 can be thus extracted for type A device, with a maximum percentage difference of 17% with respect to the value of 160, which anyway is probably not too much significant.

Excluding the value of 160 the maximum percentage difference between the quality factor from one measurement and the mean value about 0.74%. On the other hand for type B device the mean quality factor extracted by curves in Figure 116 is 232, with a maximum percentage difference between Q from one measurement and the mean value about 5.6%.

The quality factor of type B device is almost twice the quality factor of type A, thus type device probably performs better than type A with respect to both the mass sensitivity and the minimum adsorbed mass detectable.

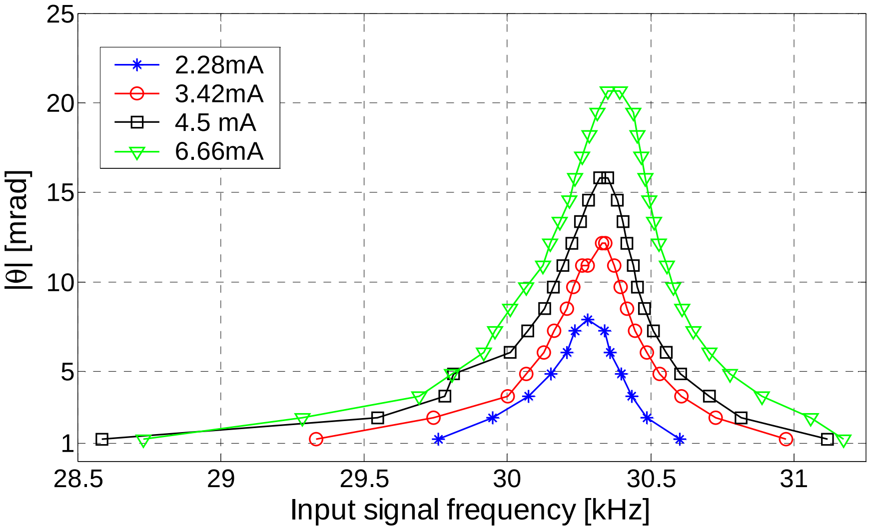

Figure 115: Amplitude of the angle of rotation of the central plate of type B microbalance as a function of the frequency. Each curve is for a different input current and is acquired with the optical method. External magnetic field is measured to be 75 mT.

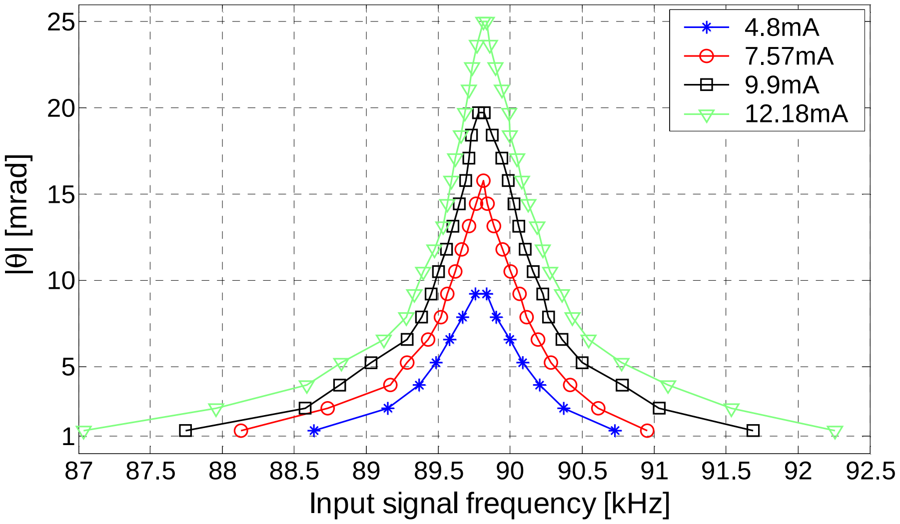

Figure 116: Amplitude of the angle of rotation of the central plate of type B microbalance as a function of the frequency. Each curve is for a different input current and is acquired with the optical method. External magnetic field is measured to be 75 mT.

On the other hand the actuation of type B device is less efficient than for type A microbalance, as expected.

The mean value for G_S extracted from measurements is 24.5 µrad/mA (= 5''/mA) and 8.6 µrad/mA (= 1.8''/mA). Which means a gain at resonance QG_S about 3.33 mrad/mA (= 0.19 degrees/mA) for type A device and 2.00 mrad/mA (= 0.11 degrees/mA) for type B device.

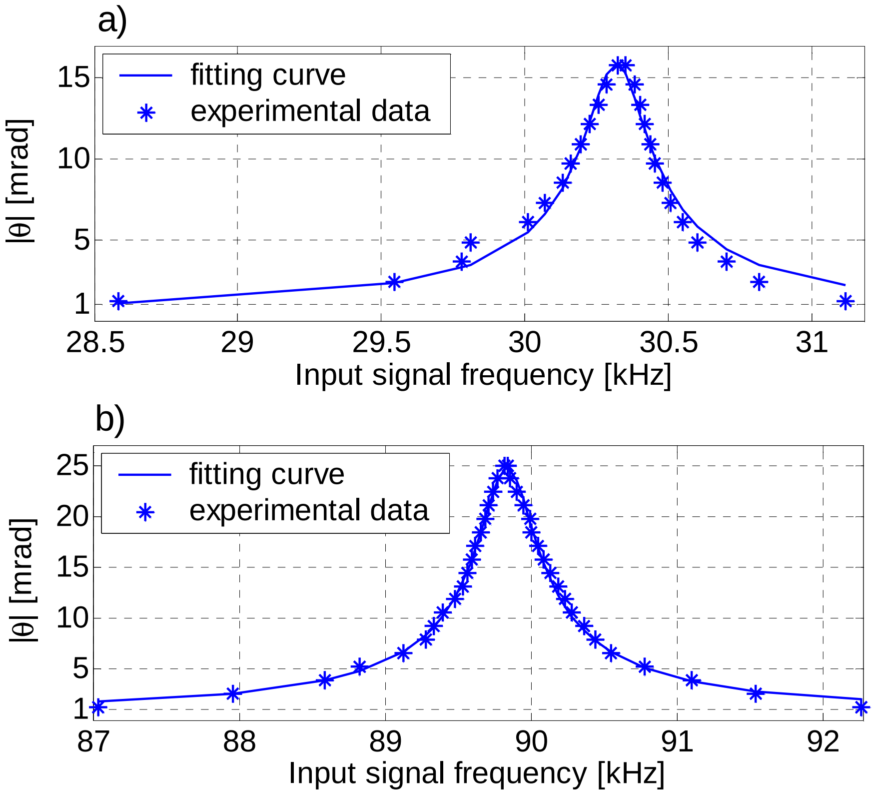

Figure 117: Example of fittings of optical measurements of the amplitude of the angle of rotation of the central plate as a function of the input signal frequency: a) type A device with input current amplitude 4.5 mA and external magnetic field 75 mT. The extracted value for f_0, Q and G_S are respectively 30.32 kHz, 135 and 26.2 µrad/mA. : b) type B device with input current amplitude 12.18 mA and external magnetic field 75 mT. The extracted value for f_0, Q and G_S are respectively 89.83 kHz, 225 and 9 µrad/mA.

	Type A		**Type B**	
	Expected value	**Value from measurements**	**Expected value**	**Value from measurements**
f_0	30.9 kHz (27 kHz from FEM simulations)	30.32 kHz	84.92 kHz (82.4 kHz from FEM simulations)	89.83 kHz
Q	---	136	---	232
G_S	16.8 µrad/mA	24.5 µrad/mA	7.1 µrad/mA	8.6 µrad/mA

Table 2: Comparison between mean f_0, Q and G_S extracted by optical measurements and their expected value.

As for the quality factor the maximum difference between G_S from one measurement to the mean value is high: 11.4% for type A, 5.8% for type B device. Anyway the value given for type A device is due to the same measurement which gives $Q = 160$ and also for G_S gives a value very different from the other. Neglecting this measurement the maximum difference between G_S from one measurement to the mean value is 7.3%.

The optical measurements are thus not easily repeatable, with respect to Q and G_S, as expected because of the errors connected with this kind of measurement, especially for low and high values of the angle of rotation. As shown in the following electrical measurements are more repeatable.

Finally, a last remark about G_S is needed: as shown in Table 2 it is anyway higher than the expected from theory, according to which $G_S = A_{in}B/(2K_t)$. Given that B is measured, while the theoretical value of A_{in} is the area of a square, which is probably very reliable, the reason of such discrepancy between theory and measurements is almost certainly due to the overetch. Indeed overetch makes each lateral spring narrower and longer than expected, reducing the stiffness $2K_t$ of the structure and leading to a G_S higher than expected.

4.6.2 Frequency responses of the devices, acquired through the electrical setup

Several frequency response of different type A and B devices were acquired. Figures 118 and 119 shown the amplitude and the phase of the voltage V_{out} read by the lock-in as a function of the frequency, respectively for a type A device different from the one whose optical measurements were previously shown and for the same type B device, whose optical measurements were presented before. Both the curves are acquired at atmospheric pressure.

Amplitude of V_{out} as a function of the frequency is theoretically proportional to the device frequency response, while its phase is equal to the one of the frequency response of the device, since no phase shift is introduced at least theoretically by the amplifier and by the driving stage.

Frequency responses of both type A and B are clearly affected by the parasitic signal due to the mutual inductance between input and output loops: as predicted by the Eq. (210) there is a couple of zeros, which leads to a local minimum in the amplitude of V_{out} and prevent the rotation of -180 degrees due to the poles, because zeros are very close to the resonance frequency of the device.

Anyway type A device is evidently less affected by the parasitic signal. Specifically, the maximum rotation is 133 degrees for type A device while it is about 75 degrees for the type B device. Thus type B microbalance is less suited than type A resonator to be used as a frequency selective element in an oscillator than type A device. The different sensitivity to the parasitic signal of the two devices is essentially the consequence of the higher efficiency of actuation and sensing of type A device.

The method of the two measurements, one without and the other with magnets, is thus needed to fit experimental data using Eq. (222) as fitting curve. In Figure 120 an example of frequency response cleaned from the parasitic component is shown. The minimum in the amplitude curve disappears while the phase shifts of about -180 degrees around the resonance frequency, as expected for an ideal second-order system.

Three different curves were fitted for each device and for each curve different input voltages V_s and consequently input currents I were used, in order to obtain an estimation of the resonance frequency the quality factor and the transresistance R_T for each device, by extracting the mean value obtained by the measurements, as done in the case of optical measurements. The input voltages were for both the resonators 1 V^{PP}, 2 V^{PP} and 3 V^{PP}, resulting respectively in an input current amplitude of 3.2 mA, 6.4 mA and 9.6 mA, according to Eq. (218). An example of one of these fitting is given in Figure 121.

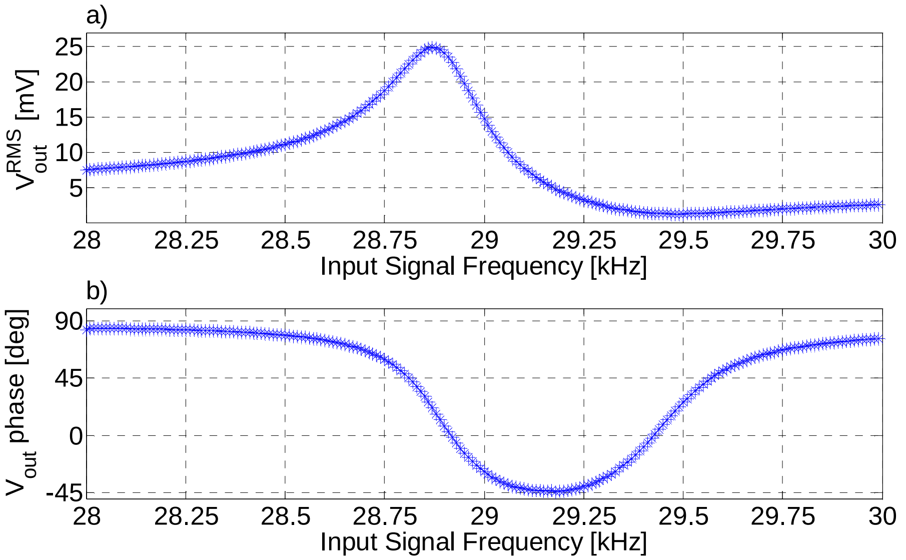

Figure 118: Amplitude (a) and phase (b) of the voltage V_{out} read by the lock-in for a type A device, driven by an input current of amplitude about 6.4 mA ($V_s = 2\ V^{pp}$) and biased with an external magnetic field of 73 mT. The amplitude is given in mV root mean square value (RMS), while the phase in degrees.

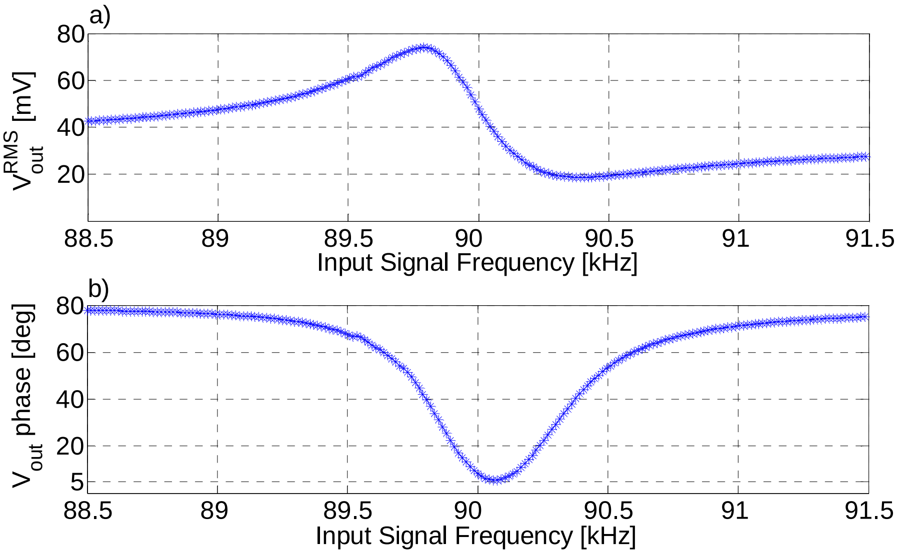

Figure 119: Amplitude (a) and phase (b) of the voltage V_{out} read by the lock-in for a type A device, driven by an input current of amplitude about 6.4 mA ($V_s = 2\ V^{pp}$) and biased with an external magnetic field of 80 mT. The amplitude is given in mV root mean square value (RMS), while the phase in degrees.

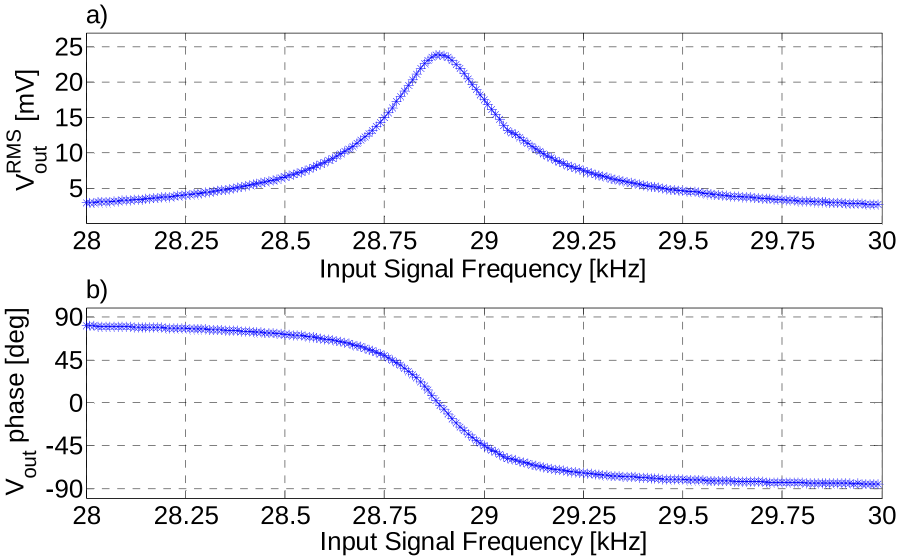

Figure 120: Example of amplitude and phase of V_{out} cleaned from the parasitic component for a type A device. The curves are obtained by removing the parasitic component from the curves in Figure 118.

The mean value for the resonance frequency is 28.899 kHz for type A device and 89.888 kHz for type B device. This value highly repeatable since the maximum difference between one measurement and the mean value is 0.006% for type A device and 0.023% for type B device: the frequency changes also of few Hz from a measurement to another and this is a preliminary demonstration of the fact that both the devices can be used as microbalance sensible to a shift of tens of Hz due to the mass loading.

Variations of the resonance frequency between two different electrical measurements performed on the same device are thus very small. Generally these variations are smaller than 10 Hz for type A microbalance and not higher than 50 Hz for type B. This means that even small changes of the resonance frequency due to the analyte mass adsorption are higher than the short time fluctuations. Thus the resolution should be good for both devices: considering the values for mass sensitivity in Table 1, type A device is expected to sense at least 1 ng of adsorbed mass, while type B device can detect even less than 1 ng of analyte.

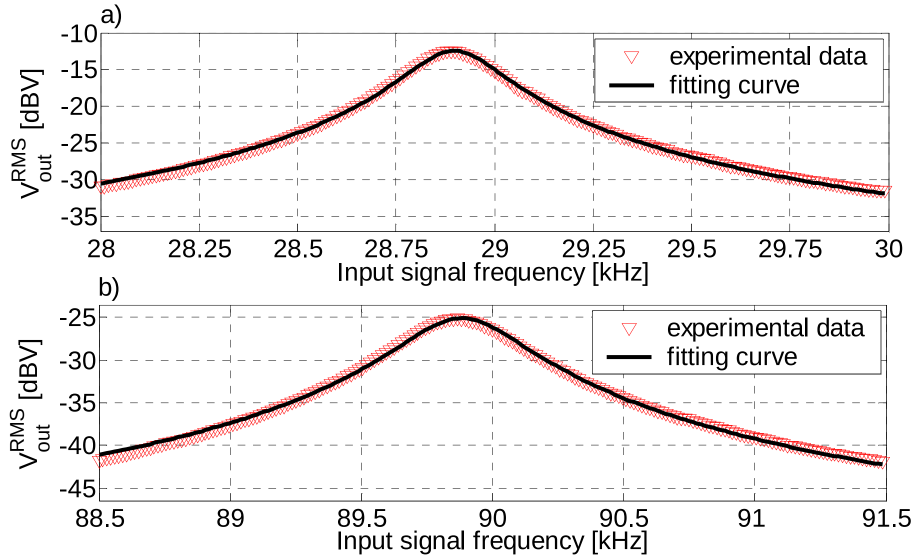

Figure 121: Examples of fittings of electrical measurements of the amplitude of V_{out} as a function of the frequency, after cleaning it from the parasitic component with the two-measurement method: a) type A device with input current amplitude 6.4 mA and external magnetic field 73 mT. The extracted value for f_0, Q and R_T are respectively 28.90 kHz, 125 and 116 mΩ. : b) type B device with input current amplitude 6.4 mA and external magnetic field 80 mT. The extracted value for f_0, Q and R_T are respectively 89.88 kHz, 202 and 27.6 mΩ. In both cases the output voltage is expressed in dbV RMS (root mean square value).

The resonance frequency extracted from electrical measurements for type B device is also quite similar to the one extracted from optical measurements: it is 58 Hz higher (see Table 2), but due to the lowest accuracy and repeatability of the optical measurements, it is possible to say that the agreement is very good.

On the other hand the resonance frequency of the type A device is about 2 kHz lower than the resonance frequency of the type A device, whose optical measurements are discussed in 4.6.1. Even considering the low accuracy of the optical measurements, this difference is very high and cannot be due to optical measurements error. Thus it is possible to conclude that from chip to chip the resonance frequency of the same device can change a lot. This is confirmed also by measurements on other type A and B device. The difference between the resonance frequencies of two devices from different chips can be as high as 7%.

This is probably due to the difficulty in controlling the overetch of the oxide layers carried out with a BHF etch during the post-processing (see 4.4.2). Anyway this dispersion in values of the resonance frequency is not so important if the device is used as a microbalance: the resonance frequency can be measured once to obtain a reference value, which can be compared with the variations due to the mass loading.

Values extracted for the quality factor are 123.5 for type A device and 197 for type device. The value extracted is slightly repeatable than in the case of optical measurements: the maximum difference between one measurement and the mean value is 1.6% for type A device and 3% for type B device. Anyway the value extracted for type B device from measurements is 15% smaller than the one extracted from the optical ones (Table 2). This difference can be due to not necessary by the less accuracy of the optical measurement, but by an aging of the device, since the electrical measurements follows the optical measurements at a distance of several days.

More measurements on different devices could be done to make any rigorous conclusion in this direction and in any case a decrease of the quality factor due to the aging is not a real problem, because these devices can be even used only once, because of the large quantity of them which can be fabricated and their low cost.

	Type A		**Type B**	
	Expected value	**Value from measurements**	**Expected value**	**Value from measurements**
f_0	30.9 kHz (27 kHz from FEM simulations)	28.899 kHz	84.92 kHz (82.4 kHz from FEM simulations)	89.888 kHz
Q	---	123.5	---	197
R_T	82.9 mΩ (B = 73 mT, Q = 123.5)	116.9 mΩ (B = 73 mT, Q = 123.5)	21.1 mΩ (B = 80 mT, Q = 197)	27.1 mΩ (B = 80 mT, Q = 197)

Table 3: Comparison between mean f_0, Q and R_T extracted by electrical measurements and their expected value. Type B device is the same device whose optical measurements are shown in Table 2, while the data given for the type A device are from electrical measurements of a device different (i.e. fabricated on a different chip) from the type A device for which optical measurements are summarized in Table 2.

Finally, from the fitting of the V_{out} amplitude cleaned from the parasitic signal it is possible to extract the transresistance R_T at the resonance: its mean value is 116.9 mΩ for the type A device and 27.1 mΩ for the type B device. The magnetic field measured in the first case is 73 mT, while in the second 80 mT.

The repeatability of the measurement is quite good: the maximum difference between one measurement and the mean value is 3.9% for type A device and 1.4% for type B device.

As expected the transresistance R_T is much higher for type A device than for type B device. Anyway in both the cases the value from measurements is higher than the expected one as shown in Table 3: this is probably due to the fact that the expected values were calculated without considering the overetch, whose value is not know and which leads to a lower value of both K_t (as shown in 4.6.1) and J_P (the higher the overetch the less the mass and thus the inertia moment). This results in an increase of R_T according to Eq. (209). The overetch and the subsequent reduction of K_t and J_P is probably the main cause of this increase: indeed B is measured with good accuracy with a Hall sensor, while A_{in} is the air of a metal loop whose value is probably very close to the expected value. The only parameter which affects R_T and can be different from the expected value is A_{out}, which is calculated by the approximated expression written in Eq. (213).

The value of A_{out} can be extracted for the type B device, by a comparison between optical and electrical measurements by the expression of R_T in Eq. (209) where the expression of the static gain for the angle of rotation G_S is substituted:

$$A_{out} = \frac{R_T}{2\pi f_0 G_S Q_e} \frac{B_o}{B_e^2} \tag{223}$$

where Q_e and B_e are the quality factor and the external magnetic field measured during the electrical measurement, while B_o is the external magnetic field measured during the optical measurements; R_T and f_0 are extracted by electrical measurements, while G_S from optical measurement.

The value of A_{out} extracted in this way is almost the same as the expected (Table 4). Even if this estimation is affected by the low accuracy of the optical measurements it is possible to conclude that Eq. (213) is probably enough accurate to evaluate A_{out}, so that the unforeseen high R_T cannot be ascribed to a difference between the real and the expected value of A_{out}. The extraction of A_{out} from measurements for a type A device was not carried out because it was not possible to perform on the same type A device both optical and electrical measurements.

	Expected value	**Value from optical measurements**	**Value from electrical measurements**	**Value from a comparison of optical and electrical measurements**
f_0	84.92 kHz (82.4 kHz from FEM simulations)	89.83 kHz	89.888 kHz	---
Q	---	232	197	---
G_S	7.1 µrad/mA (B = 75 mT)	8.6 µrad/mA (B = 75 mT)	---	---
R_T	21.1 mΩ (B = 80 mT, Q = 197)	---	27.1 mΩ (B = 80 mT, Q = 197)	---
A_{out}	0.327 mm^2	---	---	0.332 mm^2

Table 4: Comparison between parameters extracted form optical and electrical measurements and their expected value for the type B device which was characterized both with an optical and an electrical measurement.

The frequency response acquired without magnets can be used not only to cancel the parasitic component from the output but also to estimate the entity of such parasitic: according to measurements of V_{out} without magnets, the parasitic component has a phase almost 90 degrees rotated with respect to the input signal and is amplitude linearly increasing with the frequency. This confirms the assumption of a parasitic signal $j2\pi fM$ superposed to the signal.

The value of M can be extracted by the slopes of the dependence of the amplitude of V_{out} on the frequency when the magnets are not included in the measurement setup. The linear fitting gives about 87 nH for the mutual inductance of the type A device and 32 nH for the type B device.

It is possible anyway to demonstrate that this value cannot be due entirely on the mutual inductance between input and output loop. Such mutual inductance M_L can be written as function of the loops inductance:

$$M_L = c\sqrt{L_i L_o} \qquad (224)$$

where *c* is a coupling factor which is always smaller than 1. Thus in the worst case (c = 1) M_L is 23.5 nH for type A device and 4.6 nH fro type B device.

Thus there should be probably other parasitic paths introduced by connection cables, amplifier PCB board and/or other out of chip components. The influence of these parasitic paths can be reduced by integrating the amplifier on the same chip with the microbalance instead of fabricating it on a PCB board. The CMOS-compatibility of the process of microbalance fabrication allows this solution.

4.6.3 Feasibility of the device driving through NdFeB micro-magnets

To demonstrate the feasibility of the packaging of the devices with a NdFeB micro-magnet, a micro-magnet is then glued over some chips carrying type A devices as well as over other chips carrying type A resonator. A device packaged in this way is represented in the picture in Figure 122.

The magnetic field on the device changes a lot depending on the distance from the micro-magnet. Due to the difficulty of the process of magnets positioning, the external magnetic field *B* and thus R_T ($\propto B^2$), changes a lot from device to device when actuated by a micro-magnet, and the value of the field *B* is generally lower than the one obtained with the macroscopic 20x12 cm magnets.

Anyway the device actuated by a micro-magnet works almost as a device actuated by the macroscopic magnets both if they are type A and if they are type B device, as shown in Figure 123. Also in the case of device actuated by a micro-magnet the resonance frequency, the quality factor and the transresistance R_T can be extracted by doing an acquisition of the frequency response before and another after the gluing of the magnet and then making the difference between them.

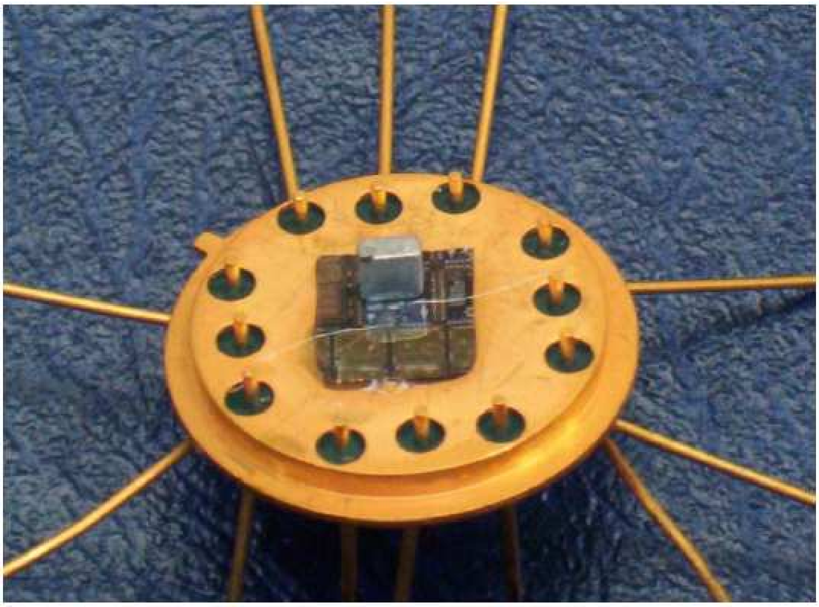

Figure 122: Chip carrying a type A microbalance on a TO-8 package and with micro-magnet glued onto the top.

The type A microbalance, which Figure 123a refers to, is the same whose electrical measurements were shown in 4.6.2. The resonance frequency and the quality factor extracted by the fitting are respectively 28.901 kHz and 126.6 and thus very close to the ones extracted by previous measurements, as expected. R_T is instead 99.9 mΩ, lower than the one in Table 3. It is logical to ascribe this lowering to a lower value B_{new} magnetic field, which can be estimated to be:

$$B_{new} = B_{old}\sqrt{\frac{R_{Tnew}}{R_{Told}}} \tag{225}$$

where B_{old} is the magnetic field generated bye the macroscopic magnet, while R_{Tnew} and R_{Told} are respectively the transresistances measured when the device is biased by the micro-magnet and when it is driven into motion because of the macroscopic magnets. The field acting on the device is thus about 67.5 mT, not too much low indeed than the one driven by the macroscopic magnets.

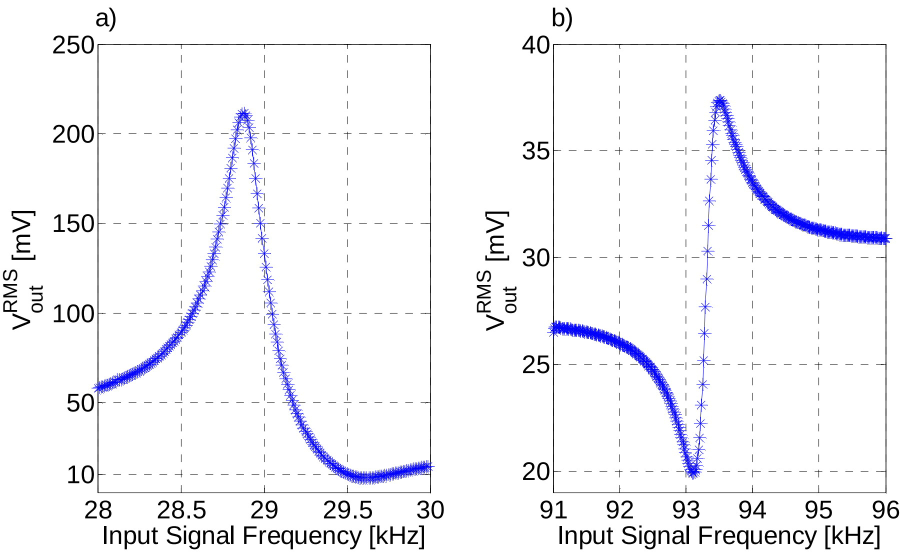

Figure 123: Amplitude V_{out} of the voltage read by the lock-in for two device driven through a magnetic field generated by a NdFeB micro-magnet: a) type A device (the same whose measurements are presented in 4.6.2), with parameters f_0 = 28.901 kHz Q = 126.6 and R_T = 99.9 mΩ, extracted by a fitting after the removing of the parasitic components . b) type B device with parameters f_0 = 93.361 kHz Q=235.8 and R_T = 5.4 mΩ, extracted by a fitting after the removing of the parasitic components .

On the other hand, Figure 123b refers to a type B devices different to the one previously measured the resonance frequency (= 93.631 kHz) is higher than in the previous case, confirming the dispersion of the value of this parameter from chip to chip. Also the quality factor (= 235.8), is higher than in the other case, while R_T is 5.4 mΩ. Such low value is probably mainly due to a lower magnetic field driven by the micro-magnet than the macroscopic magnets, even if, since the device have been fabricated in a different post-processing run, the transresistance can be smaller also because of a variation of parameters dependent on the fabrication: for example the overetch could be lower for this second device, so that K_t and J_p are higher and R_T smaller even if the magnetic field was the same. Anyway the measured value, 5 times smaller than in the other case is too small to be explained only with a higher overetch, so that it is possible to say with enough confidence that the external magnetic field is definitely lower than in the measurements on the other device.

Finally, it is interesting to observe that in Figure 123b the frequency of the zeros is lower to the resonance frequency, unlike the other characterized device: this is probably due to the fact of a phase of the parasitic signal opposite to the one assumed to find Eq. (210). This can be simply to an inversion in the connection of the input or the output loop (i.e. the terminal which in the other device previously measured was connected to the signal is now connected to ground, while the other than before was connected to ground, now carries the signal.

4.6.4 Frequency responses acquired at different levels of vacuum and effect of the humidity on the resonance frequency

The type A device previously characterized at atmospheric pressure with macroscopic magnets and NdFeB magnets was also tested at different level of vacuum. Indeed these measurements were carried out before gluing the micro-magnet but due to the logical order chosen in this thesis, their results are summarized now, after the results from electrical measurements of the device with a NdFeB magnet glued onto the top of the chip.

Device was inserted in the previously described vacuum chamber, between two magnets generating a magnetic field B = 28 mT, measured by a Hall sensor. The device was driven with a voltage V_s varying from 100 mV^{PP} to 200 mV^{PP}, leading to a driving current amplitude varying from 320 μA to 620 μA. The driving current was smaller than at atmospheric pressure to avoid to stress to much the device from a mechanical point of view: since quality factor in vacuum is expected to be higher than at atmospheric pressure the same input current drive an angle of rotation much higher under vacuum than at atmospheric pressure. On the other hand if the Q is higher also R_T is higher, thus there should be no problems in detecting the output signal, even if the driving current is reduced.

Measurements were carried out at pressures from 0.02 to 2 mbar. At these levels of vacuum the quality factor is anyway much higher than at atmospheric pressure, leading to a transresistance much higher than atmospheric pressure. Thus at least around the resonance the parasitic component of V_{out} is negligible and the there is no need to clean the output signal from the parasitic, to extract f_0, Q and R_T , through a fitting.

In Figure 124 the amplitude of output voltage read by the lock-in at different frequency is shown at different pressures.

Results extracted for f_0, Q and R_T at different pressures are compared with their value at atmospheric pressure; R_T at atmospheric pressure is lower than in Table 5, because the magnetic field is now lower (28 mT instead of 73 mT). Quality factor and thus R_T are much higher than at atmospheric pressure even at a pressure of 2 mbar. As expected [2] the quality factor is approximately proportional to 1/P.

But the surprising result of the comparison is that the resonance frequency of the device is 28.899 kHz at atmospheric pressure, while varies from 29.284 kHz to 29.288 kHz for a pressure changing from 0.02 mbar to 2 mbar. Thus in vacuum the resonance frequency of the device is almost 400 Hz higher than at atmospheric pressure. Since the measurement at atmospheric pressure was carried out both just before and just after the measurement in vacuum, giving in both the case the same results for the resonance frequency[22], it is possible to exclude any damage to the device occurred during the measurement under vacuum.

The reason of such shift is therefore due to the presence or not of the air and to its pressure. It could be due to a mechanical interaction or to adsorption/desorption of molecules.

Indeed the interaction between air and deice structure can result not only in a damping but also into a stiffening of the structure: this happens mainly if there are thin layer of air compressed, i.e. if the squeeze film damping is very high [46]. But around the device considered in this thesis there are not films compressed by the movements of the resonator: over the device there is a practically semi-infinite (= much larger than the resonator) volume of air, while under it there are 100 μm of air, which is an air layer too thick to justify a significant stiffening due to its squeezing [46]. Thus if the shift is due to a mechanical interaction it is not due to film squeezing.

Anyway the difference between the resonance frequency in vacuum and at atmospheric pressure is more likely due to mass desorption of molecules adsorbed or absorbed by the device at atmospheric pressure. In the specific silicon oxide and in particular BPSG are known as very hydrophilic material. Thus in a humid environment they could absorb a lot of water molecules, while in vacuum this molecules are desorbed. According to this hypothesis at atmospheric pressure the device is heavier than in vacuum as a consequence of the water molecules absorbed and its resonance frequency lower, as according to the results shown in Table 5.

To verify this theory the type A device was introduced in a sealed chamber where first a flow of 500 SCCM of dry air and then a flow of 600 SCCM of dry air were driven. In both the case the measured resonance frequency was about 100 Hz higher than the resonance frequency measured in the humid atmosphere. Thus, given the expected value of the mass sensitivity for a type A device (Table 1), it is possible to estimate that at atmospheric pressure almost 6 ng of water molecules are absorbed

---

[22] Or better with a small difference of about 5 Hz, which can be ascribed to measurements error or to short time fluctuation of the resonance frequency.

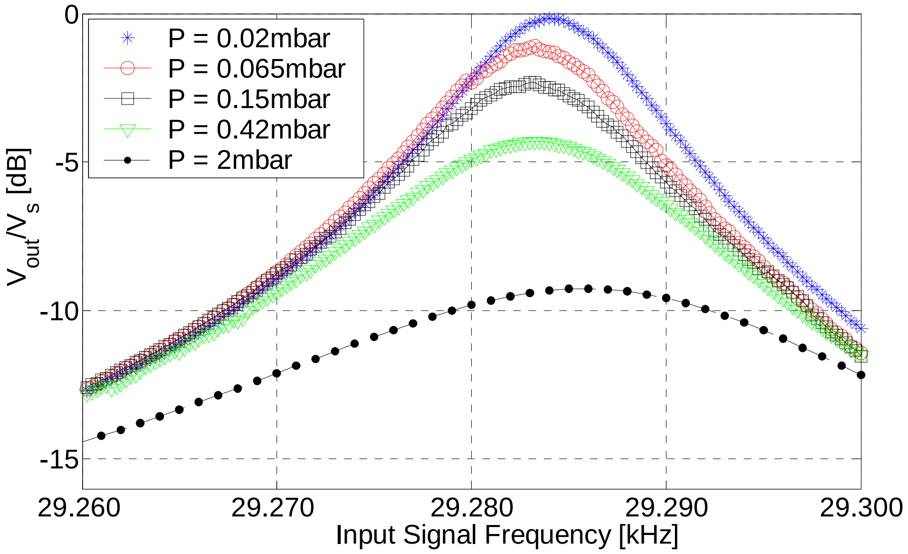

Figure 124: Amplitude V_{out} of the voltage read by the lock-in normalized by the input signal V_s a function of the input signal frequency at different pressures, varying from 0.02 mbar to 2 mbar. The normalization is required to compare the curves because the curve at 2 mbar is obtained by driving the microbalance with 200 mV^{PP}, while at the other pressures the device is driven with V_s = 100 mV^{PP}. The magnetic field is about 28 mT for each curve

In conclusion the humidity affects very much the device resonance frequency, even if it does not explain alone the whole difference between the resonance frequency measured in vacuum and at atmospheric pressure. Probably some other kinds of molecules are desorbed when the device works in vacuum. The effect of the humidity on the resonance frequency can be a problem when the device is used as a chemical sensor because the shift of resonance frequency due to the water absorption can be higher than the one due to the adsorption of small amounts of analyte, decreasing the resolution of the sensor. Anyway this problem can be easily reduced by using to device fabricated during the same run and on the same chip, one covered with a sensitive layer the other not. In this way to obtain a change in humidity leads to the same variation of the resonance frequency, while the absorption of the analyte drives a considerable variation of the resonance frequency only on the microbalance covered with the proper sensitive layer, so that the difference between the two resonance frequencies is due only to the analyte mass adsorption.

Pressure	**Measured f_0**	**Measured Q**	**Measured R_T**
atmospheric (1 bar)	28.899 kHz	123.5	17 mΩ
2 mbar	29.284 kHz	902.2	117.7 mΩ
0.42 mbar	29.283 kHz	1632.5	207.8 mΩ
0.15 mbar	29.283 kHz	2044.8	257.8 mΩ
0.065 mbar	29.283 kHz	2510.4	302.6 mΩ
0.02 mbar	29.284 kHz	2735.8	337.9 mΩ

Table 5: Resonance frequency, quality factor and transresistance R_T extracted at different pressures, for a type A device. Magnetic field is about 28 mT for each pressure.

This solution can reduce also the effect of other disturbs, like for example a change of temperature, which again leads the same frequency change in both the resonator.

4.7 Failure mechanisms

After a long usage (1 month) some of the characterized microbalances stop to work. In particular the conductance of the output loop becomes very close to zero. Practically the electrical connectivity is broken. The cause of this device failure is probably again the interruption of the metal 1 of the output loop close to the end of the left lateral beam in Figure 110 and at end of the right lateral beam in Figure 110. This region is circled in red in Figure 125. The metal in this region is very narrow and maybe slightly damaged during the aluminium etch, because even if the oxide overetch was limited by shorten the mask for BHF etch, there is still the probability that it is partially exposed to the aluminium etch (see 4.4.2). As shown previously there is also a low probability of breaking such metal during the post-processing.

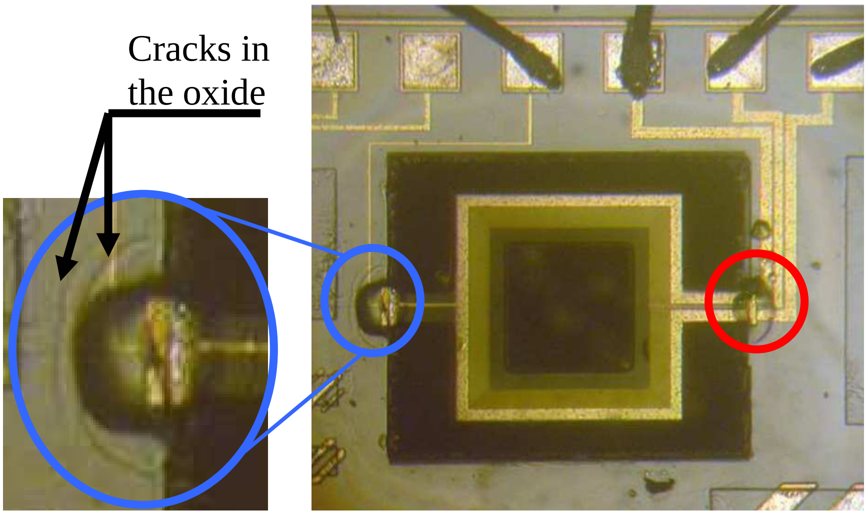

Figure 125: Picture at the optical microscope of a type A device after several cycles. The region where the output metal can break is circled in red. Both on the right and the left anchor there are some cracks in the oxide due to material fatigue, as it is especially clear from the zoom on the right.

Even if such narrow metal is not damaged, it has to endure high torsional stresses close to the anchor where the mechanical structure is maximally stressed. Thus after a lot of cycle the metal can break due to the material fatigue. Of course if the metal has been already damaged during the post-processing less cycle are needed to obtain the crash of the metal.

The high stress acting on the anchors are clear by the picture in Figure 125, especially in the magnified area on the left: circular dark lines, which do not appear on the device after few cycles (Figure 110), appears clearly around both the anchors. Such lines are the sign of some fracture of the material, probably a sliding of the intermetallic dielectrics with respect to the silicon and to each other. Probably if the metal 1 was not broken the lateral spring would break due to the fatigue, even if after a very high number of cycles.

The circular cracks in the oxide seem to not affect the device main important features, such as f_0, Q and R_T. Indeed changes of the resonance frequency of about some tens of Hz have been observed by after a lot of cycles, but they can be also due to some adsorption/desorption of particles.

In conclusion the failure of the device due to the output metal breaking has be prevented by redesign the output metal larger than in the present design. In general a rule of minimum width of the metals close to the anchors should be defined

Conclusion

After this detailed discussion about the activities carried out during the Ph.D., it is time to summarize the main results which were obtained.

The demonstration of the basic operation and the characterization of a third-mode free-free resonator with flexural supports (FF3) was certainly a very important result because of the originality of the device. The measured quality factor in vacuum (about 5000) is good if compared with other flexural-beam resonators for RF applications, presented in literature. Furthermore, according to FEM simulations, the sensitivity of the resonance frequency to temperature and axial stresses is for a FF3 resonator slightly better than for other two device based on bending beams (the clamped-clamped and the free-free first-mode resonator). Unluckily it was not possible to characterize the other innovative resonator for RF applications, that is, the free-free resonator with tuneable resonance frequency. Finally, some possible improvements of the resonators design was found by observing experimental data from device characterization, as well as results from FEM simulations.

On the other hand, the equivalent circuit proposed for free-free resonators shows a good performance, if compared with FEM simulations of the frequency response of the device: the circuit, even in a simplified topology, correctly predicts the values of the resonance frequency and the quality factor of the device, even when possible fabrication defects alter the matching condition used in the design. Acceptable results are obtained with respect to the evaluation of the maximum resonator deflection (which is related to the output signal amplitude and thus to insertion losses, as well as to the linearity of the device), only if the extended equivalent circuit is used. Anyway the difference between expected value and results from simulation is higher for the maximum deflection than for the resonance frequency and quality factor and this can be ascribed, at least to some extent, to the non-ideal behaviour of the real device with respect to the Euler-Bernoulli model for bending beams, which was assumed to extract the equivalent circuit.

If for flexural-beam resonators a complete cycle of modelling, design fabrication and characterization were carried out, for bulk-mode disk resonators a very deep and articulated modelling activity were pursued. In particular two new simulation strategies have been formalized to estimate one of the most important sources of energy dissipation in MEM resonators, namely *anchor losses*, which is expected to limit the quality factor of a MEM resonator in vacuum. These strategies, based on FEM simulations, give results very close to the simulation strategies presented by other authors, as well as to some measurements from literature. The proposed strategies does not lead to simulations faster than the others, but at least one of the two is based on a more rigorous theoretical background than in the case of the majority of the simulation strategies used to estimate anchor losses. This method (indicated in the text as *THBC* method) is based on the exact solution of the problem of the propagation of an acoustic wave in a substrate, considered as a semi-infinite space. Such a solution is exploited to find proper boundary conditions at the interface between anchor and substrate.

Because of the rigorous theoretical analysis which it is based on, the THBC method allows a deep insight into the mechanism of anchor losses, and it is probably much accurate than other methods.

Anchor losses simulations together with the estimate of another mechanism limiting the quality factor, namely *thermoelastic damping*, allow to find a design strategy to maximize the quality factor of a bulk-mode disk resonator, once the resonance frequency is fixed. Indeed thermoelastic losses were shown to be important only if anchor losses are minimized.

Simulations of anchor losses in a disk resonator demonstrated that they depend on the anchor size (or anchor/stem radius, since the anchor is circular) in an unexpected way: it is generally believed that anchor losses monotonically increases, and thus quality factor decreases, if anchor size increases. But some of the simulation results presented in this thesis show that in the dependence of quality factor only due to anchor losses on the stem radius there could be one or more local minima and maxima. This result from simulations is confirmed by a theoretical analysis and the stem radii which give the minima of the quality factor (maxima of anchor losses) can be found by a proposed theoretical model, even if the accuracy of this model is not very high if compared with simulations.

The innovatory discovery of local maxima in the dependence of anchor losses on anchor size, allow to find very low anchor losses and thus very high quality factor even without reducing the anchor size to very small values, as it is generally done nowadays with a great complication with respect to the technological process.

All the theory and the simulations discussed in this thesis about quality factor of bulk-mode disk resonators results in a very simple strategy: since anchor size does not affect the resonance frequency (as confirmed both by theory and simulations), while the disk radius influences both resonance frequency and quality factor, the disk radius is initially fixed to determine the resonance frequency and after the stem radius is chosen to maximize the quality factor according to the simulations results, finding in this way the optimum layout for a disk resonator, resonating at the frequency required by the specification. The optimization can be also achieved by an automatic synthesis tool. Besides the robustness of the design choices, which were suggested by such design strategy, was evaluated by estimating the effect of a variation of stem radius, disk radius and other geometrical dimensions of the resonator with respect to their nominal value.

Measurements on real devices are planned to demonstrate the presence of maxima and minima in the dependence of quality factor on the anchor size and to validate the strategy for the optimization of the layout, which is proposed in this thesis. For this purposes several disk resonators are now under fabrication at IMEC.

Finally, the research activity about MEM microbalances, results in a very innovative and promising device. A microbalance with magnetic actuation and sensing and with an original mechanical structure was for the first time presented. It was fabricated with a low-cost CMOS-compatible process in two different variants, one bulkier but with more efficient actuation and sensing, the other smaller, but with less effective actuation and sensing. The basic operation of both the devices was demonstrated at different pressures and using both 20x12 cm macroscopic magnets and NdFeB micro-magnets smaller than 1 mm^3, in order to generate the needed external magnetic field.

The frequency responses of both the devices were acquired, allowing to extract resonance frequency and quality factor. Resonance frequency is around 30 kHz for the bulkier device and around 90 kHz for the smaller, while the quality factor at atmospheric pressure is slightly higher than 100 for the first kind of device and about 200 for the second. Having a high quality factor at atmospheric pressure is fundamental for a resonator used as microbalance: since it is generally inserted in an oscillator as a frequency selective element, the higher the quality factor, the lower the phase noise and thus the lower the minimum resonance frequency changes due to the adsorption of the analyte molecules which can be discriminated from a variation of the resonance frequency due to the noise. In other words, a high quality factor is needed for a good sensor resolution.

Acquired resonance responses show also that the signal due to the resonator movements is enough higher than the parasitic signal around the resonance, for both the designed devices, even if, as expected, the bulkier device show a level of output signal higher than in the case of the smaller one, if the two device are driven with the same input signal.

The small effect of parasitic signal is an important result considering that the measured parasitic signal is significant, since the small output signal of the resonator is amplified by a circuit fabricated with discrete components on a PCB board and not by an integrated electronic circuit, which can be potentially fabricated on the same chip of the device to reduce parasitic signals, because of the CMOS compatibility of the fabrication process of the devices.

Some design improvements have been proposed for a next layout of the device in order to avoid some failure mechanisms observed during the fabrication and the operation of some devices.

A problem of the device was found to be the high sensitivity of the resonance frequency to the humidity, which is by the way reasonable considering that the microbalances are mainly made of BPSG. This problem can be solved by using as a sensor a pair of devices nominally equal and fabricated very close on the same chip in order to increase their matching: if one of them is covered with a proper sensitive layer to detect a particular molecule, the other is not, so that while a humidity change influences almost in the same way the two, a change in the analyte concentration in the surroundings results in a change of the resonance frequency of only the device covered with a sensitive layer. Thus if the difference between the resonance frequency of the two devices is measured, the interference of the humidity is highly reduced. This architecture is useful also to reduce the effect of temperature changes or other molecules easily absorbable by BPSG.

To complete the characterization of the microbalance presented in this thesis the only remaining step is the coating with a proper sensitive layer in order to test its performance as a sensor. For this purpose the device will be given to a group of biologists of the CNR of Pisa, which will cover the device surface with a proper sensitive layer in order to detect DNA sequences.

Appendix A: Bessel Function Properties

In this appendix demonstrate the properties of the Bessel function, which were used in chapter 3, are demonstrated:

I.

$$\int_0^\infty r\left(\frac{\partial^2 F}{\partial r^2}+\frac{1}{r}\frac{\partial F}{\partial r}\right)J_0(qr)dr=-q^2F_0 \qquad \text{(A1)}$$

can be demonstrated by applying twice integration by parts:

$$\begin{aligned}\int_0^\infty r\left(\frac{\partial^2 F}{\partial r^2}+\frac{1}{r}\frac{\partial F}{\partial r}\right)J_0(qr)dr &= \int_0^\infty \frac{\partial}{\partial r}\left(r\frac{\partial F}{\partial r}\right)J_0(qr)dr= \\ &= r\frac{\partial F}{\partial r}J_0(qr)\bigg|_0^\infty+\int_0^\infty qr\frac{\partial F}{\partial r}J_1(qr)dr= \qquad \text{(A2)} \\ &= rqFJ_1(qr)\big|_0^\infty-\int_0^\infty q^2rFJ_0(qr)dr=-q^2F_0\end{aligned}$$

where it is exploited the hypothesis that F and its first derivative with respect to r are bounded for $r \to \infty$. This hypothesis implies that $r\frac{\partial F}{\partial r}J_0(qr)\to\infty$ and $rFJ_1(qr)\to\infty$ for $r \to \infty$.

II.

$$\int_0^\infty r\left(\frac{\partial^2 F}{\partial r^2}+\frac{1}{r}\frac{\partial F}{\partial r}-\frac{F}{r^2}\right)J_1(qr)dr=-q^2F_1 \qquad \text{(A3)}$$

can be demonstrated by applying twice integration by parts:

$$\int_0^\infty r\left(\frac{\partial^2 F}{\partial r^2}+\frac{1}{r}\frac{\partial F}{\partial r}-\frac{F}{r^2}\right)J_1(qr)dr=\int_0^\infty r\frac{\partial}{\partial r}\left\{\frac{1}{r}\left[\frac{\partial\left(rF\right)}{\partial r}\right]\right\}J_1(qr)dr=$$

$$=\frac{\partial\left(rF\right)}{\partial r}J_1(qr)\Bigg|_0^\infty-\int_0^\infty q\frac{\partial\left(rF\right)}{\partial r}J_0(qr)dr= \qquad \text{(A4)}$$

$$=-rqFJ_0(qr)\Big|_0^\infty-\int_0^\infty q^2 rFJ_1(qr)dr=-q^2F_1$$

where it is exploited the hypothesis that F and its first derivative with respect to r are bounded for $r \to \infty$. This hypothesis implies that $\frac{\partial\left(rF\right)}{\partial r}J_1(qr)=\left(r\frac{\partial F}{\partial r}+F\right)J_1(qr)\to\infty$ and $rFJ_0(qr)\to\infty$ for $r \to \infty$.

III.

$$\int_0^\infty r\left(\frac{\partial F}{\partial r}\right)J_1(qr)dr=\int_0^\infty qrFJ_0(qr)dr=-qF_0 \qquad \text{(A5)}$$

can be demonstrated by integrating by parts:

$$\int_0^\infty r\left(\frac{\partial F}{\partial r}\right)J_1(qr)dr=$$

$$=rFJ_1(qr)\Big|_0^\infty-\int_0^\infty qrFJ_0(qr)dr=-qF_0 \qquad \text{(A6)}$$

where it is exploited the hypothesis that F is bounded for $r \to \infty$. This hypothesis implies that $rFJ_1(qr)\to\infty$ for $r \to \infty$.

IV.

$$\int_0^\infty r\left(\frac{\partial F}{\partial r}+\frac{F}{r}\right)J_0(qr)dr=\int_0^\infty qrFJ_1(qr)dr=+qF_1 \qquad \text{(A7)}$$

can be demonstrated by integrating by parts:

$$\int_0^\infty r\left(\frac{\partial F}{\partial r}+\frac{F}{r}\right)J_0(qr)dr=\int_0^\infty \frac{\partial\left(rF\right)}{\partial r}J_0(qr)dr= \\ =rFJ_0(qr)\Big|_0^\infty+\int_0^\infty qrFJ_1(qr)dr=+qF_1 \tag{A8}$$

where it is exploited the hypothesis that F is bounded for $r\to\infty$. This hypothesis implies that $rFJ_0(qr)\to\infty$ for $r\to\infty$.

Appendix B: Intrinsic damping in a silicon substrate

In order to get a rough evaluation of the relaxation time τ of a substrate mentioned in chapter 3, such parameter is calculated from the amount of energy dissipated in a substrate by a propagating plane wave. In principle the dissipation could depend on the shape of the propagating wave, thus this approximation could be considered very coarse. Only phonon-phonon interaction and thermoelastic damping are considered.

Starting from the phonon-phonon interaction, the absorption coefficient α due to such dissipation mechanism was found by [94], for a compressive longitudinal acoustic wave propagating in a material:

$$\alpha = 0.43\frac{C_p T \gamma^2}{\rho c_L^3}\left[\frac{\omega^2\theta}{1+\left(\omega\theta\right)^2}\right] \tag{A9}$$

In (A9) all the variables are expressed in MKS. C_p is the thermal capacitance, T temperature in Kelvin, ρ the mass density and c_L the velocity of longitudinal wave as expressed in (95); γ is the Gruneisen parameter, which is given by the average of the relative temperature change, divided by relative change of density in the material [94]. According to [52], γ can be taken as 0.4 for mono-crystalline silicon.

Finally, θ is a relaxation time necessary to exchange energy between hot and cold phonons. Its expression from [94] is:

$$\theta = \frac{3K_{th}}{C_p c_L^2} \tag{A10}$$

where K_{th} is the material thermal conductivity.

Now, considering the Young's modulus as defined in (119), with $\tau = \tau_{PH}$ (i.e. only due to phonon-phonon interaction), the generic attenuated longitudinal plane wave *Δ*, propagating along *z* direction, towards $+\infty$, is:

$$\Delta = Ae^{-h_I z} e^{j(\omega t + h_R z)}$$

with: (A11)

$$h_R = \mathrm{Re}\left[\frac{\omega}{v}\right] \qquad h_I = -\mathrm{Im}\left[\frac{\omega}{v}\right]$$

If *E* is defined as in (119), with $\tau = \tau_{PH}$ (i.e. only due to phonon-phonon interaction), h_I can be written as:

$$h_I = -\mathrm{Im}\left[\frac{\omega}{c_L\sqrt{1+j\omega\tau_{PH}}}\right] \approx -\mathrm{Im}\left[\frac{\omega}{c_L}\left(1-\frac{j\omega\tau_{PH}}{2}\right)\right] = \frac{\omega^2\tau_{PH}}{2c_L} \tag{A12}$$

where $\omega\tau_{PH} << 1$ is assumed (this hypothesis has to be verified at the end). Then, the attenuation coefficient α in dB/m can be written as:

$$\alpha = -10\frac{\partial\left[\mathrm{Log}_{10}\left(\left|\Delta\right|^2\right)\right]}{\partial z} = \frac{20}{\ln(10)}h_I = 4.33\frac{\omega^2\tau_{PH}}{c_L} \tag{A14}$$

and consequently, combining (A14) and (A9) τ_{PH} can be written as:

$$\tau_{PH} = 0.1\frac{C_p T\gamma^2}{\rho c_L^2}\left[\frac{\theta}{1+(\omega\theta)^2}\right] \tag{A15}$$

Considering that for Silicon (*E = 160 GPa*, *ρ = 2330 Kg/m*^{3}, *ν = 0.226*, *K = 148 W/(K*m)*, C_P *= 1.63 MJ/(K*m*^{3}*))* *θ = 3.64 ps*, so that for *f = ω/(2*π) = 200 MHz*, $\omega\theta = 0.005 << 1$. Thus, for the frequency the device in chapter 3 works at, the following approximation of (A15) holds:

$$\tau_{PH} = 0.1\frac{C_p T\gamma^2}{\rho c_L^2}\theta = 0.1\frac{3K_{th}T\gamma^2}{\rho c_L^4} \tag{A16}$$

where the expression in for θ written in (A10) was also substituted. According to Eq. (A16) τ_{PH} is independent on the thermal capacitance, while it is proportional to thermal conductivity, temperature and Gruneisen number. The most important parameter which determines phonon-phonon dissipation is the longitudinal velocity c_L, so that an increase of it strongly reduces τ_{PH}: the more rigid (high E) and lighter (low ρ) the material is, the lower the losses. In the case of the silicon, its very high Young's modulus leads to a very low τ_{PH}. In the specific, assuming from [52] $\gamma = 0.4$, τ_{PH} is about *0.16 fs* at $T = 300\ K$. Considering again the approximation done in (A12), it largely holds for such value for τ_{PH}, which leads $\omega\tau_{PH} = 2\text{x}10^{-7}$ at 200 MHz.

The second mechanism which can dissipate energy in the substrate by heating is the thermoelastic effect. In the range of frequencies below 1 GHz (at least for Silicon), according to [93], for a plane longitudinal wave the attenuation, given in terms of the parameter h_I defined as in (A11), can be approximated as:

$$h_I = \frac{\alpha_T^2 T K_{th} \rho}{2C_P^2 c_L} \left(\frac{1+\nu}{1+\nu} \right)^2 \omega^2 \qquad \text{(A17)}$$

Considering a Young's modulus defined as in (119) with $\tau = \tau_{TH}$ (i.e. only due to thermoelastic dissipation), repeating the same reasoning performed for phonon-phonon interaction, it is possible to find:

$$\tau_{TH} = \frac{\alpha_T^2 T K_{th} \rho}{C_P^2} \left(\frac{1+\nu}{1+\nu} \right)^2 \qquad \text{(A18)}$$

where α_T is the coefficient of thermal expansion (CTE), which plays a very important role in thermoelastic dissipation as shown also in section 3.6. From (A17) it is possible to find that for a Silicon substrate ($\alpha_T = 2.6\text{x}10^{-6}$), $\tau_{TH} = 0.67\ fs$. Thus this relaxation time is greater but comparable with phonon-phonon dissipation. The overall τ given by the two mechanism addressed in this appendix is slightly smaller than *1 fs*.

List of references

[1] C.T.-C. Nguyen, “Transceiver front-end architectures using vibrating micromechanical signal processors”, *proceeding of Topical Meeting on Silicon Monolithic Integrated Circuits in RF Systems*, Ann Arbor, MI, USA, 2001, pp. 23–32.

[2] P. Bruschi, A. Nannini, F. Pieri, “Electrical measurements of the quality factor of microresonators and its dependence on the pressure”, *Sensor and Actuators A*, vol. 114, pp. 21–29, 2004.

[3] W. C. Tang, T.-C. H. Nguyen, M. W. Judy, R. T. Howe “Electrostatic-comb drive of lateral polysilicon resonators”, *Sensor and Actuators*, vol. A21-A23, pp. 328–331, 1990.

[4] D. Lange, O. Brand, H. Baltes, “CMOS Cantilever Sensor Systems”. Springer, 2002.

[5] D. Lange, C. Hagleitner, C. Herzog, O. Brand, and H. Baltes, “Electromagnetic actuation and MOS-transistor sensing for CMOS-integrated micromechanical sensors.”, *Sensors and Actuators A*, vol. 103, pp. 150–155, 2003.

[6] D.W. Lee, Takahito Ono, Masayoshi Esashi, “Cantilever with integrated resonator for application of scanning probe microscope”, Sensors and Actuators A, vol. 83, pp. 11–16, 2000.

[7] J.H. Lee, K.H. Yoon, K.S. Hwang, J. Park, S. Ahn, and T.S. Kim, “Label free novel electrical detection using micromachined PZT monolithic thin film cantilever for the detection of C-reactive protein.”, *Biosensors and Bioelectronics* vol. 20, pp. 269–275, 2004.

[8] D. Lange, C. Hagleitner, O. Brand, H. Baltes, “CMOS resonant beam gas sensing system with on-chip self excitation”, *proceeding of IEEE MEMS*, Interlaken, Switzerland, 2001, pp. 547–552.

[9] H.A.C. Tilmans, “Equivalent circuit representation of electromechanical transducers: II. Distributed-parameter systems.” *Journal of Micromechanics and Microengineering*, vol. 7, pp. 285–309, 1997.

[10] H.A.C. Tilmans, “Equivalent circuit representation of electromechanical transducers. I. Lumped parameters systems”, *Journal of Micromechanics and Microengineering*, vol. 6, pp. 157–176, 1996.

[11] S. Roy, R. G. DeAnna, C. A. Zorman, M. Mehregany, “Fabrication and Characterization of Polycrystalline SiC Resonators”, *IEEE Transactions on Electron Devices*, vol. 49, no. 12, pp. 2323–2331, 2002.

[12] T. Mattila, O. Jaakkola, J. Kiihamaki, J. Karttunen, T. Lamminmaki, P. Rantakari, A. Oja, H. Seppa, H. Kattelus, and I. Tittonen, “14 MHz micromechanical oscillator”, *Sensor and Actuators A*, vol. 97-98, pp. 497–502, 2002.

[13] J. R. Clark, W.-T. Hsu, C. T.-C. Nguyen, “High-Q micromechanical contour-mode disk resonators”, *proceeding of IEEE Electron Devices International Meeting*, San Francisco, CA, USA, 2000, pp. 11–13

[14] W.-T. Hsu, J. R. Clark, C. T.-C. Nguyen, “A resonant temperature sensor based on electrical spring softening”, *proceeding of the 11th International Conference of Solid-State Sensors & Actuators (Transducers ’01)*, Munich, Germany, 2001, pp. 1484–1487.

[15] W.-T. Hsu, J.R. Clark, C.T.-C. Nguyen, “Mechanically temperature-compensated flexural-mode micromechanical resonators.” *proceeding of Electron Devices Meeting*, San Francisco, USA, 2000, pp. 399–402.

[16] Zs. Kàdàr, A. Bossche, P. M. Sarro, J. R. Mollinger, “Magnetic-field measurements using an integrated resonant magnetic-field sensor”, *Sensors and Actuators A*, vol. 70, pp. 225–232, 1998.

[17] P. S. Riehl, K. L. Scott, R. S. Muller, R. T. Howe, J. A. Yasaitis, “Electrostatic charge and field sensors based on micromechanical resonators”, Journal of Micromechanical Systems, vol. 12, no. 5, pp. 577–589, 2003

[18] D. Paci, “Progetto di risonatori microelettromeccanici con il processo Thelma”, *Master Degree Thesis (in Italian)*, University of Pisa, Pisa, Italy, 2003.

[19] A. N. Cleland, M. L. Roukes, “Noise processes in nanomechanical resonators”, Journal of Applied Physics vol. 92, no. 5, pp. 2758–2769, 2002.

[20] www.agilent.com

[21] S.-H. Kim, J.-H. Kim, H.-D. Park, G. Yoon, “AlN-based film bulk acoustic resonator devices with W/SiO_2 multilayers reflector for RF bandpass filter application”, *Journal of Vacuum Science Technology B*, vol. 19, no. 4, pp. 1164–1168, 2001.

[22] J. Wang, J. E. Butler, T. Feygelson and C. T.-C. Nguyen, “1.51-GHz nanocrystalline diamond micromechanical disk resonator with material-mismatched isolating support”, *proceeding of IEEE MEMS*, Maastricht, Nederland, pp. 641–644, 2004.

[23] T. Mattila, J. Kiihamaki, T. Lamminmaki, O. Jaakkola, P. Rantakari, A. Oja, H. Seppa, H. Kattelus, and I. Tittonen, “A 12 MHz micromechanical bulk acoustic mode oscillator” *Sensors and Actuators A: Physical*, vol. 101, pp. 1–9, 2002

[24] F. D. Bannon, J. R. Clark, C.T.-C. Nguyen, “High-Q microelectromechanical filters” *Journal of Solid State Circuits*, vol. 35, pp. 512–526, 2000

[25] D. Galayko, A. Kaiser, L. Buchaillot, D. Collard, C. Combi, “Electrostatical coupling-spring for micro-mechanical filtering applications”, *proceedings of International Symposium on Circuits and Systems (ISCAS '03)*, vol. 3, pp. 530–533, Bangkok, Thailand, 2003.

[26] M. Koskenvuori, T. Mattila, A. Haara, J. Kiihamaki, I. Tittonen, A. Oja, H. Seppa, “Long-term stability of single-crystal silicon microresonators.” *Sensors and Actuators A*, vol. 115, pp. 23–27, 2004

[27] C. H. Haas, M. Kraft, “Modelling and analysis of a MEMS approach to dc voltage step-up conversion”, *Journal of Micromechanics and Microengineering*, vol. 14, pp. 114–122, 2004.

[28] A. Witvrouw, M. Gromova, A. Mehta, S. Sedky, P. De Moor, K. Baert, C. van Hoof, “Poly-SiGe: A Superb Material for MEMS”, *proceedings of MRS fall meeting*, Boston, MA, USA, 2003, pp. 25–36.

[29] S. A. Bhave, D. Gao, R. Maboudian, R. T. Howe, “Fully-differential Poly-SiC Lamé-mode resonator and checkerboard filter”, *proceeding of IEEE MEMS*, Miami Beach, FL, USA, pp. 223–226, 2005.

[30] L. Yan, J. Wu, W. C. Tang, “Piezoelectric micromechanical disk resonators towards UHF band”, *proceedings of IEEE International Conference of Ultrasonics, Ferroelectrics and Frequency Control*, Montreal, Canada, vol. 2, pp. 926–929, 2004.

[31] K. Merguerre, K. Wolfel, “Mechanics of vibration”, *Sijthoff & Noordhoff*, 1979.

[32] D. Galayko, A. Kaiser, B. Legrand, L. Buchaillot, C. Combi, and D. Collard, “Clamped-clamped beam micro-mechanical resonators in thick-film epitaxial polysilicon technology.” In *Proceeding of ESSDERC2002*, Firenze, Italy, 2002, pp. 447–450.

[33] K. Wang, A.-C. Wong, C.T.-C Nguyen, “VHF free-free beam high-Q micromechanical resonator”, *IEEE Journal of Microelectromechanical Systems*, vol. 9, no. 3, pp. 347–360, 2000.

[34] Y.C. Fung, *Foundations of Solid Mechanics*. In Dynamics, Prentice-Hall International, 1965.

[35] R. Lifshitz and M. L. Roukes, “Thermoelastic damping in micro and nanomechanical systems”, *Physical Review B*, vol. 61, no. 8, pp. 5600-5609

[36] Z. Hao, A. Erbil and F. Ayazi, “An analytical model for support loss in micromachined beam resonators with in-plane flexural vibrations” *Sensors and Actuators A*, vol. 109, pp. 156-164, 2003

[37] J. Wang, Z. Ren and C.T.-C Nguyen, “1.156-GHz Self-Aligned Vibrating Micromechanical Disk Resonator”, IEEE Transactions on Ultrasonic, Ferroelectrics and Frequency control, vol. 51, no. 12, pp. 1607-1628, 2004.

[38] W.-T. Hsu, J.R. Clark, C.T.-C. Nguyen, “*Q*-optimized lateral free-free beam micromechanical resonators”, *proceeding of 11th Int. Conf. on Solid-State Sensors & Actuators* (Transducers’ 01), Munich, Germany, 2001, pp. 1110–1113.

[39] M.U. Demirci and C.T.-C. Nguyen, “Higher-mode free-free beam micromechanical resonators” *proceeding of Frequency Control Symposium and PDA Exhibition Jointly with the 17th European Frequency and Time Forum Piscataway*, NJ, USA, 2003, pp. 810–818.

[40] H.A.C. Tilmans, R. Legtenberg, “Electrostatically driven vacuum encapsulated polysilicon resonators. Part II. Theory and performance”, *Sensors and Actuators A*, vol. 45, pp. 67–84, 1994.

[41] V. Kaajakari, T. Mattila, A. Oja, J. Kiihamaki, H. Seppa, “Square extensional mode single-crystal silicon micromechanical resonator for low phase noise oscillator applications”, *IEEE Electron Device Letters*, vol. 25, no. 4, pp. 173–175, 2004.

[42] Z. Hao, S. Pourkamali, F. Ayazi, “VHF single-crystal silicon elliptic bulk-mode capacitive disk resonators – Part I: design and modelling”, *Journal of Micromechanical Systems*, vol. 13, no. 6, pp. 1043–1053, 2004.

[43] www.comsol.com

[44] B. Bircumshawa, G. Liub, H. Takeuchib, T.-J. Kingb, R. Howe, O. O’Reillya, A. Pisano, “The bulk radial annular resonator: towards a 50Ω RF MEMS filter”, *proceeding of The 12th International Conference on Solid State Sensors, Actuators and Microsystems (Transducers ’03),* Boston, MA, USA, 2003, pp. 875–878.

[45] L.D. Landau and E.M. Lifshitz, “Course of Theoretical Physics: vol. 2 Fluid Mechanics.” *Pergamon Press*, 1959.

[46] M.-H. Bao, “Micro Mechanical Transducers.” *Elsevier*, 2000.

[47] Y.-H. Cho, B. M. Kwak, A. P. Pisano, R.T. Howe, “Slide film damping in laterally driven microstructures”, ”, *Sensors and Actuators A*, vol. 40, pp. 31–39, 1994.

[48] K.-M. Chang, S.-C. Lee and S.-H. Li, “Squeeze film damping effect on a MEMS torsion mirror”, Journal of Micromechanics and Microengineering, vol. 12, pp. 556–561, 2002.

[49] M. Bao, H. Yang, Y. Sun, Y. Wang, “Squeeze-film air damping of thick hole-plate”, *Sensors and Actuators A*, vol. 108, pp. 212–217, 2003.

[50] T. Veijola, A. Pursula, P. Raback, “Surface extension model for MEMS squeezed-film dampers”, *proceeding of Design, Test, Integration and Packaging of MEMS and MOEMS (DTIP)*, Montreux, Switzerland, 2005, pp. 405–410.

[51] A. Witvrouw, C. Rusu, H. Jansen, R. Gunn, “Self-aligned 0-level sealing of MEMS devices by a two layer thin film reflow process”, *Journal of Microsystems Technologies*, vol. 10, no. 5, pp. 364–371, 2004.

[52] X. Liu, J. F. Vignola, H. J. Simpson, B. R. Lemon, B. H. Houston, D. M. Photidias, “A loss mechanism study of a very high *Q* silicon micromechanical oscillator”, *Journal of Applied Physics*, vol. 97, 2005.

[53] H. E. Bommel, K. Dransfeld, “Excitation of hypersonic waves in quartz”, *Physical Review*, vol. 117, no. 5 (1960), pp. 1245 – 1251.

[54] J.P. Berenger, “A perfectly matched layer for the absorption of electromagnetic waves” Journal of Computational Physics, vol. 114, pp. 185-200, 1994.

[55] D. S. Bindel, E. Quevy, T. Koyama, S. Govindjee, J. W. Demmel, R. T. Howe, “Anchor loss simulation in resonators”, *proceeding of IEEE MEMS*, Miami Beach, FL, USA, pp 133–136, 2005.

[56] Y.-H. Park and K.C. Park, “High-fidelity modelling of MEMS resonators – Part I: anchor loss mechanisms through substrate” *Journal of Microelectromechanical Systems*, vol. 13, no. 2, pp. 238-247, 2004

[57] Y.-H. Park and K.C. Park, “High-fidelity modelling of MEMS resonators – Part II: coupled beam-substrate dynamics and validation”, *Journal of Microelectromechanical Systems*, vol. 13, no. 2, pp. 248-257, 2004

[58] Z. Hao, F. Ayazi, “Support loss in the radial bulk-mode vibrations of center-supported micromechanical disk resonators”, *Sensor and Actuators A*, in press

[59] C. Hagleitner, A. Hierlemann, D. Lange, A. Kummer, N. Kerness, O. Brand, H. Baltes, “Smart single-chip gas sensor microsystem”, *Nature*, 414, pp. 293–296, 2001.

[60] F.M. Battiston, J.-P. Ramseyer, H.P. Lang, M.K. Baller, Ch. Gerber, J.K. Gimzewski, E. Meyer, H.-J. Guntherodt, “A chemical sensor based on a microfabricated cantilever array with simultaneous resonance frequency and bending readout”, *Sensors & Actuators B*, vol. 77, pp. 122–131, 2001.

[61] C. Di Nucci, A. Fort, S. Rocchi, L. Tondi, V. Vignoli, F. Di Francesco, M. Belén Serrano Santos, “A measurement system for odor classification based on the dynamic response of QCM sensors”, no. 4, *IEEE Transaction on Instrumentation ad Measurement*, vol. 52, pp. 1079–1086, 2003.

[62] M.Z. Atashbar, B. Bejcek, A. Vijh, S. Singamaneni, “QCM biosensor with ultra thin polymer film”, *Sensors and Actuators B*, vol. 107 pp. 945–951, 2005.

[63] J.H. Lee, K.H. Yoon, K.S. Hwang, J. Park, S. Ahn, and T.S. Kim, “Label free novel electrical detection using micromachined PZT monolithic thin film cantilever for the detection of C-reactive protein”, *Biosensors and Bioelectronics* vol. 20, pp. 269–275, 2004.

[64] J. Zang, S. O’Shea, “Tuning forks as micromechanical mass sensitive sensors for bio- or liquid detection”, *Sensors and Actuators B*, vol. 94 pp. 65–72, 2003.

[65] G. Barillaro, A. Diligenti, A. Nannini, L. M. Strambini, E. Comini, G. Sberveglieri, “Low-concentration NO/sub 2/ detection with an adsorption porous silicon FET”, *IEEE Journal of Sensors*, vol. 6, pp. 19–23, 2006.

[66] R. Gabl, H. D. Feucht, H. Zeininger, G. Eckstein, M. Schreiter, R. Primig, D. Pitzer, W. Wersing, “First results on label-free detection of DNA and protein molecules using a novel integrated sensor technology based on gravimetric detection principles”, *Biosensors and Bioelectronics*, vol. 19, pp. 615–620, 2004.

[67] J. Thaysen, R. Marie and A. Boisen, “Cantilever-based bio-chemical sensor integrated in a microliquid handling system” *proceeding of IEEE MEMS*, Interlaken, Switzerland, 2001, pp. 401–404.

[68] K. Y. Gfeller, N. Nugaeva, M. Hegner, “Micromechanical oscillators as rapid biosensor for the detection of active growth of *Escherichia Coli*”, *Biosensors and Bioelectronics*, vol. 21, pp. 528–533, 2005.

[69] M. Su, S. Li, V. P. Dravid, “Microcantilever resonance-based DNA detection with nanoparticle probes”, *Applied Physics Letters*, vol. 82, no. 20, pp. 3562–3564, 2003.

[70] M.J. Madou, “Fundamentals of Microfabrication”, *CRC Press*, 2002.

[71] Z.J. Davis, G. Abadal, O. Kuhn, O. Hansen, F. Grey, A. Boisen, “Fabrication and characterization of nanoresonating devices for mass detection”, Journal of Vacuum Science & Technology B, vol. 18, pp. 612–616, 2000.

[72] B.H. Kim, D.P. Kern, S. Raible, U. Weimar, “Fabrication of micromechanical mass-sensitive resonators with increased mass resolution using SOI substrate”, *Microelectronic Engineering*, vol. 61–62, pp. 947–953, 2002

[73] S.-H. Lee, S.-W. Hong, Y.-K. Kim, S.-K. Lee, “A planar vibratory gyroscope using electromagnetic force”, *Sensors and Actuators A*, vol. 65, pp. 101–108 , 1998

[74] D. Paci, A. Nannini and F. Pieri, “Simulations and Theoretical Analysis of the Effect of Temperature on the Resonance Frequency of Three Different Kinds of MEMS Resonators”, *proceeding of Design, Test, Integration and Packaging of MEMS and MOEMS (DTIP)*, Montreux, Switzerland, 2005, pp. 195–199.

[75] M. Mastrangeli, A. Nannini, D. Paci, F. Pieri, “Equivalent Circuit for RF Flexural Free-Free MEMS Resonators”, *proceeding of the 15th Workshop on Modelling and Simulations of Electron Devices*, Pisa, Italy, 2005, pp. 51–52

[76] D. Paci, M. Mastrangeli, A. Nannini, F. Pieri, “Modeling and Characterization of Three Kinds of MEMS Resonators Fabricated with a Thick Polysilicon Technology”, *Analog Integrated Circuits and Signal Processing*, vol. 48, no. 1, pp. 41–47, 2006.

[77] M. Mastrangeli, A. Nannini, D. Paci, F. Pieri, “Equivalent Circuit for RF Flexural Free-Free MEMS Resonators”, *Journal of Computational Electronics*, vol. 5, no. 2–3, pp. 205–210, 2006.

[78] E. A. Vittoz, M. G. R. Degrauwe, S. Bitz, “High-performance crystal oscillator circuits: theory and application”, *IEEE Journal of Solid-State Circuits*, vol. 23, no. 3, 1988.

[79] C.T.C. Nguyen, “Electromechanical characterization of microsensors for circuit applications”, *Master Degree Thesis*, UCB, Berkeley, USA, 1991.

[80] M. Mastrangeli, "Progetto, simulazione e misura di risuonatori microelettromeccanici flessionali", *Master Degree Thesis (in Italian)*, University of Pisa, Pisa, Italy 2005.

[81] "A Measurement Interface for Single-Ended and Differential Sensing of Micromachined Accelerometers at Different Vacuum Levels", P. Bruschi, A. Nannini, D. Paci, F. Pieri, *proceeding of Eurosensors XVIII*, Roma, Italy, 2004.

[82] "A Method for Cross-Sensitivity and Pull-in Voltage Measurement of MEMS Two-Axis Accelerometers", P. Bruschi, A. Nannini, D. Paci, F. Pieri, *Sensors and Actuators A*, vol. 123-124, pp. 185-193, 2005.

[83] www.ni.com/labview/.

[84] H.A.C. Tilmans, M. Elwenspoek, and J.H.J. Fluitman, "Micro resonant force gauges", *Sensors and Actuators A*, vol. 30, pp. 35–53, 1992.

[85] G. K. Fedder, Q. Jing, "A hierarchical circuit-level methodology for microelectromechanical systems", *IEEE Transactions on Circuits and Systems II*, vol. 46 pp. 1309–1315, 1999.

[86] B. Courtois, J. M. Karam, S. Mir, M. Lubaszewski, V. Szekely, M. Rencz, K. Hofmann, M. Glesner, "Design and test of MEMS, Proceedings of the Twelfth International Conference on VLSI Design, Goa, India, 1999, pp. 270–275.

[87] G. K. Fedder, "Issues in MEMS macromodeling", *Proceedings of the International Workshop on Behavioral Modeling and Simulation (BMAS 2003)*, San Jose, USA, 2003 pp. 64–69.

[88] D. Paci, S. Stoffels, H. Tilmans, "Simulations of the Anchor Losses in MEM Disk Resonators", *proceedings of NSTI Nanotechnology Conference 2006*, Boston, USA , 2006, pp. 558–561.

[89] S.P. Timoshenko, J.N. Goodier, "Theory of Elasticity", *McGraw-Hill*, 1951, pp. 486-513.

[90] D. Bindel and S. Govindjee, "Elastic PMLs for resonators anchor loss simulation", *Berkeley internal report*, downloadable from http://www.cs.berkeley.edu/~dbindel/hiqlab/.

[91] T. J. Chung, "Applied Continuum Mechanics", *Cambridge International Press*, 1996, page 74

[92] R. W. Soutas-Little, “Elasticity”, *Dover Publications*, 1999, page 343.

[93] P. Chadwick, I. N. Sneddon, “Plane waves in an elastic solid conducting heat”, *Journal of the Mechanics and Physics of Solid*, vol. 6, pp. 223–230, 1958.

[94] H. E. Bommel, K. Dransfeld, “Excitation an Attenuation of Hypersonic Wave in Quartz”, vol. 117, no. 5, *Physical Review*, pp. 1245 – 1251, 1960.

[95] http://www.cs.berkeley.edu/~dbindel/hiqlab/

[96] Daniel R. Raichel, “The Science and Applications of Acoustic”, Springer, pp. 124-129

[97] Jack R. Vinson, “Plate and Panel Structures of Isotropic, Composite and Piezoelectric Materials, Including Sandwich Construction”, *Springer*, page 72.

[98] J. Lee, W.W. Schultz, Journal of Sound and Vibration, vol. 269, pp. 609-621, 2004.

[99] B. Geist and J. R. McLaughlin, Electronic Research Announcements of the American Mathematical Society, vol. 4, pp. 12 – 17, 1998

[100] “A Behavioural Model of Resonant Cantilevers for Chemical Sensing”, D. Paci, K-U. Kirstein, C. Vançura, J. Lichtenberg, H. Baltes, *proceeding of Design, Test, Integration and Packaging of MEMS and MOEMS*, Montreux, Switzerland, 2004.

[101] D. Paci, K-U. Kirstein, C. Vançura, J. Lichtenberg, H. Baltes, “A Behavioural Model of Resonant Cantilevers for Chemical Sensing”, *Analog Integrated Circuits and Signal Processing*, vol. 44, no. 2, pp. 119-128, 2005.

[102] A. Nannini, D. Paci, F. Pieri, P. Toscano, “Design of an Integrated Chemical Sensor Based on a Torsional Microbalance with Magnetic Sensing”, *proceeding of Eurosensors XIX*, Barcelona, Spain, 2005.

[103] A. Nannini, D. Paci, F. Pieri and P. Toscano, “A CMOS-compatible bulk technology for the fabrication of magnetically actuated microbalances for chemical sensing”, *Sensor and Actuators B* vol. 118, pp. 343–348, October 2006.

[104] P. Toscano, “Progettazione di un sensore per indagini genetiche basato su una struttura microelettromeccanica risonante”, *Master Degree Thesis (in Italian)*, University of Pisa, Pisa, Italy 2004.

[105] J. M. Gere, S. P. Timoshenko, “Mechanics of materials”, *Chapman&Hall*, 1991.

[106] M.C. Pirrung, “How to make a DNA chip”, *Angewaldte Chemie International Editon*, vol. 41, pp. 1276–1289, 2002.

[107] B. El-Kareh, “Fundamentals of semiconductor processing technology”, *Springer*, 1995.

[108] G. Yan, P.C.H. Chan, I.-M. Hsing, R.K. Sharma, J.K.O. Sin, Y. Wang, “An improved TMAHSi-etching solution without attacking exposed aluminum”, *Sensor and Actuators A*, vol. 89, pp. 135–141, 2001.

[109] N. Fujitsuka, K. Hamaguchi, H. Funabashi, E. Kawasaki, T. Fukada, “Silicon anisotropic etching without attacking aluminum with Si and oxidizing agent dissolved in TMAH solution”, *Sensors and Actuators A*, vol. 114, pp. 510–515, 2004.

[110] K. Biswas, S. Das, D.K. Maurya, S.K. Lahiri, “Bulk micromachining of silicon in TMAH-based etchants for aluminum passivation and smooth surface”, *Microelectronics Journal*, vol. 37, pp. 321–327, 2006.

[111] S. Brida, A. Faes, V. Guarnieri, F. Giacomozzi, B. Margesin, M. Paranjape, G.U. Pignatel, M. Zen, “Microstructures etched in doped TMAH solutions”, *Microelectronic Engineering*, vol. 53, pp. 547–551, 2003.

[112] O. Tabata, “pH-controlled TMAH etchants for silicon micromachining”, *Sensors and Actuators A*, vol. 53, pp. 335–339, 1996.

[113] S. S. Mohan, M. del Mar Hershenson, S. P. Boyd, T. H. Lee, “Simple Accurate Expressions for Planar Spiral Inductances”, *IEEE Journal of Solid State Circuits*, vol. 34, no. 10, pp. 1419–1424, 1999.

[114] A. Franchi, “Realizzazione e caratterizzazione di microbilance risonanti basate su un processo CMOS-compatibile”, *Master Degree Thesis (in Italian)*, University of Pisa, Pisa, Italy 2006.

[115] A.G. Thorsness, A. J. Muscat, “Moisture absorption and reaction in BPSG thin films”, *Journal of the Electrochemical Society*, vol. 150, pp. F219–F228, 2003.

TABLE OF CONTENTS